Prediction of the influence of the cavitation on the performance of a Kaplan turbine

Flavia Turi

Communauté UNIVERSITÉ Grenoble Alpes

THÈSE

Pour obtenir le grade de

DOCTEUR DE LA COMMUNAUTÉ UNIVERSITÉ GRENOBLE ALPES

Spécialité : MEP : Mécanique des fluides Energétique, Procédés

Arrêté ministériel : 25 mai 2016

Présentée par

Flavia TURI

Thèse dirigée par **Régiane FORTES-PATELLA**, Professeur des Universités, Grenoble INP, G-INP
et codirigée par **Guillaume BALARAC**, Maitre de Conférences, Grenoble INP

préparée au sein du **Laboratoire Laboratoire des Ecoulements Géophysiques et Industriels**
dans **l'École Doctorale I-MEP2 - Ingénierie - Matériaux, Mécanique, Environnement, Energétique, Procédés, Production**

Prédiction de l'influence de la cavitation sur les performances d'une turbine Kaplan

Prediction of the influence of the cavitation on the performance of a Kaplan

Thèse soutenue publiquement le **13 septembre 2019**,
devant le jury composé de :

Madame Regiane Fortes-Patella
PR1, Communauté Université Grenoble Alpes, Directeur de thèse
Monsieur Guillaume Balarac
Maître de Conférences, Communauté Université Grenoble Alpes, Co-directeur de thèse
Monsieur Sofiane Khelladi
Professeur, Ecole Nationale Supérieur des Arts et Métiers-ParisTech , Rapporteur
Monsieur Michel Cervantes
Professeur, Luleå University of Technology , Rapporteur
Monsieur Stéphane Aubert
Professeur, École Centrale de Lyon, Président
Monsieur Antoine Bombenger
Ingénieur, GE Renewable Energy , Examinateur

Abstract

The presence of cavitation phenomena in hydraulic machines cause several structural damages and alter the machine performances. Hence, the investigation of the cavitation in hydraulic turbine is of great industrial interest. Among the hydraulic turbine, Kaplan turbine are known for their flexibility. The guide vane opening and the runner blade position can be continuously regulated during machine operation maximizing the efficiency for a large range of operating conditions. This implies the presence of shroud and hub gaps that leads to additional cavitation structures in the runner. In this context, the principal aim of this thesis is the development of a numerical methodology able to predict and characterize the cavitation in Kaplan turbine and its impact on the machine performance. The analysis refers to a scale model of a 5-blades Kaplan turbine. RANS/URANS equations have been solved modeling the cavitating flow by using a homogeneous approach and a barotropic state law. The methodology have been defined for optimal operating conditions and, after has been tested also on the full load operating point. Experimental data have been used to validate the developed numerical method of cavitation prediction. The numerical predictions of the performances and the vapor structures obtained by applying the new cavitation calculations strategy are in very good quantitative and qualitative agreement with the available experimental data. Once the numerical methodology has been defined in-deep analyses of the cavitating flow evolution in the machine have been performed. The developed approach appears to be very reliable, robust and precise.

Keywords: Kaplan turbines, Cavitation, Performance analysis, RANS/URANS simulations, Hydroelectric energy

Résumé

La présence de structures de vapeur dans la machine peut provoquer des dommages structurels et altérer les performances de la turbine. Ainsi, l'étude de la cavitation dans les machines hydrauliques est d'un très grand intérêt pour les industriels. Parmi les turbines hydrauliques, les turbines Kaplan sont réputées pour leur flexibilité. En effet, l'ouverture des directrices et la position des aubes de la roue peuvent être régulées en continu pendant l'utilisation de la machine, optimisant son rendement sur une large plage de fonctionnement. En contrepartie, Cela implique la présence de jeux entre les parties fixes et mobiles des turbines Kaplanà qui conduit à des structures de cavitation supplémentaires à ce niveau des machines. Dans ce contexte, l'objectif principal de cette thèse est de développer une méthodologie numérique capable de prédire et de caractériser la cavitation dans des turbines Kaplan et son impact sur les performances de la machine. Dans cette thèse, un modèle réduit de turbine Kaplan à 5 pales a été analysé. Les équations RANS/URANS ont été résolues,modélisant l'écoulement cavitant à l'aide d'une approche homogène et d'une loi d'état de type barotrope. Tout d'abord, la méthodologie a été définie pour des conditions de fonctionnement optimales, puis elle a été testée également sur un point de fonctionnement à forte charge. La méthode numérique de prédiction de la cavitation qui a été développée a pu être validée à l'aide de données expérimentales. Les prédictions numériques des performances et de l'évolution des structures de vapeur obtenues en appliquant la nouvelle stratégie de calcul de la cavitation sont en très bon accord quantitatif et qualitatif avec les données expérimentales. Une fois que la méthodologie numérique a été définie, des analyses approfondies de l'évolution des écoulements cavitants dans la machine ont été effectuées. L'approche développée apparaît très fiable, robuste et précise.

Mots clef : Turbines Kaplan, Cavitation, Analyses des performances, Simulations RANS/URANS, Energie hydroélectrique.

Contents

List of Figures

List of Tables

Chapter 1

Introduction

1.1 The development of the renewable energy

In the last decade, the global energy consumption has increased by nearly twice the averaged growth rate since 2010, reaching a growth rate of 2.3% in 2018 (figure 1.1). This rise has been driven by a robust global economy and higher heating and cooling needs in some parts of the world. Higher electricity demand was responsible for over half of the growth in energy needs.

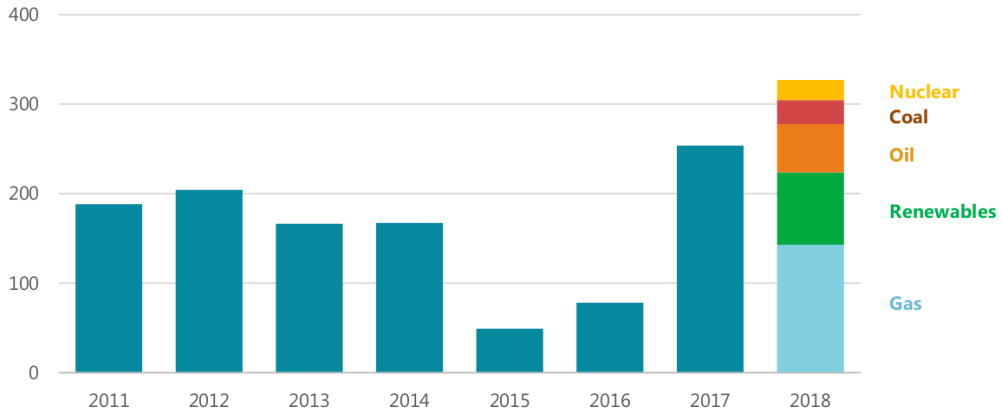

Figure 1.1 Average annual global primary energy demand growth by fuel, 2010-18 [1].

As a consequence of higher energy consumption, global energy-related CO_2 emissions rose, hitting the historical record of 33.1 $Gt\ CO_2$ in the last year. It was the highest growth rate since 2013 and 70% higher than the average increase since 2010. Looking further back, emissions have more than doubled since the early seventies and increased by around 40% since 2000. The *IEA (International Energy Agency)* assessed the impact of the fossil fuel use on global temperature increases. It found that the CO_2 emitted from coal combustion was responsible for over 0.3 C° of the 1 C° increase in the average annual surface temperatures above pre-industrial

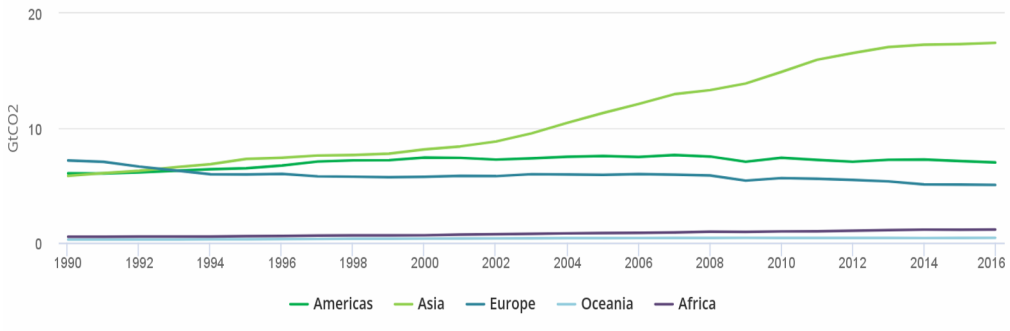

Figure 1.2 CO_2 emissions by region [1].

levels. As is shown in figure 1.2, since the early 2000s, Asia is the dominant source of emissions, reaching in 2016 twice the level of the Americas and three times the one of Europe. On the contrary, across Europe, emissions have dropped by 1.3%. The emission decline is mainly due to a drop in the coal consumption. This decrease is concentrated in the power sector, where the percentage of the renewable energies continue to rise in the energy mix. For example, France saw a significant drop in greenhouse emissions, as electricity generation from hydroelectric and nuclear power stations meant that coal and gas plants saw lower utilization in 2018 than in 2017.

This exigency to reduce the greenhouse gas emission has boosted the development of the renewable energies. Nowadays, the renewables are the second largest contributor to the global electricity production accounting the 23.8% of the world generation (figure 1.3), after the coal (39.2%). Since 1990, worldwide renewable electricity generation grew on average by 3.7% per annum, which is slightly faster than the total electricity growth rate (2.9%).

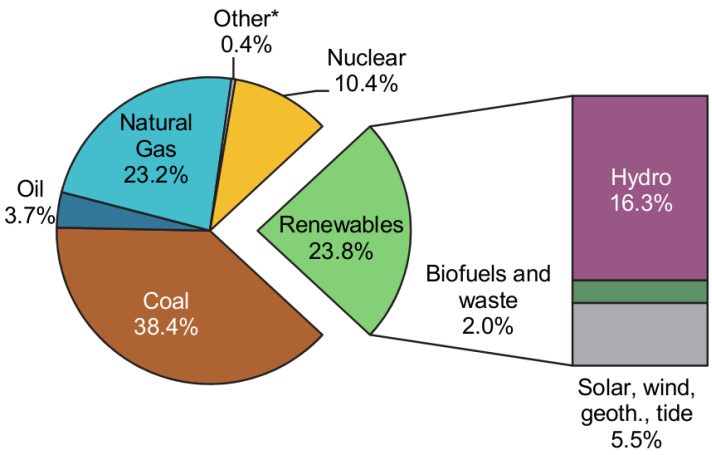

Figure 1.3 Fuel shares in world electricity production in 2016 [2].

The hydroelectricity supplies the vast majority of the renewable energy, generating 16.3% of the world electricity and the 68.4% of total renewable energy. Most of the hydro energy is produced in the OECD (Organization for Economic Co-operation and Development) countries. China, in second position, has also experienced a sharp increase of this source of energy production in the last 15 years. Similar trend has been observed in other Asian countries. The hydroelectric technology is relatively mature compared to other energy sources and is nearing its potential capacity limit in most of the OECD member states, yielding an averaged annual increase of 0.6%. Yet, the hydroelectric power is still the largest electricity producer among renewable energies. Other energy sources, such as solar photovoltaic and wind, characterized by higher growth rates (43.3% and 21.4%, respectively) are intermittent so they are not suitable for frequent changes in energy demand. On the contrary, hydropower facilities are very flexible since they can quickly go from zero power to maximum output. Moreover, since hydro power plants can generate power to the grid immediately, they provide essential back-up power during major electricity outages or disruptions. Thus, in the design phase it is necessary to ensure that the turbine can work on a very wide operating range. Using water potential energy with the efficiency over 90% it is also considered as the most efficient way to produce electricity.

Finally, another advantage of the hydro power plant is the durability. The expected life time of a plant is estimated to be around 40 years, however, there are many hydro power plants that were built more than 50 or even 100 years ago. Therefore, some upgrades and refurbishments can significantly extend the lifetime of power plants and consequently reduce the price of the electricity provided by hydropower. Moreover, the refurbishment can significantly improve the overall efficiency of the hydro power plants and increase the electricity production.

1.2 Hydroelectric power plants and hydraulic turbines

A hydraulic turbine is a machine that converts the kinetic and the potential energy of water into mechanical work. The water flowing through the machine puts in rotation the turbine blades. The turbine shaft drives an alternator which operates as a generator producing electric energy.

Hydraulic turbines can be divided into two groups:

- *Impulse turbines*: they are put in rotation using only the kinetic energy of the fluid, in the form of jets hitting the blades of the machine. The turbine blades are curved in order to change the flow direction. The resulting change in momentum (impulse) causes a force on the turbine blades. The turbine is not submerged so the pressure of the fluid is constant. The most widely used impulse turbine is the Pelton turbine. The Pelton turbines are often used in very high head applications ($H > 500\ m$).

- *Reaction turbines*: they generate electrical energy by using the mutual action of the pressure and the moving water. Contrary to the impulse turbines, the reaction turbines are completely submerged in order to induce a static pressure drop between the upstream and the downstream of the runner. Moreover, the flow is deflected by the blades generating a torque that puts the runner in rotation.

Reaction turbines can be further distinguished into Francis and axial turbines. Francis turbines are vertical axis turbines characterized by a radial inflow and an axial outflow. Due to their configuration these turbines are suitable for relatively high head ($100\ m < H < 500\ m$) applications. Kaplan turbines have also a vertical axis but they have an axial inflow and outflow so they have been developed mainly for low heads ($10\ m < H < 100\ m$) and high flow rates ($Q > 10\ m^3/s$). Contrary to Francis turbines, they have few blades, characterized by a slight curvature that allows to have low energy losses even with high flow rate. Finally, for the lowest head applications ($H < 20\ m$) the Bulb turbines are used. They are very similar to Kaplan turbines but they have a horizontal axis. The operating range of Kaplan and Bulb turbines can be further extended due to their double-regulated characteristic (see paragraph 1.3.1).

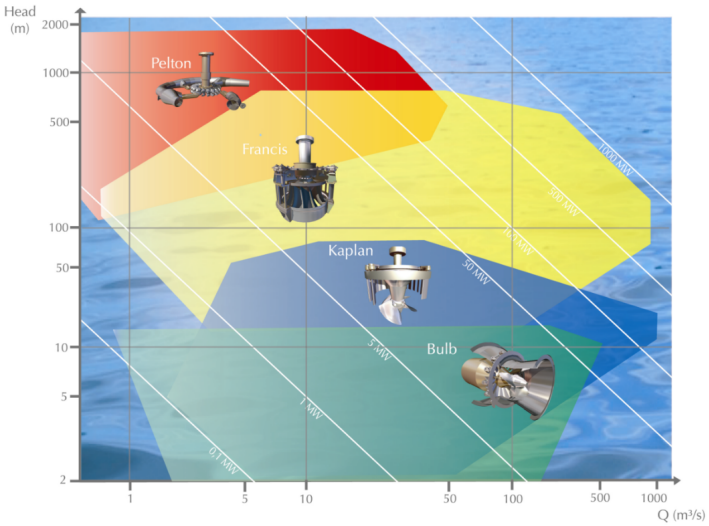

Figure 1.4 The different type of hydraulic turbine according to the head and the discharge [3].

This work is focused on the Kaplan turbines that will be presented in detail in the following section 1.3.

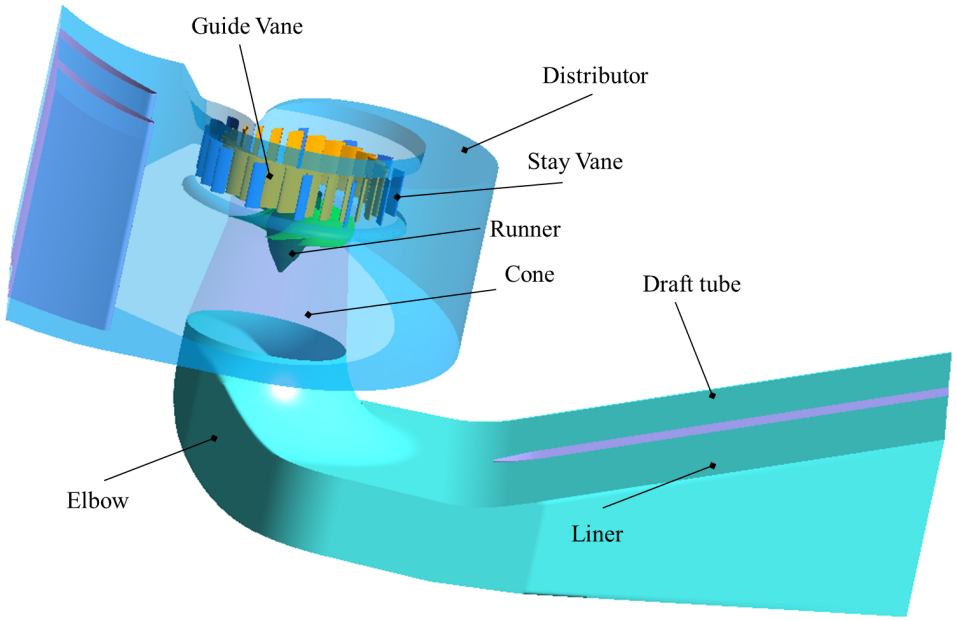

Figure 1.5 Scheme of a Kaplan turbine.

1.3 Kaplan Turbines

1.3.1 Machine description

The main parts of a Kaplan turbine (schematized in figure 1.5) are:

- the *distributor*, is connected to the upstream reservoir via a penstock and drives the flow towards the runner. It is generally spiral shaped to feed the runner evenly over the entire circumference.
- the *stay vane* composed by fixed blades with have structural function and to drive the flow to the guide vane. To support the structure, the stay vane has several large vanes which are profiled to reduce the hydraulic losses of the flow coming from the distributor.
- the *guide vane* consisting in adjustable blades. The guide ring has a double function: to provide a kinetic momentum to the upstream runner flow and to control the flow rate by adjusting the blades opening angle.
- the *runner*, the most important part of the turbine. The kinetic momentum provided by the guide vane is transformed by the runner mostly into rotational mechanical energy. In order to have an efficient production of reaction force for different flow conditions, the rotor blades angle is adjustable. For this reasons Kaplan turbines are also called *double-regulated* turbines. A flat profile is used for very low flow rates, whereas a

heavily-pitched profile is set for high flow rates. This involves that the operating range of the Kaplan turbine varies widely.

- the *draft tube*, characterized by a divergent geometry to increase the flow pressure decreasing its velocity. This allows to recover the kinetic energy presented in the flow on the runner outlet reducing the energy losses and improving the machine efficiency. In the vertical axial turbine, the draft tube is composed by three parts: the cone, the elbow and the liner.

1.3.2 Machine performance

In figure 1.6 is reported the scheme of an hydroelectric facility: the turbine works between two reservoirs, one upstream and one downstream.

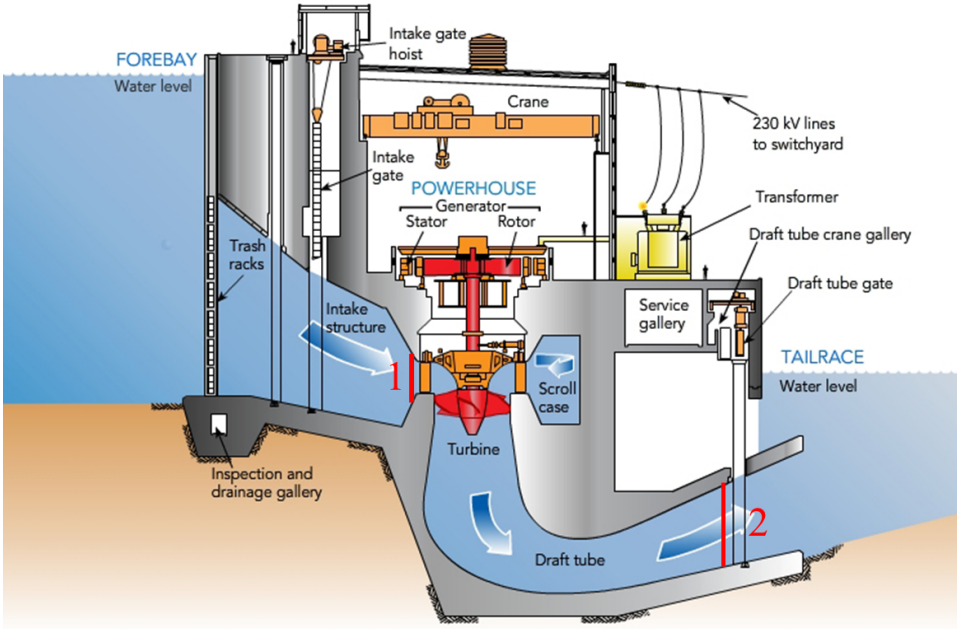

Figure 1.6 Cross-section view of a hydro power plant [4].

The hydraulic head in a given point of the system **x** can be defined as :

$$H_x = \frac{P_x}{\rho g} + z_x + \frac{V_x^2}{2g}\,, \tag{1.1}$$

where P_x is the static pressure, ρ is the fluid density, g is the gravity acceleration, z_x is the elevation from a determined reference axis and V_x is the flow velocity.

Considering the total pressure as the sum of the static, potential and dynamic pressures:

$$P_{tot} = P + \rho z g + \rho \frac{V^2}{2} , \tag{1.2}$$

the head can be expressed as a function of the total pressure:

$$H = \frac{P_{tot}}{\rho g} . \tag{1.3}$$

The amount of energy that can be transformed into electricity by the turbine and generator in an hydro power plant corresponds to the head difference between the upstream and the downstream tanks:

$$H_g = H_{up} - H_{down} = \left(\frac{P_{up}}{\rho g} + z_{up} + \frac{V_{up}^2}{2g} \right) - \left(\frac{P_{down}}{\rho g} + z_{down} + \frac{V_{down}^2}{2g} \right) . \tag{1.4}$$

In both tanks, the gauge pressure is equal to the ambient one and the flow velocities on the surface are neglectable. Thus, it can be reduced to the difference between the upstream and the downstream levels. No losses have been considered in this formulation so, the real amount of energy that can be harnessed by the turbine will be lower. This recovered energy quantity is the *net head* H_n and corresponds to the difference of the head values on the distributor inlet (section **1** in figure 1.6) and on the draft tube outlet (section **2** in figure 1.6). In the hypothesis of a stationary and uniform flow in both sections, the net head can be expressed as:

$$H_n = H_1 - H_2 = \left(\frac{P_1}{\rho g} + z_1 + \frac{V_1^2}{2g} \right) + \left(\frac{P_2}{\rho g} + z_2 + \frac{V_2^2}{2g} \right) . \tag{1.5}$$

The net hydraulic power recovered by the runner is a function of the net machine head H_n and the flow rate Q:

$$P_h = \rho g Q H_n . \tag{1.6}$$

An amount of this net power is lost in the different parts of the turbine. The actual mechanical power to the runner shaft can be calculated as a function of the rotational speed ω and the torque T resulted on the turbine shaft:

$$P_m = T \omega . \tag{1.7}$$

The efficiency of the turbine is called the *hydraulic efficiency* and can be evaluated as the ratio between the mechanical and hydraulic powers:

$$\eta_h = \frac{P_m}{P_h} = \frac{T\omega}{\rho g Q H_n} \,. \tag{1.8}$$

Introducing the *internal head* quantity H_i that represents the amount of the energy transfered from the flow to the turbine, the mechanical power can be also expressed as:

$$P_m = \rho g Q H_i \,. \tag{1.9}$$

The hydraulic efficiency η_h can be also considered as the internal and net heads ratio $\eta_h = H_i/H_n$.

Hereafter, we will be refer to the net head as head and it will be indicated with H and to the hydraulic efficiency as efficiency and it will be indicated as η.

1.3.3 Hill chart

A Kaplan turbine is defined as a double-regulated turbine since both of the guide vane opening (γ) and the runner blade (α) angles can be adjusted. It allows the machine to adapt to imposed discharge Q and head H, widening its operating range. A turbine operating point is defined by a guide vane opening γ (that fix the inlet flow rate Q), the blade angle α and the machine head H. So, the combination of these three parameters that allows to maximize the energy recovered by the runner is called the CAM relation. When the CAM relation is respected, for a given H, the guide vane opening is adapted to the blade angle and the operating point is defined as "on-cam". On the contrary, the turbine works in "off-cam"operating conditions when the guide vane and the blade angles do not respect the CAM relation (i.e. in turbine start or stop phases). The range of the turbine operating conditions can be defined by means of characteristic curves. Usually, these curves are plotted as a function of two parameters, derived from the similarity laws, that link the flow rate, the net head and the runner rotational speed as [5]:

$$Q_{11} = \frac{Q}{D^2\sqrt{H}} \qquad n_{11} = \frac{nD}{\sqrt{H}} \,, \tag{1.10}$$

where D is the runner outlet diameter, H is the net head and n is the turbine rotational speed. The parameters defined in equation 1.10 are the unitary discharge Q_{11} and the unitary rotational speed n_{11}. They represent the discharge and the rotational machine velocity of an equivalent turbine with a 1 m diameter and a 1 m head. Fixing the blade angle α, the evolution of the machine efficiency η as a function of Q_{11} is reported in figure 1.15 a. The top of this curve

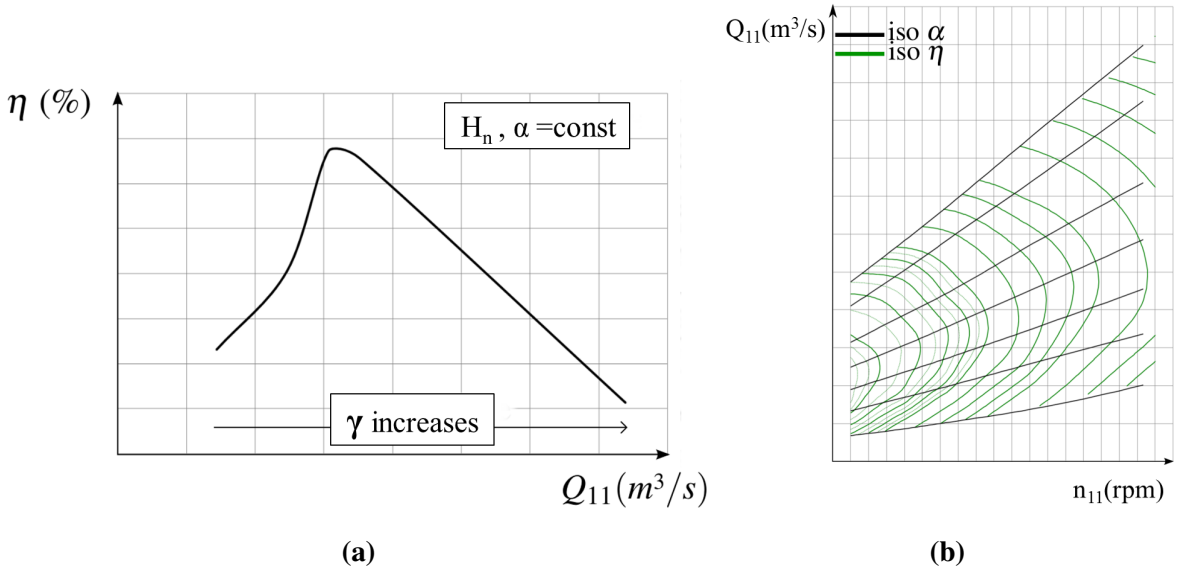

Figure 1.7 Characteristic curves of a double-regulated turbine: **(a)** with fixed blade angle α and **(b)** the final hill chart [3].

corresponds to the "on-cam"point for a given head H and blade angle α values. The set of the "on-cam"points for the different H and α values constitutes the performance hill chart of the turbine (figure 1.15 b). So, the double-regulated turbine hill chart consists in η and α iso-values curves that define the turbine performances for fixed operating conditions. They are obtained by experimental measurements.

1.3.4 Velocity triangles

In a Kaplan turbine the fluid exits from the guide vane with a radial direction. Before the runner inlet, the channel deviates the flow to ensure an axial entry in the runner. A fluid flows through the runner with an absolute velocity $\vec{V}$, in the inertial reference frame, and a relative velocity $\vec{W}$, in the reference frame that rotates with the runner at the angular velocity ω. Considering that the runner tangential velocity $\vec{U}$ can be defined as:

$$\vec{U} = \vec{\omega} \times \vec{r}\,, \tag{1.11}$$

where $\vec{r}$ is the fluid particle vector position, the following relation can be determined:

$$\vec{V} = \vec{W} + \vec{U}\,, \tag{1.12}$$

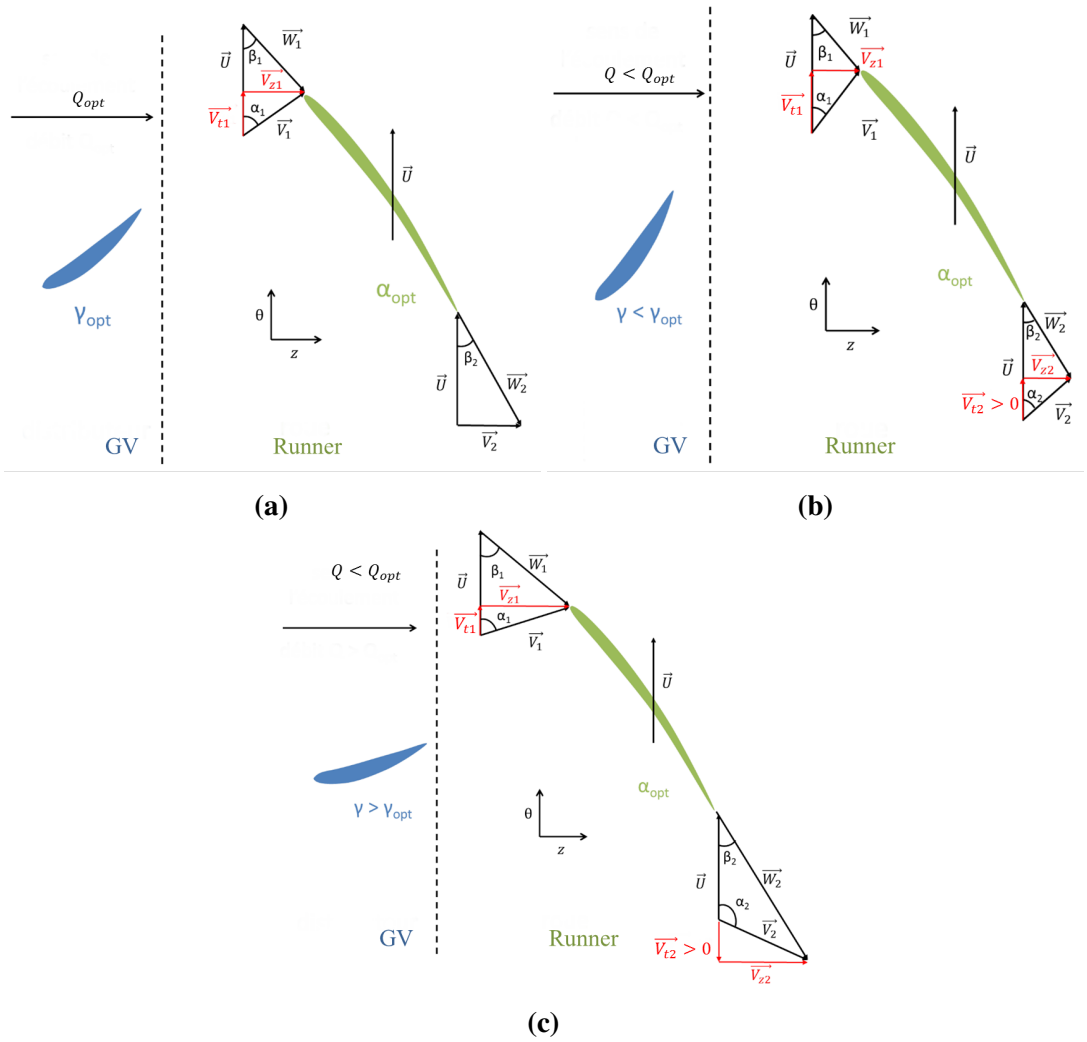

Figure 1.8 Velocity triangles in a Kaplan turbine in three different operating points: **(a)** optimal load, **(b)** partial load and **(c)** full load [3].

The equation 1.12 allows to define the fluid velocity triangle on the runner inlet and outlet. Considering a cylindric frame of reference (r, θ, z), the velocity vector $\vec{V}$ can be decomposed in three components: the radial V_r, the tangential V_t and the axial V_z velocities. Usually the flow in turbomachinery is analyzed in two planes: the meridian and the blade-to-blade planes (indicated with **a** and **b** in figure 1.9, respectively) . The component of the velocity in the meridian plane V_m is given by the vectorial sum of the radial V_r and the axial V_z velocities. In the runner of a Kaplan turbine, V_r is negligible compared to the other velocity components so axial and meridional velocities are almost equal.

In figure 1.8 are reported the velocity triangles, plot at mid-hight of the blade, for three different turbine operating points: in **a)** optimal load, **b)** partial load and **c)** full load conditions. The fluid angle α is determined by the absolute velocity $\vec{V}$ and the tangential velocity $\vec{U}$. The

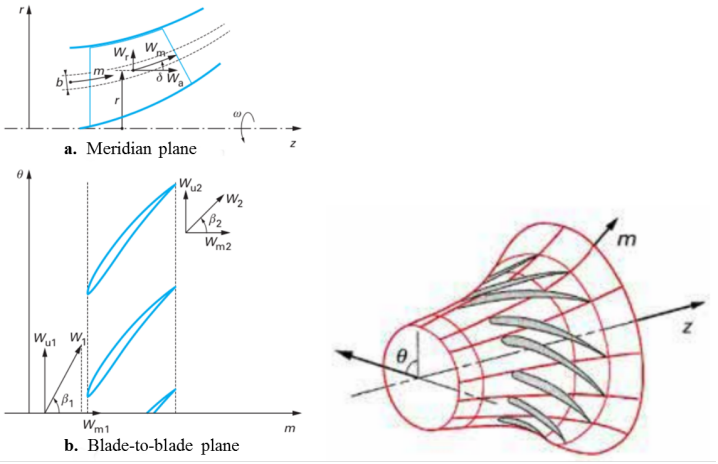

Figure 1.9 Meridian and blade-to-blade planes [6] (on the left) and their 3D visualization [7] (on the right) .

blade angle β is between the relative velocity $\vec{W}$ and the tangential velocity $\vec{U}$. The index **1** indicates the runner inlet quantities and the index **2** the runner outlet variables. So the angle β_1 is imposed to the fluid by the guide vanes while the angle β_2 is imposed by the runner blade trailing edge inclination.

In optimal conditions (figure 1.8 a) almost the entire kinetic momentum given by the guide vane to the flow is recovered by the runner. In ideal conditions, on the runner outlet, V_t is null and the flow is quasi-axial (there still remains a little radial component).

In the partial load operating point (figure 1.8 b) the guide vane opening angle γ and the flow rate Q are smaller than the optimal point. As a consequence, V_z is reduced while V_t increases. This means that, on the runner outlet, there is a V_t that puts the flow on the draft tube inlet in rotation, in the same direction than the runner rotation.

On the contrary, at full load (figure 1.8 c), the guide vane angle and the discharge values are higher than the optimal point so V_t on the runner inlet is smaller. As a result, V_t on the runner outlet is negative and puts the flow in counter-rotation with respect to the runner rotation direction.

Thus, the optimal operating conditions corresponds to a null V_t on the runner outlet in order to maximize the internal head H_i. For this reasons, the runner blades are designed to minimize the tangential velocity component on the runner outlet to avoid the flow separation phenomena in the draft tube.

1.3.5 Energy conversion in the runner

The machine torque can be correlated to the flow dynamic in the runner by means of the Euler Theory. This formulation is established for a steady inviscid flow, in a runner composed by

an infinite number of blades, in order to consider a uniform flow in the runner upstream and downstream sections.

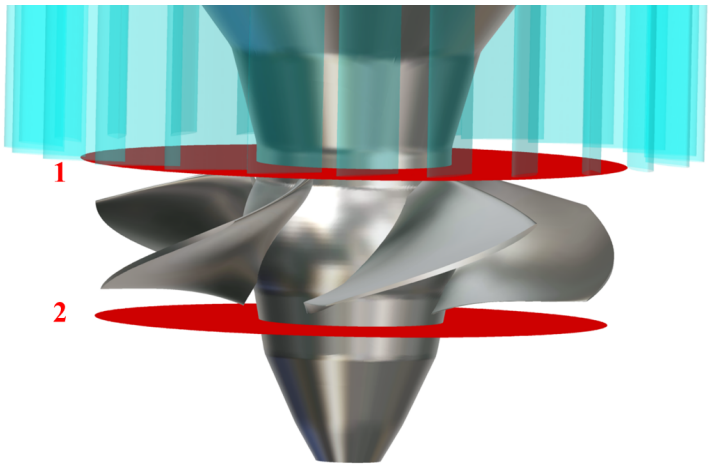

Figure 1.10 Runner inlet/outlet sections.

The torque T transfered from the fluid to the turbine shaft can be linked to the tangential velocity fields on the runner inlet and outlet (indicated as **1** and **2** in figure 1.10, respectively), applying the balance moment equation between these two sections:

$$T = \rho Q \left(R_1 V_{t_1} - R_2 V_{t_2} \right) \ . \tag{1.13}$$

Starting from this torque definition (equation 1.13), the internal head H_i becomes:

$$H_i = \frac{\omega}{g} \left(R_1 V_{t_1} - R_2 V_{t_2} \right) \ . \tag{1.14}$$

The internal head represents the amount of the theoretical head recovered by the runner. The quantity of energy that can be actually used by a turbine is much lower. Indeed, real runners consist in a finite number of blades. Moreover, the fluid flowing in the turbine has a viscosity that introduces in the system additional losses. This causes a reduction of the machine head and, as a result, the internal head. Finally, in off-cam operating conditions, losses due to the perturbation of the angle flow incidence on the blades have to be considered. Despite this, the Euler theory allows to preliminary estimate the losses in the runner. The losses in this component can be calculated as:

$$\Delta los = H_{run} - H_i = \left[\frac{P_1}{\rho g} + z_1 + \frac{1}{g} \left(\frac{V_1^2}{2} - U_1 V_{t1} \right) \right] - \left[\frac{P_2}{\rho g} + z_2 + \frac{1}{g} \left(\frac{V_2^2}{2} - U_2 V_{t2} \right) \right] \ . \tag{1.15}$$

Considering the velocity diagrams in both upstream and downstream runner sections (figure 1.8):

$$\begin{cases} V^2 = V_z^2 + V_t^2 \\ W^2 = V_z^2 + (U - V_t)^2 \end{cases} \Rightarrow \frac{1}{2}V^2 - U\,V_t = \frac{1}{2}\left(W^2 - U^2\right) . \tag{1.16}$$

Replacing the equation 1.16 in the equation 1.17 the $\Delta\, los$ in the runner can be expressed in the following form:

$$\Delta\, los = \left[\frac{P_1}{\rho g} + z_1 + \frac{1}{2g}\left(W_1^2 - U_1^2\right)\right] - \left[\frac{P_2}{\rho g} + z_2 + \frac{1}{2g}\left(W_2^2 - U_2^2\right)\right] . \tag{1.17}$$

In the study of flows within rotating system a fluid mechanic property of some importance is the Rothalpy defined as:

$$R = P + \rho g z + \frac{1}{2}\rho\left(W_1^2 - U_1^2\right) . \tag{1.18}$$

So, the losses in an hydraulic turbine runner can be calculated as a function of the Rothalpy variation between the runner inlet and outlet:

$$\Delta\, los = \frac{R_1 - R_2}{\rho g} . \tag{1.19}$$

Cavitation phenomena can occur in hydraulic turbine in different operating regimes. One of the main consequence is the introduction of additional losses terms in the energy balance of the machine.

1.4 The Cavitation

The cavitation phenomenon can be described as the appearance of vapor bubbles in an initially homogeneous liquid medium. The cavitation structures in the liquid occur due to a local pressure decrease, while the temperature remains approximately constant. The threshold value of the pressure that triggers the cavitation is called vapor pressure P_V.

Considering the $P - T$ phase diagram for the water (figure 1.11), the vapor pressure is represented by the line between the triple point Tr and the critical point C, separating the liquid phase from the vapor phase. This means that crossing the curve under static conditions causes the change of the phase from liquid to vapor. As it is possible to observe in figure 1.11, the vapor pressure of a liquid is function of the temperature and the pressure. The cavitation in cold water (operating condition of the hydraulic turbine) usually occurs at almost isothermal conditions, while the local pressure varies (a similar phenomenon to the cavitation is the boiling,

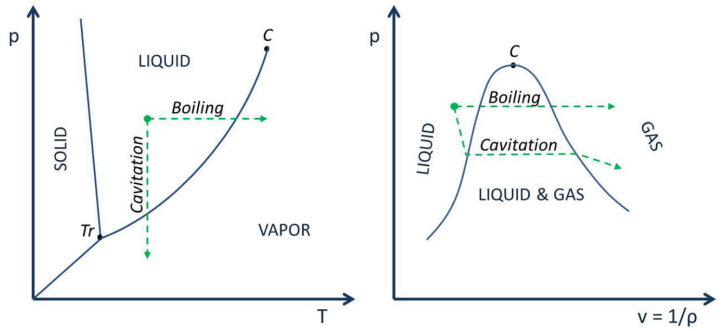

Figure 1.11 Water phase diagram on the P-T plane (on the left) and on the (P-v) plane (on the right) [8].

where the vaporisation occurs as a consequence of the temperature increase while the pressure remains constant).

Generally, after the liquid has cavitated, the pressure returns back to the initial value (above the P_V) and the produced bubbles start to implode. During the bubble collapse, strong pressure waves can be emitted, and one of the consequences can be serious damage of the nearby solid walls.

According to Franc [9, 10], four different types of cavitation can be identified depending on the generating cause:

- **Hydrodynamic cavitation**: caused by a submerged body (i.e. rotor blade, profile, etc...).
- **Acoustic cavitation**: generated by the sound waves that spread through the fluid.
- **Optic cavitation**: caused by the laser lights.
- **Particles cavitation**: caused by other elementary particles, e.g. protons.

The hydrodynamic and the acoustic cavitations is provoked by strains in the fluid; on the contrary, the optical cavitation and the cavitation of particles start because of a local energy input into the fluid. In hydraulic machines, hydrodynamic cavitation is the most important.

The appearance of the hydrodynamic cavitation is due to several effects as the shape of the submerged body, the surface roughness, the presence of a boundary layer between the vapor and water which have different velocities and the vibrations of the submerged body.

Different types of cavitation are observed depending on the flow conditions and the geometry of the submerged body. Five different hydrodynamic of cavitation exist, presented on the figure 1.12:

- **a) Transient isolated bubbles**. Type of cavitation where individual bubbles form in the liquid and move with the flow. They occur in low pressure regions, travel with the flow until they implode in the regions with high pressure.

- **b) Sheet cavitation**. It is attached to the leading edge of the submerged bodies, i.e. low pressure side of blades and foils. The shape of the sheet can change with time.
- **c) Cloud cavitation**. Cloud cavitation is the origin of the most engineering problems related with hydrodynamic cavitation, including erosion, vibrations and noise. It is provoked by the vorticity in the flow field. The periodic shedding of cavitation clouds is caused by the re-entrant jet.
- **d) Supercavitation**. This cavitation occurs when the sheet cavitation envelopes the whole submerged solid body.
- **e) - f) Cavitating vortices**. Usually occurs as a result of high shear stresses in the region inside the low-pressure cores of vortices. It is most commonly observed on the tips of the rotating blades or behind the outlet of the runner.

1.4.1 Cavitation in hydraulic turbines

In different types of hydraulic machines, the cavitation phenomena and their effects have been studied and presented by [11, 12]. The vapor structures in the turbine lead to several issues :

- **Turbine performance alteration**: the attached cavitation sheets on the runner blades deviate the flow path influencing its incidence angle on both of the leading and the trailing edge. This leads to an alteration of the torque on the shaft T and, as a result, of the machine efficiency η.
- **Modification of the mechanical stresses applied on the machine**: the dynamic of the vapor structures in the liquid, in proximity of the blade, influences the equilibrium of the efforts applied by the flow on the runner.
- **Material erosion**: the implosion of the cavitation bubbles nearby walls generates a premature erosion of the runner components. In Kaplan turbines, major erosion effects are observed on the blades and on the discharge ring.
- **Pressure and discharge fluctuations**: The cavitation is an unsteady phenomenon that generates low and high frequency pressure and flow rate oscillations.
- **Noises and vibrations**: The pressure oscillations are linked to the cavities dynamic and collapses. As a result, vibration and acoustic noises are generated and propagated through the hydrodynamic and mechanical system.

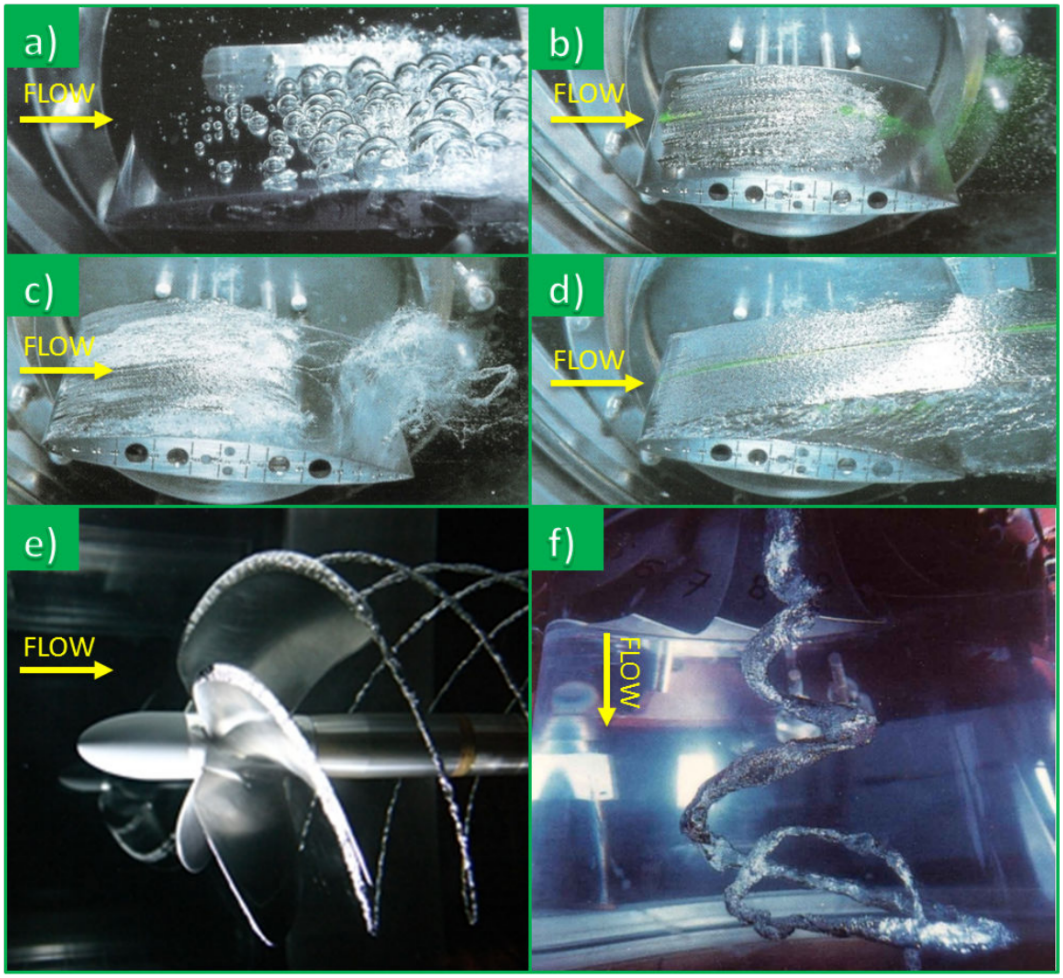

Figure 1.12 Types of cavitation: **a)** Traveling bubble cavitation, **b)** Sheet cavitation, **c)** Cloud cavitation, **d)** Supercavitation, **e)** and **f)** Cavitating vortices [10].

Consequently, the cavitation must to be prevented in turbomachinery and its prediction is essential in order to improve the turbine design.

As mentioned before, the cavitation occurs in the turbine when the local pressure drops under the critical vaporisation pressure. To characterize the level of cavitation, the *Thoma number* (or *cavitation number*) σ is used and is defined as:

$$\sigma = \frac{NPSH}{H} \,. \tag{1.20}$$

where $NPSH$ is the Net Positive Suction Head and H is the machine head (see section 1.3.2).

The $NPSH$ is the net available energy at the low pressure side of the machine since it corresponds to the difference between the available energy on the machine outlet and the vapor

pressure P_V

$$NPSH = \frac{P_2 - P_V}{\rho g} + \frac{V_2^2}{2g} - \left(z_{ref} - z_2\right) \ , \tag{1.21}$$

where the subscript **2** denotes the low pressure reference section (the draft tube outlet) and z_{ref} is the machine reference level. The *NPSH* represents the safety margin to complete cavitation conditions; the lower, the higher the cavitation risk. So, the limit of the *NPSH* define the setting level $h_s = z_{ref} - z_2$ to avoid the cavitation.

Lower cavitation number σ leads to more intense cavitation phenomena. Usually, the evolution of the influence of the cavitation on the turbine performance is evaluated by means of the σ-*break cavitation*. This curve represents the machine efficiency η as a function of the Thoma number σ (as is shown in figure 1.13).

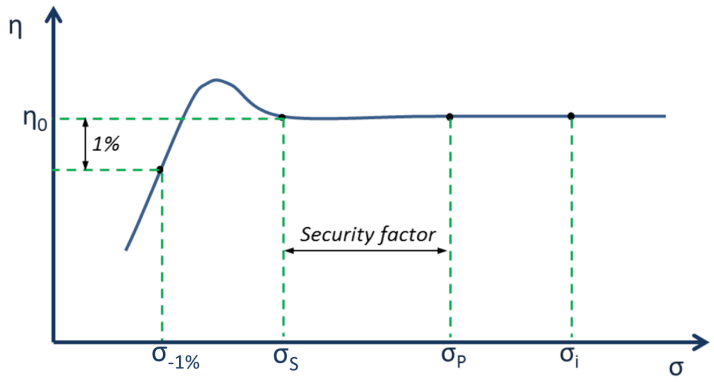

Figure 1.13 σ-break curve.

According to the the International Electrotechnical Commission IEC 60193 Code [13], several typical values of the cavitation number are marked on the chart:

- σ_i: the incipient cavitation value. Usually it is set by a visual experimental observation. The incipient cavitation value is lower when the flow rate is close to optimal load conditions, therefore the attack angle is well adapted to the blades. On the contrary, increasing or decreasing the inlet discharge value, this value raises due to a variation of the flow incidence angle.

- σ_p: the lowest Thoma number value when the machine is still allowed to operate.

- σ_s: the smallest cavitation number value when the level of the cavitation does not influence the turbine performance curve.

- $\sigma_{-1\%}$: marks the level of the cavitation that causes 1% of the machine efficiency drop $\eta_{-1\%}$ (sometimes also $\sigma_{-0.5\%}$ is considered).

An increase of the efficiency is observed in figure 1.13 during high cavitating flow for σ lower than σ_s. This behavior is not always present and usually occurs at the partial load conditions. The origin of the phenomenon is a better flow adaptation to the blades due to the presence of the cavitation sheets on the turbine blades [13].

1.4.2 Cavitation phenomena in Kaplan turbines

The peculiarity of the Kaplan turbine is its flexibility: the guide vane opening γ and the runner blade position α can be continuously regulated during machine operation to maximize the efficiency for a large range of operating conditions. However, this implies the presence of shroud and hub gaps that leads to additional cavitation phenomena in the runner.

For the design operating range a cavity development occurs at the root of the blade (figure 1.14). This type of cavitation is known as **hub cavitation** and is due to the combination of the spherical shape of the hub and to the presence of a gap between the blade and the runner hub. Among the cavitation phenomena, the hub cavitation most affects the turbine performance [12]. When the hub cavity reaches the trailing edge of the blade a drop of the machine efficiency is observed. It depends significantly on the σ and determines the machine $NPSH$.

Figure 1.14 Hub cavitation [14].

Likely at the hub the presence of a tip clearance between the shroud and the blades causes two cavitation phenomena [14]. The first type is called the **tip clearance cavitation** and takes place on the tip of the blade (figure 1.15 a). The pressure difference between the pressure and the suction sides of the blades causes a flow through the tip clearance. When the local pressure drops below the vapor pressure, the tip clearance cavitation occurs. The second type of cavitation is the **tip vortex cavitation**. It occurs when the tip clearance flow leaves the gap creating a jet (see figure 1.15 b). The jet leaves the suction side of the blade generating a vortex near the tip. The vortex begins nearby the blade leading edge, detaches the blade

surface and continues downstream along the blade profile, in the trailing edge direction. The flow in the shroud gap does not contribute to the torque causing a consequent reduction of the turbine efficiency. Moreover the tip cavitation phenomena cause erosion of the blade tip and the discharge ring. Several possibilities exist in order to avoid the tip cavitation. For instance the gap between the shroud and the blade can be reduced to its technological minimum. In addition, anti-cavitation lips can be installed on the blade tip that push the tip vortex core away from the blade surface [14]. The tip cavitation usually occurs as the first from all types of cavitation and it is not very dependent on the Thoma number. Depending on the head, limited amounts of tip clearance and vortex cavitation are tolerated in standard operating conditions [12].

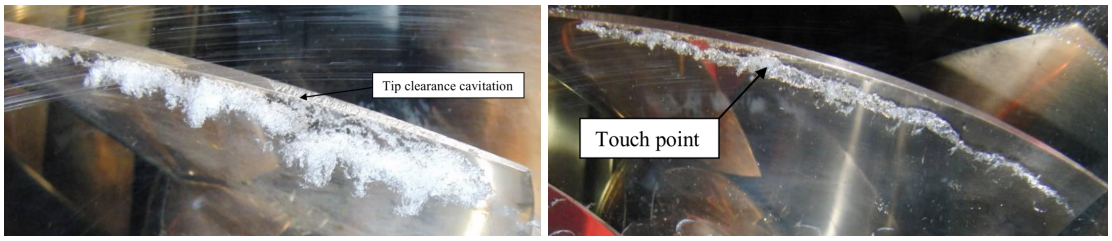

(a) **(b)**

Figure 1.15 Cavitation phenomena on the runner tip : **(a)** tip clearance and **(b)** tip vortex cavitation [14].

Cavitation phenomena can occur on the blade leading edge due to a deviation of the flow incidence angle from the design value. Attached cavities can be observed on the blade suction side at higher head than the optimal operating conditions and also on the pressure side at lower head values (see figure 1.16). If unstable, the **leading edge cavitation** is a very aggressive cavitation and can lead to erosion phenomena. This type of cavitation can be avoided by improving the shape of blade leading edge.

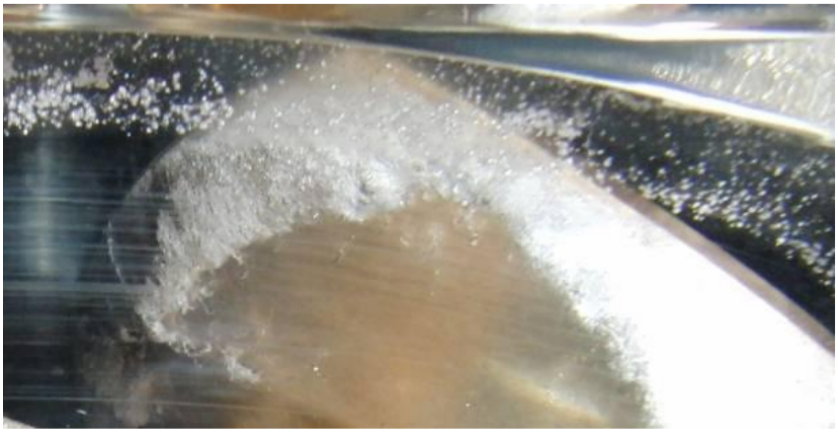

Figure 1.16 Leading edge cavitation [14].

Finally, the **vortex rope cavitation**, shown in figure 3.3, can occurs in both partial and full load conditions. Due to the presence of a residual tangential velocity component on the runner outlet, a vortex-core cavitation flow can be formed in the draft tube. This vortex rotates in the same direction than the runner in partial load conditions and in the opposite direction in overload. At partial load, the vortex rope introduce in the system low frequency circumferential pressure pulsations. If they match one of the free natural oscillation frequencies of the draft tube strong vibrations can occur which can damage the draft tube structure [15, 16].

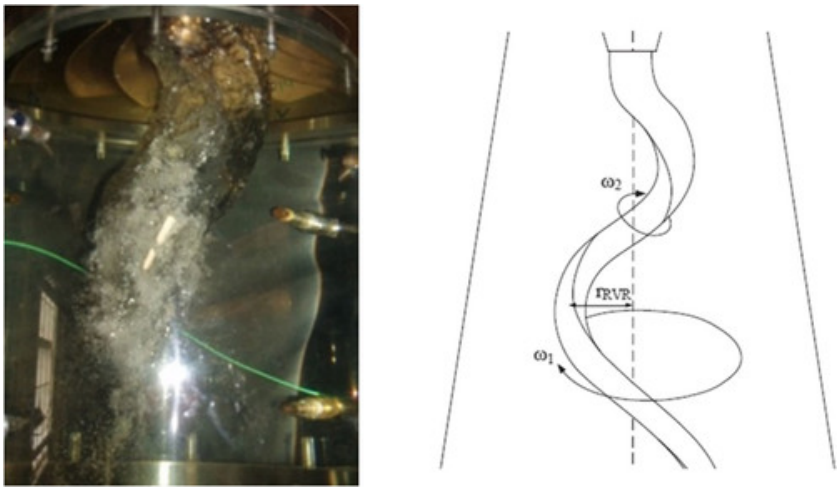

Figure 1.17 Leading edge cavitation [16].

1.5 Thesis Objectives

The cavitation in hydraulic machinery is a very dangerous phenomenon that lead to several negative effects, e.g. the risks of erosion and the alteration of the turbine performances. Experimental cavitation tests allow, for each investigated operating point, to identify the limit of the cavitation, to plot the σ-break curve, to observe the appearance and the evolution of the vapor structures and to estimate the pressure fluctuations introduced in the system by the cavitating flow. But, experiments are expensive, time-consuming and do not allow in-deep analyses of the cavitating flow. CFD simulations provide a useful, cost-efficient tool to analyze complex flows in turbomachinery. Therefore, the development of a numerical methodology able to accurately reproduce the flow behavior in cavitating conditions is very attractive for the industry. The present study focuses on the prediction and the analysis of cavitation phenomena inside a Kaplan turbine. The objectives of the thesis are the following:

- The main objective is to develop a numerical approach to enable the accurate prediction of the cavitation influence on the Kaplan turbines performances. The computational

methodology have to predict, as accurate as possible, the shape and the evolution of the vapor structures in the turbine and the consequential alterations of the machine performances. The knowledge of the cavitation limits is very useful in the turbine concept phase in order to improve the design of the machine components increasing the turbine flexibility.

- Another objective is to make a detailed analysis of the cavitating flow in the turbine. The analysis should include the investigations, all along the σ-break curve, of the velocity and the pressure fields in the runner and in the draft tube, the two most critical parts of the machine. The identification of the different sources of energy losses in the turbine and their evolution with the increase of the vapor amount in the runner is essential to relate the modification of the performance to the cavitation. Finally, the analysis of the pressure spectra and of the vapor structure in several cavitating conditions has a fundamental role in order to characterize the dominant cavitation frequencies. These analyses allow to perform more sophisticated investigation of the cavitation flow in the turbine and its related phenomena.

The methodology, the developed numerical tools and the analyses could be an important basis for the future studies of the cavitating phenomena in Kaplan turbines, not only for the presented geometry and operating conditions, but also for any kind of Kaplan turbine, in different points of the turbine hill chart.

1.6 Document organization

In this first chapter, the general context of the study has been described. The importance of the renewable energies and in particular of the hydroelectricity in the current energy scenario has been presented. Afterwards, the main peculiarity of hydro power plants and hydraulic turbines have been introduced. The description have been focused on the Kaplan turbine defining its fundamental characteristics. In the second part of the introduction, the phenomenon of the cavitation was explained, detailing the effects on the Kaplan turbines. Finally, the objective of the thesis in correlation to the described background have been clarified.

The second chapter (2) will describe the numerical and the physical models applied in this work. The governing equations, the turbulence and the cavitation modeling used will be presented followed by a brief description of the numerical schemes. This chapter will end with the state of the art of the numerical simulation of the cavitating flow in Kaplan turbines. This overview will be very useful in order to understand the starting background of the developed numerical methodology.

The third chapter (3) will start with an overview of the literature for cavitation experiments in Kaplan turbines. Indeed, the previous works have been fundamental to the determination of the experimental tests planning. Subsequently, the experimental setup and techniques used in this work will be described.

The developed numerical methodology will be detailed in chapter four (4). Firstly, the reduced scale model and the operating points investigated will be presented. For the two operating conditions (optimal load and full load), the discretization meshes, the tested turbulence models and the determination technique of the boundary conditions setup will be described.

The results will be divided into two chapters: the fifth chapter (5) will be dedicated to the results of the steady simulations and the chapter six (6) to the results of the unsteady investigations. In the first part of the chapter five (5) the numerical strategy definition steps will be presented and validated thanks to comparisons with experimental data. In the second part, after the methodology will be fully determined, in-deep analyses of the cavitating flow and of the losses in the different components of the machine will be shown. In the sixth chapter (6) the results obtained in optimal load conditions will be firstly analyzed and compared with steady investigations. Secondly, to validate the generality of the developed calculation methodology, the analyses in unsteady conditions of the full load operating point will be presented.

In the seventh chapter (7), the conclusions and the perspectives of this work will be drawn.

Chapter 2

Numerical and physical models

In this chapter, the numerical and physical models applied in the present work will be presented. The first section is dedicated to the numerical models used to simulate a single phase flow in turbomachinery. In the second part the two-phases flow modeling techniques will be introduced focusing on the cavitating flow models. Afterwards the numerical schemes of FINE™/Turbo will be described. Finally, a literature review of the numerical studies of cavitating flow in Kaplan turbines will be proposed.

2.1 Single phase flow modeling

2.1.1 Governing equations

In order to describe the behavior of the fluid an Eulerian approach can be used. The flow is considered as a deformable continuum where variable fields changing in the space and in the time (i.e. velocity, pressure, density, ...) are defined in every point of the domain, hence defining a field for the considered variable. In the hypothesis of a Newtonian fluid, the mass and the momentum balance equations in the vectorial form, in a Cartesian coordinate system can be written in the form:

$$\frac{\partial \rho}{\partial t} + \nabla \cdot \left(\rho \vec{V} \right) = 0 \,, \tag{2.1}$$

$$\frac{\partial \rho \vec{V}}{\partial t} + \left(\vec{V} \cdot \nabla \right) \rho \vec{V} = -\nabla p + \nabla \cdot \overline{\overline{\tau}} + \vec{F} \,, \tag{2.2}$$

where:

- the left side of the equation represents the Lagrangian acceleration;
- ∇p is the pressure forces;

- $\vec{F}$ is the volume external forces applied on the fluid (in the case of study only the gravity force will be considered);

- $\bar{\bar{\tau}}$ is the shear stress tensor. For a Newtonian fluid it can be defined as:

$$\bar{\bar{\tau}} = \nabla \cdot \left(\mu \left(\nabla \vec{V} + \nabla \vec{V}^T \right) \right) - \frac{2}{3} \mu \left(\nabla \cdot \vec{V} \right) \bar{\bar{I}} \, . \tag{2.3}$$

In the present thesis, the investigated fluid is cold water so it can be considered as isothermal and the energy balance equations can be neglected.

In the turbomachinery analysis, the momentum equation can be defined in the runner rotating reference frame. In the case of a constant rotation speed ω, two additional source terms appear in the equation, which account for the centrifugal and Coriolis forces. The balance equation of the momentum in the relative reference of frame is written as:

$$\frac{\partial \rho \vec{W}}{\partial t} + \left(\vec{W} \cdot \nabla \right) \rho \vec{W} = -\nabla p + \nabla \cdot \bar{\bar{\tau}} + \vec{F} - 2\vec{\omega} \wedge \vec{W} - \vec{\omega} \wedge (\vec{\omega} \wedge \vec{r}) \ , \tag{2.4}$$

where $\vec{W}$ is relative velocity (see chapter 1).

2.1.2 RANS and URANS models

A turbulent flow is characterized by chaotic changes in pressure and flow velocity. It is in contrast to a laminar flow, which occurs when a fluid flows in parallel layers, with no disruption between those layers. Thus, the resolution of Navier-Stokes equations for a turbulent flow can be more complex than in laminar case. The limit between laminar and turbulent regimes is determined by means of the Reynolds number. It is the ratio of inertial and viscous forces within a fluid which is subjected to relative internal movement due to different fluid velocities :

$$Re = \frac{\rho v L}{\mu} = \frac{\rho U D}{\mu} \, . \tag{2.5}$$

The value of the Re in the case of study reaches $7.8 \cdot 10^6$, which means that the turbulence is fully developed. Three different approaches exist to solve turbulence flows, classified according to the decreasing computational cost and turbulence modeling fidelity (figure 2.1):

1. The *DNS (Direct numerical simulation)*: the Navier-Stokes equations are solved without any turbulence model. This means that the whole range of spatial and temporal scales of the turbulence are solved;

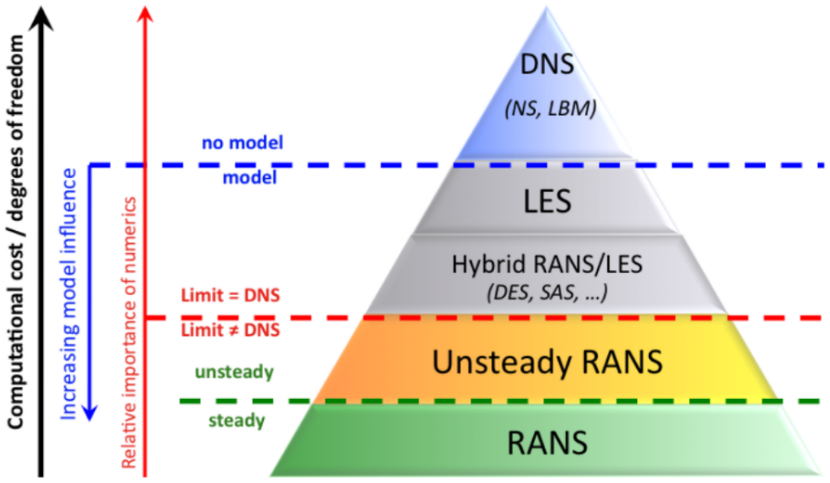

Figure 2.1 Classification of the turbulence models [17].

2. The *LES (Large eddy simulation)*: only the large energy-containing scales are directly computed, while the influence of the smallest scales is modeled;

3. The *RANS (Reynolds averaged Navier-Stokes equations)*: the average flow is solved and the impact of the fluctuations on the flow is modeled.

The DNS and the LES methods furnish more accurate solutions than the RANS equations application. However, they are still computationally too expansive. For this reason, the RANS approach remaining the most widely used, specially in industrial applications.

The RANS method is based on the Reynolds decomposition: the instantaneous flow variable are decomposed into mean $\langle v \rangle$ and fluctuating v' quantities. The instantaneous velocity is defined as

$$v_i = \langle v_i \rangle + v_i' \, . \tag{2.6}$$

Analogously for the pressure:

$$P = \langle P \rangle + P' \, . \tag{2.7}$$

In a statistical steady flow, the variables can be written as the sum of a time-averaged value and a fluctuation about the value:

$$v_i(\vec{x},t) = \underbrace{\langle v_i \rangle(\vec{x})}_{solved} + v_i'(\vec{x},t) \, . \tag{2.8}$$

The time-averaged value is calculated as:

$$\langle v_i \rangle(\vec{x}) = \lim_{T \to \infty} \frac{1}{T} \int_0^T v(x_i,t)\, dt \, . \tag{2.9}$$

where t is the time and T is the averaging interval. This interval T must be large compared to the typical time scale of the fluctuations. If T is large enough, $\langle v_i \rangle$ does not depend on the time at which the averaging is started. In the case of an unsteady flow, the time averaging cannot be used and it must be replaced by the ensemble averaging defined as:

$$\langle v_i \rangle (\vec{x},t) = \lim_{N\to\infty} \frac{1}{N} \sum_{n=1}^{N} v(x_i,t) \; . \tag{2.10}$$

where N is the number of members of the ensemble and must be large enough to eliminate the effects of the fluctuations. Hence, in the URANS formulation variables can be defined as:

$$v_i(\vec{x},t) = \underbrace{\langle v_i \rangle (\vec{x},t)}_{solved} + v_i'(\vec{x},t) \; . \tag{2.11}$$

The determination of the physical time step in the unsteady resolution has a fundamental role to correctly reproduce the flow behavior. Indeed, it should be large enough to consider a mean value and short enough to capture changes in the flow. In the case of study, local variation of the flow density can occur. The Reynolds decomposition must to be applied also to the instantaneous ρ:

$$\rho = \langle \rho \rangle + \rho' \; . \tag{2.12}$$

Decomposing the flow density, additional correlations are introduced in the system, complicating the flow modeling. In order to avoid this problem, a new density weighted average, called *Fauvre average*, can be applied. So the generic variable f can be expressed as:

$$f = \widetilde{f} + f'' = \frac{\langle \rho f \rangle}{\langle \rho \rangle} \; . \tag{2.13}$$

Thus, the governing equations (2.1 and 2.2) in the local form can be written as :

$$\frac{\partial \langle \rho \rangle}{\partial t} + \frac{\partial}{\partial x_j} \left(\langle \rho \rangle \widetilde{v_j} \right) = 0 \; . \tag{2.14}$$

$$\frac{\partial \langle \rho \rangle \widetilde{v_j}}{\partial t} + \frac{\partial}{\partial x_j} \left(\langle \rho \rangle \widetilde{v_i} \widetilde{v_j} \right) = \frac{\partial \langle P \rangle}{\partial x_j} \left(\tau_{ij} - \langle \rho v_i'' v_j'' \rangle \right) + f_i \; . \tag{2.15}$$

In the equation 2.15, the term $\langle \rho v_i' v_j' \rangle$ is the Reynolds stress and it represents the influence of the small turbulent scale on the large eddies. This tensor introduces further six unknowns into the system of equations. In order to close the system an approximation of the Reynolds stress term is required, involving the turbulence modeling.

2.1.3 Turbulence models

In literature several approaches are presented to model the Reynolds stress term. The most common for RANS equation is based on the Boussinesq hypothesis which supposes that the Reynolds stress proportional to the eddy viscosity μ_T :

$$\langle \rho v_i'' v_j'' \rangle = \mu_T \left(\frac{\partial \widetilde{v}_i}{\partial x_j} + \frac{\partial \widetilde{v}_j}{\partial x_i} \right) - \frac{2}{3} \langle \rho \rangle \widetilde{k} \delta_{ij} \, . \tag{2.16}$$

where $\widetilde{k}$ is the kinetic turbulent energy and δ_{ij} is the Kronecker symbol. The kinetic turbulent energy represents the kinetic energy associated with eddies in turbulent flow $\left(\widetilde{k} = \frac{1}{2} \frac{\widetilde{v_i'' v_i''}}{\langle \rho \rangle} \right)$.

The turbulence models are usually classified according to the number of additional equations introduced in the system to calculate the eddy viscosity:

- **0 - equation models** *(Algebraic models)*: the definition of the turbulence characteristic length and velocity are based on the characteristics of the flow. The determination of the eddy viscosity depending on these two quantities, is not accurate since they change as a function of the investigated flow. This kind of model is typically used for fast and numerically stable calculations. However, to simulate more precisely the turbulent quantities with good rate of convergence, the higher level turbulence models are advised. An example of the algebraic model is Baldwin-Lomax model [18];

- **1 - equation models**: these approaches are very robust numerically and less demanding in the near-wall resolution. This type of model, as Spalart-Allmaras model [19], are largely used to simulate external flows, which use a modified viscosity to compute the Reynolds stress term; this variable is computed thanks to a transport equation.

- **2 -equations models**: two additional transport equations are used to define the intensity and the length scale of turbulence. The most widely used groups of models for industrial and academic applications are based on the $k-\varepsilon$ and the $k-\omega$ models;

- **Reynolds stress models (RSM)** *(Second order closure models)*: The Reynolds stress term is defined by six separate transport equations. It is the most generalized of all turbulence models and works relatively well for a wide range of engineering problems. However, is computationally very expensive since 6 transport equations are solved. Moreover, compared to 2 - equations models, it required high mesh quality and is more demanding to achieve the satisfying converged solution. GE Renewable Energy's experience in hydraulic turbine calculations shows that the improvements provided by the RSM models are not significant enough to justify this additional cost [20].

More information about the presented turbulence models and their application to the turbomachinery can be found in [21].

In this work, according to the literature and the previous know–how of the LEGI laboratory and GE Renewable Energy, two 2 – equations models have been used and compared: the $k-\varepsilon$ and the $k-\omega$ SST. All the details of the two turbulence models and of the wall treatments will be presented in the following subsections.

2.1.3.1 The k-ε turbulence model

In the standard $k-\varepsilon$ model, initially proposed by [22], a additional transport equations for the kinetic energy k and for the dissipation rate ε are added to the system. Hence, the dissipation ε and the turbulent kinetic energy k are related by the turbulence length scale L:

$$\varepsilon \approx \frac{k^{3/2}}{L} \,. \tag{2.17}$$

The turbulent eddy viscosity μ_T can be expressed as a function of the turbulent kinetic energy k and the dissipation ε:

$$\mu_T = \rho C_\mu \frac{k^2}{\varepsilon} \,. \tag{2.18}$$

Where C_μ is a constant equal to 0.09. This model is very robust and, as a consequence, is widely used in industrial application [23]. Commonly, it gives good results in the free stream areas away from the walls but is inadequate to predict the flow separation in the boundary layers. The flow inside a hydraulic turbine is characterized by very large gradient pressure, so a wall function is required to correctly model the flow behavior near the walls and, consequently, to accurate predict the performances evolution.

2.1.3.2 The k-ω turbulence models

The $k-\omega$ model introduced by Wilcox [24] defines the eddy viscosity μ_T using the turbulent kinetic energy k and the specific turbulent dissipation rate (or turbulence frequency) ω:

$$\mu_T = \rho \frac{k}{\omega} \quad ; \quad \omega = \frac{\sqrt{k}}{C_\mu L} \,. \tag{2.19}$$

The $k-\omega$ model is substantially more accurate than the $k-\varepsilon$ in the near wall regions and has therefore been successful for flows with adverse pressure gradients but the flow in the free stream is very sensitive to the boundary conditions. Menter [25] has proposed the $k-\omega$ SST (shear stress transport) model, combining the approach of the $k-\omega$ model in the boundary layers and the $k-\varepsilon$ in the free stream flow,. The $k-\omega$ SST model is not significantly more

complicated than the original $k-\omega$ model. A blending function F_1, null near the wall and equal to 1 out of the boundary layer is introduced on the model. The equations system of the $k-\omega$ model is multiplied by F_1 while the equations of the $k-\varepsilon$ are multiplied by $(1-F_1)$. Finally, the two obtained system are added together. The final system consisting in two equations for k and ω. The constants of the model are the linear combinations of the constants of the two turbulence models:

$$c = F_1 c_1 + (1-F_1)\, c_2 \ , \tag{2.20}$$

where the indexes 1 and 2 refer respectively to the $k-\omega$ and to the $k-\varepsilon$ models. In order to limit the turbulent viscosity production in the boundary layer, another blending function is defined F_2 equal to 1 on the wall and null in the free-stream. So the turbulent viscosity becomes:

$$\nu_T = \frac{\mu_T}{\rho} = \frac{a_1 k}{max\left(a_1\omega; SF_2\right)} \ , \tag{2.21}$$

where a_1 is a constant and S is the scalar invariant of the strain rate tensor.

Thus, the $k-\omega$ SST model compensates the weakness of one model by the qualities of the other one, adapting to the different flow areas. The advantages and the experiences of the $k-\omega$ SST model application on turbomachinery are presented in [26].

2.1.4 Wall treatments in applied turbulence modeling

The adhesion of the fluid on the walls implies the presence of a region inside the flow, called the boundary layer, characterized by high velocity gradients. To properly capture those large gradients in a numerical simulation, it is important to have a sufficient amount of grid points inside the boundary layer. Moreover, an appropriate size of the first inner cell is necessary to obtain a correct prediction of the turbine performance. The boundary layer can be described using the following dimensionless variables:

$$y^+ = \frac{y u_\tau}{\nu} \ ; \quad u^+ = \frac{\langle u_\tau \rangle}{u_\tau} \ ; \quad \text{with} \quad u_\tau = \sqrt{\frac{\tau_w}{\rho}} \ . \tag{2.22}$$

The y^+ and the u^+ represent, respectively, the dimensionless distance from the wall and the dimensionless velocity parallel to the wall.

The inner region of a turbulent boundary layer in equilibrium (without pressure gradients) can be separated into three different parts, shown in figure (2.2), depending on the importance of the laminar and turbulent stress tensor components:

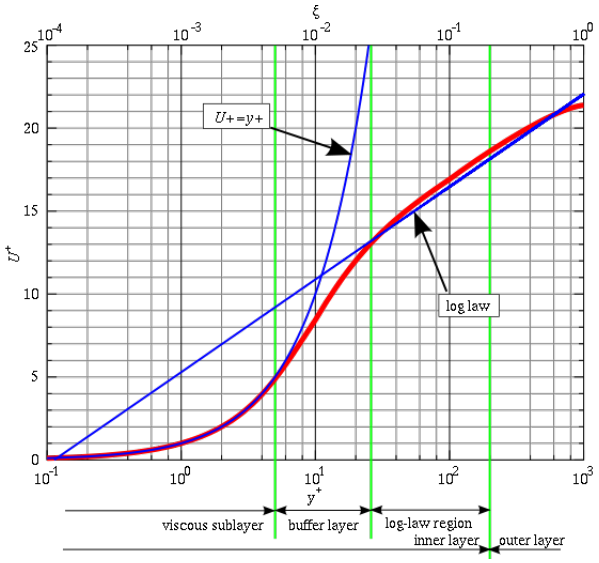

Figure 2.2 Boundary layer description [27].

- The **viscous sublayer:** $(y^+ < 5)$

  Thin region where the viscous effects are predominant over the inertial (laminar) effects. In this zone, the velocity profile is linear:

$$u^+ = y^+ \,. \tag{2.23}$$

- The **logarithmic region:** $(y^+ > 30)$

  In this region, the turbulent effects are stronger than the viscous effects. The extension of this zone is difficult to define since it depends on the Reynolds number and the pressure gradient. The velocity profile in this part of the boundary layer follows a logarithmic law:

$$u^+ = \frac{1}{\kappa} \ln\left(y^+\right) + C \,. \tag{2.24}$$

  where C is a constant.

- The **buffer layer:** $(5 < y^+ < 30)$

  It is the zone of connection between the two previous regions where the properties of the viscous sublayer and the logarithmic zones coexist.

In order to accurately model the boundary layer region of the flow two approaches are possible:

1. The velocity profile is modeled by means of wall laws based on the boundary layer description presented before. This method allows to use a coarse discretization near the

wall, reducing the computational costs. This approach is applied in particular with the $k-\varepsilon$ standard model since it does not use any dumping function and therefore produces excessive turbulence in the viscous and buffer sublayers. Several modification of the $k-\varepsilon$ turbulence model are proposed in literature to simulate the flow in the boundary regions [28–30].

The approach used in this PhD study is the *Extended wall function* (EWF) presented initially by Hakimi *et al.* [31] and implemented in the Numeca CFD solver FINE™/Turbo. In this improved $k-\varepsilon$ model the turbulent equations are not solved in the first layer close to the wall, as in classic low Reynolds models (i.e. the $k-\omega$ turbulence models). Instead, a dumping function is applied which is consistent with the wall functions for k and ε derived from the DNS data of Kim *et al.* [32], for a fully-developed plane channel. To take advantage of the EWF use, an adequate discretization is required. The FINE™/Turbo guide [33] advises to locate the first inner node in the viscous sublayer ($y+ < 5$).

2. The second approach consists in directly solving the turbulent equations in the boundary layer. In contrast, a fine mesh is required. This method is suitable for turbulence models based on the $k-\omega$ model, known also as low-Reynolds models, referring to the laminar viscous sublayer. For the $k-\omega$ SST model, a $y^+ < 2$ is required [26]. In case of complex industrial flows this requirement remains a challenge and in most cases not is not achieved.

   To get around the problem the $k-\omega$ SST model has been implemented in FINE™/Turbo with a wall function similar to the EWF. This law is automatically used when the mesh is not fine enough to properly solve the boundary layer.

2.2 Cavitating flows modeling

The numerical modeling of cavitating flows can be very difficult due to three principal factors: the thermodynamic equilibrium, the modifications induced by the cavitation on the turbulence field and the numerical stability [34].

From a thermodynamic point of view, the cavitation is a very complex phenomenon. The phase changes occur in a non-equilibrium state, difficult to simulate. So, simplifying assumptions are required (see, for example section 2.2.1).

The simultaneous presence of the liquid and the vapor phases and their interactions introduce compressibility effects that modify the level of the turbulence. Source terms related to the flow

compressibility could be included in the turbulence model equations but this is not a common practice.

Finally, the high density gradients and the local reduction of the Mach number cause numerical instabilities. For these reasons, specific numerical methods are required to obtain a correct numerical reproduction of the cavitation phenomena.

The two-phases models can be divided into two macro categories: the *2-flows models* and the *homogeneous models*.

In the 2-flows models, the behavior of each fluid is considered including in the formulation terms of exchanges at the interfaces. Depending on the volume fractions of both phases, they can be modeled as:

- *separated flows*: the lengths of the characteristic scales of the two phases are comparable and they are separated by clear and distinct interfaces. Its applications are limited to simpler problems where the cavity can be described as a well-defined closed volume of pure gas or in case of stratified flow.

- *dispersed phase flows*: the characteristic scale of one phase (dispersed) is much smaller than the other one (continuous). In the case of a cavitating flow, the liquid phase is considered as the continuous while the gas (vapor) is the dispersed phase.

For the dispersed phase flows two possible approaches exist:

- *Eulerian-Lagrangian* approach: the liquid is considered as a continuum while the dispersed phase consisting in particles that are tracked during the simulation. Applications of this method concerning mostly simulations of very simple cavitation structures (i.e. single bubbles [35] and cloud cavitation [36]) or cavitating flow in case of basic geometries (i.e. diesel injector nozzles [37] and hydrofoils [38]).

- *Eulerian-Eulerian* approach: both of the phases are considered as continua interacting each other by means of interfaces. Examples are the 6-equations model used by Mimouni *et al.* [39] to model a critical flow in a nozzle, the 4-equations model proposed by Goncalvès and Charrière [40] to a sheet cavitation developing along a Venturi tube.

For 2-flows models, a system of governing equations is solved for each phase. An additional equation is introduced in the system for the volume fraction of the disperse phase. The interactions between the phases are taken into account by adding source terms in the governing equations. These interactions are related to the phase changes (i.e. mass transfers) or they have an hydrodynamic origin (i.e. the drag and the lift forces, surface tension, etc...).

Contrary to the 2-flows models, the homogeneous methods treat the cavitating flows as a mixture of the two fluids behaving as one. So, a single set of equations is required.

Comparing these approaches, the 2-flows models generally provides a more accurate reproduction of the cavitating flows. On the other hand, they are more complex and require higher computational costs. Moreover, the source terms introduced in the equations system to simulate the interaction between the interfaces are difficult to determine. For these reasons, they are not suitable in case of complex geometries. On the contrary, the homogeneous models, because of their simplicity are widely used to investigate the cavitating flow in different type of hydraulic turbomachinery. In literature, many examples exist of their application for the cavitation study in pumps (i.e. centrifugal pumps [41], pump-turbines [42]) and in turbines (i.e. Pelton turbines [43], Francis turbine [44], double-regulated turbines [45], [46] and [47]). Based on these previous works and on the LEGI experience about simulation in cavitating conditions in hydraulic machines, in the present investigation, the two phases flow has been modeled as an homogeneous mixture.

2.2.1 Homogeneous approach

In the homogeneous approach the cavitating flow is considered as a mixture of liquid and vapor phases. It relies on the hypothesis that the two phases are in local kinematic and thermodynamic equilibrium: the slip velocity on the border between the phases are negligible, and they share the same instantaneous velocity, turbulence and pressure fields. The proprieties of the flow depend on the local void ratio α, defined, under homogeneous hypothesis, as:

$$\alpha = \frac{\Omega_v}{\Omega} \, . \tag{2.25}$$

where Ω_v is the vapor volume in the single discretization element and Ω is the total cell volume. The void ratio α should be comprised between 0 and 1 for the volume conservation. If α is equal to 1, the full cell is filled with vapor. On the contrary, if α is equal to 0, the cell is filled with liquid.

The density ρ and dynamic viscosity μ of the mixture can be expressed as function of the void ratio α of the liquid-vapor mixture according to equations (2.26) and (2.27), as initially proposed by [48]. The index l represents the liquid phase and v the vapor phase of the considered fluid.

$$\rho = \alpha\rho_v + (1-\alpha)\,\rho_l \, . \tag{2.26}$$

$$\mu = \alpha\mu_v + (1-\alpha)\,\mu_l \, . \tag{2.27}$$

So, the mixture density ρ is not a constant but changes in the flow field between the vapor density ρ_V and the liquid density ρ_L. Consequently, a cavitation model is required to determine the mixture density. In literature, two type of models can be distinguished:

- **The void ratio transport equation models**: an additional mass conservation equation for one of the phases is introduced in the governing equations system, including source terms;
- **The Barotropic model**: the mixture density is directly defined by the local pressure field.

The two cavitation models will be presented in the following sections. For a more detailed description of these two approaches see [34].

2.2.2 Void ratio transport equation

In this approach a mass balance equation for the vapor phase is added to the homogeneous model equation system. The additional equation is defined as (2.28):

$$\frac{\partial(\rho_v \alpha)}{\partial t} + \frac{\partial(\rho_v \alpha u)}{\partial x} = m^+ + m^- \ . \tag{2.28}$$

with m^+ and m^- the vaporization and the condensation source terms. Different modeling techniques of the source terms have been developed in the last decades, e.g. see table (2.1), most based on a simplified Rayleigh-Plesset equation that relates pressure and bubble volume. In this approach the time influence on the mass transport is taken into account by means of empirical equations to model the source terms. However, the main difficulty of these models relies on the determination of the source terms, which depend on different constants of the vapor production and destruction, respectively C_{prod} and C_{dest}, that are not universally defined. In the table 2.1 are reported the equations of the source terms for the most common void transport models.

Among these models, the most used in hydraulic turbomachinery applications are:

- the *Kunz et al.* [49], applied in centrifugal pumps [50] and in propellers [51] studies;
- the *Shingal et al.* [52], used to investigate pumps and inducers [53], Francis turbines [54] and also Kaplan turbines [55];
- the *ZGB et al.* [56], employed for pumps studies [57] and also turbine studies, in particular Francis [58], Kaplan [46, 45] and also Pelton [43] turbines.

Table 2.1 Vaporization/condensation source terms in different void ratio transport equation cavitation models

Authors	m^+	m^-
Kunz *et al.* [49]	$\frac{C_{prod}\rho_v(1-\alpha)min\left(0,p-p_{vap}\right)}{0.5\rho_l^2 C_{ref}^2 t_\infty}$	$\frac{C_{dest}\rho_v(1-\alpha)^2\alpha}{t_\infty}$
Li, Merkle [59]	$\frac{C_{prod}\rho_l(1-\alpha)min\left(0,p-p_{vap}\right)}{0.5\rho_l^2 C_{ref}^2 t_\infty}$	$\frac{C_{dest}\rho_v\alpha max\left(0,p-p_{vap}\right)}{0.5\rho_l^2 C_{ref}^2 t_\infty}$
Schenerr, Sauer [60]	$\frac{3C_{prod}}{R_b}\frac{\rho_v\rho_l\alpha(1-\alpha)}{\rho}\sqrt{\frac{2}{3}\frac{max\left(0,p-p_{vap}\right)}{\rho_l}}$	$\frac{3C_{dest}}{R_b}\frac{\rho_v\rho_l\alpha(1-\alpha)}{\rho}\sqrt{\frac{2}{3}\frac{max(0,p-p_{vap})}{\rho_l}}$
Shingal *et al.* [52]	$\frac{C_{prod}C_{ref}\rho_l\rho_v}{\sigma_S}\left[\frac{2}{3}\frac{max(0,p_{vap}-p}{\rho_l}\right]^{1/2}(1-f_v)$	$\frac{C_{dest}C_{ref}\rho_l\rho_v}{\sigma_S}\left[\frac{2}{3}\frac{max(0,p-p_{vap}}{\rho_l}\right]^{1/2}f_v$
Zwart-Gerber-Belamri (ZGB) [56]	$\frac{3C_{prod}\alpha_{nuc}\rho_v(1-\alpha)}{R_b}\sqrt{\frac{2}{3}\frac{max\left(0,p_{vap}-p\right)}{\rho_l}}$	$\frac{3C_{dest}\alpha\rho_v}{R_b}\sqrt{\frac{2}{3}\frac{max\left(0,p-p_{vap}\right)}{\rho_l}}$

2.2.3 Barotropic model

The objective of the barotropic formulation is to join the state laws that describe each pure phase. Thus, the evolution of the mixture density ρ in the cells will be strongly related to the local pressure p by a barotropic law ($\rho = f(p)$). Different kind of barotropic laws have been proposed in the last decades such as the logarithmic laws (i.e. Schmidt [61]), the sinusoidal laws (as the one presented by Delannoy and Kueny [62]) and more complex laws (i.e. the law proposed by Sinibaldi *et al.* [63]). The simplest and the largest used to predict cavitation phenomena in hydraulic machines, e.g. in pumps see Refs. [41, 64, 42], is the sinusoidal function, shown in figure (2.3). This connection law has been developed, tested and implemented in the numerical code FINE™/Turbo in collaboration between the LEGI laboratory and Numeca International and has been used in this work. When the local pressure p is lower than $p_v - \Delta p/2$, the whole cell is filled with vapor. On the contrary, when the local pressure is higher than $p_v - \Delta p/2$, the full cell is filled with liquid. The pure phases are considered as incompressible. The mixture region, where $p_v - \Delta p/2 < p < p_v + \Delta p/2$, is defined by the minimal speed of sound in the liquid-vapor mixture c_{min} and it can be written as a $c_{min}^2 = \frac{\partial p}{\partial \rho}$. To provide a smooth density transition from the liquid to the vapor phase, the

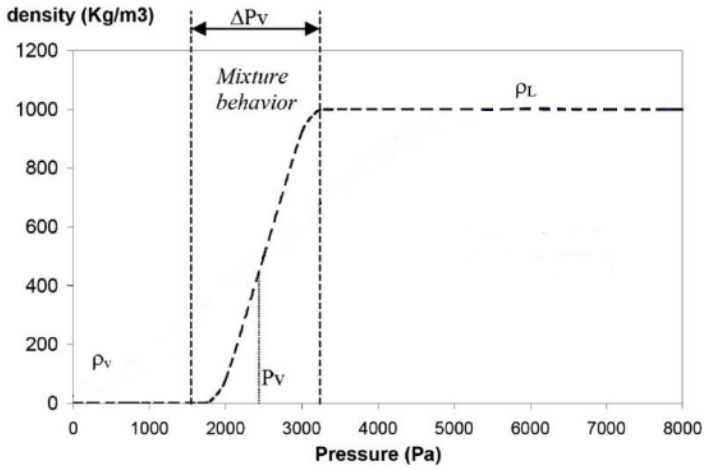

Figure 2.3 Barotropic state law $\rho = \rho(P)$.

density ρ is described by the following sinus function (2.29):

$$\rho = \frac{\rho_l + \rho_v}{2} + \frac{\rho_l - \rho_v}{2} sin\left(\frac{p - p_v}{c_{min}^2} \frac{2}{\rho_l - \rho_v}\right) . \tag{2.29}$$

The slope of the evolution law is defined by the inverse of the minimum speed of sound in the mixture, $\frac{1}{c_{min}}$. As a consequence, smaller c_{min} leads to smaller mixture region. In FINE™/Turbo it is not possible to directly set c_{min}. So, the parameter A_{min} is used instead of c_{min} and can be defined as (2.30):

$$A_{min} = \sqrt{\frac{\rho_l - \rho_v}{2} c_{min}^2} . \tag{2.30}$$

The void ratio inside a cell can be calculated by the local density of the mixture as (2.31):

$$\alpha = \frac{\rho - \rho_l}{\rho_v - \rho_l} . \tag{2.31}$$

The vapor density ρ_v is a function of the temperature. The typical value at 20°C and 100% humidity is $\rho_v = 17.3 g/m^3$. In spite of that, in literature different values for the vapor density ρ_v have been tested, always comprised between $1 g/m^3 < \rho_v < 100 g/m^3$, to increase the robustness of the simulations. Modeling cavitation by the barotropic law has normally shown a good agreement between experimental and numerical results, especially for cavitating flows in complex geometries, with a reduced impact on computational costs.

Comparing the advantages and the disadvantages of the two family cavitation models presented and considering the LEGI experience in calculations of cavitating flows the barotropic law has been finally considered the most suitable model for the thesis purposes.

Following previous studies [65–67] on cold water, c_{min} has been imposed equal to 1 m/s (consequently an $A_{min} = 23$) and the density ratio between the vapor and the liquid phase has been set to 0.01.

2.3 Numerical schemes

All the simulations presented in this work of thesis have been performed with the commercial solver of Numeca International FINE™/Turbo. It is a density-based code characterized by a cell-centered spatial discretization approach. The resolution algorithm is based on an explicit time-marching method: every iteration a multistage Runge-Kutta temporal discretization scheme is therefore applied. The calculation convergence is enhanced by a multigrid approach. For low Mach number applications a preconditioning method is used. Hereafter, the main generalities of the discretization schemes, the multigrid and preconditioning method are introduced. Detailed descriptions are reported in [66, 68].

2.3.1 Spatial discretization approach

The spatial discretization is based on a cell centered control volume approach. In this methods, the governing equations are integrated on the computational cell of volume Ω limited by a surface Σ, with an outer normal $\vec{n}$, applying the theorem of Gauss-Ostrogradki (2.32):

$$\frac{\partial}{\partial t}\int_{\Omega}\vec{V}d\Omega + \oint_{\Sigma}\vec{F}d\Sigma = \int_{\Omega}\boldsymbol{S}d\Omega\ . \tag{2.32}$$

In this equation, $\vec{V}$ is the vector of the conservative variables and $\boldsymbol{S}$ is a source term. The vector of the conservative variables is defined as:

$$\vec{V} = \begin{bmatrix} \rho \\ \rho V_x \\ \rho V_y \\ \rho V_z \end{bmatrix}\ . \tag{2.33}$$

The flux term $\vec{F}$ can be divided into an inviscid $\vec{F}_I$ and a viscous $\vec{F}_V$ parts, $\vec{F} = \vec{F}_I - \vec{F}_V$.

The inviscid vector consists in:

$$\vec{F}_I = \begin{bmatrix} \rho V_i \\ \rho V_x V_i + n_x P \\ \rho V_y V_i + n_y P \\ \rho V_z V_i + n_z P \end{bmatrix} . \tag{2.34}$$

While, the viscous part is defined as:

$$\vec{F}_I = \begin{bmatrix} 0 \\ n_x \tau_{xx} + n_y \tau_{xy} + n_z \tau_{xz} \\ n_x \tau_{yx} + n_y \tau_{yy} + n_z \tau_{yz} \\ n_x \tau_{zx} + n_y \tau_{zy} + n_z \tau_{zz} \end{bmatrix} . \tag{2.35}$$

The viscous fluxes $\vec{F}_V$ can be determined using a pure central scheme so gradients must be evaluated on the cell faces (as reported in figure 2.3.1). Applying the theorem of Gauss-Ostrogradki, the gradient of the generic variable Φ can be calculated as (2.36):

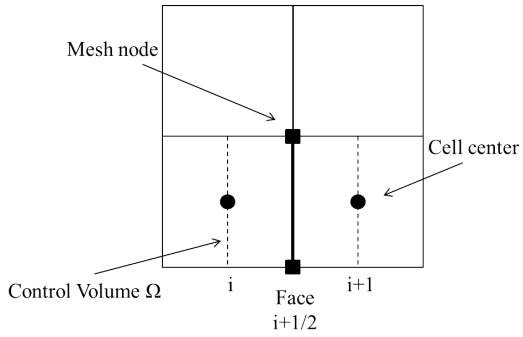

$$\nabla\Phi = \frac{1}{\Omega}\int_{\Omega} \nabla\Phi d\Omega = \frac{1}{\Omega}\int_{\Sigma} \Phi d\Sigma \, . \tag{2.36}$$

Figure 2.4 Control volume used to calculated gradients in cell faces

In the inviscid flux formulation, artificial dissipation terms are added to the purely central evaluation of the flux:

$$\left(\vec{F}_I \vec{n}\right)_{i+1/2} = \underbrace{\left\{ \frac{1}{2}\left(\vec{F}_I \vec{n}\right)_i + \left(\vec{F}_I \vec{n}\right)_{i+1} \right\}}_{purely\ central} - \underbrace{d_{i+1/2}}_{dissipation} . \tag{2.37}$$

Following the scheme proposed by Jameson *et al.* [69] the numerical dissipation is modeled by means of tunable second-order and four-order terms.

2.3.2 Time discretization approach

In the steady simulations a pseudo-time step ($\Delta\tau$) is defined and for each iteration a 4 steps Runge-Kutta scheme is applied to reach the convergence. The pseudo-time step can be global or local. On one hand, if the pseudo-time is local, it is different from cell to cell and it is defined as :

$$\frac{\Delta\tau}{\Omega} = \frac{CFL}{u} \,. \tag{2.38}$$

Where CFL is the Courant-Friedrichs-Lewy number, Ω is the cell volume and u is the flow velocity that cross the cell. In FINE™/Turbo the CFL is set constant in the whole domain. A higher value of the CFL number results in a faster convergence but will lead to divergence if the stability limit is exceeded. As has been investigated by Pouffary [66], the CFL stability limit is 3. But in cavitating conditions, the CFL must be reduced to 1 in order to avoid instability problems. Contrary to the CFL number which is a global parameter, both of u and Ω are local parameters and depend on the cell dimensions. On the other hand if the pseudo-time step is global, it is set as the minimum local pseudo-time step on all the numerical domain. Consequently, the calculation time increases. So, a local pseudo-time step allows to accelerate the convergence although it requires more memory. In the unsteady calculations, a dual-time stepping technique is applied: each physical time step is considered as a steady problem in which the solution is obtained iterating in each pseudo-time step.

In this thesis a local time step has been used.

2.3.3 The preconditioning

The described time-marching algorithm is designed for compressible flows and is unsuitable for low Mach number applications. Indeed, in case of incompressible flows, the magnitude of the flow velocity becomes small in comparison with the acoustic speeds and the time-marching compressible codes converge very slowly.

In order to provide a fast convergence and accurate solutions, a low speed preconditioner has been developed. This method consists in multiplying the pseudo-time derivative terms in the governing equations by a preconditioning matrix. This allows to reduce the convergence time without consequence on the final solution since the pseudo-time terms are not physical and it goes to zero when the convergence is reached.

The preconditioning technique implemented in FINE™/Turbo has been developed by Hakimi [70] in which the preconditioning matrix is defined as:

$$\overline{\overline{\Gamma}}^{-1} = \begin{pmatrix} \frac{1}{\beta^2} & 0 & 0 & 0 \\ \frac{(1+\alpha)v_x}{\beta^2} & \rho & 0 & 0 \\ \frac{(1+\alpha)v_y}{\beta^2} & 0 & \rho & 0 \\ \frac{(1+\alpha)v_z}{\beta^2} & 0 & 0 & \rho \end{pmatrix} . \tag{2.39}$$

The parameters used to regulate the preconditioning system are α, generally considered equal to -1, and β, defined as a function of the reference velocity: $\beta^2 = \beta^* \cdot \vec{U}_{ref}^2 = \beta^* \cdot \left(\frac{\vec{\omega} R}{2}\right)^2$. The value of the parameter β changes as a function of the Reynolds number, Re. The default value of β^* is 3. The FINE™/Turbo theory guide [33] recommended to increase this value in presence of convergence difficulties at the very beginning of a computation. However, a too large value of β^* could introduce excessive artificial dissipation into the solution.
Introducing the preconditioning matrix in the equations system, the physical acoustic waves are replaced by pseudo-acoustic modes that are much closer to the flow velocity, reducing the stiffness and enhancing the convergence.

2.3.4 The multigrid method

The multigrid method is an algorithm for solving differential equations using a hierarchy of discretization. The main idea of the multigrid approach is to accelerate the convergence by solving the system of equations on different grid levels. The information is propagated from one level to another allowing to eliminate low frequency errors.

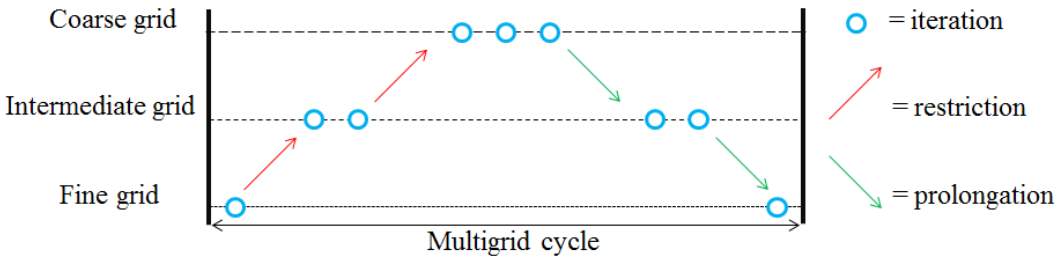

Figure 2.5 Multigrid cycle scheme **V 1-2-3** .

The interactions suppress more effectively the high frequency errors. Each level of the mesh is correlated to a frequency level: at smaller cell dimensions correspond higher frequencies. Thus, iterating on a grid level coarser than the real one, the lowest frequencies of the fine level become the highest frequencies of the coarse level, smoothing the errors.

The most used multigrid cycle is characterized by a scheme **V 1-2-3**, reported in figure 2.5. Starting from the finest grid level, the result of one iteration on this grid level is restricted (one takes for each node on the coarse grid simply the value of the grid function at the corresponding node on the fine grid to the next mesh level) dampening the residual errors. Subsequently, two iterations are performed on the intermediate grid and the result is restricted to the coarse mesh level. Three iterations are computed on the coarse mesh and the solution is prolongated (interpolated) to the intermediate level, interpolating the correction computed on the coarse grid. Afterwards, two iterations are performed on the intermediate grid and the solution is prolongated on the finest mesh level, obtaining the final solution of the multigrid cycle.
The application of the multigrid method is mostly limited by two factors. Firstly, the use of this technique introduces constraints in the discretization process. Indeed, in order to define less refined grid levels one point out of two of the starting mesh, in all the directions, must be deleted. The other aspect to consider is that, as all convergence acceleration techniques, it can destabilize the numerical scheme. This occurs especially when increasing the iterations on the coarse level.

2.4 The State of the art of the numerical investigations of the cavitating flow in Kaplan turbines

To fix the starting point of the development of the numerical methodology and to contextualize the present work of thesis it is necessary to introduce the current state of the art about the investigated subject. The bibliographic review presented hereafter is focused on the numerical works in the cavitating regime only in Kaplan turbines. This choice is based on two principal reasons:

- Even if Similitudes can be found with propellers and bulb turbines, the Kaplan turbines differ from all the others hydraulic turbines. Indeed, the blades of a propeller are fixed and they are not wrapped in a casing that interfere with the flow on the blade tip. Regarding, bulb turbines, they work mostly in very low head conditions and the water does not flow through a spiral casing before to enter in the runner. Therefore, the phenomena that occur in this kind of machines are very different from those observed in the Kaplan turbines and, consequently, their numerical modeling concentrates on different aspects.

- The cavitating flow are characterized by the simultaneous presence of two phases, sudden variations and compressible aspects. Thus, the numerical modeling of a single-phase flow is not similar to a two-phases modeling.

The main objective of the present thesis is to develop a numerical methodology able to predict the cavitation phenomena inside a Kaplan turbine and their effect on the machine performances. This is the same purpose of the work presented in 2006 by Balint *et al.* [71]. This research mostly focused on steady numerical simulations in order to obtain the σ-break curve and the cavitation structures in the case of a Kaplan turbine in optimal conditions. The considered calculation domain consists in a single full-periodic interblade runner channel. The velocity and turbulence profiles imposed on the inlet were computed from a decoupled calculation of the distributor while a radial pressure equilibrium has been imposed on the outlet. The two-phase flow has been considered as an homogeneous flow and the mass transfer rates due to cavitation were regulated following the ZGB model [56]. From the analysis of the computed iso-density surfaces and the cavitation curves a correlation between the occurrence of the leading edge cavitation and the efficiency reduction has been identified. Unfortunately, no experimental data have been presented in order to support this thesis and to validate the developed numerical methodology.

A more complete study was presented in 2015 by Jošt *et al.* [72]. Using the same approach applied by Balint *et al.* [71], the evolution of the cavitating flow in a 6-blades Kaplan turbine has been investigated out of the optimal operating conditions. The mass flow rate has been considered as the inlet boundary condition and the average static pressure has been imposed on the computational outlet. Steady and unsteady simulations were performed in order to find the most suitable configuration to accurately reproduce the cavitation phenomena and the turbine behavior. The efficacy of the numerical model was validated by means of the experimental data. The best results in terms of performance and cavities predictions have been obtained for the unsteady case (see figure 2.6). Discrepancies between numerical results and measurements wereobserved mostly due to different values of the head and the flow rate. The numerical methodology can be further improved changing the boundary conditions on the inlet.

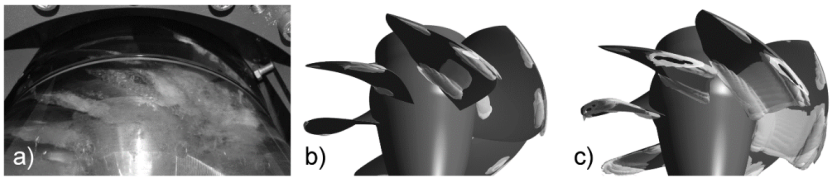

Figure 2.6 Comparison of shape and size of cavity in experiments and simulations performed by Jošt *et al.* [72] in **a** experiment, **b** steady state simulation, tuned coefficients and **c** time dependent simulation, tuned coefficients.

Another investigation of the cavitating flow in the Kaplan turbine has been proposed in 2017 by Leguizamón *et al.* [46]. The main objective of this study, developed in collaboration between the EPFL university and GE Renewable Energy, is to characterize the efficiency alteration mechanism due to cavitation in Kaplan turbines. For this purpose, two different

Kaplan geometries operating in full and in partial load conditions, respectively, have been tested and compared. As in the other two works, the cavitating flow has been modeled by means of the transport-equation-based homogeneous ZGB model. Steady simulations have been performed on a simplified computational domains comprising a single one blade-to-blade passage (using the periodicity boundary conditions) including the guide vane and the turbine blade. The total pressure is proposed as inlet boundary condition instead of the mass flow rate. The static pressure, which is extrapolated from the draft tube pressure drop measurements, is defined et the outlet. The analysis of the results, supported by the experimental observations (as reported in figure 2.7), have shown that, in both investigated cases, along the σ-break curve, the evolution of the vapor structures causes firstly the reduction of the dissipation energy. In a second step the occurrence of turbulent phenomena on the blade trailing edge leads to an increase and a subsequently reduction of the machine efficiency.

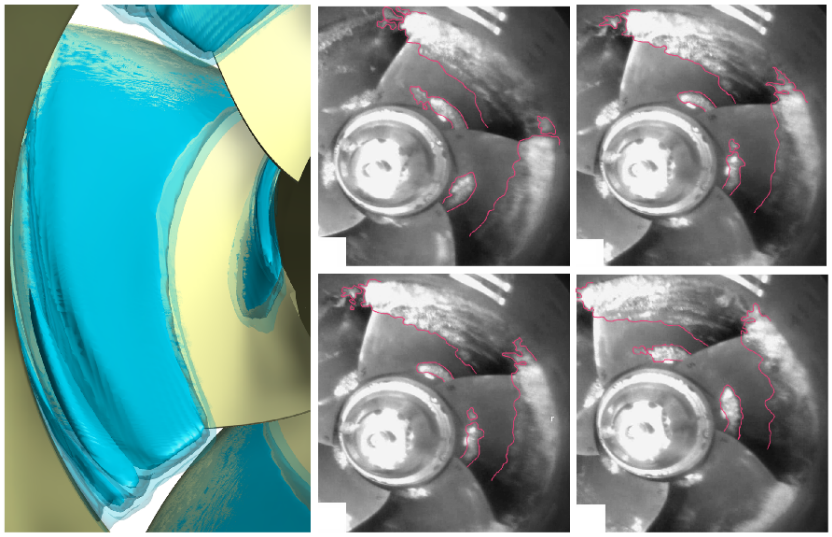

Figure 2.7 Comparison of shape and size of cavity in experiments and simulations performed by Leguizamón *et al.* [46].

In the table 2.2 are summarized the calculation setups of the cited works.

Table 2.2 Computational setup of numerical cavitation studies in Kaplan turbine.

Authors	Domain	Inlet BC	Turbulence model	Cavitation model
Balint *et al.* [71].	runner single channel	velocity profiles	k-ω SST	ZGB model [56]
Jošt *et al.* [72]	whole machine	Q		
Leguizamón *et al.* [46]	GV + runner single channel	P_{tot}		

Other numerical studies on cavitating flow in Kaplan turbine focus on a single cavitation phenomena: the cavitation at the blade tip. This phenomenon occurs due to the presence of the gap between the blade and the shroud and in Kaplan turbines usually arises before all other

types of cavitation. Moreover, depending on the machine head, the limited amount of the cavitation on the tip is allowable in standard operating points. This cavitation type is known to cause only a mild efficiency variation but generates erosion phenomena (a detailed review of the different cavitation types that occur in Kaplan turbine is presented in the introduction 1). For these reasons, the development of experimental (refer to the state of the art in chapter 3) and numerical methodologies able to predict tip cavitation in this hydraulic turbine is of great industrial interest.

Two-phases unsteady simulations have been performed in 2007 by Nennemann *et al.* [73] using the homogeneous approach and a Reyleigh-Plesset based cavitation model to investigate the evolution of the cavitation structures on the blade tip and their impact on the pressure fluctuations in the discharge ring region. The whole guide vane and the runner have been considered as the numerical domain. The comparison of the computed and the experimental pressure spectra has allowed to find the frequency signature of the tip cavitation.

In a more recent paper presented in 2012 by Motycak *et al.* [14] the analysis of the computed cavitation structures and pressure profiles on the runner blade has allowed to validate the experimental observations of the tip cavities.

From all these works, it is clear that in order to develop a numerical methodology able to predict the cavitating phenomena in Kaplan turbines and applicable to any geometry in any operating conditions, it is necessary to consider the following aspects:

- The two-phases flow and cavitation models: the suitable use of the homogeneous model in this kind of hydraulic turbines has been demonstrated. For what concerns the cavitation model, the most used is the ZGB model [56]. This model depends on condensation and vaporization coefficients that have to be calibrated according to the simulated problem. For this reason, the barotropic law has been preferred for the present investigation.

- The **turbulence model** and the **mesh refinement** : these two aspects have a huge influence on the simulations results in particular on the shape of the cavitation sheet near walls.

- The **computational domain** and the **boundary conditions** : computational domain and tested model have to be in fluid dynamic similitude to obtain numerical results consistent with respect to the experimental data. The positions of the inlet and outlet sections and the boundary conditions setup affect the cavitation parameters value (i.e. H, $NPSH$) influencing the correct reproduction of the cavitating flow in the turbine.

Starting from these observations, the computational strategy to predict cavitating flow in Kaplan turbines has been developed and validated. This is presented in details in the chapter 4.

Chapter 3

Experimental setup

In the present study, experimental test in non-cavitating and in cavitating regimes have been performed in order to validate the developed numerical methodology of cavitation prediction in Kaplan turbines. A brief review of the main experimental works in cavitation conditions in Kaplan turbine will be presented. Starting from bibliographical the experimental tests planning was set. Afterwards, the experimental setup and techniques used in our work will be described.

3.1 State of the art of cavitation experiments in Kaplan turbines

In the literature, experimental studies on Kaplan Turbine in cavitation regime are mostly focused on the detection and the characterization of the cavitation structures. Motycak *et al.* [14], by means of a high speed camera, observe four different cavitation types: the hub, the leading edge, the tip clearance and vortex cavitations (figure 3.1). The hub and the leading edge cavitations are surface cavitations They depend significantly on the Thoma number and they are mainly responsible for the machine efficiency reduction. Depending on the head, a limited amount of cavitation on the tip is allowed in standard operating points. The tip cavitation slightly affects the turbine performance but can cause erosion phenomena on the runner blade. For this reason, it is considered as a very dangerous cavitating phenomena and an accurate prediction of the vortex cores shape and intensity is essential to avoid runner pitting.

The same cavitation phenomena have been recognized by Grekula and Bark [74],who focused their investigations on creation and transformation mechanisms (figure 3.2). The vapor structures observed on the leading edge are attached sheets resulting from a flow separation caused by a mismatched incidence angle. In the closure region, these structures disintegrate, generating bubbles, re-entrant jets and vortices. On the hub region, the cavitation sheets are

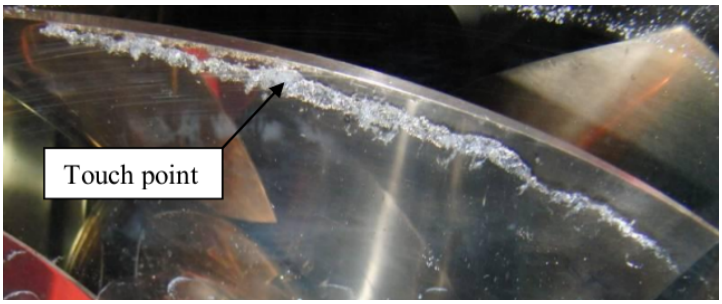

Figure 3.1 Experimental observation of the tip vortex cavitation by Motycak *et al.* [14].

originated from traveling bubbles gathering together. Finally, a detachment and a reattachment phases have been observed in the tip vortex mechanism, repeating over the blade length. A link between the vortex pattern and the vortices and wakes generated by the guide vanes is assumed. This hypothesis is confirmed by the pressure spectra analysis presented in the works

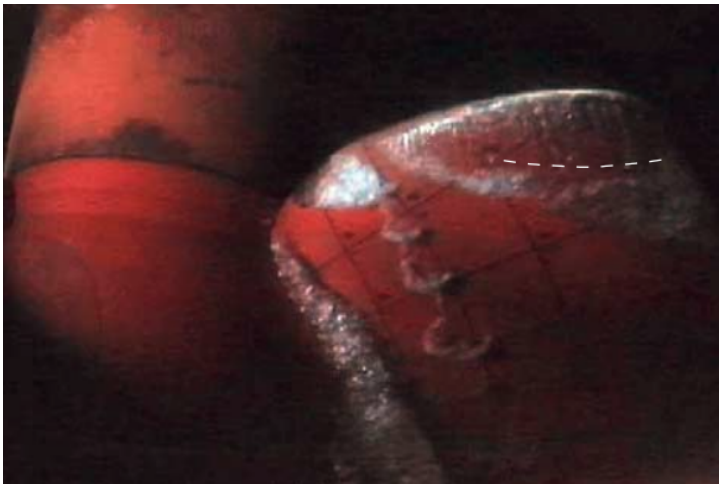

Figure 3.2 Experimental observation of the hub and the leading edge cavitation by Grekula and Bark [74].

of Nennemann and Vu [73] and Rus *et al.* [75]. An amplification of the pressure amplitudes at the guide vane passing frequency has been observed in the tip vortex cavities vicinity. The signature frequency of the leading edge cavitation has been found by Escaler *et al.* [76]. A vibration analysis in different load conditions has shown that the vibration amplitude increase in full load conditions. This confirms that the leading edge cavitation occurs mostly when the machine operates at maximum load.

Finally, Jonsson *et al.* [77], by means of air injection have identified and characterized a vortex rope in the draft tube occurring in partial loading conditions in non-cavitating regime (figure 3.3) This turbulent structures generally occurs out of the optimal load conditions, due to the presence of a residual circumferential component of the velocity on the draft tube inlet. The

vortex becomes a cavitation structures when the pressure in the core is lower than the vapor pressure threshold.

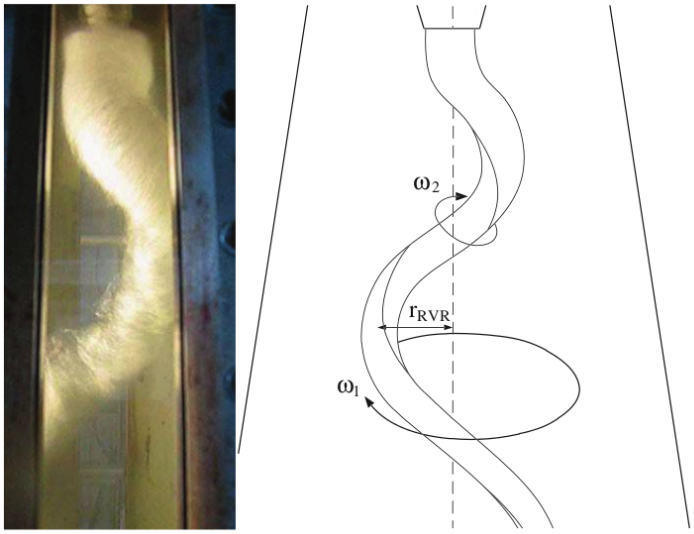

Figure 3.3 Experimental observation of the vortex rope cavitation by Jonsson *et al.* [77].

The principal aim of all of these experimental works is to investigate the cavitation structures in order to define the erosion limits. The effect of the cavitation structures on the machine performances have been rarely analyzed.

3.2 Objective of the experimental tests in the work

In the present work, the experimental investigations aim to support and validate the numerical methodology of cavitation prediction. The measurements of the machine performance and the runner outlet velocity fields in free-cavitation regime have allowed to calibrate the numerical strategy. Indeed, mesh refinement level, turbulence model and the boundary conditions setup are chosen to approach as much as possible the numerical operating point to the experimental one (see chapters 4 and 5). The predictive ability of the developed numerical strategy is evaluated by the qualitative comparison of the experimental σ-break curves and the cavitation structures. The visualizations of the vapor structures allow to firstly identify a correlation between the cavitating flow evolution and the machine performance reduction. This will be further investigated and confirmed by numerical analyses (chapters 5 and 6). Finally, the experimental investigation of the pressure fluctuations on the runner outlet evidences the presence of unsteady phenomena impacting the turbine performances.

3.3 Test rig

Any hydraulic machine must be specifically designed to cover the head and the discharge range associated with the installation site. So, every design is unique and the turbine installed on the site is called the prototype. To evaluate its performances for different operating conditions, experiments are carried out on a reduced scale model respecting, as much as possible, the geometrical, hydraulic and mechanic similitudes. This is necessary to transpose the reduce model results to the prototype. The experimental tests on the scale model are regulated by the International Electrotechnical Commission IEC 60193 Code [13]. This code defines the physical quantities that characterize the model operating points, the measurement methods, the test conditions and the formulas used to link the scale model to the prototype.

In this thesis, the Kaplan turbine scale model has been tested on the GE Renewable Energy laboratory platform. The main elements of the closed loop hydraulic system (figure 3.4) are:

- Two tanks, upstream and downstream of the reduced model;
- A pumping unit, which allows the fluid flow into the loop providing the machine head;
- A vacuum pump regulates the pressure at the free surface of the downstream tank and the absolute pressure level in the tested model;
- A generator, that sets the turbine rotation speed and allows the torque measurement;
- Different transducers measure the hydraulic and mechanical parameter characteristics for the different operating points.

The regulation of the rotation speed n sets the net head H between the upstream and the downstream of the reduced model. The power supply to the generator imposes the rotational speed of the shaft and the runner. The mass flow rate Q on the turbine inlet is determined by changing the guide vane opening γ. In a Kaplan turbine, also the runner blade angle α can be changed. Hence, the operating point is defined by regulating both the γ and the α (see chapter 1).

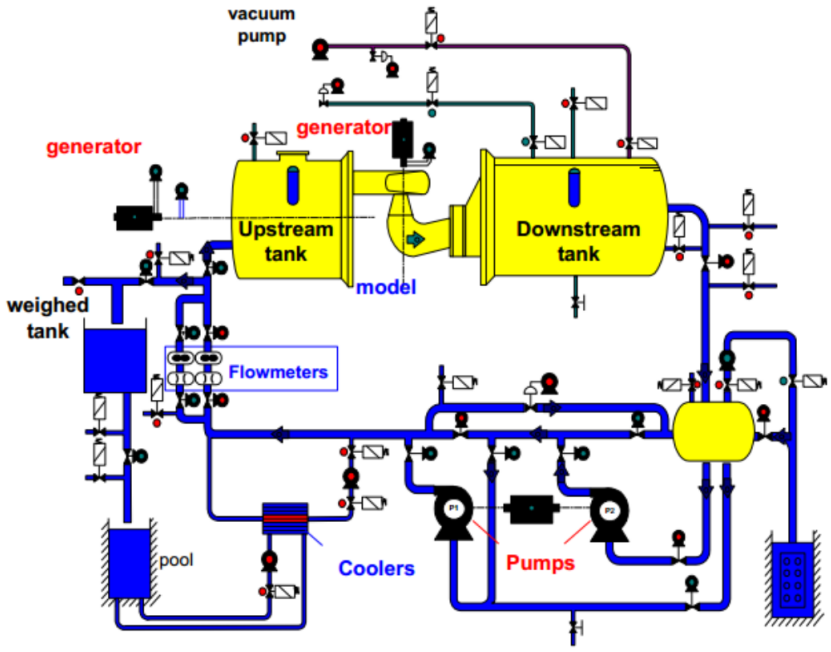

Figure 3.4 Scheme of a test platform at GE Renewable Energy laboratory [78]

3.4 Static measurements

3.4.1 Performance measurements

The turbine hydraulic efficiency is defined as the ratio of the mechanical output power of runner P_m and the hydraulic input power P_h:

$$\eta = \frac{P_m}{P_h} = \frac{T\omega}{\rho g H Q} \,. \tag{3.1}$$

On the laboratory platform, the error on the efficiency measurement does not exceed the 0.25% of its value.

To define P_m, it is necessary to measure:

- The *rotating speed* of the turbine ($\omega = 2\pi n$), measured by an encoder located on the generator shaft.
- The *mechanical torque* (T): is evaluated considering the contributions of the shaft torque T_s of the runner and the friction torque T_l, due to seal and bearing arrangement ($T = T_s + T_l$). On the test rig, the stator of the generator is supported by a hydrostatic bearing. If a torque is applied on the rotor, the stator starts to rotate with it. So, the torque T_s corresponds to the momentum necessary to block the stator. This momentum is evaluated as the product of the force applied to a lever arm attached to the stator and

the lever arm length. This force applied to balance the stator is measured by weighing masses on a lever system (calibrated weights and calibrated lever arm). A torque sensor is used to measure the residual momentum necessary to completely balance the stator. The friction torque T_l due to the shaft mechanical connections is measured by means of a special device mounted on the shaft line. The uncertainty on the torque value is 0.1%.

P_h is evaluated by measuring :

- The *fluid density* (ρ), evaluated from the measured water temperature. The temperature is measured in the downstream tank with an error of $\pm 0.1\ C^{\circ}$.

- The *gravity acceleration* (g), whose value is corrected according to the geographic coordinates of the test laboratory.

- The *volumetric water discharge* (Q), which is measured using two electromagnetic flowmeters placed in series upstream of the turbine. The measurement is doubled to ensure that the value does not derived over time. The electromagnetic flow meters do not generate any disturbance of the flow nor pressure loss and are not sensitive to wear. The uncertainty on the flow rate measurement is 0.1% of the value.

- The *net head* of the machine (H). Following the IEC 60193 standards [13], it is evaluated as:

$$H = \underbrace{\left(\frac{1}{\rho g}\right)(P_1 - P_2)}_{Static} + \underbrace{\frac{Q^2}{2g\rho^2}\left(\frac{1}{S_1^2} - \frac{1}{S_2^2}\right)}_{Dynamic} . \tag{3.2}$$

The static and dynamic parts of the head are assessed separately. The static head is measured by pressure differential transducers. The pressure transducers are located on the wall of the distributor inlet section (**1** in figure 3.5) and the draft tube outlet (**2** in figure 3.5).The measure sensors may be manifolded through a connecting pipe and the final pressure is the average of the measured pressure values on each sensor. The difference between inlet and outlet sections levels, $(z_1 - z_2)$, is included in the static pressure difference term by means of a constant value. In the hypothesis of a turbulent uniform flow on the machine inlet and outlet sections, the dynamic head is estimated as function of the bulk velocity (Q/S). As for the discharge, the H measurement is doubled. The error in the net head evaluation is about 0.1%. During the experimental tests, the H and the Q are constantly adjusted by controlling the rotation speed of the circuit pump.

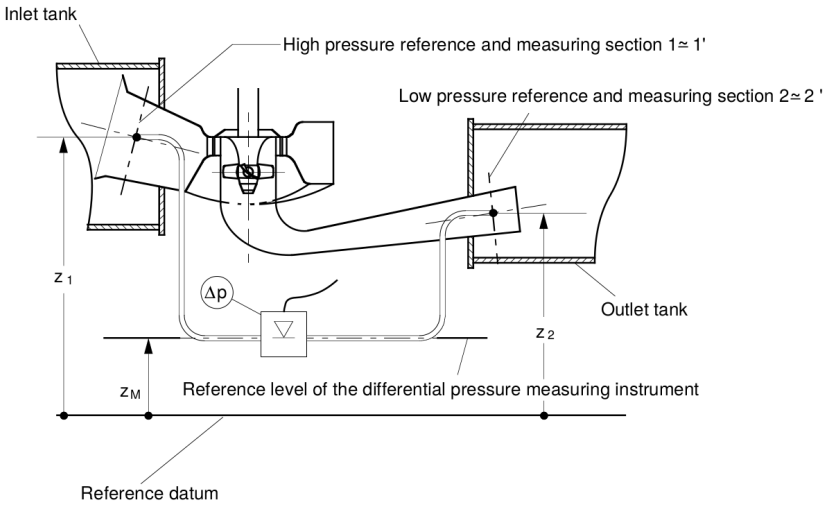

Figure 3.5 Pressure measurement setup according to the IEC code [13]: **1** distributor inlet and **2** IEC plane in the draft tube outlet.

3.4.2 Measurements of the losses in the draft tube

The draft tube is one of the main losses sources, especially for operating conditions, which deviate from the optimal ones. As it is shown in figure 3.6, pressure transducers have been located on a section near the inlet of the cone. The chosen probing plane is placed at 170*mm* from the reference axis (which corresponds to the blade axis according to the IEC code). So, the static head in the draft tube is assessed as the pressure difference between the probing plane (**3**, figure 3.6) and the IEC plane on the draft tube outlet (**2**, figure 3.6).

3.4.3 Velocity profiles on the runner outlet

Velocity profiles at the runner outlet were measured by a LDV (Laser Doppler Velocimetry) technique. The LDV is a non-intrusive, unsteady, optical measurement technique of the seeding particles velocity in a flow. Two laser beams focused on the same point in the flow and their intersection creates a measurement volume of a few millimeters (figure 3.7). Due to the Doppler effect, the particles passing through this measurement volume diffuse the laser light at a frequency different from the laser beam frequency. The particle velocity is calculated as the difference between the frequency of the laser beam and the frequency emitted by the particle. Thus, it is an indirect and local measurement technique of the flow velocity since it measures the velocity of particles supposed to follow perfectly the flow.

In order to perform LDV measurements, particles have to be added to the flow. In the General Electric laboratory, for environmental reasons, it is not possible to add particles to the water passing through the turbine. But, as particles and bubbles are naturally present in the

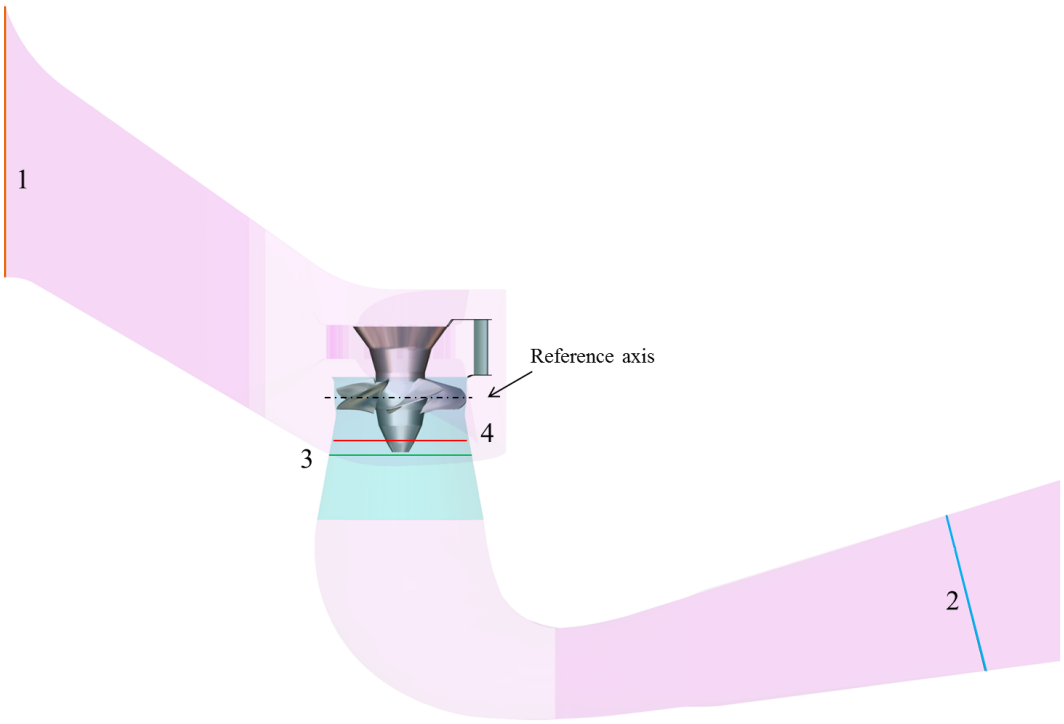

Figure 3.6 Probing planes positions on the scale model: **1** distributor inlet; **2** IEC plane in the draft tube outlet; **3** probing plane for the differential pressure transducers and for the LDV measurements; **4** pressure fluctuations probing plane.

water, it is possible to perform these measurements. The optical measurement is carried out along a diameter which is discretized by an acquisition grid, refined in the boundary layers. At each point of the grid the measurement is limited by the acquisition time, set at $20s$ (≈ 16 runner rotations), or by the maximum number of particles tracked, set at 5000. The mean velocity in each point of the diameter is obtained by the averaging every acquired particle velocities. The uncertainty in the resulting velocity profiles varies from 1% to 10%, depending on the quality of the acquisition. More information about the LDV technique can be founded in [80]. The LDV measurements have been performed at $170mm$ from the reference axis (**3**, figure 3.6). Only the axial V_z and tangential V_t velocity components have been measured. The velocity profiles obtained by laser measurement are not symmetric since the probing area is influenced by different factors (as is shown in figure 3.8):

- The presence of two stagnation areas, one due to the runner tip and one due to the presence of an observation window. This local modification of the cone geometry is necessary to ensure the orthogonality between the laser beam and the observation window.

- The measurement length is limited by the maximum length of the laser beam.

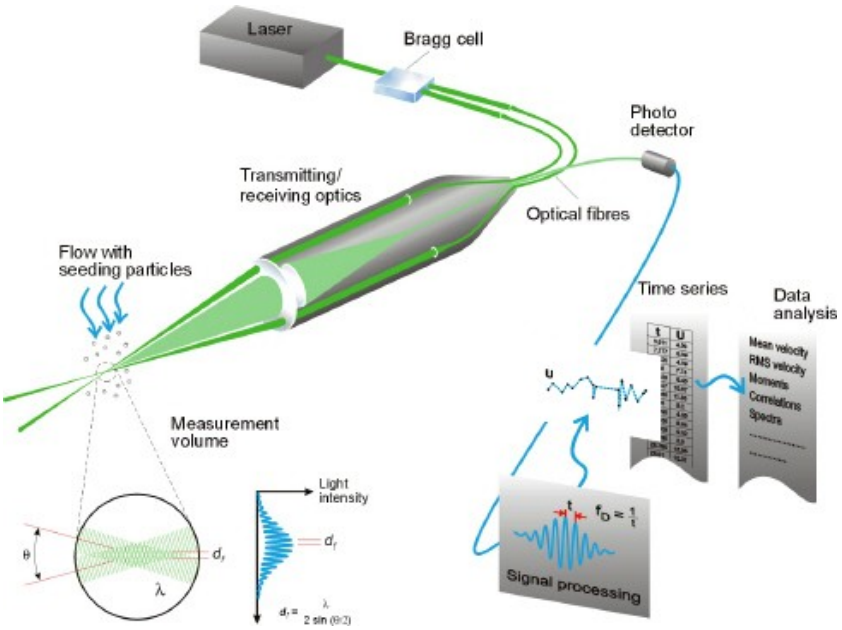

Figure 3.7 Scheme of the operating principle of the LDV (Laser Doppler Velocimetry) measurement technique [79].

The measurements were performed only in the non-cavitating regime. In developed cavitating regime the vapor structures disturb the laser.

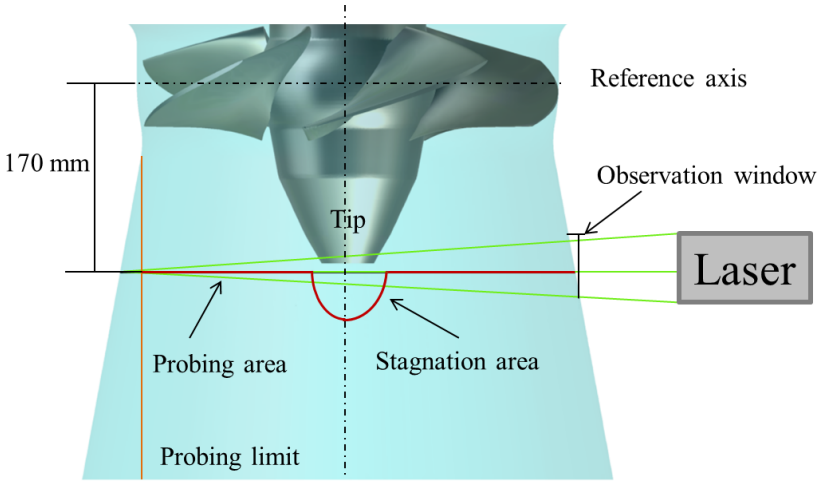

Figure 3.8 Scheme of the LDV setup.

3.4.4 Cavitation measurements

The objective of the cavitation model test is to monitor the effect of cavitation development on the hydraulic characteristics of the machine, as well as establishing the type of cavitation

that could develop during the operation of the machine [12]. Common practice [13, 12] is to monitor the evolution of σ-break curve ($\eta = f(\sigma)$, see chapter 1). In the cavitation tests, the pressure in the downstream tank is progressively reduced inducing cavitation phenomena in the machine. During these experiments, the temperature, the net head and the rotating speed are keep constant. The experimental *NPSH* is estimated as:

$$NPSH = \underbrace{\frac{(P_2 - P_V)}{\rho g}}_{Static} + \underbrace{\frac{1}{2g}\left(\frac{Q}{S_2}\right)^2}_{Dynamic}, \tag{3.3}$$

where:

- P_2 is the static pressure measured on the IEC plane (**2**, figure 3.6);
- P_V is the water vapor pressure which depends on the test temperature and pressure;
- $\frac{Q}{S_2}$ is the bulk velocity in the hypothesis of a turbulent uniform flow at the draft tube outlet.

It is important to state that the cavitation curves are strongly influenced by the nuclei content in water, i.e. number and size distribution of micro bubbles [9]. At present, knowledge is not enough to standardize the minimum nuclei and dissolved gas content for cavitation tests [13]. Measurements show that water is always saturated at prototype scale hydraulic installations (i.e. the cavitation phenomenon at prototype is not limited by a lack of active nuclei) [9]. It is thus recommended to have saturated water for cavitation model tests; this saturation condition is achieved by injecting micro bubbles until the efficiency stops decreasing for a given sigma value. In other words, for a threshold value of nuclei content, efficiency stops decreasing by increasing nuclei content, for a given value of Thoma number [9, 12].

The appearance and evolution of the cavitating structures is recorded by two high-speed cameras. The cameras setup is illustrated in figure 3.9.

3.5 Dynamic measurements

During the experiments, the fluctuations of several physical quantities of interest could be measured. In the present work, considering that in Kaplan turbine cavitation phenomena are concentrated on the runner, the evolution of the pressure fluctuations with the σ reduction have been measured at the downstream of the runner. Four piezoelectric pressure transducers have been positioned on a fixed wall, around the cone diameter, a 120*mm* from the reference axis (plane **4** in figure 3.6). This kind of pressure sensors use the property of the piezoelectric

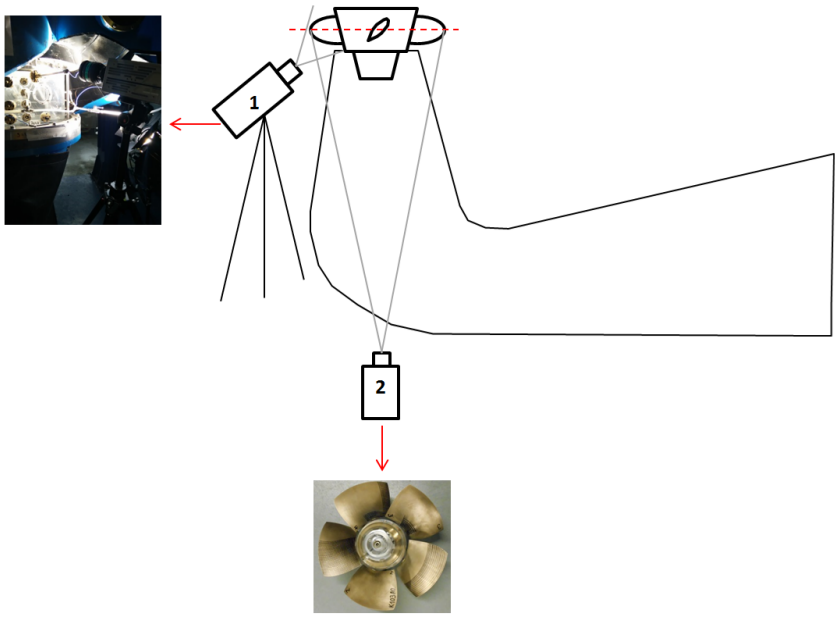

Figure 3.9 High-speed cameras setup.

materials to produce a voltage under mechanical stresses. Therefore, the dynamic part of the pressure applied on the sensor sensitive surface generates voltage variations, which correspond to the fluctuations on the reduced model walls. Raw data of pressure fluctuations can be difficult to analyze and a spectral analysis can allow us to identify peculiar pressure phenomena. Indeed, some frequencies can indicate particular phenomena that occur in the machine during its operations. Considering the runner rotation frequency f_0, the sample frequency used is equal to $\frac{f}{f_0} = 156$ corresponding to a blade rotation of 4.5°. So, the signal analysis is only possible for frequencies below about $\frac{f}{f_0} = 78$ (Nyquist-Shannon sampling theorem). This limit is much higher than the frequency signatures analyzed in this study, i.e. the tip cavitation frequency (Chapter 6).

3.5.1 Spectra analysis

Considering the real signal $x(t)$, N values $x_1, ..., x_N$ of this signal are recorded during the time T at the sample frequency f_s. In the hypothesis of a periodic signal, it can be decomposed in Fourier series. So the time signal is decomposed into a sum of sinusoidal signals with different amplitudes, frequencies and phases. These parameters can be deduced from the

Fourier transform $\widehat{X_T}(f)$ of the periodic signal $x(t)$, defined as:

$$\widehat{X_T}(f) = \int_{\mathbb{R}} x(t) exp^{-i2\pi ft} dt \ . \tag{3.4}$$

The module of the transform is the spectrum signal that describes the evolution of the different amplitudes as a function of the frequency. The fundamental hypothesis of the Fourier transform formulation of a periodic signal over the time T is not verified since it very difficult that the first and the last values of the measured signal are equal. The discontinuity of the measured signals disturbs the estimation of the frequency content. So, the signal is multiplied by a function which is zero at the edges of the measurement interval $[0;T]$, called *window*, obtaining a T-periodic signal. However, windowing causes a loss of information at the edges of the measurement interval. Several window types exist in signal processing. The most used in the turbomachinery applications is the Hann's window [81], defined as:

$$h(t) = \begin{cases} \frac{1}{2} - \frac{1}{2} cos\left(2\pi \frac{t}{T}\right) & t \in [0;T] \\ 0 \end{cases} \ . \tag{3.5}$$

Chapter 4

Numerical methodology

In the present chapter, the numerical methodology of cavitation prediction will be described. For the two investigated operating points the steady and the unsteady computational strategies will be presented. The tested numerical domain, mesh levels and boundary conditions setup will be introduced. Details also on the computational resources used will be furnished. The results obtained will be analyzed in chapters 5 and 6).

4.1 Reduced-scale Kaplan turbine model

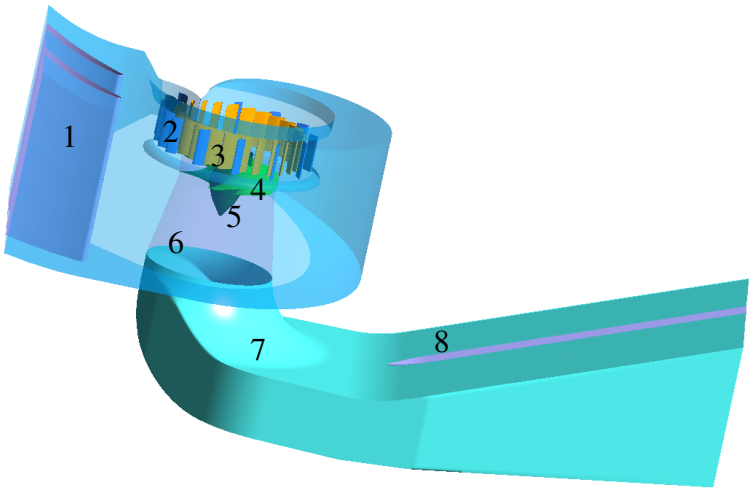

Specific speed n_s	170
Number of stay vanes	14
Number of guide vanes	24
Number of runner blades	5
Number of draft tube piers	1

(a) **(b)**

Figure 4.1 (a): Scheme of the tested turbine model: (1) The semi-spiral distributor; (2) the stay ring; (3) the guide vanes; (4) the runner blades and (5) the runner tip; (6,7,8) the draft tube: (6) the cone, (7) the elbow and (8) the pier. **(b)**: table summarizing the geometrical characteristics of the tested turbine.

The investigated machine is a reduced-scale Kaplan turbine model developed and tested at the *GE Renewable Energy Laboratory* in Grenoble (France), whose schematic is reported in figure 4.1 **a**. The water is conveyed by a spiral distributor into the turbine. Crossing the stay ring and the guide vanes, the flow then passes through a 5-blades runner. Finally, a draft tube recovers the flow kinetic energy. The main characteristics of the tested turbine are enlisted in the table reported in figure 4.1 **b**. Experiments and simulations have been performed for two operating points, highlighted on the hill chart shown in figure 4.2:

1. In optimal load conditions (OP_1) (indicated with the blue circle in figure 4.2): guide vanes opening, $\gamma = 39.53°$ and a blade angle, $\alpha = 25.93°$;

2. In full load conditions (OP_2) (indicated with the red circle in figure 4.2): $\gamma = 51.19°$ and $\alpha = 40.16°$.

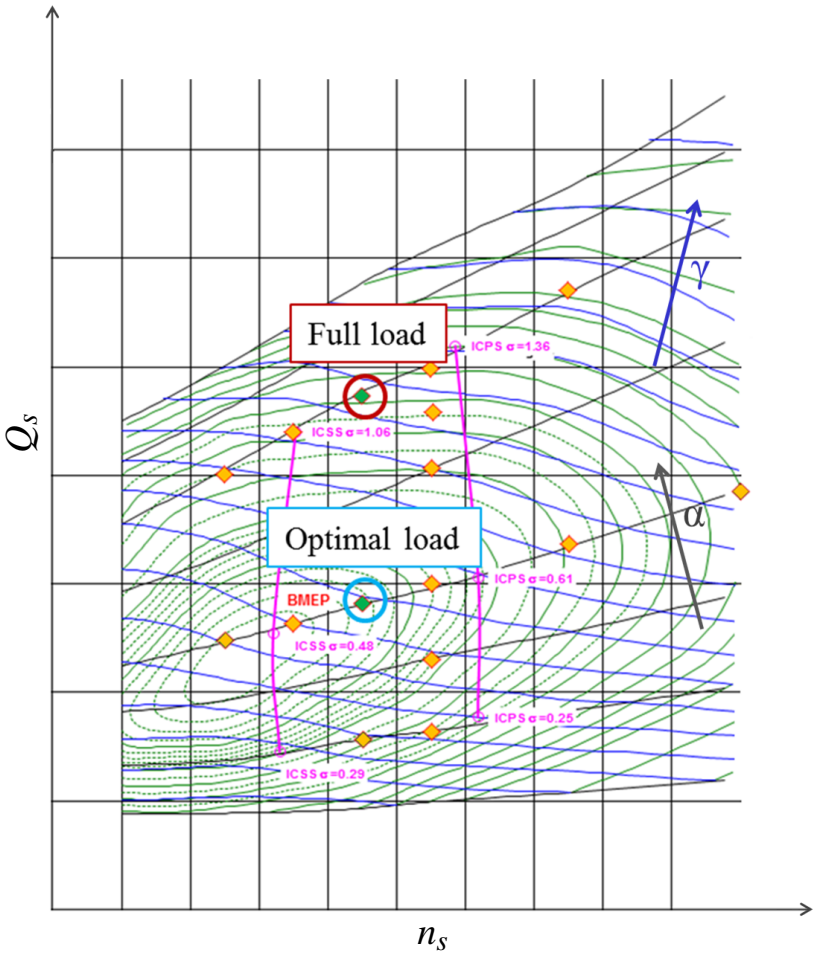

Figure 4.2 Kaplan turbine model hill chart.

The OP_1 is the machine design point and, for this reason, it has been chosen as a starting point for the development of the numerical methodology. Given the high flow stability, cavitation predictions with both steady and unsteady analyses have been performed in these conditions. Afterwards, to check the generality of the calculation strategy, the numerical analyses are repeated also for the OP_2 point. Differently from the OP_1, this is a full load operating point where the machine works out of the design operating conditions. This results in a strongly unstable flow, for which only unsteady simulations have been possible. In the following sections the developed numerical methodology for the cavitation prediction will be presented starting from the numerical investigation of the optimal load point OP_1 and after of the full load point OP_2. The results in terms of global performances evolution and flow analyses of the two analyzed operating points will be described in the chapter 5 and in the chapter 6.

4.2 Numerical investigation of the optimal load operating point OP_1

4.2.1 Computational domains

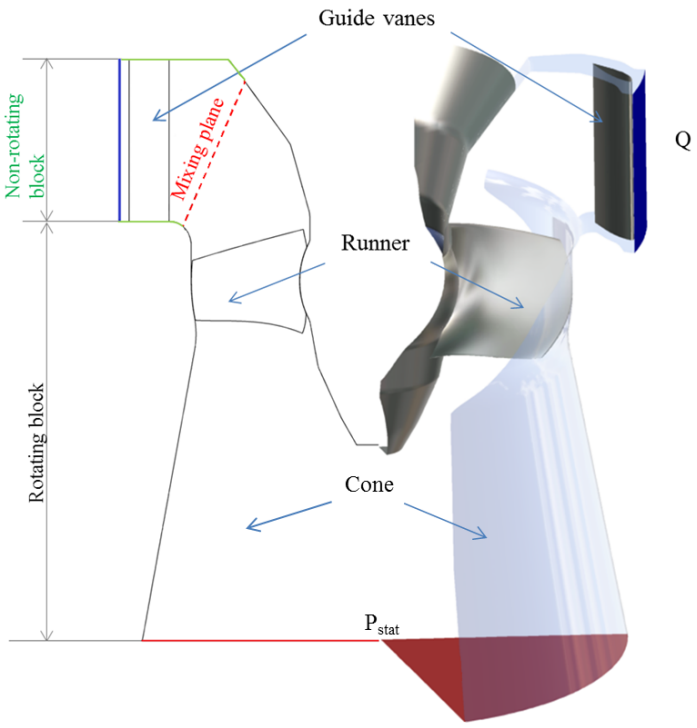

Figure 4.3 Numerical domain D_1 with the boundary conditions used; the inlet is in blue and the outlet in red. Left: meridional view. Right: 3D view.

In the numerical methodology for the steady simulations different levels of geometry details of the analyzed system figure 4.1 have been tested. At first, preliminary simulations have been performed on the partial domain shown in figure 4.3 (this configuration will be referred to as D_1), comprising only a single interblade channel consisting of the guide vane, the runner blades and the cone. The tip and hub clearances, typical of Kaplan turbines, are included in the numerical model since well description of the flow through these gaps is fundamental to determine the behavior of the hub and the blade tip cavitation regions. A periodic boundary condition is imposed to account for the entire machine. Then, the draft tube has been included in

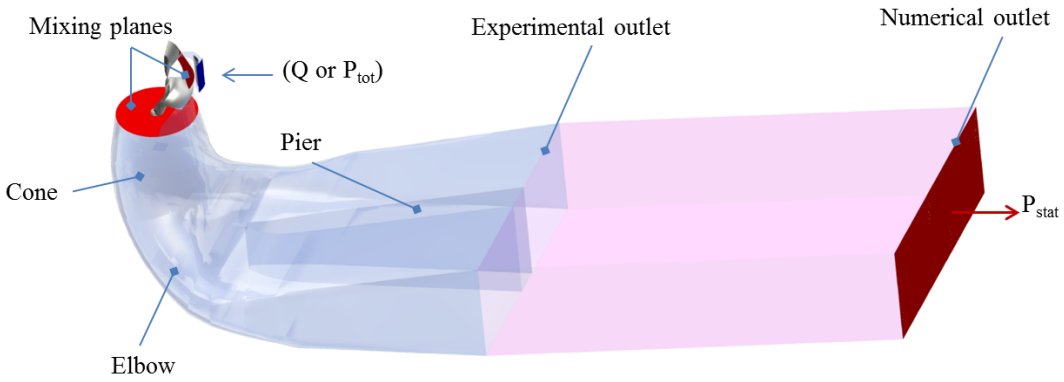

Figure 4.4 3D view of the numerical domain D_2 with the boundary conditions used; the inlet is in blue and the outlet in red.

the analysis and the numerical domain has been extended (domain D_2 presented in figure 4.4).

Differently for the steady case, the unsteady calculations have required the complete geometry. This in order to simulate all the interblade channels in the guide vane and in the runner. The periodicity condition was not used anymore so all the 24 guide vanes and the 5 runner blades have been modeled as shown in figure 4.5 (domain referred to as D_3).

Should be further underlined that to improve the numerical stability of the simulations an additional volume (highlighted in pink in figure 4.4) has been added after the draft tube outlet in both steady and unsteady analyses. On the contrary, the spiral casing was neglected given its negligible influence. A detailed analysis and influence study of the spiral casing are reported in the Annex A.

4.2.2 Discretization of the numerical domains

The generation of a high quality computational mesh for the analyzed Kaplan turbine is not a trivial operation. This is because multiple constrains should be respected. The most important of them are listed hereafter:

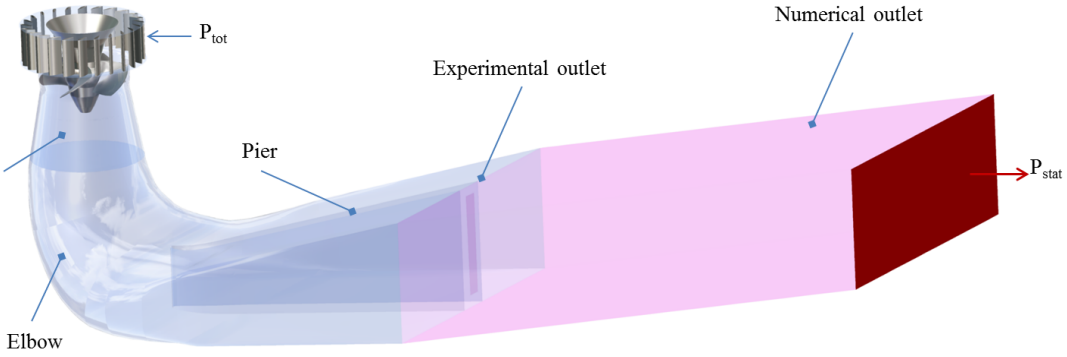

Figure 4.5 3D view of the numerical domain D_3 with the boundary conditions used; the inlet is in blue and the outlet in red.

1. *The geometry configuration*: compared to the blade or to the hub of the runner, the partial gaps on the hub have reduced dimensions. A local mesh refinement is required, which could not allow to ensure the homogeneity of the grid.

2. *The phenomena to simulate*: cavitating flows are characterized by huge density gradients due to the presence of vaporization and condensation processes. Thus, during simulations, it is possible that two contiguous cells are filled one by pure vapor and one by pure water. This density discontinuity could be difficult to manage from a numerical point of view on an extremely fine discretization [82]. On the other hand, to obtain a correct reproduction of the flow behavior in the turbine, a refinement of the mesh near to the wall is required.

3. *The turbulence model and the wall functions*: the determination of the dimensions of the inner cells depends on the turbulence model and on the wall functions used. A coarse mesh ($y^+ > 20$) could strongly influence the numerical results (see paragraph 2.1.4).

4. *The application of the multigrid strategy* (see paragraph 2.3.4).

5. *The computational costs*.

For these reasons, at first an optimization study of the mesh has been performed in steady conditions on the reduced domain D_1 (figure 4.3). Starting from an initial coarse mesh M_1, the numbers of elements have been increased until a more adequate fine mesh (M_2) was obtained. A fully-structured discretization approach involving only hexahedral cells was used in this analysis. Meshing was performed by using the *Numeca* software *AutoGrid 5*. The characteristics of these two grids, the initial coarse mesh M_1 (figure 4.6 a) and the final optimized one M_2 (figure 4.6 b), are summarized in details in table (4.1). A particular mesh treatment was required for the discretization of the numerical domain D_1 (figure 4.3). Indeed, the particular shape of the tip of the runner induced a distortion of the grid. To improve the

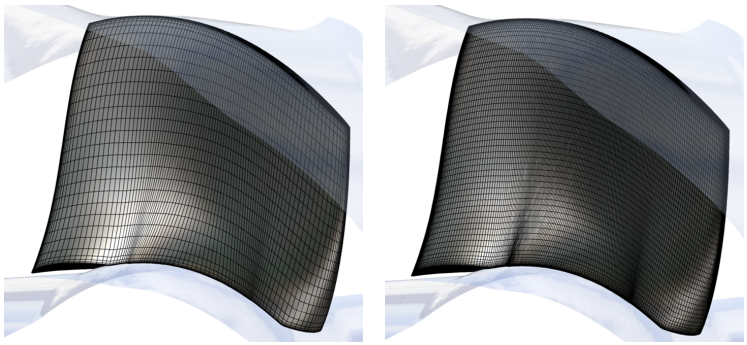

(a) **(b)**

Figure 4.6 Mesh levels tested: **(a)** coarse M_1 and **(b)** fine M_2.

Table 4.1 Characteristics of the meshes of the domain D_1 (M_1 and M_2).

	Component	**Number of elements**	**Min.skewness**	**Max. expansion ratio**	y^+_{mean}
$\boldsymbol{M_1}$: Level 1, coarse mesh	Guide vane	0.1M	38°	3	3
	Runner	1M	9°	4.5	4.7
	Cone	0.6M	15°	1.8	3.6
	Total	1.7M			4.3
$\boldsymbol{M_2}$: Level 0, fine mesh	Guide vane	0.8M	38°	3	1.3
	Runner	8.1M	9°	4.5	2
	Cone	4.7M	15°	1.8	1.1
	Total	13.6M			1.2

quality of curved geometry meshes, a multi–blocks method, called the *butterfly technique*, has been applied. This consists in splitting a single block in an inner block surrounded by other blocks (as is shown in figure 4.7). Doing this the mesh is better adapted to the shape of the geometry is achieved, at the price of incrementing the total number of mesh elements (for more details about the this technique see [33]).

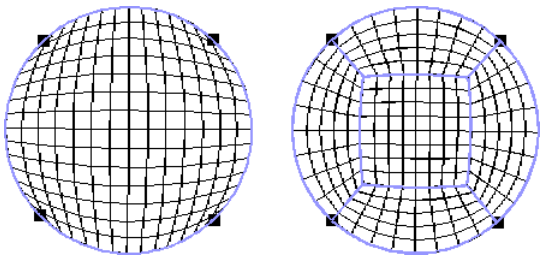

(a) **(b)**

Figure 4.7 **(a)** Classical and **(b)** butterfly topology on a circle.

From the analyses performed on the domain D_1 (presented in chapter 5), the extended domain D_2 has been studied. The domain D_2 (figure 4.4) has been discretized using two fully-structured meshes. The mesh of periodic interblade channel of the guide vane and the runner was obtained cutting the fine mesh of the domain D_1 above the runner tip. Then, the

runner tip and the draft tube have been discretized separately. This second mesh was performed with the software *IGG*. This has allowed to reduce the number of the grid elements in the first part of the domain since the butterfly technique is no more used. Finally, the mesh of the draft tube was also joined to the first part of the domain obtaining the final computational domain (M_3). The main characteristics of the mesh M_3 are listed in the table 4.2.

Table 4.2 Characteristics of the mesh of the domain D_2 (M_3).

Component	**Number of elements**	**Min.skewness**	**Max. expansion ratio**	y^+_{mean}
Guide vane	0.8M	38°	3	1.3
Runner	7.3M	9°	4.4	2
Draft tube	6M	18°	1.8	8.7
Total	14.1M			8.4

Table 4.3 Characteristics of the mesh of the domain D_3 (M_4).

Component	**Number of elements**	**Min.skewness**	**Max. expansion ratio**	y^+_{mean}
Guide vane	19.2M	38°	3	1.3
Runner	36.5M	9°	4.4	2
Draft tube	6M	18°	1.8	8.7
Total	61.7M			8.4

In the case of the numerical domain D_3 used in unsteady calculations, the periodicity has not been used as a boundary condition neither in the guide vane nor in the runner. The mesh M_4 of the numerical domain D_3 was created starting from M_3. Since, the simulations have been performed on the fine level of the grid, to compute the total number of grid elements one need to multiply the number of the nodes of the mesh M_3 by 24 for the guide vane and by 5 for the runner. This results in about 61.7 M elements (the characteristics of the mesh M_4 are reported in table 4.3).

Mesh quality is now discussed focusing the attention on three fundamental parameters: the dimensionless number y^+, the skewness and the expansion ratio. The mean value of the y^+ for the meshes M_1 and M_2 is less than 5 (see table 4.1). This in order to locate the first inner node in the viscous sublayer (for the y^+ limit values, see paragraph 2.1.4). For both grids, the highest y^+_{max} values, i.e., $y^+_{max} = 14$ for the mesh M_1 and $y^+_{max} = 7.5$ for the mesh M_2, are reached on the leading edge near the blade tip where the flow has the highest velocity. Concerning the meshes M_3 and M_4, the average y^+ in the draft tube is between 5 and 20, so the inner cells are located in the buffer layer. Values of $y^+ = 20$ are reached in the additional volume (colored in pink in figure 4.4), whereas in the nose of the pier a lower value of $y^+ = 12$ is achieved, since this is a stagnation point. Considering that an accurate prediction of the losses in the draft tube is not in the main interest of this thesis, these values of y^+ are considered acceptable and no more mesh refinements are required.

The other two parameters used to asses mesh quality are the skewness, an index of the cells orthogonality and the expansion ratio, which represents the change in volume between two neighboring cells. Generally, a minimum skewness of 15° and a maximum expansion ratio of 5 are sufficient to ensure a proper mesh (see [33]). The characteristics of the structured meshes created accord to these limit values, as indicated in tables 4.1 and 4.2. The only value out of the acceptability ranges is the minimum skewness on the runner which is equal to 9°. Indeed, due to the complex shape of the blade and considering the presence of thin gaps on the hub and on the shroud, a structured discretization of this part of the domain is very difficult. The final mesh has been obtained after several optimization studies and was considered appropriate for our applications.

4.2.3 Rotating blocks and interfaces

To accurately reproduce the real behavior of the turbine, the numerical domain must be divided in stationary and rotating parts. The software FINE™/Turbo, as default, solves the governing RANS and URANS equations for the relative velocity components in the relative system. This means that for the blocks with a rotational speed equal to zero, the source terms composed by the Coriolis and the centrifugal forces are neglected. As shown on the left side of figure 4.3, in the computational domain D_1 while the guide vanes has been set as a non–rotating block, the rotor and the cone consist of a single rotating block. All the solid parts were assumed as adiabatic non-slip walls. Inside the rotating block, non-rotating walls have been defined. The shroud and the upper part of the hub, nearest to the guide vane, are set to be static with respect to the rotational frame.

In the numerical domains D_2 and D_3 (figure 4.4), the draft tube has been considered as a non-rotating block with the boundary with the runner placed at the middle of the runner tip. Consequently, the part of the tip inside this stationary block has been considered as rotating with respect to this frame. The connection between stationary and rotating blocks has been ensured by means of the interfaces. In this work, for the steady calculations the interfaces were modeled by a *Full Non Matching Mixing Plane*, which allows to conserve the mass flow and the momentum between the static and the rotating parts (for more informations about the Full Non Matching Mixing Plane see Ref. [33]). For the unsteady simulations, the *Domain Scaling* method is used to simulate the rotor/stator interfaces. Using this technique the effect of displacement due to rotation is taken into account. At each time step, the rotor is set at its correct position and equations are solved for that particular time step for the whole computation domain. The final solution is therefore a succession of instantaneous solutions for each increment of the rotor position. This explain why all the guide vanes and the blades runner were included in the computational domain.

4.2.4 Numerical methodology for steady calculations

All the steps of the developed methodology for steady simulations are detailed in the following paragraphs. The description of the computational strategy is structured as follows: at first, the discussion focus on the simulations performed on the reduced domain D_1. Then, the calculations performed on the extended computational domain D_2 are presented.

4.2.4.1 Simulations performed on the domain D_1

The preliminary simulations on the reduced domain D_1 (figure 4.3) have been performed to define the optimal numerical setups of the methodology aiming to a reduction of the computational costs. The tested geometry and the meshing characteristics have been presented in the paragraphs 4.2.1 and 4.2.2, respectively. The strategies used to determine the appropriate turbulence model and the grid refinement level, and the boundary conditions treatment are set out in the following subsections.

Turbulence model and mesh refinement In the conception process of a numerical methodology, the first step consists in the determination of the turbulence closure. Indeed, in simulations, turbulence models and wall functions can influence the correct reproduction of the flow and of the cavitation structures in the turbine and, as a consequence, the prediction of the machine performances evolution. Another very important aspect in numerical calculations is the evaluation of the level of the mesh refinement. The domain discretization have a fundamental role in the flow simulation and it is strictly linked to the criterion of the turbulence model and wall functions used (see chapter 2). The $k-\varepsilon$ with *Extended wall function* (EWF) and the $k-\omega$ SST turbulence models, detailed in chapter 2, have been tested and compared on the two different grid levels, i.e., the coarse mesh M_1 and the one optimized fine M_2, presented in the paragraph 4.2.2. At first, simulations have been performed in non-cavitating regime imposing classical boundary conditions for incompressible calculations: the experimental mass flow rate value Q_{exp} as inlet and a static pressure equal to the ambient one P_{amb} as outlet. The mass flow rate Q on the inlet has been coupled with the velocity profiles that come from the stay ring and supposed to be linear. The law to determine these profiles has been furnished by *GE Renewable Energy Laboratory, Grenoble, France*. Afterwards, the cavitation has been induced in the system by decreasing the *Cavitation number* (or the *Thoma number*) σ. The downstream Thoma number in FINE™/Turbo is defined as 4.1:

$$\sigma_{downstream} = \frac{P_{ref} - P_{VAPS}}{\rho U^2} \ , \tag{4.1}$$

where the P_{ref} is the reference pressure imposed equal to the ambient pressure value P_{amb}, P_{VAPS} is the relative saturation pressure and $U = \omega R$ is the reference velocity. In order to decrease the cavitation number σ, the relative saturation pressure P_{VAPS} is increased to reach different values of the σ, keeping the downstream pressure P_{out} constant. All the calculation parameters are summarized in table 4.4.

Table 4.4 Numerical setup for the turbulence model and grid level determination strategy.

Case	Turbulence model	Mesh level	Inlet BC	Outlet BC	Cavitation model
1	$k-\varepsilon$ (EWF)	M_1	$Q = Q_{exp}$	$P = P_{amb}$	Barotropic law
2	$k-\omega$ SST				
3	$k-\varepsilon$ (EWF)	M_2			
4	$k-\omega$ SST				

Inlet and outlet boundary conditions As for the turbulent model, imposed boundary conditions will greatly influence the stability and the results of the simulations. So, their correct definition is another fundamental step of the setup of a calculation strategy. At first, starting from the classical set of boundary conditions for incompressible flows, a mass flow rate equal to the experimental one, Q_{exp}, has been imposed at the inlet of the guide vane channel and the ambient pressure value P_{amb} was fixed at the outlet (*Case A*). Each operating point of a turbine is identified on the machine hill chart by a couple of machine speed n and mass flow rate Q values. Moreover, for a fixed value of the head H, at each couple (n, Q) will correspond a single value of the efficiency η. Considering this, a correct comparison of the numerical results with experimental data will be achieved only if a small mismatch is obtained between the numerical and experimental values of the machine speed n, the head H and the mass flow rate Q. However, in a numerical computation it is possible to control only two of these three parameters.

In the simulations performed on the reduced domain D_1, the mass flow rate Q and the machine speed n are imposed, whereas the machine head H is computed. However, as will be discussed in more details in section 4.2.4.2, considering that the extension of the computational domain D_1 is reduced compared to the real geometry, it was not possible to have the same experimental and numerical head H value. This suggested that to ensure the fluid dynamic agreement between the experimental and the simulated machine another parameter should be fixed. Among the machine performance indicators, the torque T has been chosen since its determination is strictly linked to the flow incidence on the blades and on the hub of the runner.

Indeed, the machine torque T can be calculated as 4.2:

$$T = \int_S \boldsymbol{r} \times \bar{\boldsymbol{F}} dS \,, \tag{4.2}$$

where $\boldsymbol{r}$ is the vector distance from the rotation axis z and $\boldsymbol{F} = \boldsymbol{F}_V + \boldsymbol{F}_p$ is the sum of all the viscous and pressure forces acting on the considered surface S. Furthermore, a numerical torque value closer to the experimental one ensures that the work of the turbine is correctly reproduced.

At first, keeping the experimental mass flow rate Q_{exp} as inlet boundary condition, various tests in non-cavitation conditions have been computed to reduce the difference between the experimental and numerical torque :

- The guide vanes opening γ and the blade angle α have been modified within the measurement uncertainty range ($\pm 0.2°$). In this range, several (γ, α) combinations have been tested in non-cavtating regime. Slight improvements in terms of torque value and velocity profiles at the runner outlet predictions have been achieved reducing only the blade angle of $0.2°$. Hence, this geometrical configuration has been used for all the following calculations;
- The velocity and the turbulence profiles obtained from the simulation of the single distributor have been imposed as inlet boundary condition on the domain D_1 (more information about this test are in Annex A). Considering that this method has not led to any significant improvement of the torque value and it requires higher computational costs, it has not been further used in the rest of the present study.

Finally, the following iterative procedure is tested: starting from the experimental value Q_{exp}, the mass flow rate is varied until the target value of torque is obtained (*Case B*). The corrected numerical mass flow rate will be referred to as Q_{cor}. This correction could be justified by the fact that during cavitation experiments, the machine head H is the parameter that is kept constant, whereas the mass flow rate on the inlet Q could change with the cavitation development of about 2.5% of its nominal value. This procedure has been applied in a non-cavitating regime and, once the Q_{cor} has been fixed, simulations have been performed also in cavitating conditions. These simulations have been performed on the fine mesh M_2, applying the $k-\omega$ SST turbulence model. The used numerical parameters are summarized in the table 4.5.

4.2.4.2 Simulations performed on the domain D_2

After the preliminary tests on the reduced domain D_1, the extended domain D_2 (shown in figure 4.4) is considered. In this domain the draft tube has been included in the analysis in

Table 4.5 Numerical parameters used on the inlet boundary condition tests on D_1.

Case	Inlet BC	Outlet BC	Mesh level	Turbulence model	Cavitation model
A	$Q = Q_{exp}$	$P_{out} = P_{amb}$	M_2	$k-\omega$ SST	Barotropic law
B	$Q = Q_{cor}$				

order to estimate its effect on the flow and, consequently, on the machine performance leading to an accurate comparison between simulations and experiments. This appears more evident if the definition of the turbine head H is recalled. Assuming an uniform flow at the distributor inlet S_{in} and at the draft tube outlet sections S_{out}, the experimental value of the turbine head H_{exp} is evaluated as 4.3:

$$H_{exp} = \frac{(P_{in} - P_{out})}{\rho g} + \frac{1}{2g}\left(\frac{Q}{\rho}\right)^2 \left(\frac{1}{S_{in}^2} - \frac{1}{S_{out}^2}\right) , \tag{4.3}$$

The equation (4.3) shows that the machine head definition depends on the position of the inlet and outlet sections of the machine. In the reduced numerical domain D_1, the outlet differs from the experimental setup so the computed and measured heads cannot be directly compared. Furthermore, also modifying the inlet mass flow rate value to fix the torque, is not possible to ensure that the computed flow is the same than experimental observations. On the contrary, considering the draft tube in the numerical domain, the numerical and the experimental outlet sections will match.

Concerning the position of the inlet section, in both domains D_1 and D_2, the spiral case has not been taken into account for computational costs reasons so experimental and numerical inlet sections are different. However, experimentally it has been observed that the contribution of the distributor in the turbine head is negligible (it is almost 0.1% of the total amount) and numerical analyses (described in detailed in the Annex A) have shown that it has no influence on the non-cavitating flow behavior. This justifies the chosen to neglect this component in the present study.

The new numerical domain D_2 has been discretized with the mesh M_3 (presented in detail in section 4.2.2) and two different inlet boundary conditions have been tested in both non-cavitating and cavitating regimes:

1. *Case C*: The mass flow rate value Q_{cor} obtained from the iterative procedure performed on D_1 has been imposed on the inlet. The calculation with this boundary condition has been performed to estimate the influence of the draft tube on the flow by comparing the results obtained on the numerical domains D_1 and D_2;

2. *Case D*: The total pressure P_{tot}, computed from the previous simulation on the domain D_2 (*Case C*), has been imposed as inlet boundary condition. In this way, the machine

head has been fixed whereas the flow rate has not been controlled during the development of the cavitation, exactly how is done for the real machine.

As done for the calculation with domain D_1, a static pressure equal to the ambient pressure is imposed on the draft tube outlet ($P_{out} = P_{amb}$) and the cavitation has been introduced increasing the relative saturation pressure P_{VAPS}. The used calculation parameters are summarized in the table 4.6.

Table 4.6 Numerical parameters used on the inlet boundary condition tested on D_2.

Case	Inlet BC	Outlet BC	Mesh	Turbulence model	Cavitation model
C	Q_{cor}	$P = P_{amb}$	M_3	$k-\omega$ SST	Barotropic law
D	P_{tot}				

4.2.5 Numerical methodology for unsteady calculations

Unsteady simulations have been performed in optimal load conditions, OP_1 to improve and complete the numerical methodology to predict the cavitation evolution inside the analyzed Kaplan turbine. As previously discussed, the points of the σ-break curve at low Thoma number (σ) values are characterized by intense and unsteady cavitation phenomena. So, calculations in steady regime could not be adapted to represent the cavitating flow behavior for these points.

The main properties of the numerical setup used for the steady calculation strategy (see 4.2.4) have been re-used also to perform the the unsteady simulations. In particular:

- The mesh refinement level;
- the turbulence model;
- the inlet and outlet boundary conditions.

are the ones chosen for the steady cases.

Differently from steady calculations, all the 24 guide vanes and the 5 runner blades have been considered in the computational domain (D_3, see figure 4.5) in order to ensure a different flow behavior in each interblade channel of the runner.

One of the most important parameter to define for unsteady calculations is the physical time step Δt since it can greatly affects the duration and precision of the simulations and have a strong impact on the the computational cost. Typical time discretization choices for hydraulic turbine are of the order of 1°, 2° or 3° of the rotation of the machine, depending on the typology of the phenomena that should be captured by the simulations. In this work, the main objective is to predict the appearance and the evolution of the cavitation structures on the

runner blades and their effects on the machine performances. So, the value of the physical time step has been chosen to ensure the observations of the only high frequency phenomena. In a previous study on the prediction of the efficiency of a Kaplan turbine presented by Jošt *et al.* [83], a physical time step Δt of 0.5° of the rotation of the turbine is suggested in order to obtain an accurate solution.

Therefore, two values of Δt=0.5°and Δt=1°of the machine rotation have been initially tested. Having notice a negligible impact on the results, the time step equal to 1°has been imposed for all the unsteady simulations obtaining a reduction of the computational cost. The main calculation parameters are reported in the table 4.7.

Table 4.7 Numerical parameters used to perform unsteady calculation on the optimal load operating point OP_1.

Case	Computational domain	Mesh	Inlet BC	Outlet BC	Turbulence model	Cavitation model	Δt
E	D_3	M_4	P_{tot}	$P_{out} = P_{amb}$	$k-\omega$ SST	Barotropic law	1°

4.3 Numerical investigation of the full load operating point OP_2

Another operating point of the studied Kaplan turbine indicated on the turbine hill chart (figure (4.2)) as OP_2, is successively studied. This point has been chosen far from the optimal load conditions in order to check the applicability range of the proposed numerical methodology. In OP_2 the machine works at same head H and rotational speed n as in the optimal load operating point OP_1, but with a higher mass flow discharge Q. This raises more developed and unstable cavitation phenomena even at higher σ values. This makes the steady calculations of this point not reliable and therefore only the chosen methodology for the unsteady simulations will be discussed below.

4.3.1 Computational domain

The computational domain used in the investigation (referred to as D_4) comprises all the elements considered for the unsteady study of the point OP_1 (domain D_3 represented in figure 4.5): all the guide vanes and the blades runner have been modeled and the distributor is not taken into account. However, compared to the domain D_3, the opening angle of the guide vanes and the inclination of the blades of the runner have been changed to 51.19°and to 40.16°, respectively.

4.3.2 Discretization of the numerical domain

The discretization procedure is the same used for the study of the OP_1: the computational grid consists of two structured meshes. At first, the guide vanes and the runner have been discretized together, then this mesh has been merged with the one of the draft tube, which is the same used for the analyses of previous operating point. Only the coarse mesh level M_5 has been tested. Its main characteristics are reported in table (4.8).

Table 4.8 Mesh characteristics of the domain D_4 (M_5).

	Component	**Number of elements**	**Min.skewness**	**Max. expansion ratio**	y^+_{mean}
M_5 : Level 1, coarse mesh	Guide vane	2M	34°	1.9	3.4
	Runner	3M	13°	4.6	5
	Draft Tube	1M	18°	1.8	30
	Total	6M			12.8

The values of the minimum skewness and maximum expansion ratio are within the prescribed range to ensure a good discretization (see the paragraph 4.2.2). An exception to this is the skewness in the runner that, also in this case, is slightly lower than 15°. This is due to the complex shape of the blade and to the presence of the hub gap. The y^+_{mean} is lower than 5 in the guide vanes and in the runner domains, ensuring that the cells near to the wall are in the viscous sublayer. The maximum registered value of y^+ in the runner is of $y^+_{max} = 15$. However, this concern only few cells on the leading edge and in the middle of the blade tip, where the fluid is more accelerated. In the draft tube, the y^+_{mean} is higher than 20 so the inner cells are placed in the logarithmic layer. The quality of this meshes have been considered adequate for preliminary investigations of OP_2.

4.3.3 Rotating blocks and interfaces

As for unsteady calculations in optimal load conditions, OP_1, the guide vanes and the draft tube have been considered as stationary blocks, whereas the runner is rotating. The interfaces between rotor/stator parts have been placed respectively at the guide vanes outlet and at the middle of the runner tip and they have been simulated by using the *Domain scaling* technique.

4.3.4 Numerical methodology for unsteady calculations

The turbulence model, the inlet/outlet boundary conditions and the physical time step Δt are the same used for the unsteady simulations in the OP_1 (see paragraph 4.2.5). To reduce the computational costs, the study was performed on a coarse mesh level, M_5. The characteristics of the numerical setup are summarized in the table 4.9.

Table 4.9 Numerical parameters used to perform unsteady calculation on the full load operating point OP_2.

Case	Mesh	Inlet BC	Outlet BC	Turbulence model	Cavitation model	Δt
F	M_5	P_{tot}	$P_{out} = P_{amb}$	$k-\omega$ SST	Barotropic law	1°

4.4 Convergence criteria

In the performed steady and unsteady simulations a good convergence should be ensured in order to achieve reliable results. If this is not a difficult goal to accomplish in the operating points close to the BEP (as the OP_1) and in non-cavitating regime, things are less straightforward when cavitation phenomena occur, especially in high load conditions points (i.e. at the OP_2). Chosen convergence criteria are now described.

4.4.1 Convergence criteria for steady simulations

Typically, the convergence of steady state CFD analyses is assessed by monitoring the residuals values, the solution imbalances and the stability of the quantities of interest. Undoubtedly , among these the global residuals are the most fundamental parameters: they measure the local imbalance of a conserved variable in each control volume. The lower the residual value is, the more accurate the solution is. However, in iterative numerical solutions the residuals will never be exactly zero, therefore the stability of the convergence curve should be monitored and limit values and fluctuation ranges for monitored integrated quantities, such as mass flow rate, torque and total pressure difference, can be defined to establish the simulations convergence. A further obstacle to convergence is the presence of important flow instabilities, as the one usually obtained in presence of cavitation conditions. For cavitating simulations usually the considered convergence limits are less strict. Also the imposed boundary conditions, the complexity of the numerical domain and the mesh refinement level could influence the convergence. The convergence criteria for steady simulations applied in this thesis are based on:

- **Mass flow convergence:** the difference between the inlet and outlet mass flow rates. For the optimal load operating points OP_1, in non-cavitating conditions with the mass flow imposed at the inlet the maximum acceptable imbalance is 0.02%. When the total pressure is imposed an higher difference of 0.05% is accepted given since flow instabilities are introduced. Finally, in cavitating regime, difference below 0.3% are accepted.

- **Torque convergence:** For points in non-cavitating regime the fluctuations are less than 0.01%. In cavitation conditions, a satisfying convergence level is reached when fluctuations are less than 0.3%.

- **Total pressure difference convergence:** For the calculations on the reduced domain D_1, the fluctuations of the total pressure difference between the inlet and the outlet of the domain in cavitation condition reaches the value of 0.02%. On the contrary, in the case of the complete domain D_2, the fluctuations for converged solution are negligible, also in cavitating conditions.

Satisfying convergence is usually reached in non-cavitating conditions after 2000 iterations on the coarse mesh level and up to 4000 iterations on the fine mesh. In cavitating regime the iterations required to obtain a converged calculation are, in both regimes, two times higher.

4.4.2 Convergence criteria for unsteady simulations

For the unsteady simulations the *Dual Time Stepping* approach is applied. The convergence should be achieved on two levels: first of all, each physical time step must converge and secondly, a stabilization of the global quantities should be obtained. Each time step Δt is considered similar to a steady simulation. The number of the internal iterations of a physical time step is the *Pseudo-time step*, $\Delta\tau$, and it can fix to a chosen value or by setting a satisfying convergence level for the global residuals. The convergence is reached when the residuals of several consecutive iterations have the same level of convergence. To achieve the convergence in each time step of the present simulations, a *Pseudo-time step* $\Delta\tau = 20$ has been chosen.

In addition to the condition on the Δt, reliable solutions are obtained when a certain level of stability of the fluctuations of the mass flow, of the torque and of the total pressure difference is achieved. The number of the machine rotations required to stabilize the global quantities can be different depending on the physical time step considered, on the amount of the cavitation and on the stability of the investigated operating point. In the studied cases, considering that a time discretization $\Delta t = 1°$ has been chosen, for the optimal load operating point OP_1 only 3 rotations of the turbine have been proved to be enough to reach a good convergence level, also in presence of cavitation phenomena. On the contrary, for the full load operating point OP_2, at least 7 machine rotations, in non-cavitating regime, and 12 turbine rotations, in cavitating conditions, have been required

4.5 Calculation strategies and computational resources

In the setup of a simulation, the initial conditions have a fundamental role in order to obtain a correct solution reducing the convergence time. This is especially true for calculations in a strong cavitating regime where the density gradient between to adjacent cells could be very intense. Initializing a calculation with a field near to the final solution helps to solve this

problem and, as a consequence, to reduce the residual values. For the steady and unsteady calculations performed in this work, calculations strategies have been developed to impose the best initial conditions optimizing computational times and resources.

4.5.1 Calculation strategies and computational resource for steady simulations

For the steady simulations, to obtain well-converged solutions for each investigated point of the σ-break curve, the developed calculation strategy consists in five steps:

1. A preliminary simulation is performed in non-cavitating regime, on the coarse mesh level, with the one-equation turbulence model *S-A*. The simulation is initialized by using constant values: the numerical domain is divided in stationary and rotating blocks and the static pressure, the velocity field and the turbulent viscosity μ_T are uniformly imposed on each part

2. The results of the simulation at step (1) is imposed as initial condition on the entire domain to carry on a second calculation in non–cavitating conditions on the coarse mesh level, using a two-equations turbulence model (in the case of this work the $k-\varepsilon$ or the $k-\omega$ SST model) to close the system of equations.

3. The converged solution of the calculation at step (2), is used to initialize the first simulation in cavitation conditions. So, the cavitation module is activated and a very little relative saturation pressure value P_{VAPS} is firstly imposed (near to zero or in some case also a negative value).

4. The relative saturation pressure value P_{VAPS} is increased from a point to point, in order to numerically replot the σ-break curve. The converged solution of each point is imposed as initial condition for the simulation of the following point.

5. Once the complete σ-break curve is calculated on the coarse mesh level, all of the points of the curve are recalculated on the fine mesh level using as initial condition the converged result of the simulation performed at the same relative saturation pressure value P_{VAPS} on the coarse mesh.

For the optimal load operating point OP_1, eight points of the σ-break curve have been considered for the steady analyses. The computational resources needed to perform each simulation and the time required to reach a satisfying converged result can be very different depending on the considered numerical domain, the mesh size, the turbulence model and the account of

vapor in the flow. The approximate estimation of the necessary computational resources for a non-cavitating simulation with a two-equations turbulence model are presented in the table 4.10. Since the computational time are affected by the intensity of the cavitation phenomena, simulations in cavitating conditions could be require 2-3 times more CPU hours comparing to non-cavitating points.

Table 4.10 Computational resources to steady simulations on the OP_1 (domains D_1 and D_2).

Computational Domain	Number of elements	Cores	CPU h	Output
D_1	1.7 M (Level 1)	16	24	0.4 GB
	13.6 M (Level 0)	32	224	2.5 GB
D_2	1.9 M (Level 1)	43	1.8	0.4 GB
	14.1 M (Level 0)	48	480	3 GB

4.5.2 Calculation strategies and computational resource for unsteady simulations

In optimal load conditions OP_1, only six points of the σ–break curve of the eight considered in the steady analysis have been investigated in unsteady regime. The calculation domain has been modified including all the guide vanes and the runner blades (computational domain D_3). Following the steady calculation methodology (see paragraph 4.2.4.1), unsteady simulations have been carried out on a fine mesh M_4. The procedure applied to obtain converged results is detailed below:

1. Chosen points of the σ-break curve are recalculated in steady conditions on the domain D_3, using the calculation strategy presented in the previous section 4.5.1;

2. Each point is simulated in unsteady regime using as initial conditions the converged results obtained from the steady simulation preformed with the same relative saturation pressure value P_{VAPS}.

An estimation of the computational resources required to carry out steady and unsteady simulations on the numerical domain D_3, in low cavitation conditions are presented in the table 4.11. From a computational point of view unsteady simulations are more expensive

Table 4.11 Computational resources to unsteady simulations on the OP_1 (domain D_3).

Type	Number of elements	Cores	CPU h	Output
Steady	61.7 M	128	1280	8 GB
Unsteady			16/rev	2048 GB/rev

than the steady ones. Indeed, using a $\Delta\tau = 20$ and a $\Delta t = 1°$, for each revolution 190 GB of storage and 16 CPU hours are required. Moreover, it is important to consider that in case of calculation in strong cavitation conditions, the computational time needed could be two times higher. For these reasons, not all the points of the σ-break curve have been recalculated in unsteady conditions. Concerning the analysis of the operating point in full load conditions OP_2, it was not possible to perform preliminary analyses in steady regime in cavitation conditions. Unsteady simulations have been directly carried out on a coarse mesh (M_5). Consequently, the

Table 4.12 Computational resources to steady and unsteady simulations on the OP_2.

Mesh	M_5	
Type	Steady	Unsteady
Number of elements	6 M	
Cores	32	
CPU h	2	12/rev
Output	2 GB	15 GB/rev

calculation strategy have been modified compared to the optimal load case:

1. A preliminary steady calculation is performed in non-cavitating conditions on the coarse discretization level M_5.

2. The converged result of the simulation at step (1) is used to initialized a second steady simulation, on the coarse mesh M_5, in cavitation regime, with a very little relative saturation pressure value P_{VAPS}.

3. The results of the steady calculation at step (2) are imposed as initial conditions for a unsteady simulation at the same relative saturation pressure value P_{VAPS}.

4. The relative saturation pressure value P_{VAPS} is increased to reach different σ values using as initial conditions the converged results of the last revolution of the calculation performed with the precedent P_{VAPS}.

The computational time and storage dimensions required for a simulation with a low P_{VAPS} value, in steady and unsteady conditions,are reported in the table 4.12.

In developed cavitation conditions, the computational time required to reach converged solutions is 2-3 times higher.

Chapter 5

Steady investigation of the optimal load point ($OP1$)

The numerical methodology to predict the appearance and the evolution of the cavitation phenomena in a Kaplan turbine has been developed starting from the investigation of the optimal load operating point OP_1. Simulations have been performed firstly on the reduced computational domain D_1 (figure 4.3) determining the main calculation parameters as the turbulence model, the mesh refinement level and the adequate set of inlet/outlet boundary conditions. Subsequently, the domain has been extended (D_2, figure 4.4) including in the analysis also the draft tube. The total pressure has been finally imposed on the inlet of the domain, instead of the mass flow, defining the new numerical methodology for the cavitation prediction (for more details, refer to chapter 4). In this chapter, the results obtained from the steady simulations performed on both numerical domains will be presented. In non-cavitating regime, the global quantities (η, T, H and Q) and the velocity profiles on the runner outlet will be compared with the experimental data. Cavitation analysis will be mostly focus on the performances curves and on the cavitation sheets. Calculations performed on D_2, will be further investigated. In particular, analysis of the losses evolution in the machine and of the flow in the runner and in the draft tube will be presented.

5.1 Results on the computational domain D_1

5.1.1 Turbulence models and mesh refinement

The $k-\varepsilon$ turbulence model with the extended wall function (EWF) and the $k-\omega$ SST model with a wall function (WF) have been tested on two different grid levels, M_1 and M_2 (for more details about the numerical setup see chapter 4). In order to determine the most suitable

turbulence model and mesh refinement level for the aim of this thesis, results have been compared in non-cavitating and in cavitating conditions with the experimental data.

The calculation parameters already presented in chapter 4 are recalled in table 5.1.

Table 5.1 Numerical setup for the turbulence model and grid level determination strategy.

Case	Turbulence model	Mesh level	Inlet BC	Outlet BC	Cavitation model
1	$k-\varepsilon$ (EWF)	M_1	$Q = Q_{exp}$	$P = P_{amb}$	Barotropic law
2	$k-\omega$ SST				
3	$k-\varepsilon$ (EWF)	M_2			
4	$k-\omega$ SST				

5.1.1.1 Analyses in non-cavitating regime

In this step of the numerical methodology definition, a mass flow rate value Q equal to the experimental one Q_{exp} has been imposed on the inlet of D_1. Thus, the torque T and the machine head H are considered as results of the calculation. The torque is computed summing the viscous and pressure force acting on the runner blades and on the hub (equation 4.2 in chapter 4). Considering that the inlet and the outlet sections of the calculation domain D_1 are not the same than the tested machine (see figure 5.1), for preliminary comparison in non-cavitating conditions, a correction has been applied on the machine head definition (5.1):

$$H = \Delta H_{dist} + \left(\frac{P_{inD1} - P_{prob}}{\rho g}\right) + \Delta H_{DT} + \frac{1}{2g} Q^2 \left(\frac{1}{S^2_{indist}} - \frac{1}{S^2_{outIEC}}\right) . \tag{5.1}$$

Where:

- ΔH_{dist} is the static pressure difference between the inlet of the distributor, **1**, and the inlet of the guide vanes **2**, computed from a previous calculation of the distributor and the guide vanes (see Annex A);

- ΔH_{DT} is the measured static pressure difference between the probing plane **3** and the draft tube outlet reference section (IEC plane [13]) **5**;

- P_{inD1} is the static pressure value computed as the mass flow average on the inlet surface on the domain D_1, **2**:

$$P_{inD1} = \frac{1}{\iint_S \rho\,(\vec{v}\cdot\vec{n})\,dS} \iint_S P \times \rho\,(\vec{v}\cdot\vec{n})\,dS\,. \tag{5.2}$$

- P_{prob} is the static pressure value calculated on the probing plane, **5**, as the average of the values of four control points located on the runner shroud in the same position of the experimental transducers (the pressure measurements are detailed in the chapter 3);
- S_{indist} is the measured value of the inlet section of the distributor **1**;
- S_{outDT} is the measured value of the outlet reference section of the draft tube (IEC plane) **5**.

In the numerical approach the elevation z of the reference surfaces is taken into account in the static pressure value. This formulation has been used to evaluate the machine head in non-cavitating conditions, in all the follow simulations performed on the reduced computational domain D_1.

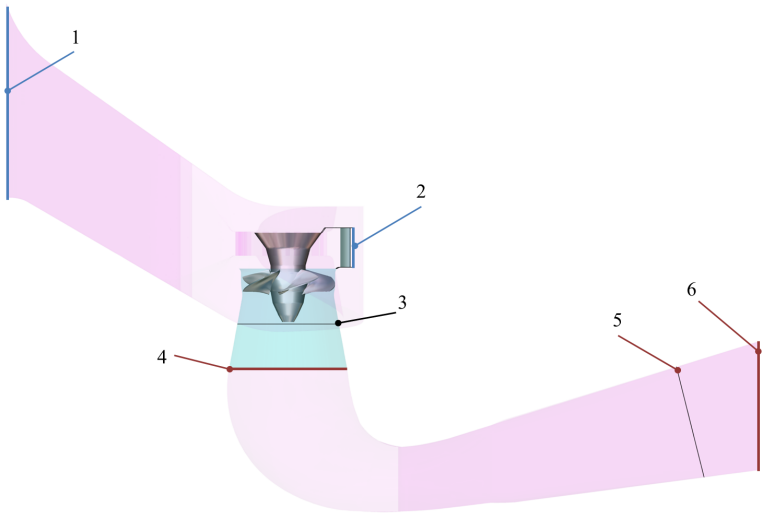

Figure 5.1 Scheme of the machine with the experimental and the numerical inlet and outlet positions. The parts colored in pink are not considered in D_1. **1** Distributor inlet **2** D_1 inlet **3** Probing plane **4** D_1 outlet **5** Draft tube outlet reference section (IEC plane) **6** Real draft tube outlet.

At first, the discrepancy between experiments and simulations has been evaluated in non-cavitating conditions comparing measured and computed global quantities (η, T and H). Table 5.2 summarizes the numerical global results obtained with the both mesh levels (M_1 and M_2) and turbulence models ($k-\varepsilon$ and $k-\omega$ SST) in terms of difference from the experimental values. The global quantities in table 5.2 show that the discrepancy between numerical and experimental torques is reduced using a $k-\omega$ SST turbulence model (Case 2) instead of the $k-\varepsilon$ model (Case 1). The agreement with measurement has been further improved refining the mesh (Case 4). The machine head value, in all the configurations, has not been correctly predicted. Considering that the static pressure differences in the distributor and in the draft tube

Table 5.2 Performance parameters computed on D_1 in the mesh and turbulence model test.

Case	Mesh level	Turbulence model	$\Delta T = \frac{(T_{exp}-T_{num})}{T_{exp}}$	$\Delta H = \frac{(H_{exp}-H_{num})}{H_{exp}}$	$\Delta\eta = \frac{(\eta_{exp}-\eta_{num})}{\eta_{exp}}$
1	M_1	$k-\varepsilon$	15.9%	13.8%	2.4%
2		$k-\omega$ SST	13.5%	14.6%	1.8%
3	M_2	$k-\varepsilon$	15.7%	13.5%	2.5%
4		$k-\omega$ SST	10.8%	13.7%	3.4%

are constants, the only contribution to the machine head evaluation computed is the difference of the static pressure between the guide vane inlet and the probing plane. Indeed, the different position of the outlet sections in the numerical domain D_1 and in the real test rig geometry (see figure 5.1) does not allow a direct comparison between computed and measured head values. Finally, concerning the efficiency value η, the best result has been obtained in using a $k-\omega$ SST on a coarse mesh (Case 2) but the analysis of the efficiency is biased by cross-variations in H and T.

Subsequently, the numerical and experimental profiles of tangential, V_t, and meridional, V_m, components of velocity on the runner outlet, in non-cavitating conditions have been compared. The analysis of the velocity fields helps to determine the mesh refinement level and the turbulence model more suitable to purposes of this study evaluating the difference between the real and the computed flow in terms of flow angles on the runner outlet and, consequently, of the turbine work. The measurements of the velocities on the test rig were performed by means of a Laser Doppler velocimetry (LDV) technique. The probing plane was placed under the runner, at 170 *mm* from the blade axis (as indicated by **5** in figure 5.1). The velocity measurements are presented in the details in the chapter 3. According to experimental measurements, the velocity values have been calculated by the weighted integration in θ direction, along the radius. Computed and measured velocities have been normalized by ωR and plotted along the normalized radius for all the four computational cases. Figure 5.2 presents the evolution of (a) the $V_m/\omega R$ and (b) the $V_t/\omega R$, measured and computed on the coarse mesh level M_1, using the $k-\varepsilon$ (Case 1) and the $k-\omega$ SST (Case 2) turbulence models.

The computed meridional component of velocity profiles with both turbulence models have a similar behavior (5.2 a). Near the hub (placed in the 0 of the normalized radius) and in the middle of the channel, the $k-\varepsilon$ model allows to better approximate the measured data. On the contrary, close to the shroud (the 1 of the normalized radius), the curve computed with the $k-\omega$ SST fits better with the experimental one. On the coarse mesh level M_1, both turbulence models are not able to correctly reproduce the peak of V_m near the hub. In the two cases, the difference between experimental and numerical value of the peak is about 15%. The tangential component of velocity profile (5.2 b) calculated in the Case 1 agrees better with experimental data than the

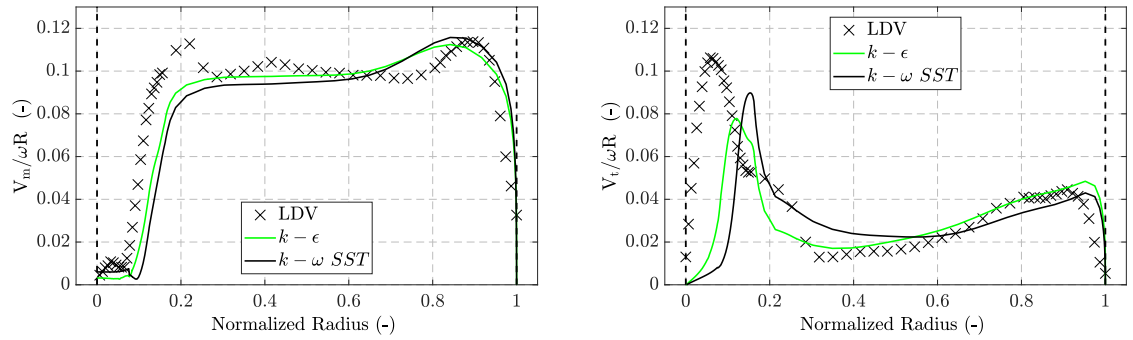

(a) **(b)**

Figure 5.2 Evolution of the normalized **(a)** meridional, V_m, **(b)** and tangential, V_t, velocities along the normalized radius, measured by LDV (black crosses) and computed on the coarse mesh M_1 using the $k-\varepsilon$ (Case 1 - green line) and the $k-\omega$ SST (Case 2 - black line) turbulence models. 0 is the hub and 1 is the shroud.

profile calculated in the Case 2. Only close to the hub, the curve obtained by using the $k-\omega$ SST turbulence model has a peak higher and similar to the experimental measurements than the curve computed using the $k-\varepsilon$ model. In Case 2 the peak value deviates by 15% from the experimental one compared to Case 1, where the deviation is about 27%. In both cases, the calculated peak is shifted to the middle of the channel, compared to the experimental position. For calculations performed on a coarse grid level (i.e. the M_1), best results in terms of velocity profiles are obtained applying the $k-\varepsilon$ turbulence model.

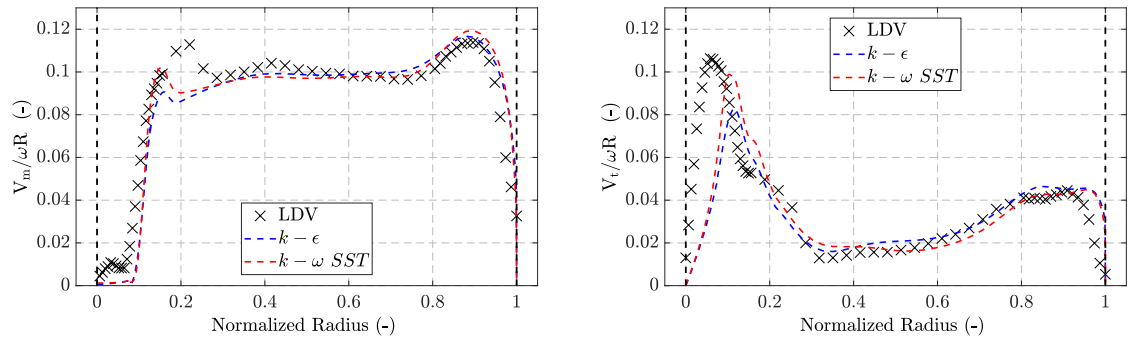

(a) **(b)**

Figure 5.3 Evolution of the normalized **(a)** meridional, V_m, and **(b)** tangential, V_t, component of velocity along the normalized radius, measured by LDV (black crosses) and computed on the fine mesh M_2 using the $k-\varepsilon$ (Case 3 - blue dashed line) and the $k-\omega$ SST (Case 4 - red dashed line) turbulence models. 0 is the hub and 1 is the shroud.

However, due to the presence of the tip, a coarse mesh does not allow the correct reproduction of the flow in the hub region. The velocities profiles obtained applying the two turbulence models on the fine mesh M_2 have been also compared. Figure 5.3 shows that the meridional (a) and the tangential (b) component of velocity are better predicted by using the $k-\omega$ SST model

(Case 4) than by applying the $k-\varepsilon$ model (Case 3). Near the hub, the difference between the height of the measured and the calculated peak of the V_m in Case 4 is 10% while in Case 3 is about 27%. Concerning the peak of the V_t, in Case 4 the discrepancy from the experimental data is 7%, compared to Case 3 where is about 22%. Also the shift from the real position is reduced using the $k-\omega$ SST model.

Thus, the analyses of the global quantities and the velocity fields on the runner outlet, have shown that the best agreement between numerical results and experimental measures in non-cavitating conditions is reached performing simulations on the fine mesh level M_2 using the $k-\omega$ SST turbulence model.

5.1.1.2 Analyses in cavitating regime

The effects of the cavitation development on the machine performance are generally evaluated by means of the σ-break curve. This curve, already presented in the chapter 1, represents the evolution of the efficiency η as a function of the reduction of the cavitation number, σ. In simulations carried out on D_1, the quantitative comparison between experimental and numerical machine head H and Net Positive Suction Head, $NPSH$ is not accurate. The correction on H definition proposed in non-cavitating conditions (equation 5.1) cannot be used anymore. In investigations in cavitating regime, the numerical H has been evaluated as the difference of the total pressure average computed on the inlet and on the outlet of D_1 (indicated in figure 5.1 as **2** and **4**, respectively) as :

$$H = \frac{1}{\rho g}\left(P_{tot\mathbf{2}} - P_{tot\mathbf{4}}\right) . \tag{5.3}$$

This computed value of H has been used to estimate both σ and η. The total pressure in FINE™/Turbo is calculated as :

$$P_{tot} = P_{stat} + \rho\frac{V^2}{2} + \rho k . \tag{5.4}$$

where P_{stat} is the static pressure, V is the absolute velocity of the fluid and k is the turbulent kinetic energy. Generally, the contribution of the turbulent kinetic energy term to the total pressure is less important than the other two. Also the $NPSH$ has been computed as a function of the total pressure outlet value :

$$NPSH = \frac{1}{\rho g}\left(P_{tot\mathbf{4}} - P_{VAPS}\right) . \tag{5.5}$$

Considering that σ is defined as the ratio between the $NPSH$ and H, higher is the relative saturation pressure value P_{VAPS}, lower is the σ.

Figure 5.4 reports the cavitation curves computed with both turbulence models, on the coarse mesh M_1 (a) and on the fine mesh M_2 (b). To help the comparison between numerical and experimental σ-break curves, the efficiency values η have been divided for the first value of each curve in non-cavitating conditions.

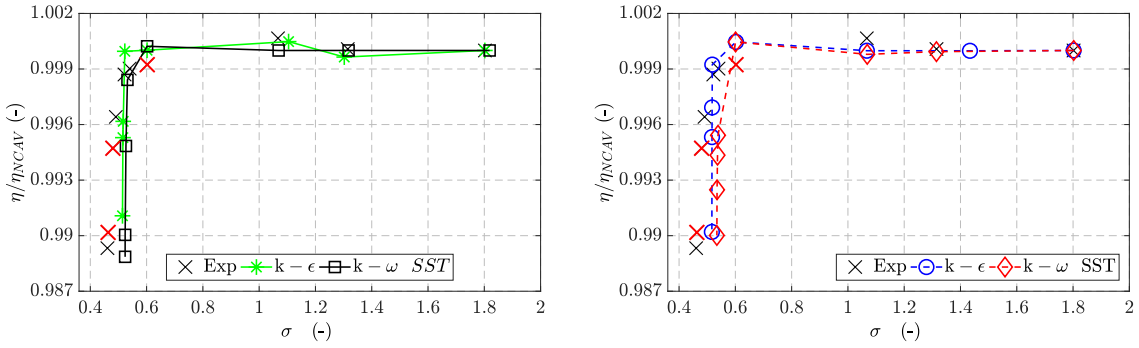

Figure 5.4 σ-break curves measured (black crosses) and computed on **(a)** M_1 and on **(b)** M_2 with the k-ε (Case 1 - green line with the stars and Case 3 - blue dashed line with circles) and with the k-ω SST (Case 2 - black line with squares and Case 4 - red dashed line with the diamonds) turbulence models. The experimental points σ_s, $\sigma_{-0.5\%}$ and $\sigma_{-1\%}$ are plotted with red crosses.

Common practice to evaluate the prediction ability of the numerical model is to estimate the discrepancy between measured and calculated σ values at three point (represented in figure 5.4 by red crosses): the efficiency starting drop point (σ_s) and at a drop of 0.5% ($\sigma_{-0.5\%}$) and 1% ($\sigma_{-1\%}$) of the efficiency. In all the four cases, the computed Thoma number values at σ_s differ from the experimental one of less than 1%. On the contrary, the $\sigma_{-0.5\%}$ and the $\sigma_{-1\%}$ are predicted with a discrepancy between 10% and 15%. Even without having the corrected values of Thoma number and efficiency, the overall aspect of the σ-break curves may provide valuable information concerning the cavitation performance of a turbine. For instance, the fact that the efficiency is almost constant until the efficiency starts to drop suggests that at this point there is suction side leading edge cavitation as well as hub cavitation. However, the analysis of the efficiency evolution as a function of the cavitation number seems to not provided enough information about the turbulence model and the mesh refinement level adequate to correctly predict the cavitation in the turbine. Indeed, similar curves have been obtained in the four computational cases. The efficiency is function of three parameters: the mass flow rate Q, the net head H and the torque T. In simulations performed on D_1, the Q is always imposed as inlet boundary condition and it is kept constant during the P_{VAPS} augmentation (see chapter 4). On the contrary, the H and the T result from the calculations. Experimentally, the machine head is almost fixed during the cavitation development while, numerically, is free to vary even outside the range of the measurement uncertainty ($\pm 0.2\%$). This contributes to improve the

error on the efficiency determination. In order to quantify the real impact of the turbulence model and the mesh refinement on the performances, also an analysis of the evolution of these two parameters with the σ reduction is required.

The computed and the measured head and torque divided for the first value of each curve, in non-cavitating conditions, have been plotted as function of the σ, for all the calculations performed.

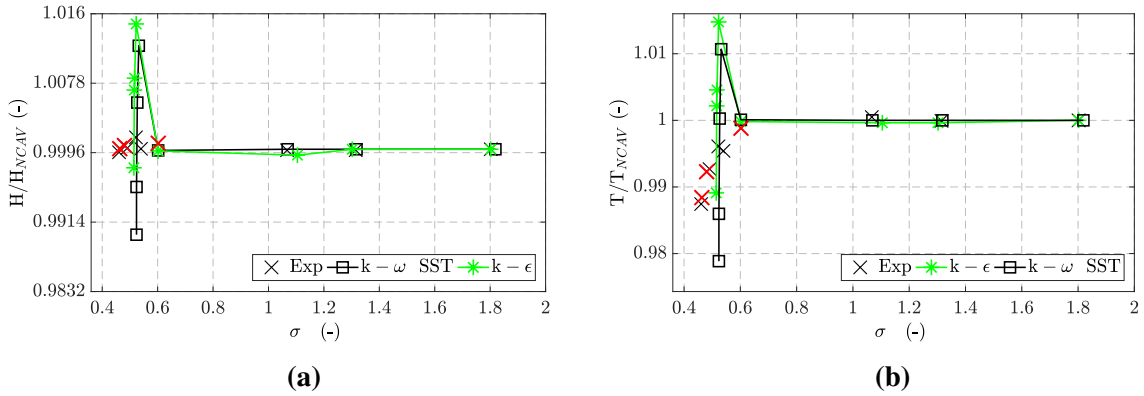

(a) **(b)**

Figure 5.5 (a) The head and **(b)** the torque evolution with the σ reduction measured (black crosses) and computed on M_1 with the k-ε (Case 1 - green line with the stars) and with the k-ω SST (Case 2 - black line with squares) turbulence models. The experimental points σ_s, $\sigma_{-0.5\%}$ and $\sigma_{-1\%}$ are plotted with red crosses.

In the figure 5.5, the head (a) and the torque (b) evolution with the Thoma number reduction, computed on the coarse mesh M_1, applying both turbulence models are compared with experimental data. The trend of the head and the torque curves is very similar between the two cases. According to measurements, before the efficiency drop starting points ($\sigma_s = 0.602$, reported with a red cross on the graph), H and T are almost constant. After this point, numerical torque and head values suddenly increase by 1.5%. This discrepancy from the experimental data is not observable from the σ-break curve since T and H increase in the same amount compensate each other. In both computational cases, at $\sigma_{-0.5\%}$, the torque values are higher than the experiments so the efficiency reduction of 0.5% is mainly linked to a numerical head augmentation. At $\sigma_{-1\%}$, the torque is better predicted in Case 1 but the numerical head still drops. From figure 5.6, it is possible to observe that, also for the simulations performed on the fine mesh M_2, the head and the torque curves show the same tendency with both turbulence models. Comparing to the results of the calculations on M_1, the T and the H peaks are more slight (less than 0.6%). In the last part of the curves, for the lowest σ values, the head drop predicted using the $k-\omega$ SST model is less huge and agrees better with experimental measurements. Concerning the torque, at $\sigma_{-0.5\%}$, is better predicted using the $k-\varepsilon$ model. On the contrary, in the last point of the curve ($\sigma_{-1\%}$) the decrement of the torque computed with the $k-\omega$ SST model is closer to the measured value. Finally, the head and torque curves computed applying the $k-\omega$ SST

model fits better with the experimental data. In conclusion, the best results in terms of head and torque prediction, have been obtained using a $k-\omega$ SST turbulence model and performing simulations on M_2.

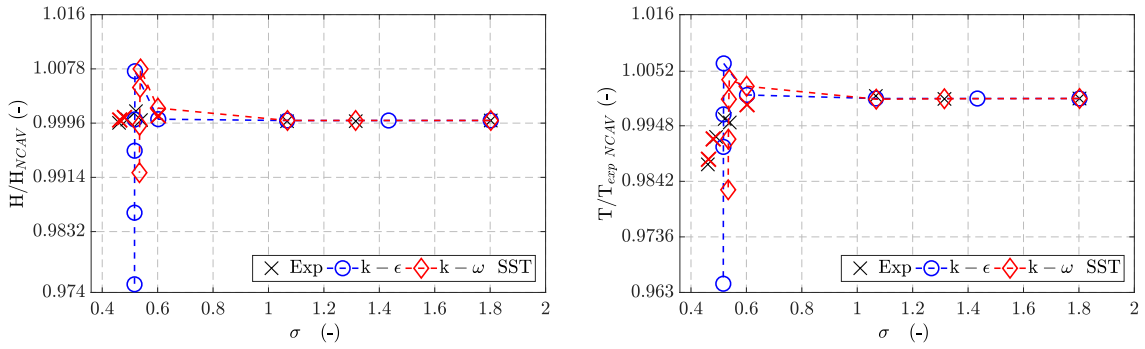

(a) **(b)**

Figure 5.6 (a) The head and **(b)** the torque evolution with the σ reduction measured (black crosses) and computed on M_2 with the $k-\varepsilon$ (Case 3 - blue dashed line with circles) and with the $k-\omega$ SST (Case 4 - red dashed line with the diamonds) turbulence models. The experimental points σ_s, $\sigma_{-0.5\%}$ and $\sigma_{-1\%}$ are plotted with red crosses.

Indeed, with this configuration the peaks on the torque and on the head have been minimized. However, the presence of this abruptly augmentation is mainly due to the boundary condition imposed on the inlet of the domain. In all the investigated cases, the σ value of the efficiency drop starting point is perfectly predicted. On the contrary, the computed σ values at 0.5% and at 1% of the efficiency drop are predicted for higher σ values than the measured ones.

In addition to the performances analysis, the shape and the position of the computed vapor structures are compared with the available experimental data. The cavities in the runner of the scaled model have been observed using of a high speed camera for two points of the investigated σ-break curve: the efficiency drop staring point ($\sigma_s = 0.602$) and the point that corresponds to an efficiency drop of 0.5% ($\sigma_{-0.5\%} = 0.480$).

The videos have been recorded from two different points of view: one bellow the runner (one frame is reported on figure 5.7 a) and one on the side of the runner (one frame is represented on figure 5.7 b). The experimental setup are detailed in the chapter 3. The calculated cavities are visualized by means of iso-density surfaces at $\rho = 980\ kg/m^3$ that corresponds to a void fraction $\alpha = 10\%$. Experimentally, at $\sigma_s = 0.602$, two vapor structures have been observed in the flow:

- An attached cavitation sheet appears near the shroud. It starts from about 1/3 of the runner tip and ends just before the trailing edge, covering part of the blade profile (figure 5.7a);
- A little vapor structure appears on the root of the blade, near the leading edge, starting to develop in the opposite direction of the machine rotation.

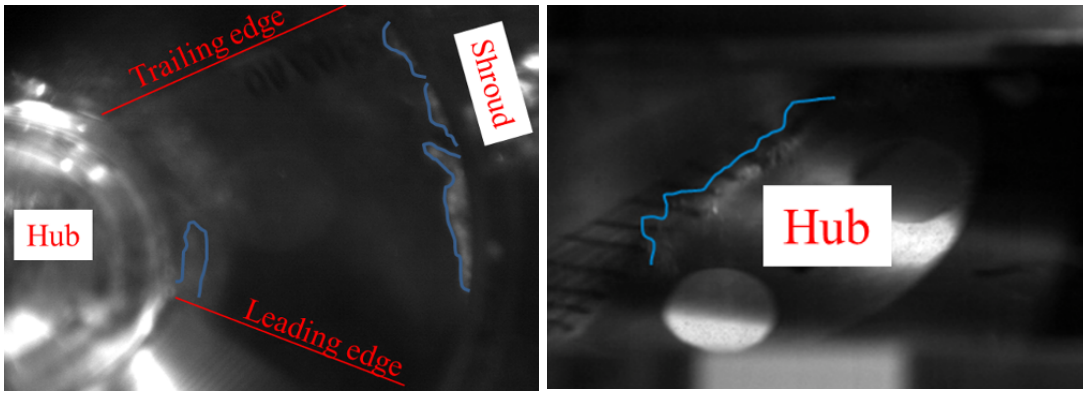

(a) **(b)**

Figure 5.7 Experimental visualizations of cavitation structures at $\sigma_s = 0.602$.**(a)** Meridian and **(b)** lateral views.

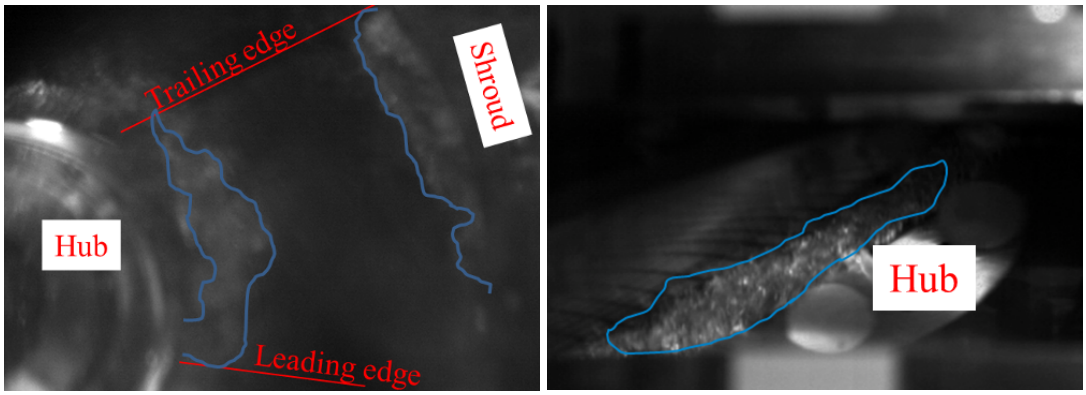

(a) **(b)**

Figure 5.8 Experimental visualizations of cavitation structures at $\sigma_s = 0.480$.**(a)** Meridian and **(b)** lateral views.

The position of the cavity close to the shroud is correctly predicted in all the computational cases (figure 5.9). However, only in the Case 4 (5.9 d), the cavitation starts to grow in the trailing edge direction, according to experimental visualizations. In all the computational cases, the start point of the vapor structure on the root of the blade is in good qualitative agreement with the experimental observation but its size seems to be underestimated.

At $\sigma = 0.480$ (figure 5.8), point where the efficiency value is reduced of 0.5%, the two cavitation sheets observed at $\sigma = 0.602$ (figure 5.7) on the tip and on the root of the blade evolve :

- The size of the vapor structure near the shroud increase, coming up to the trailing edge and covering more on the blade profile;
- The cavity on the hub expands toward the trailing edge.

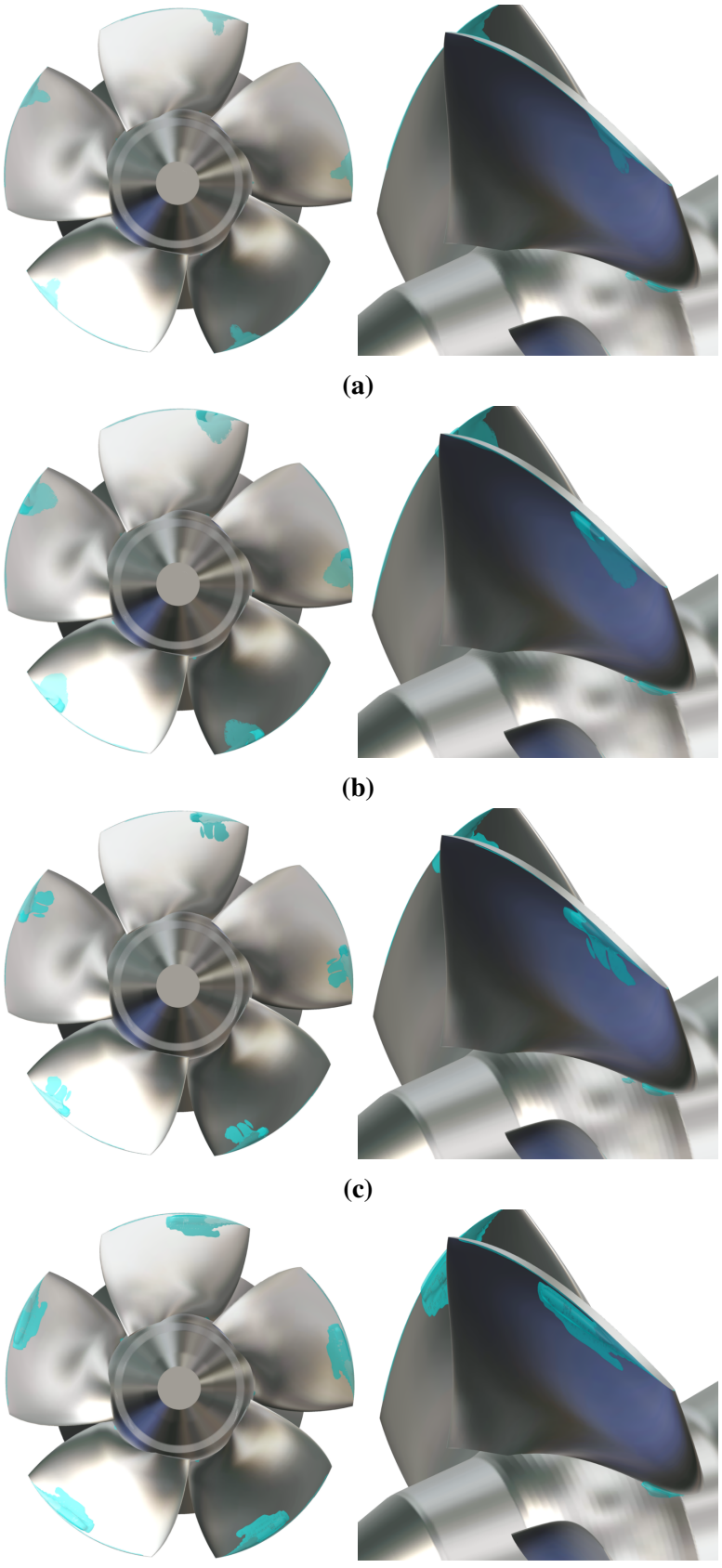

Figure 5.9 Frontal and lateral views of the computed iso-density surfaces ($\rho = 980\ kg/m^3$) in **(a)** Case 1 ($\sigma = 0.601$), **(b)** Case 2 ($\sigma = 0.602$), **(c)** Case 3 ($\sigma = 0.601$), and **(d)** Case 4 ($\sigma = 0.601$).

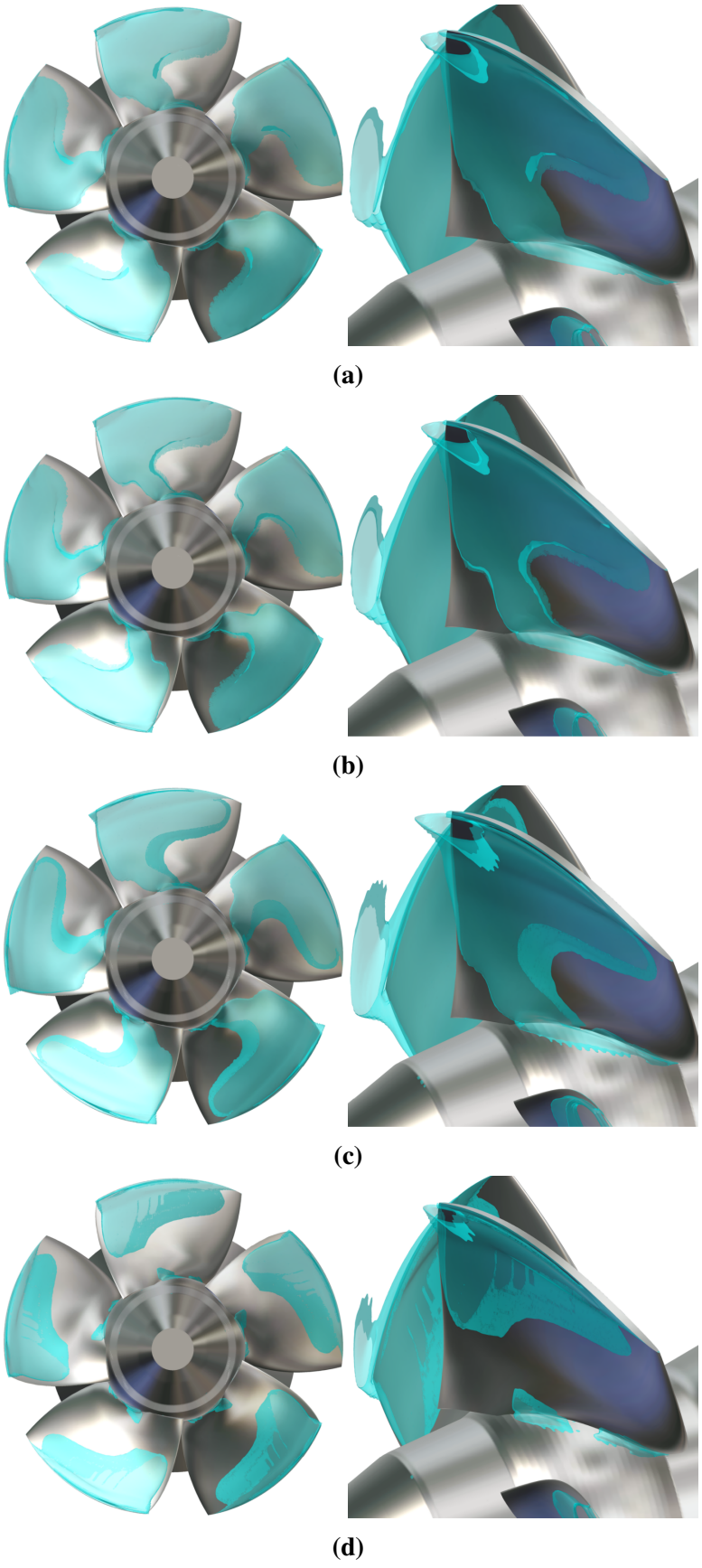

Figure 5.10 Frontal and lateral views of the computed iso-density surfaces ($\rho = 980\ kg/m^3$) in **(a)** Case 1 ($\sigma = 0.520$), **(b)** Case 2 ($\sigma = 0.526$), **(c)** Case 3 ($\sigma = 0.517$), and **(c)** Case 4 ($\sigma = 0.536$).

Observing the frontal views of the computed iso-density surfaces reported in figure 5.10 it is evident that only in the Case 4 (figure 5.10 d) two separated cavitation sheets are predicted, according to the experimental visualizations in figure 5.8. In the other cases (figures 5.10 a-b-c), from the hub to the shroud, only one big cavity is computed covering also the blade profile. The analyses of the results of simulations performed in cavitation conditions, have shown that a better agreement with experimental data in terms of performances and cavitation structures prediction has been obtained refining the mesh and applying as turbulence closure the $k-\omega$ SST model. The discretization level achieved on the fine mesh M_2 seems to be suitable for the purposes of the present work. No more mesh refinement has been done. Based on the results of this preliminary tests in non-cavitating and in cavitating conditions, all the subsequent simulations presented in this work have been performed on the fine mesh level using the $k-\omega$ SST model.

5.1.2 Inlet boundary conditions

After the refinement mesh level (M_2) and the turbulence model ($k-\omega$ SST) have been defined, the following step of the methodology was to approach the numerical operating point to the real one. This can be achieved reducing the difference between computed and measured torque values. For this purpose, the value of the mass flow rate on the inlet has been iteratively changed, in non-cavitating regime, targeting the experimental torque. The iterative procedure is summarized with the graph in figure 5.11.

Once the new value of the inlet mass flow Q_{cor} has been determined, simulations have been performed also in cavitating conditions (Case B). To determine the impact of this new boundary condition, the results have been compared with the ones obtained imposing the experimental mass flow rate value Q_{exp} on the inlet (Case A) and with experimental data. The main calculation parameters, presented in chapter 4, are recalled in table 5.3.

Table 5.3 Numerical parameters used on the inlet boundary condition tests on D_1.

Case	Inlet BC	Outlet BC	Mesh level	Turbulence model	Cavitation model
A	$Q = Q_{exp}$	$P_{out} = P_{amb}$	M_2	$k-\omega$ SST	Barotropic law
B	$Q = Q_{cor}$				

5.1.2.1 Analyses in non-cavitating regime

Firstly, the performance parameters (η, T, H and Q) computed in Case A and in Case B have been compared. Also in this analysis, the numerical H has been evaluated, in non-cavitating

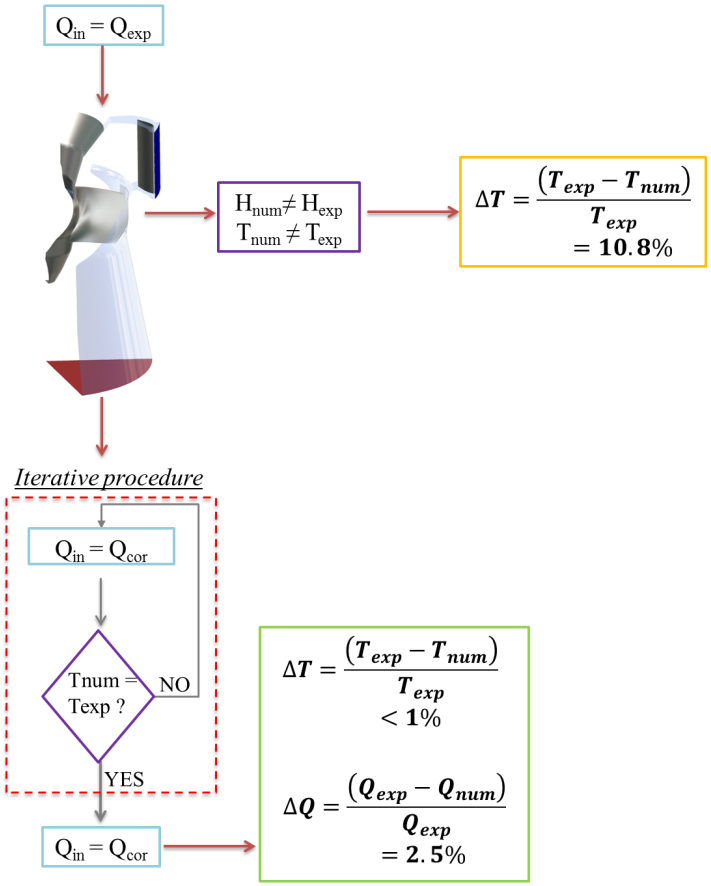

Figure 5.11 Scheme of the iterative procedure of modification of the mass flow rate value on inlet of D_1.

conditions, by means of the equation 5.1. In the table 5.4, the global results calculated imposing Q_{exp} and Q_{cor}, are reported as the difference in percentage from the measured values.

Table 5.4 Performance parameters computed on D_1 in the inlet boundary condition test.

Case	Mesh level	Turbulence model	$\Delta Q = \frac{(Q_{exp}-Q_{num})}{Q_{exp}}$	$\Delta T = \frac{(T_{exp}-T_{num})}{T_{exp}}$	$\Delta H = \frac{(H_{exp}-H_{num})}{H_{exp}}$	$\Delta\eta = \frac{(\eta_{exp}-\eta_{num})}{\eta_{exp}}$
A	M_2	$k-\omega$ SST	0%	10.8%	13.7%	3.4%
B			2.5%	1%	6.6%	5.4%

Applying the iterative procedure, the mismatch between experimental and computed torque has been reduced from the 10.8% in Case A to the 1% in Case B, with a discrepancy of 2.5% between experimental and numerical mass flow rate (see table 5.4). Considering that the measured value of the mass flow can vary with the cavitation development of maximum 2.5%, this discrepancy could be still considered acceptable. Also the difference on the head value has been lessened from the 13.7% to the 6.6%, even if it is necessary to keep in mind that computed and experimental heads cannot be directly compared. On the contrary, the computed η value seems to be farther from the measured value in Case B (5.4%) than in Case A (3.4%). The

increment of the discrepancy on the η value in the Case B is due to the concurrent errors on T, H and Q. For this reason, all the performances parameters have to be analyzed in the validation process of the numerical results.

To further assess the effect of the variation of the discharge value on the inlet, the velocity profiles computed, in non-cavitating conditions, on the probing plane (see figure 5.1) in Case B have been compared with the numerical distribution obtained in Case A and with experimental data. The evolution of the meridional, V_m, and the tangential, V_t, components of velocity along the normalized radius are reported in figures 5.12 a and b, respectively. The meridional velocity

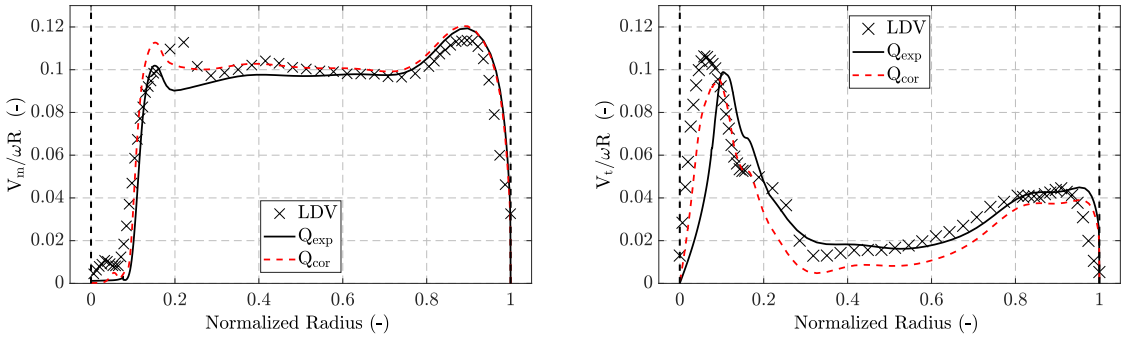

Figure 5.12 Evolution of the normalized **(a)** meridional, V_m, and **(b)** tangential, V_t, components of velocity along the normalized radius, measured by LDV (black crosses) and computed on the fine mesh M_1 using the $k-\omega$ SST turbulence model with Q_exp (Case A - black line) and Q_cor (Case B - red dashed line) as inlet boundary condition. 0 is the hub and 1 is the shroud.

profile computed with Q_{cor} seems to be in better agreement with the experimental results than the distribution calculated with Q_{exp} (see figure 5.12 a). Best improvements are observed near the hub: the difference between the height of the V_m measured and the calculated peaks is 0.1% in Case B while is about 10% in the Case A. The change of the inlet discharge value leads also to improve the prediction of the V_t profile, mostly in the middle of the channel and in the shroud region (figure 5.12 b). Close to the runner tip, the discrepancy between the computed and experimental peak is higher in Case B (10%) than in Case A (7%).

Thus, the correction on the mass flow rate inlet value, allows to improve the numerical prediction in non-cavitating conditions of the global quantities and the velocity fields on the runner outlet.

5.1.2.2 Analyses in cavitating regime

In figure 5.13, the σ-break curves computed in Case A and in Case B are compared with the measured efficiency evolution. No major improvements are observed imposing the new value

of the discharge Q_{cor} as inlet boundary condition: in both cases, the σ_s value is predicted with a discrepancy from the experimental value less than 1% while numerical $\sigma_{-0.5\%}$ and $\sigma_{-1\%}$ values are higher than experimental ones.

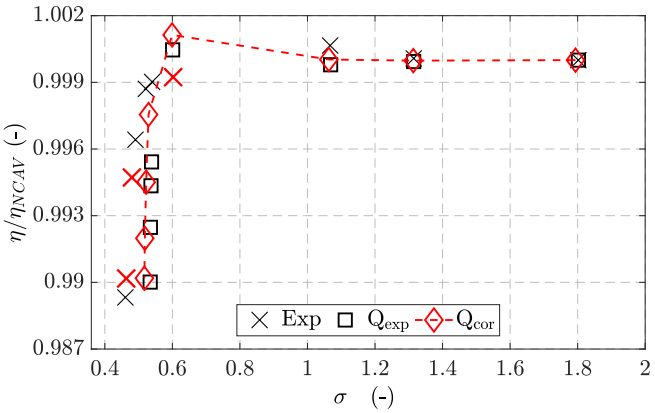

Figure 5.13 σ-break curves measured (black crosses) and computed on M_2 with the k-ω SST imposing Q_{exp} (Case A - black line with squares) and Q_{cor} (Case B - red dashed line with the diamonds) as inlet boundary conditions. The experimental points σ_s, $\sigma_{-0.5\%}$ and $\sigma_{-1\%}$ are plotted with red crosses.

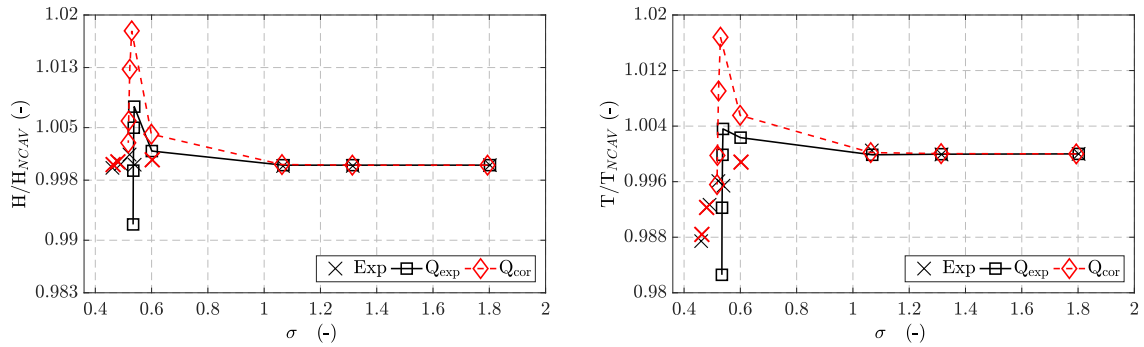

(a) **(b)**

Figure 5.14 H and T as function of σ measured (black crosses) and computed on M_2 with the k-ω SST imposing Q_{exp} (Case A - black line with squares) and Q_{cor} (Case B - red dashed line with the diamonds) as inlet boundary conditions. The experimental points σ_s, $\sigma_{-0.5\%}$ and $\sigma_{-1\%}$ are plotted with red crosses.

Observing the evolutions of T (figure 5.14 b) and H(figure 5.14 a) with the σ reduction, their behavior are worse predicted modifying the discharge inlet value. Indeed, in Case B at $\sigma = 0.530$, the head and the torque rise abruptly, increasing of about 1.7% while in Case A the augmentation of these two quantities was limited to 0.7%. At $\sigma_{-0.5\%}$ and $\sigma_{-1\%}$, head and torque values are overestimated and the discrepancy with experimental data is higher than in Case A.

The torque behavior with the cavitation development could be explained comparing the cavities structures computed in the two cases in the torque peak point (that corresponds to $\sigma = 0.538$ in Case A and to $\sigma = 0.530$ in Case B). The iso-density surfaces computed near the hub in Case B (figure 5.15 b) are under predicted with respect to the vapor structures calculated in Case A (figure 5.15 a). In Case B, the cavitation sheet near the shroud is less extended on the blade profile than the one computed in Case A. Moreover, in the hub region only one structures is predicted in Case B, contrarily to Case A where two cavities are observed. The absence of vapor structures in the middle of the blade root and profile in Case B involves an excessive increase of the torque value, not observed experimentally.

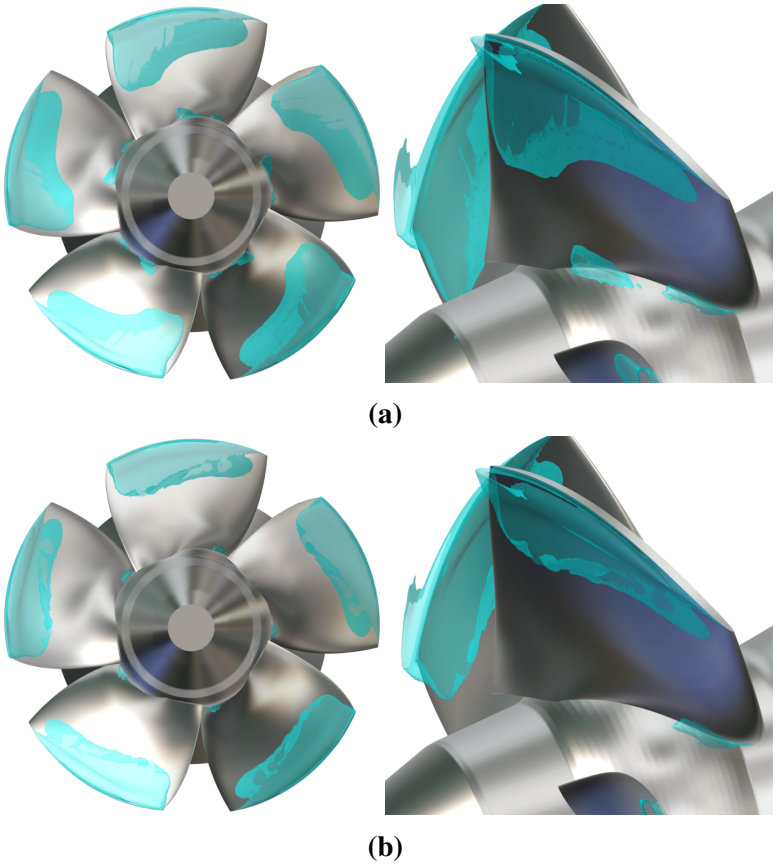

(a)

(b)

Figure 5.15 Frontal and lateral views of the computed iso-density surfaces ($\rho = 980\ kg/m^3$) in **(a)** Case A ($\sigma = 0.538$) and in **(b)** Case B ($\sigma = 0.530$).

Thus, modifying the discharge value on the inlet, the prediction of the global quantities and the velocity fields on the runner outlet in non-cavitating conditions is improved but the flow behavior in cavitating regime is deteriorated. This inadequate prediction of the cavitating flow behavior is a consequence of the fact that numerically the operating point changes with the σ reduction. This variation could results from two main factors:

- Considering that the draft tube is not included in the computational domain D_1, experimental and computed cavitating flow can never been the same;
- Using the mass flow rate as inlet boundary condition, it is not possible to fix the machine head during the cavitation development as in the experiments.

5.2 Results on the computational domain D_2

In order to investigate the role of the draft tube in the analysis and to fix the head during the σ decrease procedure, the computational domain D_2 (presented in chapter 4 in figure 4.4) has been considered. As a consequence of the preliminary tests carried out on the domain D_1 (see paragraph 5.1), the analyses on D_2 have been performed on the fine mesh level, using the $k-\omega$ SST turbulence closure.

5.2.1 Study of the draft tube influence

The inlet boundary condition test performed on the domain D_1 (see paragraph 5.1.2) have shown that the correction on the inlet discharge value leads, in non-cavitating regime, to approach the numerical operating point to the experimental one. On the contrary, with the development of the cavitation in the machine, the numerical operating point moves from the real position on the hill chart. A first solution may be to include the draft tube in the analysis. In order to estimate the influence of the draft tube on the flow simulations, the results obtained in non-cavitating and cavitating conditions, imposing the Q_{cor} on the inlet of D_1 and D_2 will be compared hereafter. In table 5.5 are recalled the main calculation parameters for the two investigated cases, already presented in chapter 4.

Table 5.5 Numerical parameters used on the draft tube influence study.

Case	Domain	Inlet BC	Outlet BC	Mesh	Turbulence model	Cavitation model
B	D_1	Q_{cor}	$P = P_{amb}$	M_2	$k-\omega$ SST	Barotropic law
C	D_2			M_3		

5.2.1.1 Analyses in non-cavitating regime

The effect of the draft tube on the flow is already evident in non-cavitating regime. At equal inlet boundary condition, the torque computed on D_2 deviates from the experimental value of 1.5%, more than the one computed on D_1 (table 5.6). The heads computed in the two cases can not be compared directly since the domains outlet sections are not the same. In simulations

performed on D_1, the computed head is corrected using the equation 5.1. On the contrary, no corrections are needed to evaluate the head in simulations on D_2 since the static pressure on the draft tube outlet reference section (IEC plane, reported with **5** in figure 5.1 can be computed by means of equation 4.3 presented in chapter 4. Despite the draft tube has been included in the analysis, the numerical head still differs from the experimental one of 8.3%. The discrepancy between computed and measured efficiency is reduced (4.7%) as a consequence of the complementary variation of the torque and head. The draft tube affects also the velocity

Table 5.6 Performance parameters computed on D_1 and D_2 in the draft tube influence study.

Case	Domain	Turbulence model	$\Delta Q = \frac{(Q_{exp}-Q_{num})}{Q_{exp}}$	$\Delta T = \frac{(T_{exp}-T_{num})}{T_{exp}}$	$\Delta H = \frac{(H_{exp}-H_{num})}{H_{exp}}$	$\Delta\eta = \frac{(\eta_{exp}-\eta_{num})}{\eta_{exp}}$
B	D_1	$k-\omega$ SST	2.5%	1%	6.6%	5.4%
C	D_1			1.5%	8.3%	4.7%

distribution on the runner outlet. Improvements of the meridian velocity V_m prediction are observed in Case C in the shroud region while the peak near to the hub disappears (figure 5.16 a). The tangential velocity V_t profile (figure 5.16 b) has been greatly changed compared to Case B. The peak close to the tip is overrated of 25% and the computed profile near the shroud deviates more from the experimental distribution. Slightly improvements are observed only in the middle of the channel.

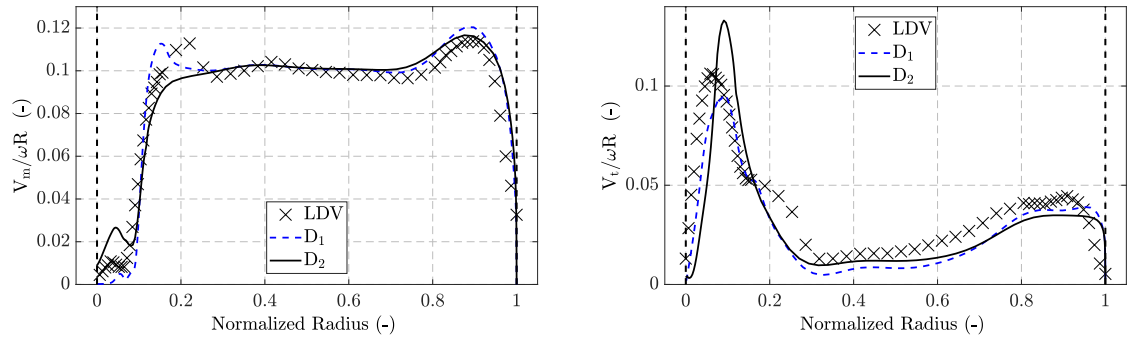

(a) **(b)**

Figure 5.16 Evolution of the normalized **(a)** meridional, V_m, and **(b)** tangential, V_t, components of velocity along the normalized radius, measured by LDV (black crosses) and computed using the $k-\omega$ SST turbulence model with Q_cor imposed on the inlet of D_1 (Case B - blue dashed line) and D_2 (Case C - black line). 0 is the hub and 1 is the shroud.

The investigation about the influence of the draft tube on the flow in non-cavitating conditions could be finally completed comparing the losses evolution in the two numerical domains. The calculation method used to determine the head losses in the machine has been already presented in chapter 1. Several sections have been created in D_1 and in D_2 (as is shown

in figure 5.17 a and b, respectively) to individuate the contribution to the net head of each component of the machine. The net machine head, H, can be defined as :

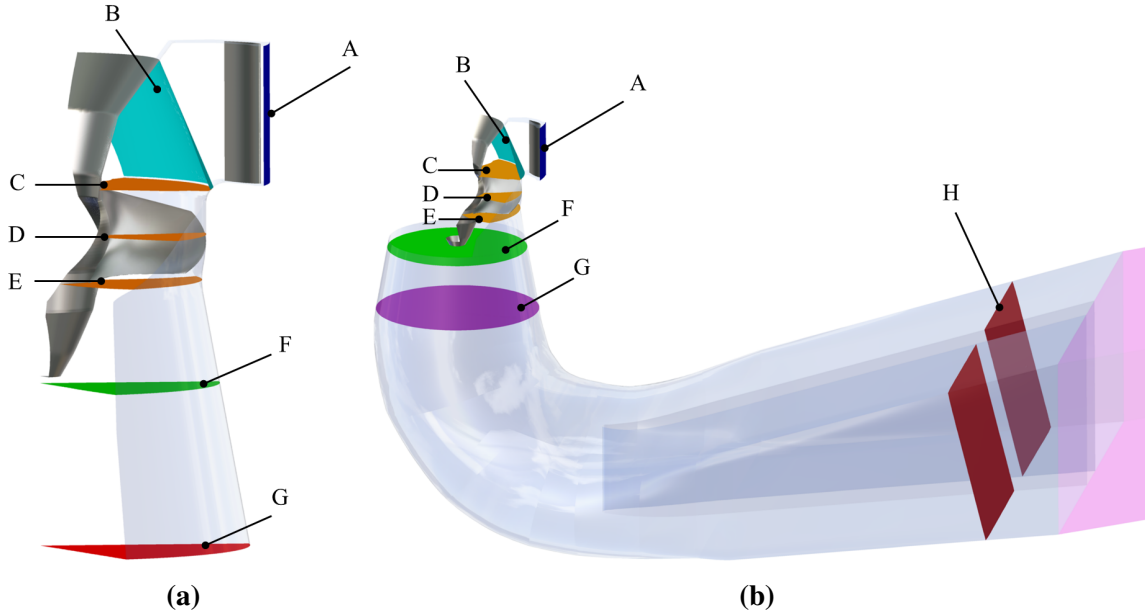

Figure 5.17 Sections for losses investigation in **(a)** D_1 and **(b)** D_2. Guide vane: **(A)** inlet and **(B)** outlet; Runner: **(C)** leading edge, **(D)** middle and **(E)** trailing edge of the blade; Cone: **(F)** probing plane and **(G)** D_1 outlet; Draft tube outlet: **(H)** IEC plane.

$$H = \Delta_{los} + H_i = \Delta_{los}^{dist} + \Delta_{los}^{gv} + \Delta_{los}^{run} + \Delta_{los}^{dt} + H_i \ . \tag{5.6}$$

Where:

- Δ_{los}^{dist} are the losses in the distributor. Since in both computational domains the distributor is not taken into account , this term is not considered in the present analysis;
- $\Delta_{los}^{gv} = \frac{1}{\rho g}\left(P_{tot}^{A} - P_{tot}^{B}\right)$ are the guide vanes losses computed as the difference between the total pressure on the inlet **A** and on the outlet **B** of the guide vanes;
- $\Delta_{los}^{run} = \frac{1}{\rho g}\left[\left(P_{tot}^{B} - P_{tot}^{C}\right) + \left(Rot^{C} - Rot^{E}\right)\right]$ are the losses in the runner calculated as the sum of the losses in the fix part (considered as the total pressure difference between the guide vanes outlet **B** and the runner blade leading edge **C**) and in the rotating part (computed as the difference of the rothalpy values between the leading edge **C** and the trailing edge **E** of the blade);
- $\Delta_{los}^{dt} = \frac{1}{\rho g}\left(P_{tot}^{E} - P_{tot}^{H}\right)$ are the losses in the draft tube. To directly compare the results of D_1 and D_2, the draft tube has been divided into two parts: the cone (between the trailing

edge of the blade, **E**, and the outlet of D_1, **G**) and the draft tube outlet (between the D_1 outlet, **G**, and the IEC plane **H**).Only the losses in the cone have been compared between the two domains;

- $H_i = \frac{T\omega}{\rho g Q} = \Delta H_{run} - \Delta^{run}_{los} = \frac{1}{\rho g}\left[\left(P^C_{tot} - P^E_{tot}\right) - \left(Rot^C - Rot^E\right)\right]$ is the internal head. It represents the amount of energy transferred to the turbine.

The total pressure and the rothalpy values are computed as the mass weighted average on each surface. In figure 5.18 are reported the values of H_i and of the losses calculated in each part of the machine in the two cases, divided by the experimental H. Due to the presence of the draft tube, the head predicted on D_2 is higher than the one computed on D_1 (see figure 5.18 a). Including the draft tube in the analysis, the energy absorbed by the turbine, H_i, decreases while the total amount of the losses increases. As it is possible to observe in figure 5.18 b, also the distribution of the losses between the components of the machine changes from Case B to Case C. In particular, in Case C, the losses decrease in the guide vanes and increase in the runner with respect to Case B. The losses in the cone are almost constant between the two computational cases. The H_i reduction and the increase of the losses in the runner observed in

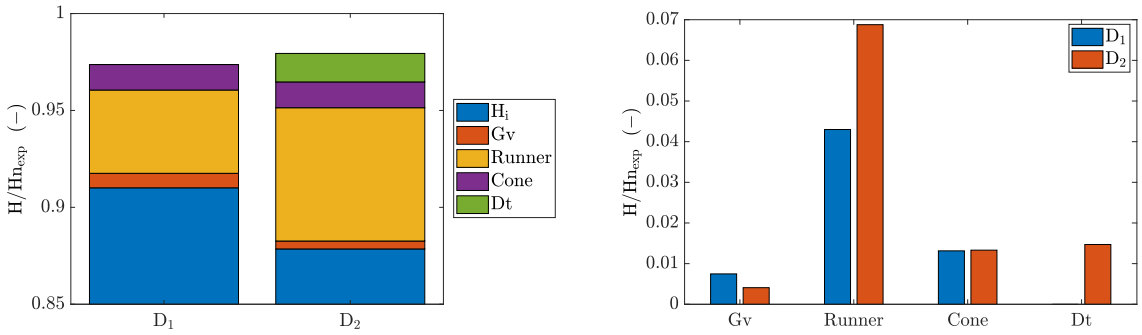

(a) **(b)**

Figure 5.18 Investigation of **(a)** the H_n and **(b)** the losses in D_1 and D_2.

Case C could be explained considering that the draft tube influences the flow on the outlet of the runner. The analysis of the velocity fields on the probing plane (figure 5.16) has shown that the in Case C the tangential velocity is higher than in Case B. The H_i can be approximated by means of the Euler equation 5.7 between the inlet (**C**) and the outlet (**E**) of the runner :

$$H_i = \frac{\omega}{g}\left(R_C V_t^C - R_E V_t^E\right) . \tag{5.7}$$

In equation 5.7 R is the radius and V_t is the tangential component of the velocity, computed as the mass weighted average on the inlet (**C**) and outlet (**E**) runner surfaces. Considering that

the inlet boundary condition is the same in the two cases, in Case C increasing V_t on the outlet the H_i will decrease. On the contrary, no evident reasons could explain the link between the presence of the draft tube and the losses decrease observed in the guide vane in Case C. A first step could be to locate the losses in the guide vanes. The dot product of the momentum equation for a steady flow (equation 2.2 in chapter 2) by the velocity $\vec{V}$ gives the kinetic energy balance equation :

$$\nabla \cdot \left(\rho \frac{V^2}{2} \vec{V} \right) = -\nabla \cdot \left(p\vec{V} \right) + \nabla \cdot \left(\bar{\bar{\tau}} \cdot \vec{V} \right) - \bar{\bar{\tau}} : \bar{\bar{\nabla}}(\vec{V}) - \nabla (\rho g z) \ . \tag{5.8}$$

A control volume Ω bounded by the guide vanes inlet (**A**), outlet (**B**), shroud and hub surfaces can be defined. Applying the divergence theorem (or Gauss-Ostrogradsky theorem) and integrating the equation 5.8 on Ω, we obtain:

$$\oiint_S \left(\underbrace{P + \frac{1}{2}\rho V^2 + \rho g z}_{P_{tot}} \right) \vec{V} \cdot \vec{n} dS = \oiint_S \left(\bar{\bar{\tau}} \cdot \vec{V} \right) \vec{n} dS - \iiint_\Omega \bar{\bar{\tau}} : \bar{\bar{\nabla}}(\vec{V}) d\Omega \ . \tag{5.9}$$

The left side of the equation represent the global losses in the machine while on the right side there are the local losses.

$$\Delta_{los}^{tot} = \sum \Delta_{los}^{global} = \sum \Delta_{los}^{local} \ . \tag{5.10}$$

The local losses can be divided in two contributions: the losses due to the shear stress (first term on the right side of equation 5.9) and the losses due to the viscous dissipation (second term on the right side of equation 5.9). In the viscous dissipation term also account for the energy transfer due to turbulent fluctuations (the eddy viscosity μ_T). Considering the shear stress term negligible compared to the viscous dissipation term, only the dissipation losses will be considered in the analysis. The viscous dissipation term, in an inertial frame of reference, can be expressed as :

$$\Delta_{los}^{dis} = \frac{1}{\rho g Q} \iiint_\Omega \bar{\bar{\tau}} : \bar{\bar{\nabla}}(\vec{V}) d\Omega = \frac{1}{\rho g Q} \iiint_\Omega \delta_{los}^{dis} d\Omega \ . \tag{5.11}$$

where δ_{los}^{dis} is defined as:

$$\delta_{los}^{dis} = 2(\mu + \mu_t) \left\{ \left(\frac{\partial u}{\partial x} \right)^2 + \left(\frac{\partial v}{\partial y} \right)^2 + \left(\frac{\partial w}{\partial z} \right)^2 + \frac{1}{2} \left(\left(\frac{\partial u}{\partial y} + \frac{\partial v}{\partial x} \right)^2 + \left(\frac{\partial v}{\partial z} + \frac{\partial w}{\partial y} \right)^2 + \left(\frac{\partial u}{\partial z} + \frac{\partial w}{\partial x} \right)^2 \right) \right\} d\Omega \ .$$

where μ is the dynamic viscous of the considered fluid and μ_t is the turbulent viscosity. To compare the losses in the guide vanes, the dissipation term has been computed in the control volume Ω in the two cases. The difference between the Case B (characterized by higher global losses in the guide vane) and the Case C, $\delta_{los}^{dis} = \delta_{los\ D1}^{dis} - \delta_{los\ D2}^{dis}$, has been plotted on the guide vanes blade by means of iso-value surfaces (figure 5.19). The negative values of the losses difference, reported in blue, mean that the losses increase adding the draft tube (domain D_2). On the contrary, the positive values, plotted in red, indicate that the losses are higher in D_1.

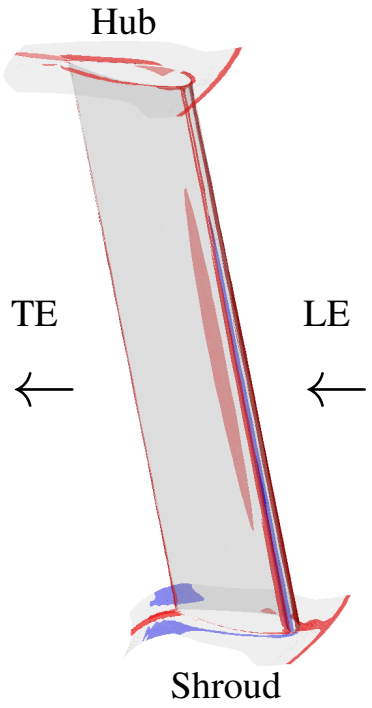

Figure 5.19 Iso-value surfaces of the difference of losses due to the dissipation in the guide vanes between D_1 and D_2, plotted on the guide vane $\delta_{los}^{dis} = \delta_{los\ D1}^{dis} - \delta_{los\ D2}^{dis}$. The negative values (blue surfaces) represent higher losses in D_2; the positive values (red surfaces) mean higher losses in D_1.

The red surfaces are more extended than the blue ones. This means that the local losses in the guide vanes are greater in D_1 than in D_2, according to the global losses analysis (figure 5.18). On the hub, on the pressure side and on the trailing edge of the blade the red regions are more developed than the blue ones. For the instance the cause of the increment of the losses in these regions of the guide vanes is under investigation but could be have a numerical origin.

The comparison between Case B and Case C in non-cavitating regime have shown that the draft tube has an influence on the global quantities, on the velocity profiles on the runner outlet and on the losses in the different parts of the machine.

5.2.1.2 Analyses in cavitating regime

At first, in cavitating regime, the torque (figure 5.20 a) and the head evolution (figure 5.20 b) with the Thoma number, computed on the extended domain D_2 are compared with the results obtained on the reduced domain D_1 and with the measured data. In order to emphasize the discrepancy between calculations and experiments, the numerical T curves are normalized by the first value of the experimental curve in non-cavitating conditions. The effects of the introduction of the draft tube in the analysis begin evident after the efficiency starting drop point ($\sigma_S = 0.600$). The torque values predicted at σ_S and $\sigma_{-0.5\%}$ in Case C are closer to the experimental measurements than the values predicted at same σ in Case B. However, even including the draft tube, the torque evolution is still characterized by a peak after σ_S linked to the numerical head variation with the σ reduction (figure 5.20 a).

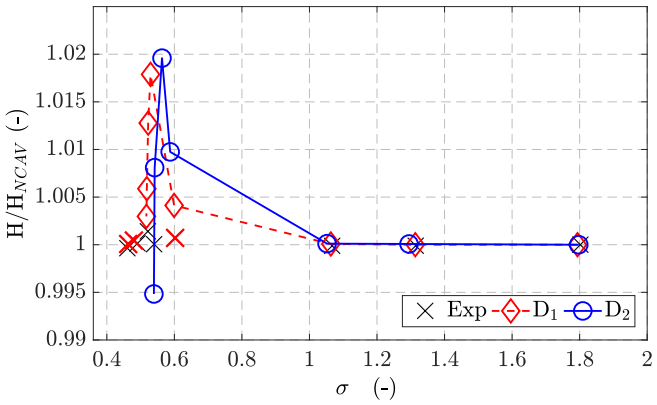

(a)

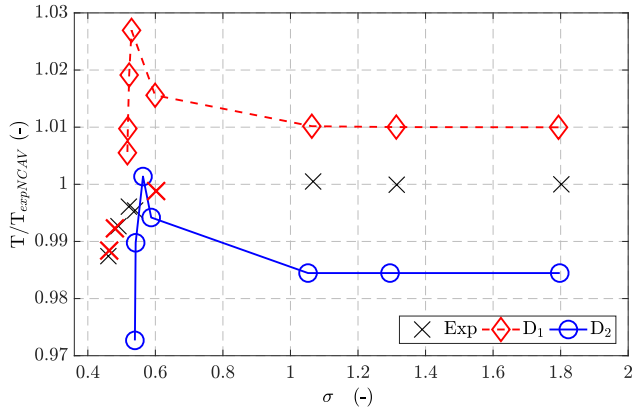

(b)

Figure 5.20 (a) H and **(b)** T as function of σ measured (black crosses) and computed imposing Q_{cor} as inlet boundary condition on D_1 (Case B - red dashed line with the diamonds) and on D_2 (Case C - blue line with the circles). The experimental points σ_s, $\sigma_{-0.5\%}$ and $\sigma_{-1\%}$ are plotted with red crosses.

The draft tube influences also the evolution of the cavitation structures. The greatest differences between the two computational cases are observed at $\sigma_{-0.5\%}$: in Case C (at $\sigma = 0.542$, reported in figure 5.21 b) two cavities appear near the hub, covering the blade root, close to the leading edge and at mid-chord of the blade, in agreement with experimental observations (see figure 5.8). In Case B (figure 5.21 a at $\sigma = 0.5231$), in the equivalent point of the σ-break curve, only one vapor structure is computed in the hub region.

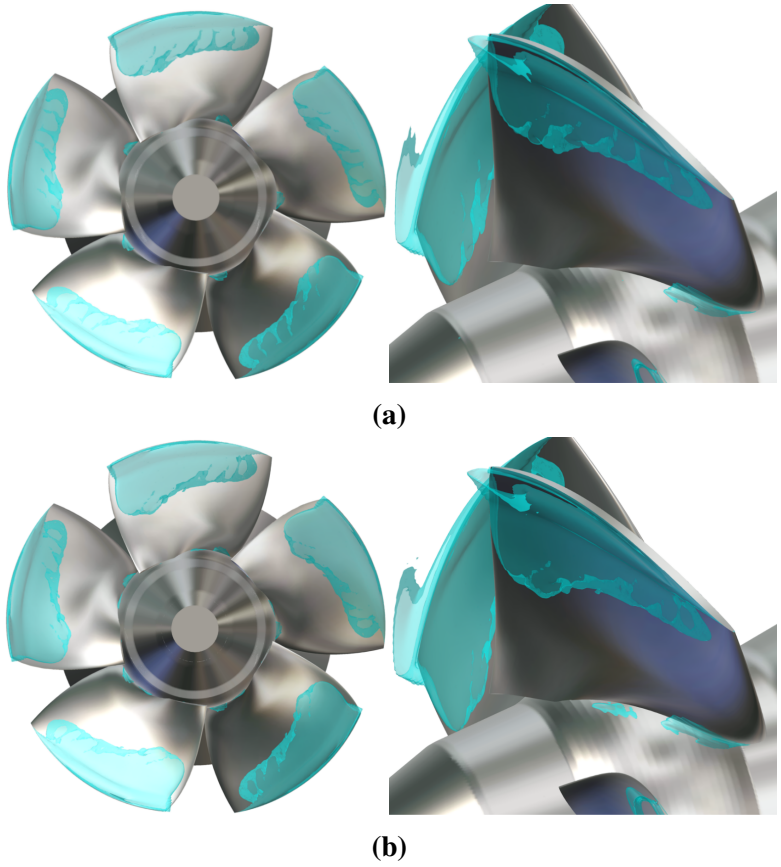

(a)

(b)

Figure 5.21 Frontal and lateral views of the computed iso-density surfaces ($\rho = 980\ kg/m^3$) at $\sigma_{-0.5\%}$ in **(a)** Case B ($\sigma = 0.523$) and in **(b)** Case C ($\sigma = 0.542$).

In conclusion, the draft tube has a great influence on the flow in the turbine in both non-cavitating and cavitating regimes. In order to correctly predict the effects of the cavitation phenomena on the machine, this geometrical component will be considered in the analysis. On the other hand, the mass flow imposed as inlet boundary condition does not allow to correctly reproduce the real behavior of the turbine in cavitating regime. To improve the numerical methodology, a new inlet boundary condition is required.

5.2.2 New inlet boundary condition

In order to keep constant H during the cavitation development, the total pressure P_{tot} has been imposed on the inlet of D_2 instead of the discharge value Q_{cor}. The results obtained with the two inlet boundary conditions in both non-cavitating and in cavitating regimes have been compared. The numerical setup for the two computational cases are recalled in table 5.7 (for more details see chapter 4). Finally, further investigations of the losses evolution in the machine

Table 5.7 Numerical parameters used on the inlet boundary condition test on D_2

Case	Inlet BC	Outlet BC	Mesh	Turbulence model	Cavitation model
C	Q_{cor}	$P = P_{amb}$	M_3	$k-\omega$ SST	Barotropic law
D	P_{tot}				

with the cavitation development and of the cavitating flow have been performed for the Case D.

5.2.2.1 Comparison in non-cavitating regime

The total pressure value used as inlet boundary condition in the Case D has been calculated from Case C. As a consequence, the computed global quantities (T, Q and H) are almost the same in the two cases (difference $< 0.3\%$). On the contrary, the flow in the turbine is greatly affected by the change of the inlet boundary condition. In figure 5.22, the meridional (a) and the tangential (b) velocity profiles computed on the runner outlet in Case C and in Case D are compared with the velocity distributions measured by LDV.

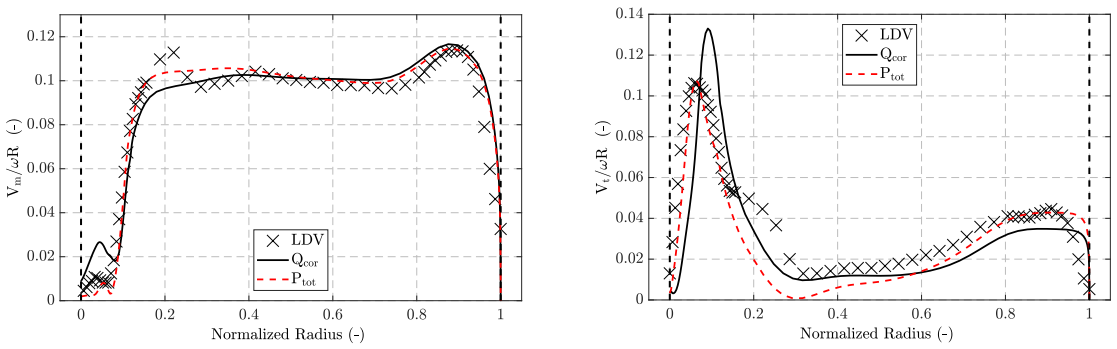

Figure 5.22 Evolution of the normalized **(a)** meridional, V_m, and **(b)** tangential, V_t, components of velocity along the normalized radius, measured by LDV (black crosses) and computed using the $k-\omega$ SST turbulence model with Q_cor (Case C - black line) and P_{tot} (Case D - red dashed line) imposed on the inlet of the domain D_2. 0 is the hub and 1 is the shroud.

Both velocity profiles are in better agreement with experimental data in Case D than in Case C. The prediction of the meridional velocity is improved in the hub region, with a discrepancy

between the computed and experimental highest velocity value of 7%. Also the tangential velocity fit better with experimental data, mostly near the shroud and the runner tip. In the hub region, the difference between experimental and computed peak value is 0.8%.

In order to analyze and compare the losses in each part of the machine in the two computational cases, the same method used in the draft tube influence analysis (see paragraph 5.2.1) has been applied. In figure 5.23 are reported the H_i and the losses values, divided by the experimental H, computed using the two inlet boundary conditions. The H computed in Case

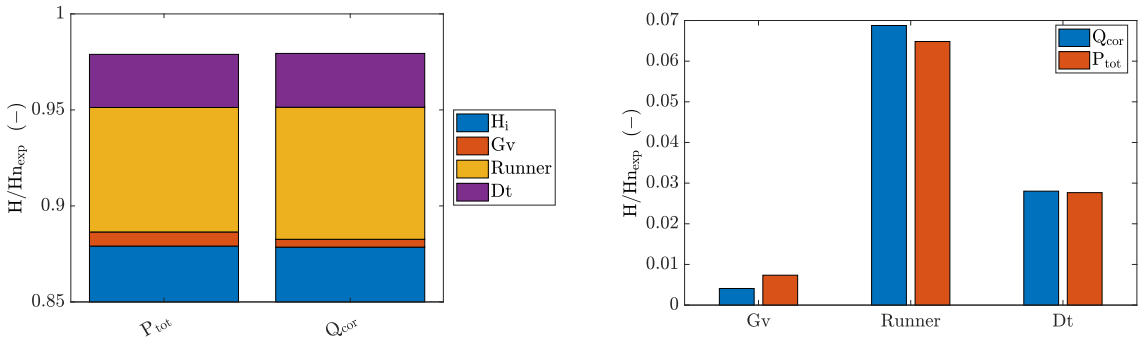

(a) **(b)**

Figure 5.23 Investigation of **(a)** the H_n and **(b)** the losses in D_2 imposing Q_{cor} and P_{tot} as inlet boundary conditions.

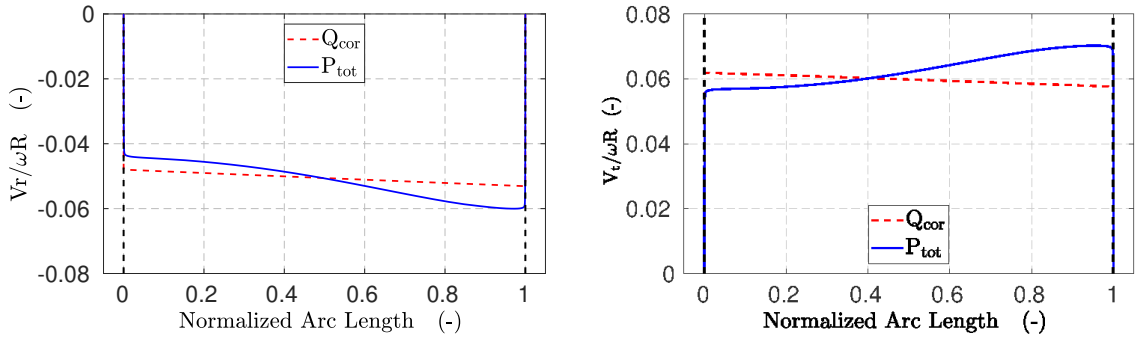

(a) **(b)**

Figure 5.24 Evolution of the normalized **(a)** radial, V_r, and **(b)** tangential, V_t, components of velocity along a normalized arc length computed using the $k-\omega$ SST turbulence model with Q_{cor} (Case C - red dashed line) and P_{tot} (Case D - blue line) imposed on the inlet of the domain D_2.

C and in Case D are very similar (difference $< 0.1\%$). Main discrepancies are observed in the distribution of the losses between the guide vanes and the runner. Imposing the P_{tot} on the inlet, the losses in the guide vanes increase with a consequent decrease of the losses in the runner. This variation in the losses distribution can be explained considering that the velocity profiles on the inlet of the domain are different in the two cases (figure 5.24). Indeed, imposing

a constant value of P_{tot} is not possible to control anymore the velocity profiles on inlet. So the velocity distribution will slightly changes adapting to the total pressure value. Thus, in non-cavitating conditions, using this new inlet boundary condition, the performance values are unchanged while the velocity profiles on the runner outlet are improved.

5.2.2.2 Comparison in cavitating regime

Imposing the P_{tot} on the domain inlet instead of Q the variation of the head during the cavitation development are limited. As it possible to observe in figure 5.25 a, the maximum variation of H in Case D is 0.5% while in Case C is 2%. Thus, the results computed in cavitating regime in Case D are not influenced by the head variation so they can be directly compared with the measurement data.

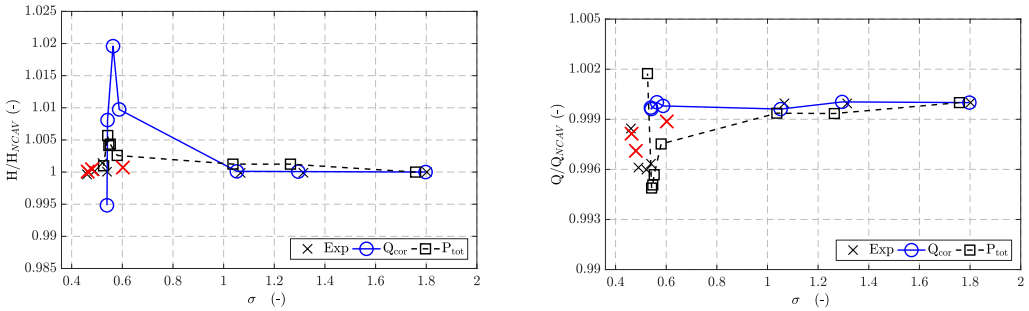

Figure 5.25 **(a)** H and **(b)** Q as function of σ measured (black crosses) and computed imposing Q_{cor} (Case C - blue line with the circles) and P_{tot} (Case D - black dashed line with the squares) as inlet boundary condition on the domain D_2. The experimental points σ_s, $\sigma_{-0.5\%}$ and $\sigma_{-1\%}$ are plotted with red crosses. The variations observed on the Q outlet value in Case C are $< 0.1\%$ and are mostly due to numerical dissipation.

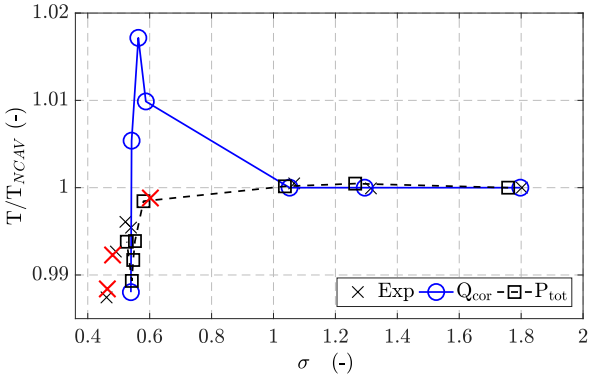

Figure 5.26 T as function of σ measured (black crosses) and computed imposing Q_{cor} (Case C - blue line with the circles) and P_{tot} (Case D - black dashed line with the squares) as inlet boundary condition on the domain D_2. The experimental points σ_s, $\sigma_{-0.5\%}$ and $\sigma_{-1\%}$ are plotted with red crosses.

As a consequence, differently from Case C, in Case D the mass flow value on the outlet is a result of the simulation so it can change with the Thoma number reduction. The Q curve plotted in Case D fits well with the experimental one (see figure 5.25 b). In the last point of the curve, the cavitation phenomena are very strong and a sudden increment of the mass flow value is numerically predicted. This means that the simulated operating point differs from the experimental one.

The torque evolution with the σ reduction calculated in Case D is in better agreement with the experimental data than the torque curve computed in Case C. In the efficiency drop starts point σ_S, the exaltation of the torque value computed imposing Q_{cor} on the inlet disappears changing the inlet boundary condition, according to the measured curve. The reduction of the torque value at $\sigma_{-0.5\%}$ is more closer to the experimental observations in Case D than in Case C. The percentage of the torque drop compared to the first value of the curve at $\sigma_{-1\%}$ is correctly predicted in both computational cases. Finally, as for the mass flow value, an augmentation of the torque value is predicted in Case D at the lowest σ value. The simultaneous increase of the discharge and the torque could means that, in developed cavitating conditions, the flow becomes unstable and the steady approach is no longer suitable. For these reasons, this last point of the curve is not anymore considered in the follow steady analyses.

At σ_S, the H and the T computed in the two cases have an opposite behavior: in Case C, both head and torque start to increase while in Case D they begin to decrease. In order to explain this, the cavities sheets computed at σ_S in the two cases have been compared. As it is possible to see in figure 5.27, no major differences are observed between the two cases in the vapor structures shape or location. So, the augmentation or the reduction of the torque value is due to a different distribution of the force acting on the blade that is not necessarily linked to the presence of different kind of cavities. Considering that the greatest contribution to the

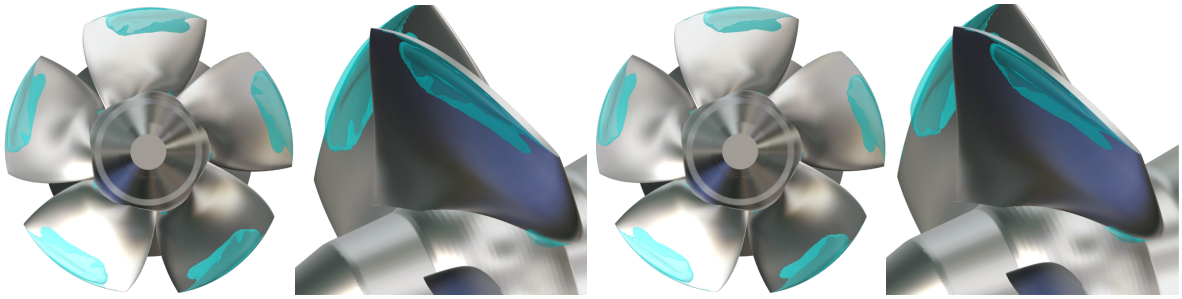

(a) **(b)**

Figure 5.27 Frontal and lateral views of the computed iso-density surfaces ($\rho = 980\ kg/m^3$) at σ_S in **(a)** Case C ($\sigma = 0.590$) and in **(b)** Case D ($\sigma = 0.580$).

torque is due to the inviscid force, in order to visualize the difference in the force distribution, the static pressure fields computed on the blade in the two cases at σ_S can be compared. The

static pressure can be represented by means of a dimensionless pressure coefficient:

$$Cp_1 = \frac{P - P_{ref}}{\frac{1}{2}\rho\left(\omega R\right)^2} \,. \tag{5.12}$$

In figure 5.28 are plotted the Cp_1 fields on the runner blade in Case C and in Case D. The parts colored in dark blue are the regions of the blade where the static pressure is less than the vaporization pressure so their contours correspond to the extension of the cavities. In Case D (figure 5.28 b), a second area at low pressure is detected in the middle of the blade root, not observed in Case C (figure 5.28 a). The presence of this low pressure zone could be explain the different behavior of T at same σ value in the two cases. This discrepancy observed in the

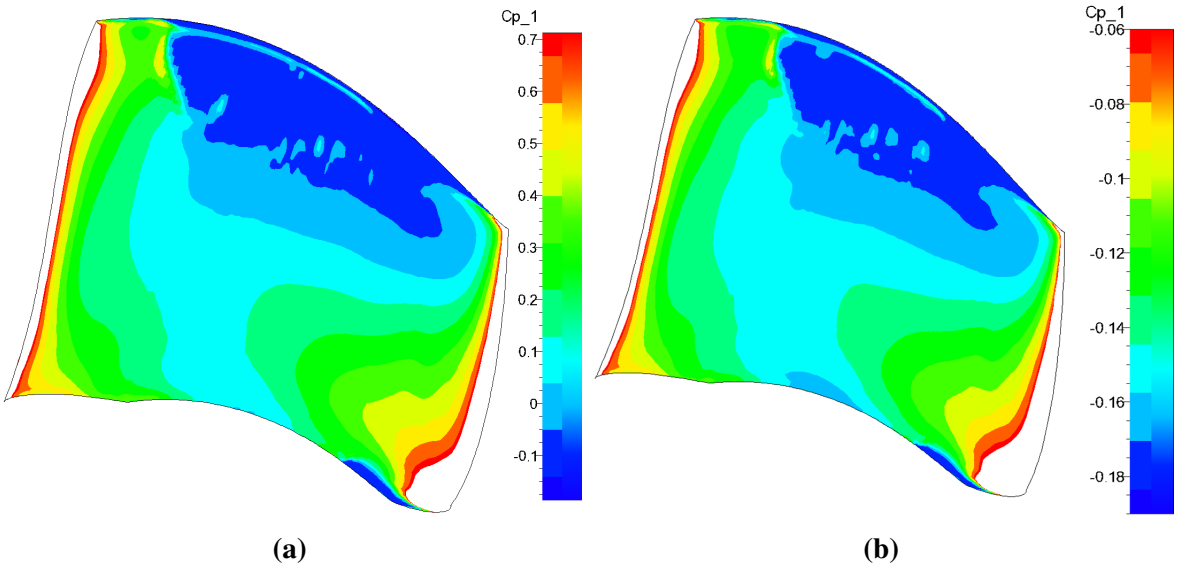

Figure 5.28 Contours of Cp_1 plotted at σ_S in **(a)** Case C ($\sigma = 0.590$) and in **(b)** Case D ($\sigma = 0.580$).

static pressure fields between the two cases is related to the boundary conditions chosen on the inlet. Indeed, imposing the P_{tot} is not possible to impose the velocity distribution on the inlet. Consequently, the flow angle on the runner blade leading edge will be different, changing the pressure distribution on the blade.

In conclusion, by imposing P_{tot} on the calculation domain inlet instead of Q, the prediction of the flow in both non-cavitating and cavitating conditions is improved. The velocity profiles computed on the runner outlet in non-cavitating regime fit better with the measured profiles. In cavitation conditions, the total pressure as inlet boundary condition allows to fix the head while the discharge varies during the cavitation development (as during the laboratory tests). Consequently, the performances curves and the vapor structures computed in Case D are in better agreement with experimental data than the ones predicted in the Case C.

The overall aspect of the T, H and Q curves computed with the new inlet boundary conditions fit perfectly with the experimental curves. The computed σ values after σ_S are still higher than the experimental ones. On the other hand, the first objective of this work of thesis is to correctly reproduce the shape of the performance curves also with a discrepancy on the σ values. Unsteady calculations (see chapter 6) have been performed in order to try to reduce this discrepancy and to improve the cavitating flow reproduction. For unsteady calculations, the same computational configuration will be used (see chapter 4).

5.2.3 Cavitating flows investigations

Once the methodology for steady simulations has been defined, losses and cavitating flow in different parts of the machine have been analyzed in details. The investigations will be hereafter discussed.

5.2.3.1 Evolution of the losses in the machine with the cavitation

In order to investigate the evolution of the losses in the machine with the cavitation development, the first and the last points of the computed σ-break curve have been analyzed and compared. The point in non-cavitating conditions and at $\sigma_{-1\%}$ are reported in figure 5.29 with the **1** and the **7**, respectively.

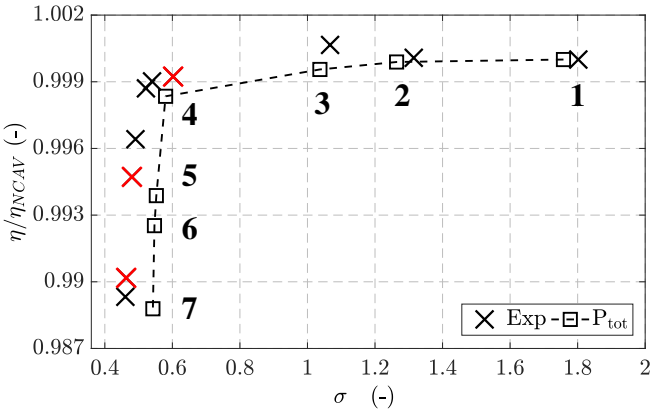

Figure 5.29 σ - break curve measured (crosses) and computed imposing P_{tot} (Case D - black dashed line with the squares) as inlet boundary condition on the domain D_2. The experimental points σ_s, $\sigma_{-0.5\%}$ and $\sigma_{-1\%}$ are plotted with red crosses.

The methodology applied to estimate the losses and the H_i has been detailed in paragraph 5.2.1. The difference of the net head values computed in the two conditions is less than 0.1%. On the contrary, the percentage of losses and energy transfered to the turbine has been changed (figure 5.30): at $\sigma_{-1\%}$ the H_i has been reduced of the 1% while the losses have been

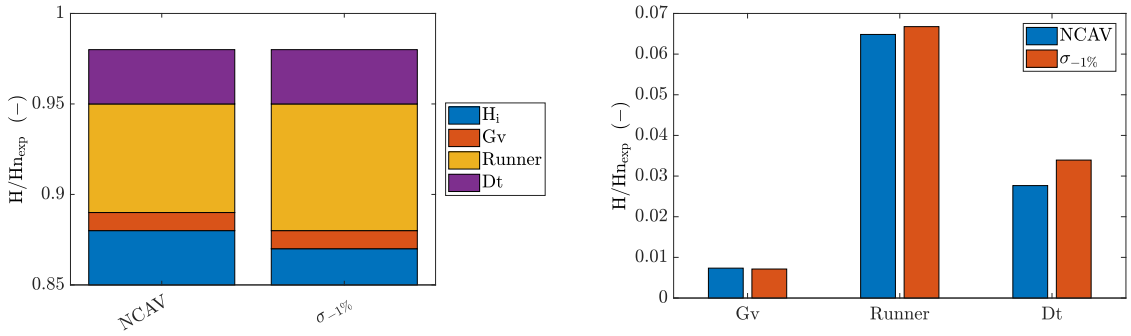

(a) **(b)**

Figure 5.30 Investigation of **(a)** the H_n and **(b)** the losses imposing P_{tot} on the inlet of D_2 in the first (*NCAV*) and in the last ($\sigma_{-1\%}$) point of the σ-break curve.

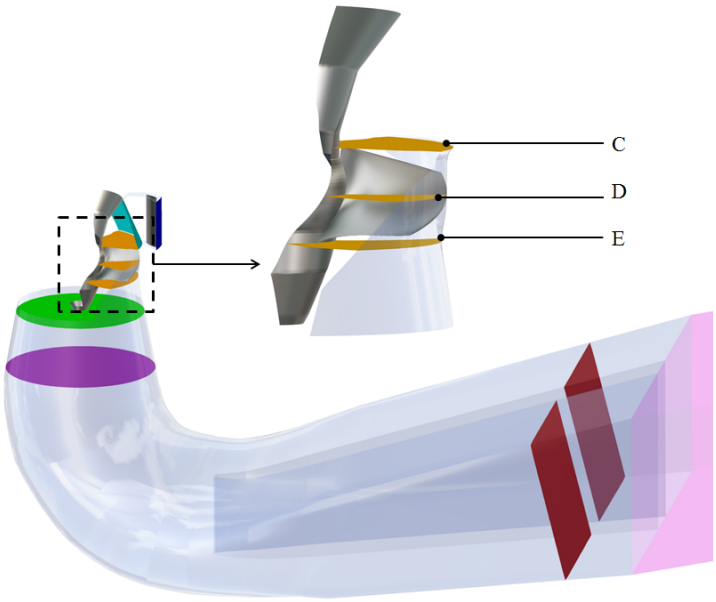

Figure 5.31 Cutting surfaces defined for the runner losses analysis. **C** is near the leading edge, **D** is near the middle of the blade and **E** is near the trailing edge

increased of the same amount. In figure 5.30 b are reported the contribution to the total losses furnished by each component of the machine. The losses in the guide vanes are the same in the two points. This means that the cavitation does not affect the flow in the guide vanes ring. An augmentation of the losses amount is observed in the runner where the contribution to H increase from 6.5% in non-cavitating conditions to the 6.8% at $\sigma_{-1\%}$. Also in the draft tube the losses increase from 2.8% to 3.5% with the development of the cavitation.

A detailed investigation of the evolution of the cavitating flow in the runner and in the draft tube will be presented in the following sections.

5.2.3.2 Losses evolution in the runner

In order to evaluate the losses in the runner, three cutting planes have been created (see figure 5.31): **C** on the leading edge (LE), **D** on the middle and **E** on the trailing edge (TE) of the runner blade.

The losses have been divided in two contributions:

- $\Delta_{los} = R_C - R_D$ are the losses in the first part of the blade (from the leading edge to the middle of the blade);
- $\Delta_{los} = R_D - R_E$ are the losses in the last part of the blade (from the middle to the trailing edge of the blade).

In the present analysis, the same point of the σ-break curve considered in the analysis of the losses in all the machine have been investigated (the points in non-cavitating conditions, **1**, and at $\sigma_{-1\%}$, **7**). The evolution of the losses distribution on the blade is given in figure 5.32. The histogram shows that with the cavitation development the losses decrease on the leading edge part while increase on the trailing edge part.

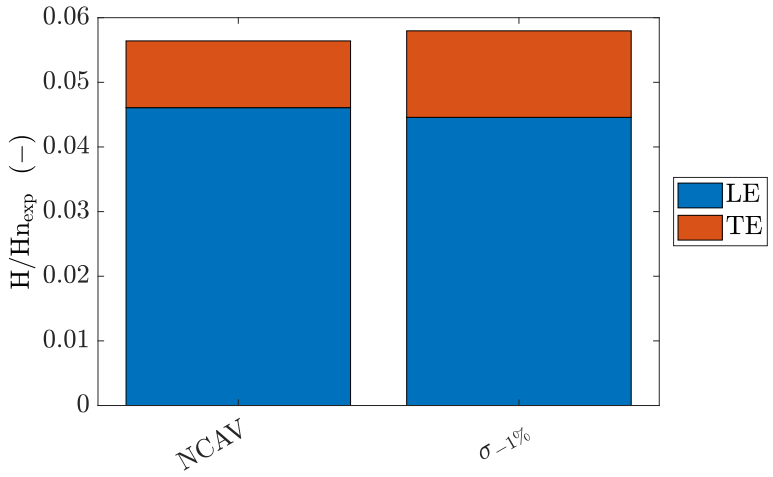

Figure 5.32 The losses on the runner blade computed in non-cavitating conditions and at $\sigma_{-1\%}$, shared between the leading edge (LE) and the trailing edge (TE).

To improve the losses visualization on the blade a control volume Σ, delimited by the surfaces **2** and **4** and by the shroud and hub of the runner, is determined. Defining the equation 5.8 in the rotating reference frame and integrating the equation on Σ, we finally obtain the dissipation losses term as a function of the relative velocity $\vec{W}$:

$$\Delta_{los}^{dis} = \frac{1}{\rho g Q} \iiint_{\Sigma} \overline{\overline{\tau}} : \overline{\overline{\nabla}}(\vec{W}) d\Omega \frac{1}{\rho g Q} \iiint_{\Sigma} \delta_{los}^{dis} d\Omega \,. \tag{5.13}$$

The difference between the dissipation terms computed at $\sigma_{-1\%}$ and in non-cavitating conditions ($\delta_{los}^{dis} = \delta_{los\ CAV}^{dis} - \delta_{los\ NCAV}^{dis}$) is plotted in figure 5.33 by using iso-value surfaces. Considering that the losses are higher at $\sigma_{-1\%}$, the red surfaces are the regions where the losses have been increased while the blue surfaces represent the zones where the losses have been decrease with the development of the cavitation phenomena.

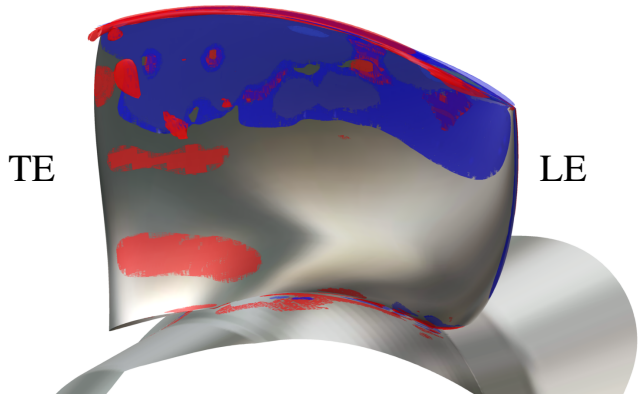

Figure 5.33 Iso-value surfaces of the difference of losses due to the dissipation in the runner in non-cavitating conditions and at $\sigma_{-1\%}$, plotted on the runner blade $\delta_{los}^{dis} = \delta_{los\ CAV}^{dis} - \delta_{los\ NCAV}^{dis}$. The negative values (blue surfaces) represent higher losses in non-cavitating conditions; the positive values (red surfaces) mean higher losses at $\sigma_{-1\%}$.

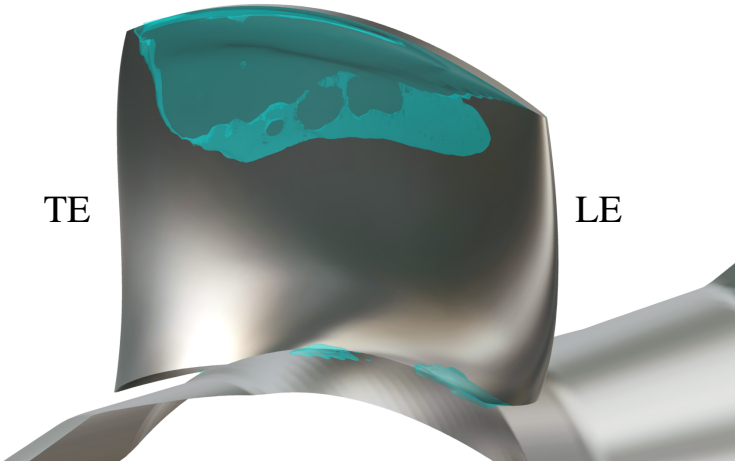

Figure 5.34 The computed iso-density surfaces ($\rho = 980\ kg/m^3$) at $\sigma_{-1\%}$ in Case D ($\sigma = 0.550$).

The red surfaces are mostly located on the hub and on the shroud regions. Near the shroud gap, the losses increase mostly close to the trailing edge. The blue surfaces are concentrated on the blade profile and near the shroud. In the shroud gap regions, the losses reduce near the leading edge. According to the histogram in figure 5.32, as a consequence of the presence of the

cavities structures, the losses decrease near the leading edge and increase close to the trailing edge. The extension of the blue zones (the regions of the losses reduction) is very similar to the shape of the computed vapor structures at $\sigma_{-1\%}$ (figure 5.34). The red surfaces are mostly concentrated near the shroud gap in a region characterized by strong flow recirculation.

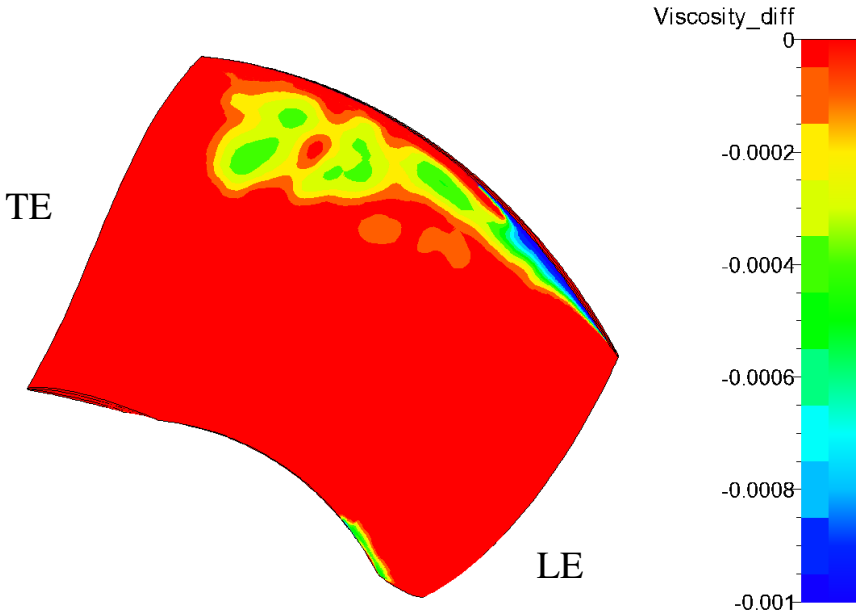

Figure 5.35 The difference of $(\mu + \mu_T)$ computed in the runner in non-cavitating conditions and at $\sigma_{-1\%}$, plotted on the runner blade.

The term of dissipation is function of the turbulent and the fluid viscosities and of the gradient of velocity. In the vapor regions, $(\mu + \mu_T)$ decreases and, consequently, the losses due to the dissipation will be reduced. Indeed, plotting the difference between $(\mu + \mu_T)$ computed at $\sigma_{-1\%}$ and in non-cavitating conditions (figure 5.35) it is evident that the most negative difference value regions are almost in the same position of the blue surfaces plotted in figure 5.32. On the contrary, near the shroud gap the presence of huge velocity gradients causes the increase of the dissipation losses term.

In conclusion, it is possible to stated that the reduction of the torque value with the cavitation development is mostly linked to the hub and tip cavitation. Indeed, vapor structures in the gaps regions provoke flow recirculation, increasing the dissipation losses.

5.2.3.3 Cavitation structures and pressure profile on the runner blade

In order to validate the developed methodology for the cavitation prediction based on the new inlet boundary condition, the computed iso-density surfaces have been compared to the experimental observations for two σ values:

- At σ_S (the efficiency drop starts point), the position and the extension of the cavities structures predicted on the hub and on the shroud in figure 5.36 b are in very good agreement with the experimental observations (figure 5.36 a);
- At $\sigma - 0.5\%$, the computed cavity on the shroud (figure 5.37 b) is congruent with the vapor structure observed experimentally (figure 5.37 a). Near the hub, the starting points of the cavitation sheets are correctly predicted. However, it is not possible to reproduce the detachment of the structure and its expansion towards the trailing edge by using the numerical models applied in this work. In order to simulate cavitation shedding, URANS approach with the correction on the turbulent viscosity term proposed by Reboud *et al.* [84] must to be used.

The static pressure distributions around the runner blade for the same σ values have been analyzed and compared with the blade loads computed in non-cavitating regime to investigate the influence of the cavitation on the pressure fields. Figure 5.38 shows the different blade sections considered for the study of the pressure fields: a section near the hub (1% of the blade height, plotted with the green line), at 75% of the blade height (plotted with a blue line) and a section near the shroud (95% of the blade height, plotted by the purple line).

A dimensionless coefficient Cp_2 has been defined to represent the static pressure:

$$Cp_2 = \frac{P - P_v}{\frac{1}{2}\rho\,(\omega R)^2}\,. \tag{5.14}$$

In equation 5.14, P_v is the vapor pressure of the water at the reference temperature. In non-cavitating regime the pressure distributions in figure 5.39 a show two peaks of depression close to the hub :

- The first one, located on the leading edge, is not linked to cavitation phenomena but it is due to a defect of incidence;
- The second one, more slightly than the first one, placed at streamwise 0.18. However, the local static pressure value is not low enough to allow the generation of the vapor.

At σ_S (corresponding to $\sigma = 0.580$ on the computed cavitation curve), others depression regions begin to appear: one on the hub (figure 5.39 a), extending from the leading edge to the streamwise= 0.19, and two others on the shroud (figure 5.39 c), the larger one from 0.14 to 0.63 of the streamwise and a smaller one from 0.66 to 0.75 of the streamwise. According to the blade loads, the computed iso-density surfaces in figure 5.36 b, show three vapor structures: one is located near the hub, on the leading edge, and the other two are on the blade tip. This alteration of the pressure distribution on the blade could leads, in combination with the increase

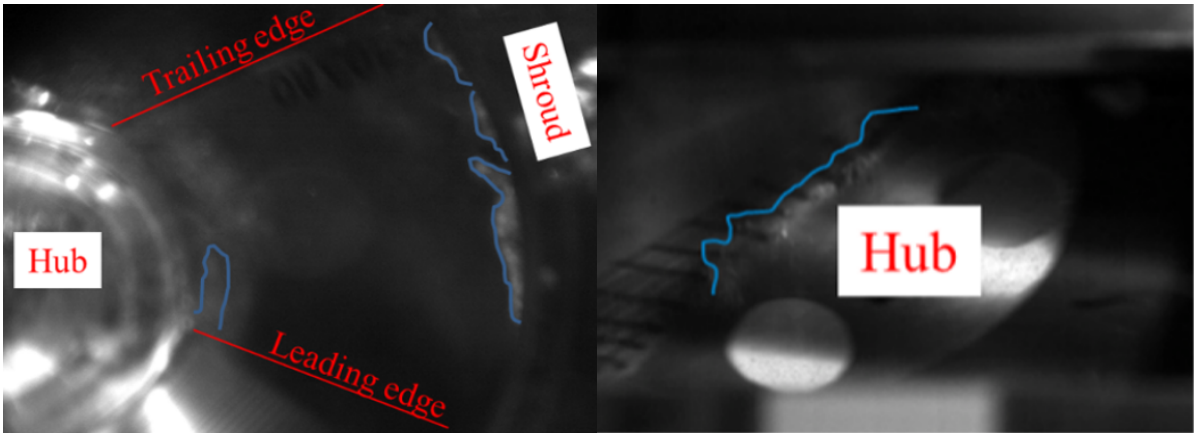

(a)

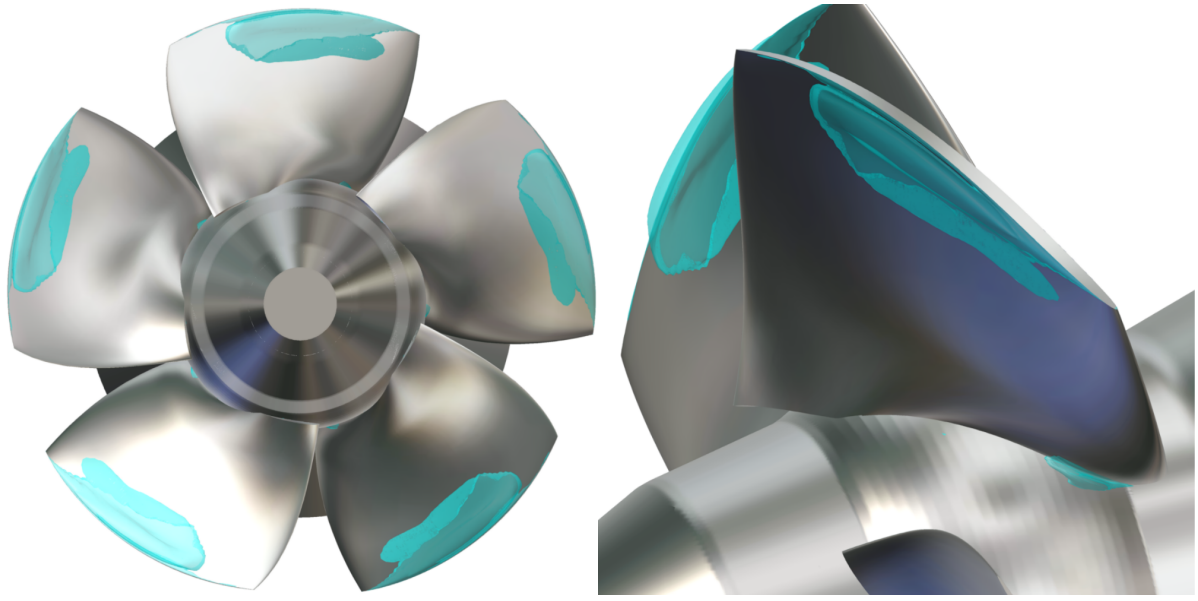

(b)

Figure 5.36 (a) Experimental vapor structure ($\sigma = 0.600$) and **(b)** Frontal and lateral views of the computed iso-density surfaces ($\rho = 980\ kg/m^3$) ($\sigma = 0.580$).

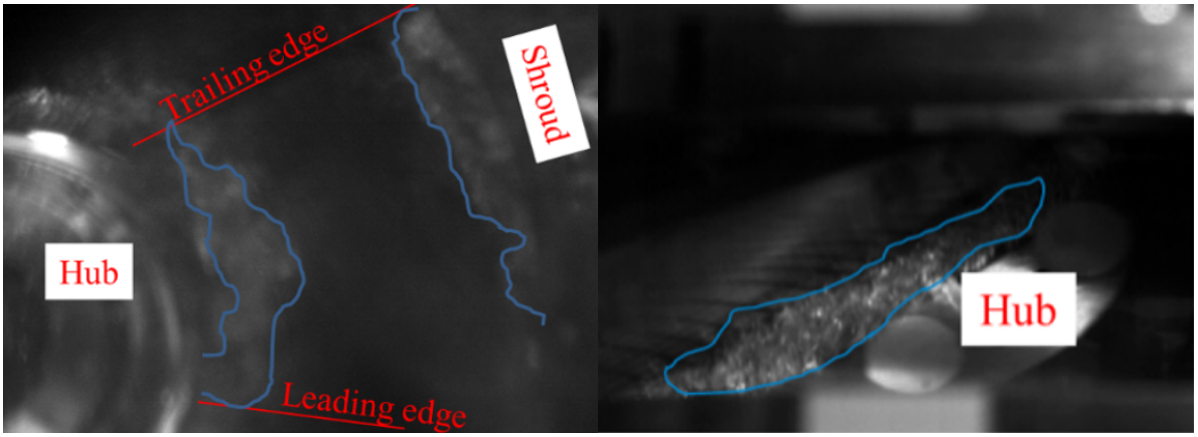

(a)

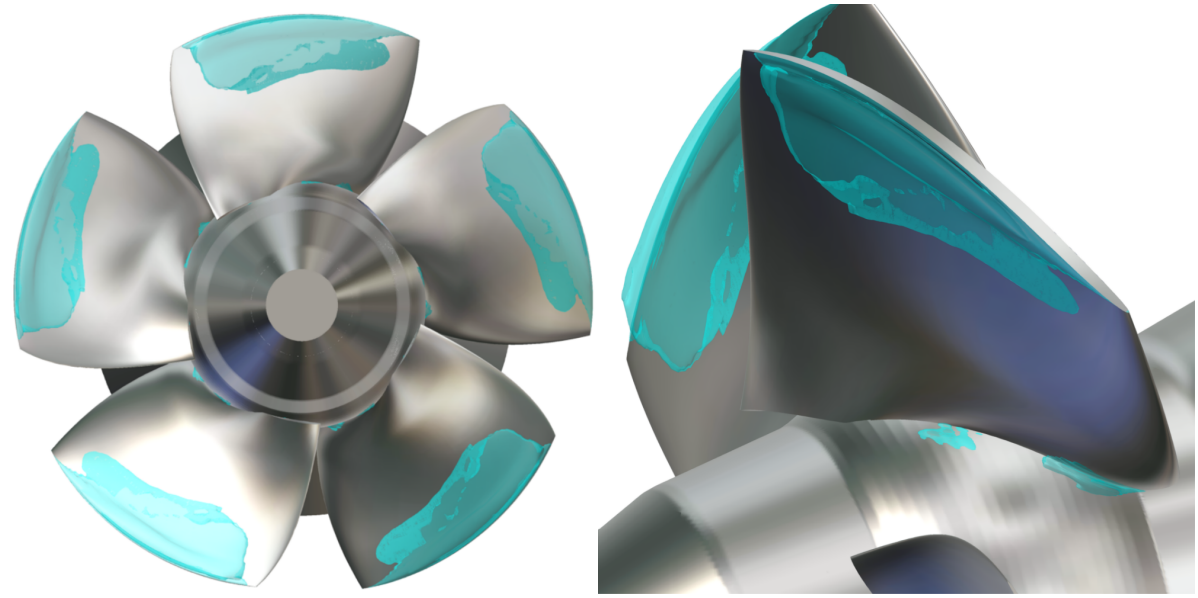

(b)

Figure 5.37 (a) Experimental vapor structure ($\sigma = 0.480$) and **(b)** Frontal and lateral views of the computed iso-density surfaces ($\rho = 980\ kg/m^3$) ($\sigma = 0.560$).

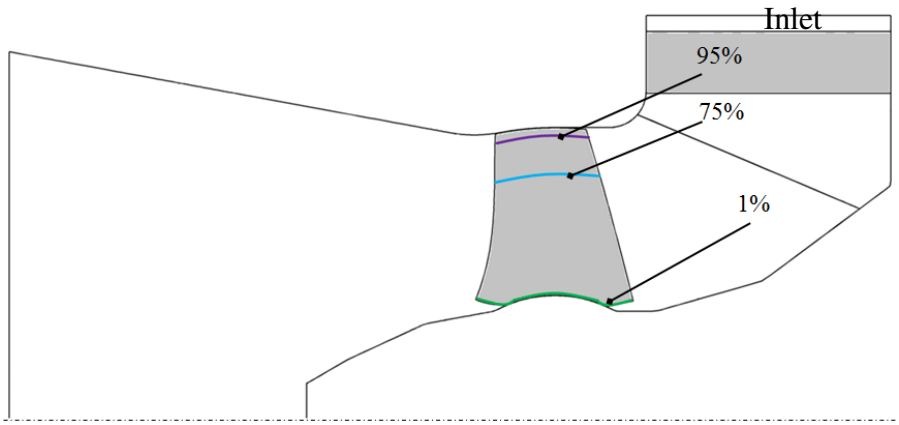

Figure 5.38 Blade sections at 1%(green line), 75% (blue line) and 95%(purple line).

of the dissipation losses, to a slight reduction of the torque (graph in figure 5.26) with respect to the non-cavitating value. At $\sigma = 0.560$, when the efficiency is reduced of -0.5%, the low pressure region on the blade tip increases (figure 5.39 a). Close to the shroud (figure 5.39 c), the blade load has been changed and a single huge depression region extends in the trailing edge direction. A low pressure zone appears also at 75% of the blade height (figure 5.39 b). This means that the vapor structure has been covered a part of the blade profile, deviating the flow and causing a reduction of torque value. The analysis of the blade loads agree well with the cavities computed at $\sigma_{-0.5\%}$ in figure 5.37 b: comparing to the iso-density surfaces computed σ_S (figure 5.36 b), the two cavities on the blade root and tip have been increased. The vapor structure observed on the middle of the hub, due to is position, cannot be detected by the blade load.

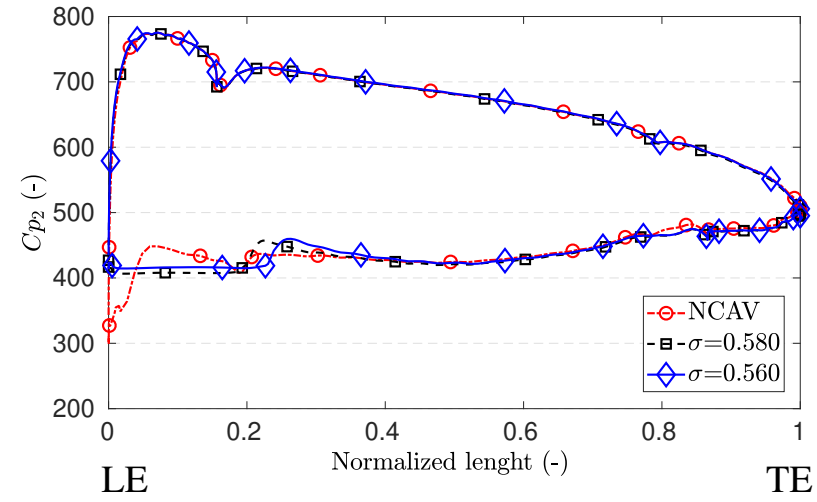

(a)

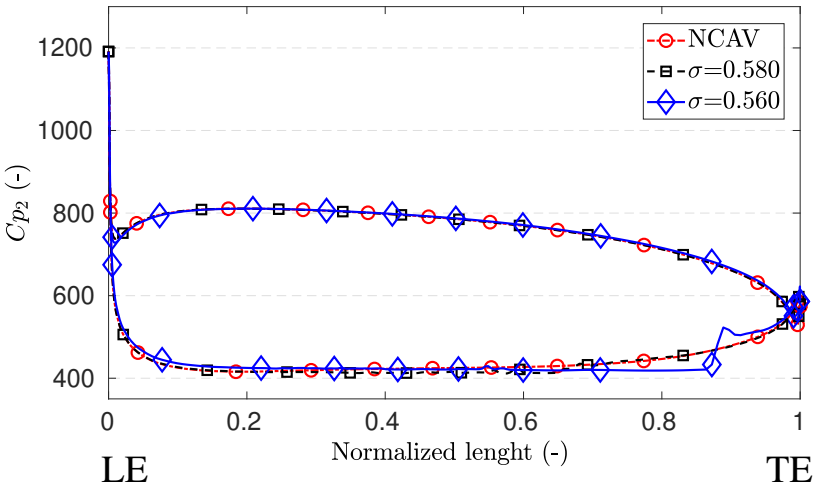

(b)

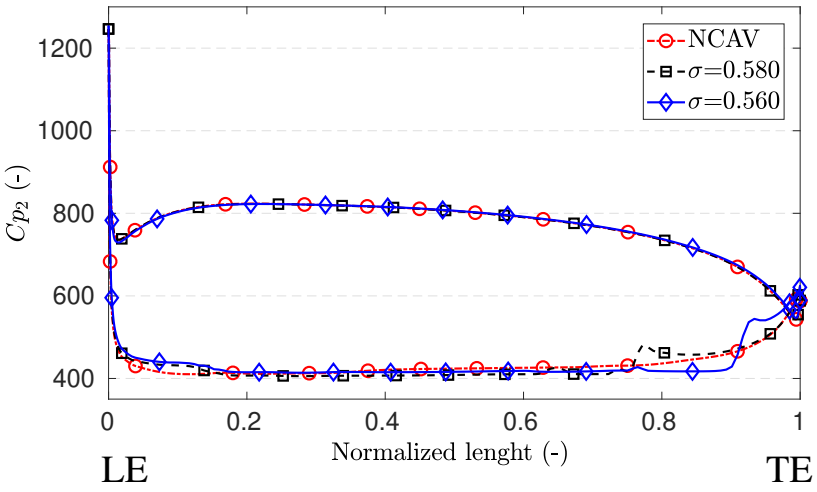

(c)

Figure 5.39 Pressure distribution around the blade for decreasing σ values at **(a)** near the hub (1%), **(b)** at (75%) and **(c)** near the shroud (95%).

5.2.3.4 Cavitating flow analysis in the runner

Two parameters have been considered to analyze the cavitating flow behavior: the meridional velocity, V_m and the normalized helicity, H. The helicity is a scalar quantity defined as the dot product of relative velocity and vorticity vectors. In the rotating frame of reference can be defined as :

$$He = \vec{W} \cdot \left(\nabla \times \vec{W} \right) \ . \tag{5.15}$$

The physical meaning of helicity becomes clearer when is used in the normalized form. The normalized helicity is defined as:

$$He_{norm} = \frac{\vec{W} \cdot \left(\nabla \times \vec{W} \right)}{\|\vec{W}\| \cdot \|\nabla \times \vec{W}\|} \ . \tag{5.16}$$

where $\|\vec{W}\|$ and $\|\nabla \times \vec{W}\|$ are the magnitudes of the relative velocity and the vorticity vectors, respectively. The normalized helicity physically represents the angle between velocity and vorticity vectors so its value ranges from -1 to 1. As such, the normalized helicity can be used as an indicator of the velocity vector orientation with respect to vorticity vector field for a given flow field. The normalized helicity value will be very close to 1 or -1 at the core of the streamwise vortices. This leads to locate the core of those streamwise vortices. The meridional velocity and the normalized helicity have been investigated in three different sections of the interblade channel, perpendicular to the streamwise direction, reported in figure 5.40: on the leading edge (**1** - the blue line), in the mid-chord (**2** - the green line) and on the trailing edge (**3** - the red line). Two points of the σ-break curve have been considered for the analyses: the point

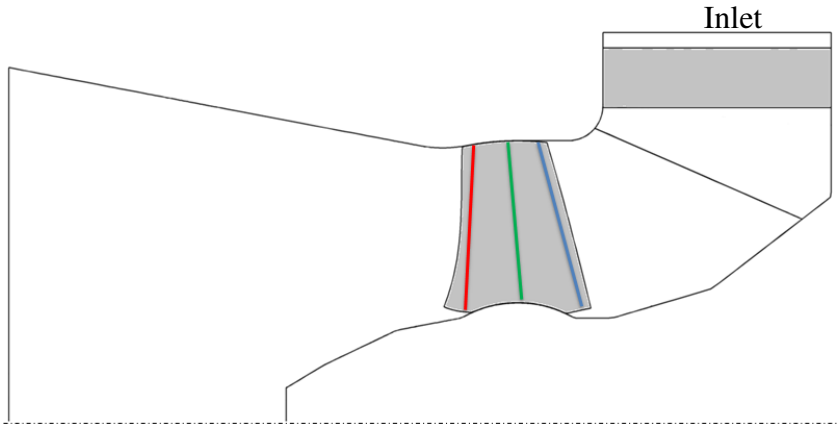

Figure 5.40 Blade sections at 1%(green line), 75% (blue line) and 95%(purple line).

in non-cavitating regime and the point at $\sigma_{-1\%}$ ($\sigma = 0.550$). The analysis of the normalized helicity in plane **1** (figure 5.41) shows that, in non-cavitating conditions, the greatest vorticity

structures are observed near the shroud ($H_{norm} = +1$) and the hub ($H_{norm} = -1$) gaps. As it is possible to observe in figures 5.41 b and c, in developed cavitating conditions the vapor structure near the hub influences the helicity field and the vorticity structure at $H_{norm} = +1$ disappears. Before the appearance of the cavities (figure 5.42 a), the distribution of the mass flow on the inlet is uniform in the interblade section **1**. An acceleration zone is observed near the blade profile, mostly close to the gaps. However, the development of the cavitation does not greatly affect the mass flow distribution (figures 5.42 b and c). In non-cavitating regime, at mid-chord (plane **2**), the vortices observed near the hub and shroud on plane **1**, are more developed (see figure 5.43 a). At $\sigma_{-1\%}$ a large vapor structure on the blade tip deviates the flow changing the sign of the helicity field in this region (figures 5.43 b and c). Observing the velocity fields in section **2** (figure 5.44), the development of the cavity sheet leads to a slight increase of V_m close to the root of the blade. Perturbations of the mass flow field are also observed near the shroud, where the velocity slightly increases. In plane **3**, close to the trailing edge (figure 5.45 a), already in non-cavitating regime the flow is perturbed also far from the blade. Indeed, a vorticity structure characterized by a $H_{norm} = +1$ appears in the middle of the interblade channel. The region near the shroud is the most influenced by the cavitation (see figures 5.45 b and c). Flow alterations with the development of the cavitation are observed also in the velocity fields (figure 5.46) close to the blade tip where an increase of V_m value is observed. This augmentation of the velocity leads to increase the losses on the blade tip close to the trailing edge, according to the runner blade losses analysis (figure 5.33).

The analysis of the velocity and the helicity fields in the interblade channel has been shown that the vapor structures developing on the blade influence the flow in the runner. These cavities modify the flow path, especially on the runner outlet, altering the machine work, according to the performances and the blade loads predictions. In the optimal load condition, the cavitation phenomena are concentrated in some parts of the blade and they cause only minor flow alterations.

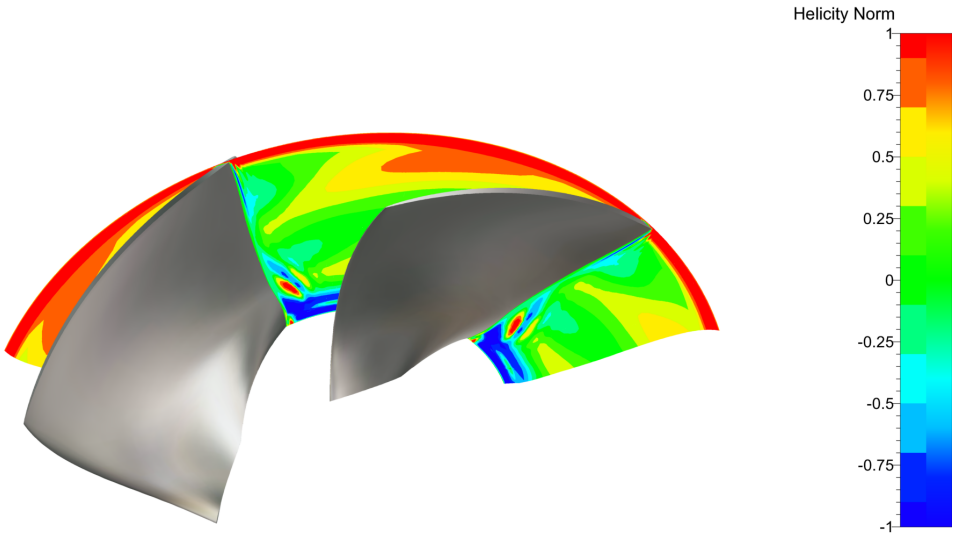

(a)

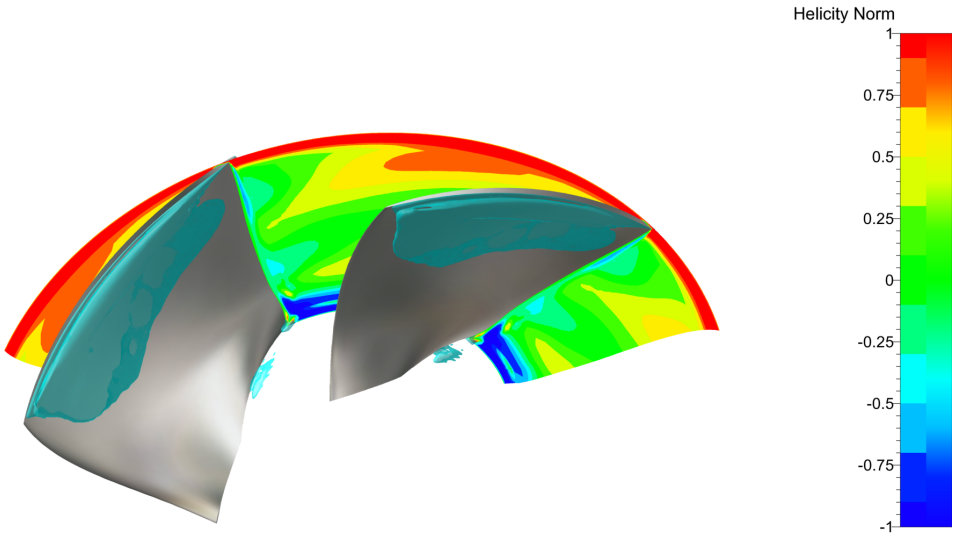

(b)

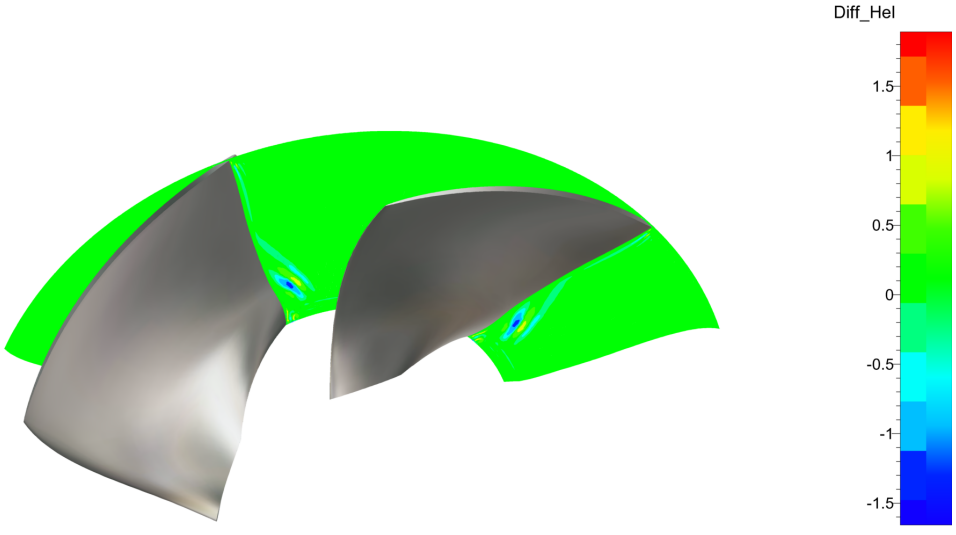

(c)

Figure 5.41 Normalized Helicity **(a)** in non-cavitating conditions and **(b)** at $\sigma_{-1\%}$ and **(c)** their difference plotted near the leading edge of the blade (plane **1**).

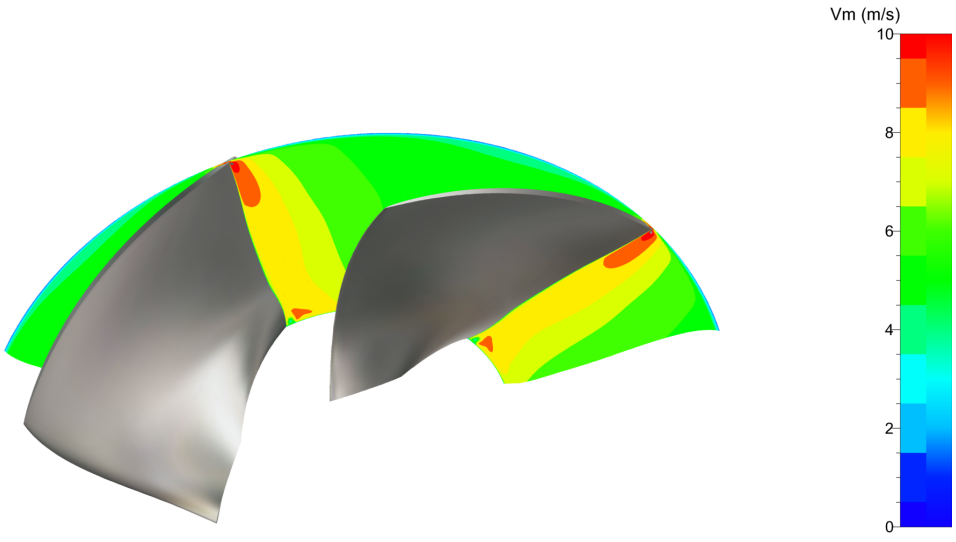

(a)

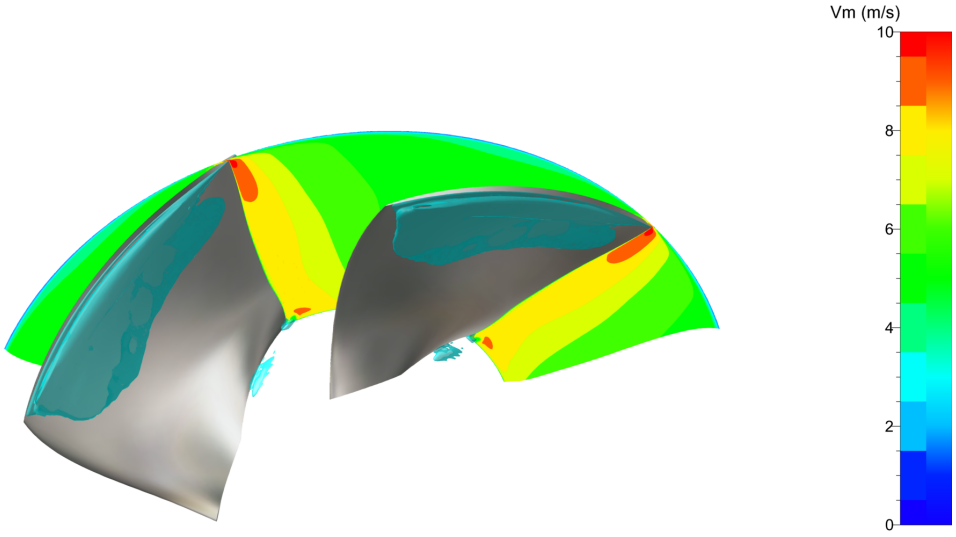

(b)

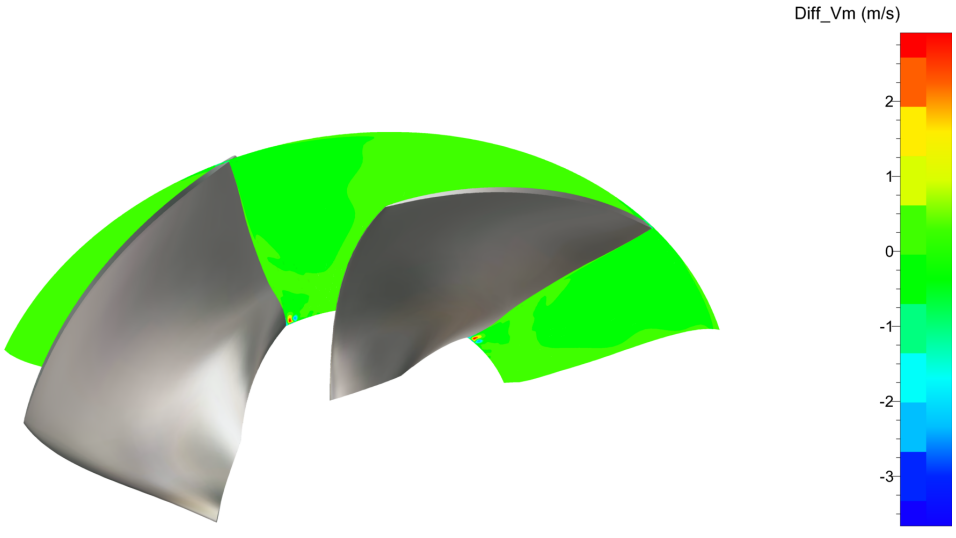

(c)

Figure 5.42 Meridian velocity **(a)** in non-cavitating conditions and **(b)** at $\sigma_{-1\%}$ and **(c)** their difference plotted near the leading edge of the blade (plane **1**).

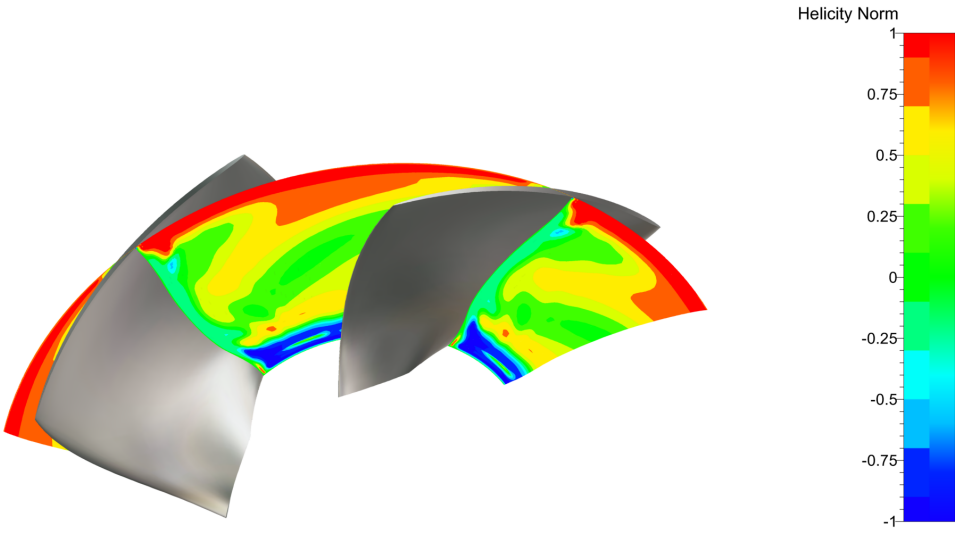

(a)

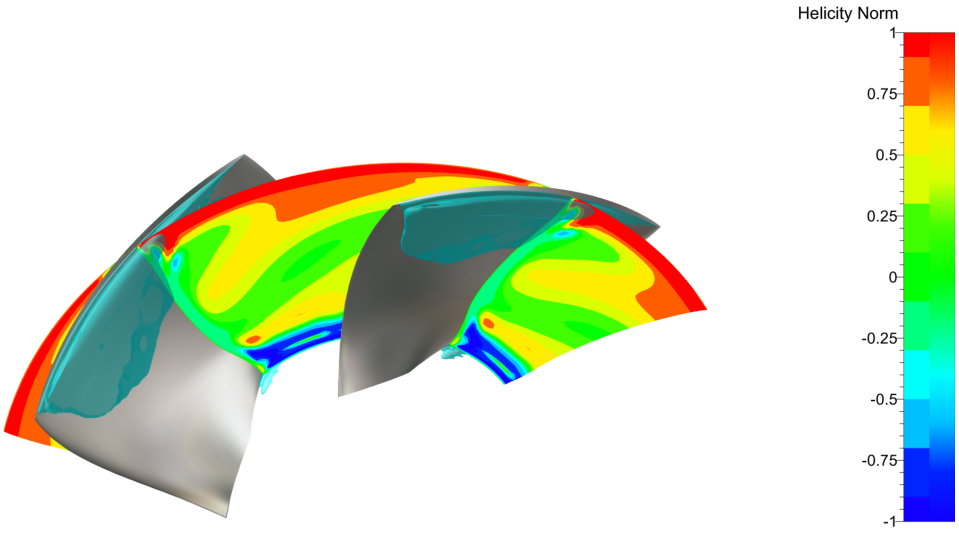

(b)

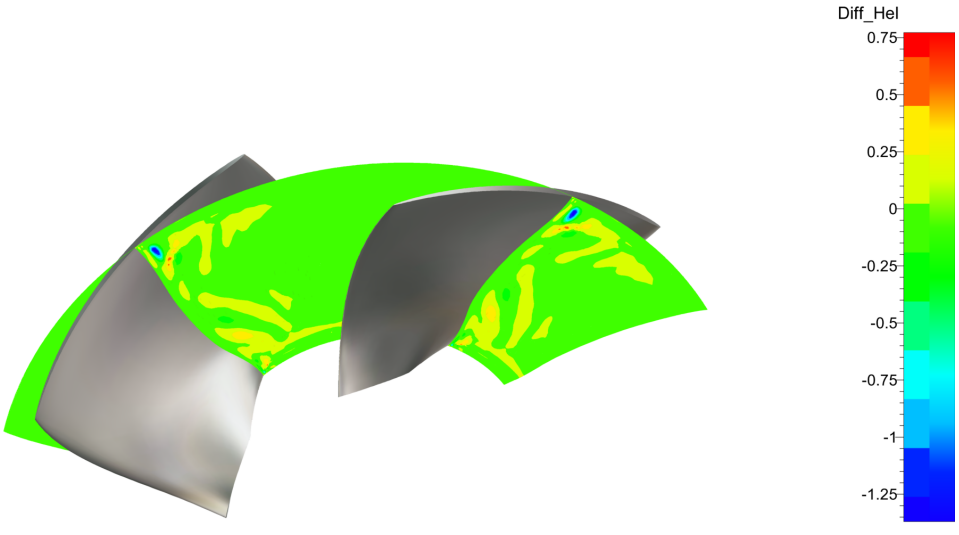

(c)

Figure 5.43 Normalized Helicity **(a)** in non-cavitating conditions and **(b)** at $\sigma_{-1\%}$ and **(c)** their difference plotted mid-chord of the blade (plane **2**).

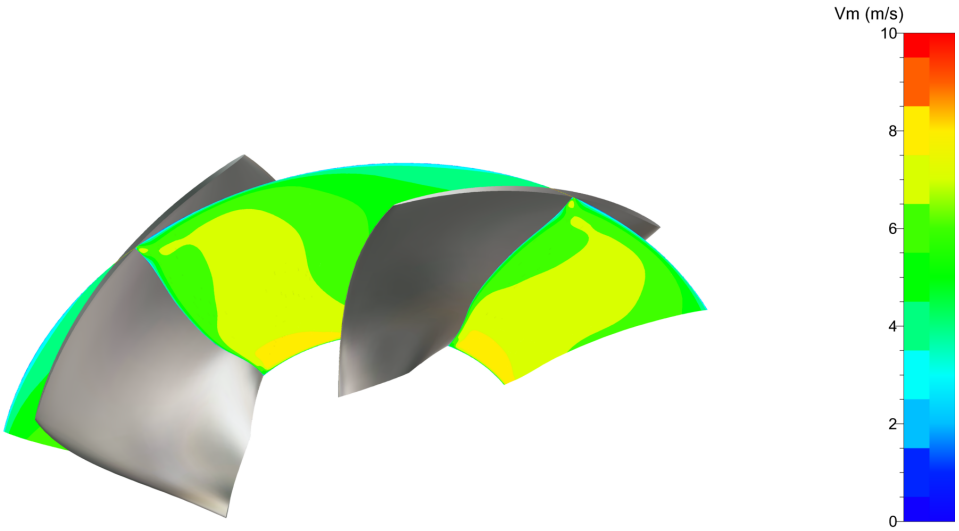

(a)

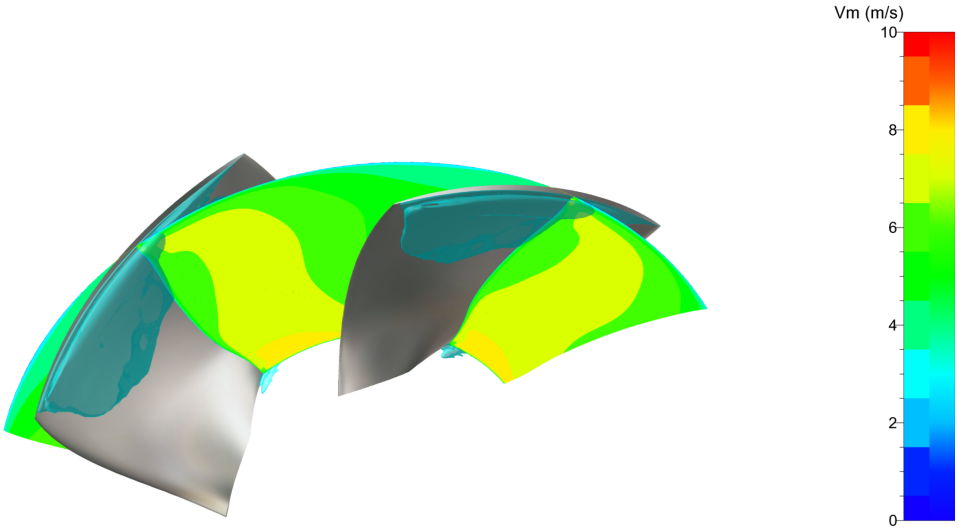

(b)

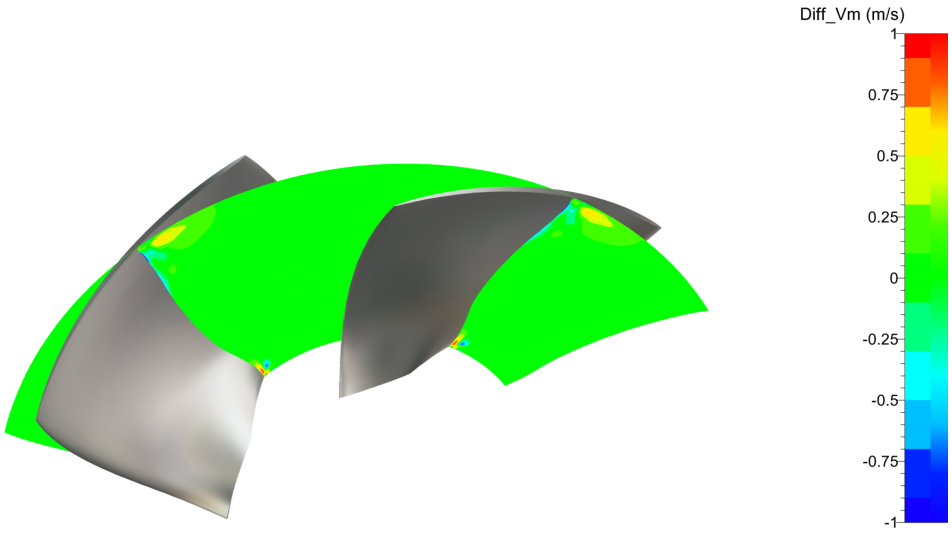

(c)

Figure 5.44 Meridian velocity **(a)** in non-cavitating conditions and **(b)** at $\sigma_{-1\%}$ and **(c)** their difference plotted mid-chord of the blade (plane **2**)

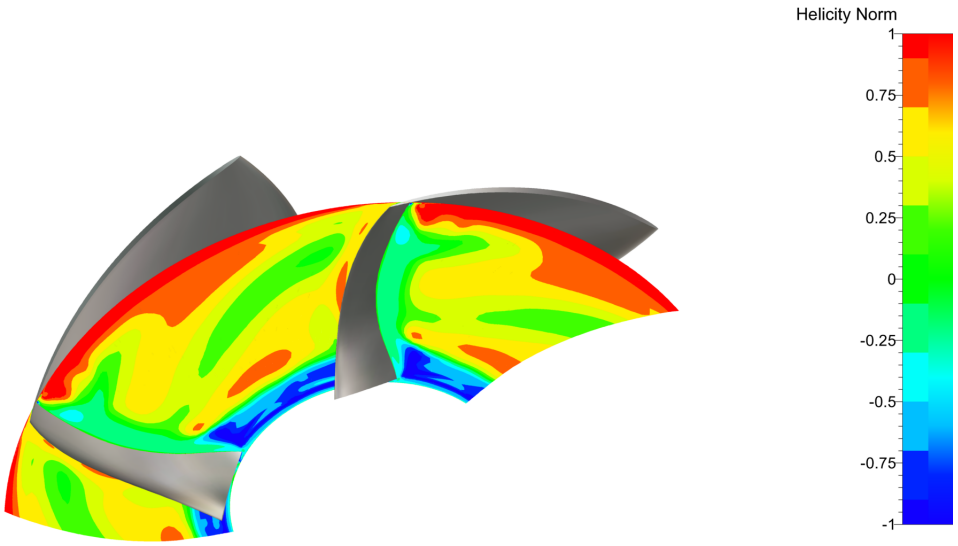

(a)

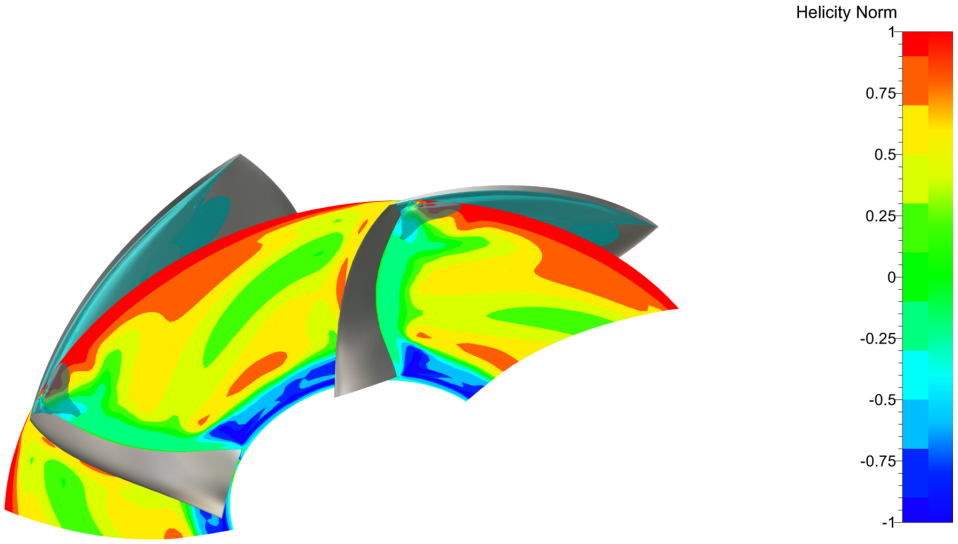

(b)

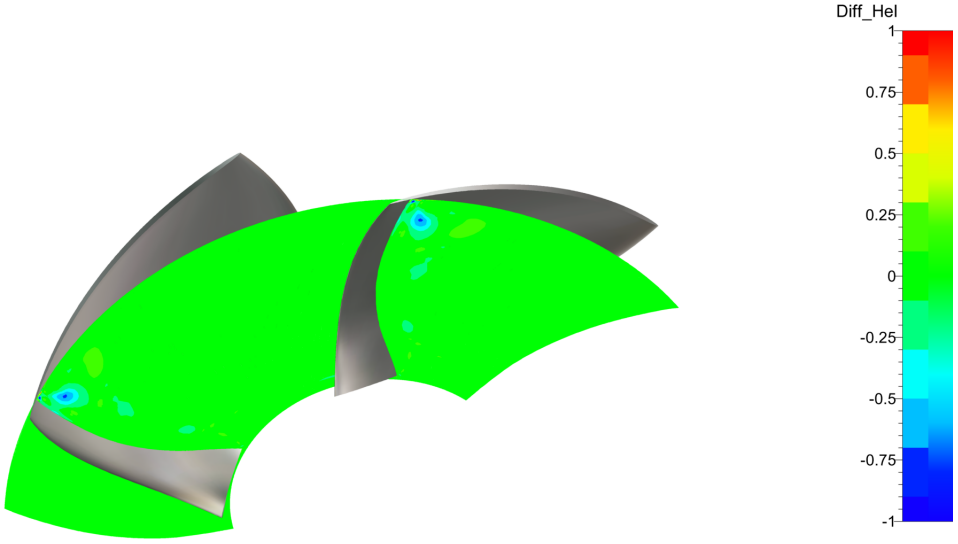

(c)

Figure 5.45 Normalized Helicity **(a)** in non-cavitating conditions and **(b)** at $\sigma_{-1\%}$ and **(c)** their difference plotted near the trailing edge of the blade (plane **3**).

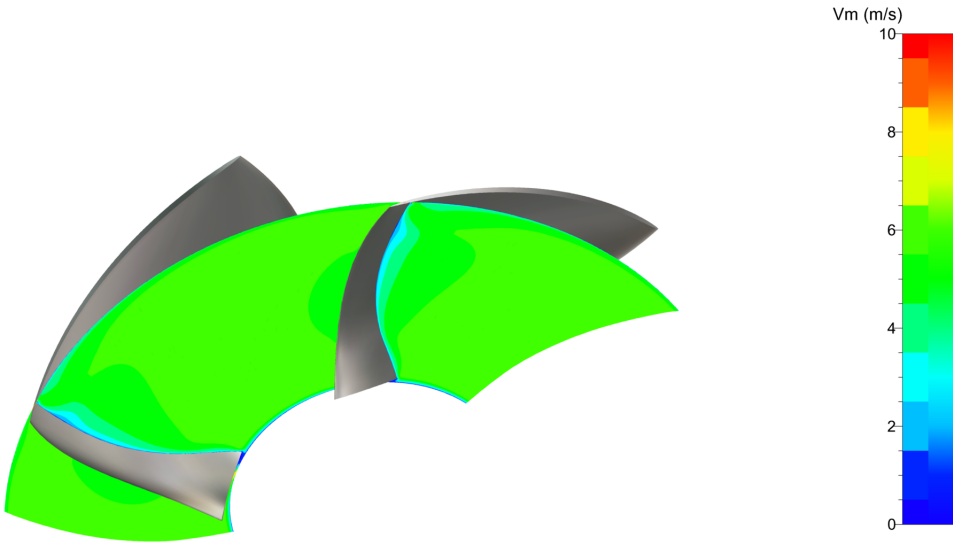

(a)

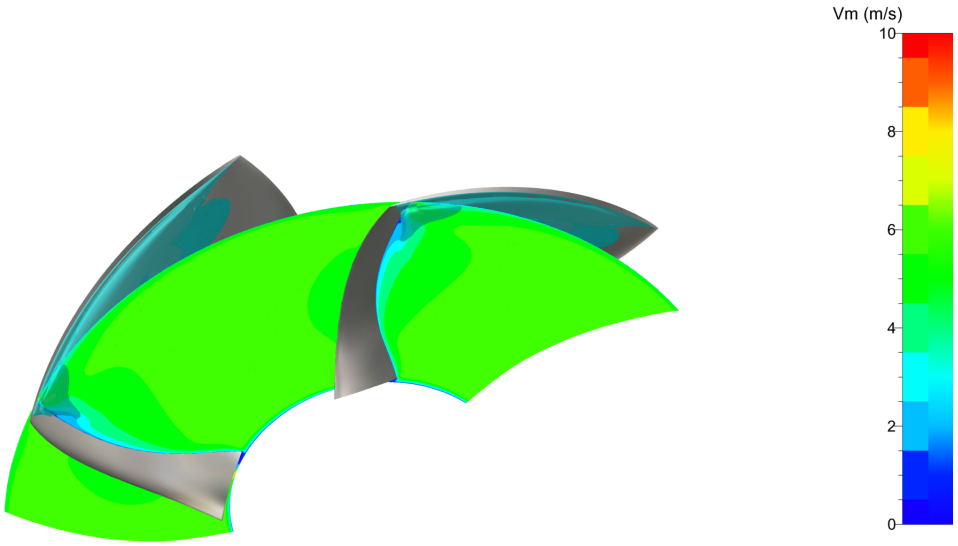

(b)

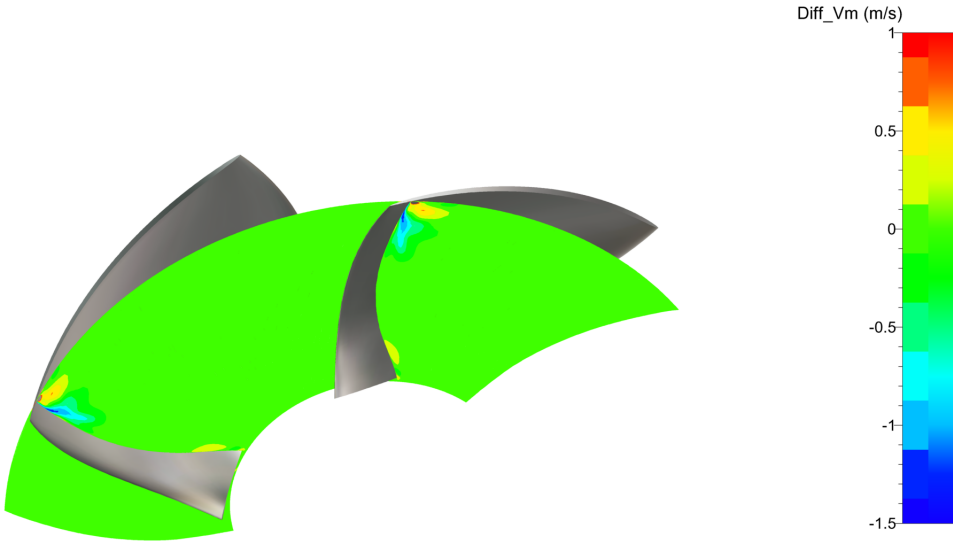

(c)

Figure 5.46 Meridian velocity **(a)** in non-cavitating conditions and **(b)** at $\sigma_{-1\%}$ and **(c)** their difference plotted near the trailing edge of the blade (plane **1**).

5.2.3.5 Cavitating flow analysis in the draft tube

The analysis of the losses evolution with the cavitation have been shown that the losses in the draft tube increase with the development of the cavitation. The evolution of the flow in the draft tube with the Thoma number reduction has been analyzed to investigate the influence of the cavitation in this part of the machine. Three points of the σ-break curve have been considered: the point in non-cavitating conditions, the efficiency drop starting point (σ_S) and the $\sigma_{-1\%}$.

Firstly, the evolution of the streamlines (plotted in figure 5.47), from the inlet to the outlet of the draft tube, has been investigated. Out of the cavitating regime (figure 5.47 a) the flow rate is

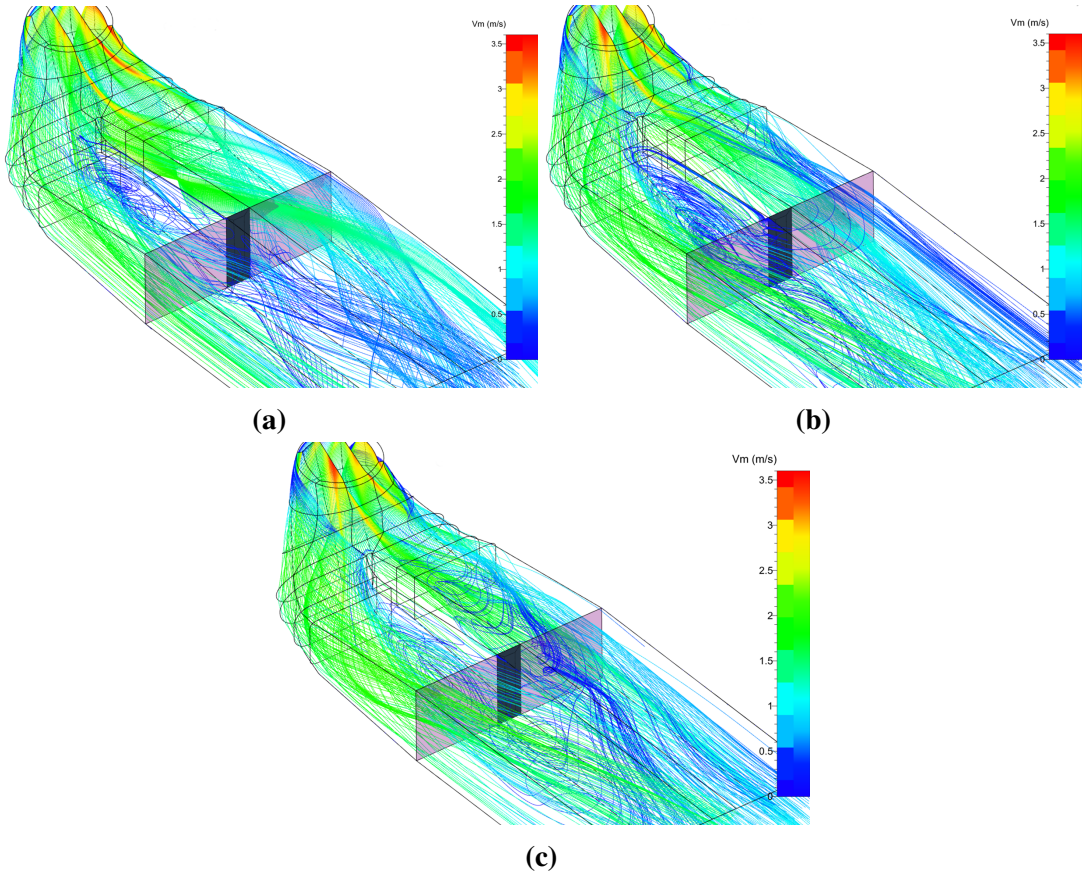

Figure 5.47 Streamline in the draft tube **(a)** in non-cavitating conditions, **(b)** at σ_S and **(c)** at $\sigma_{-1\%}$.

higher in the channel on the right. In the left channel, a recirculation zone is observed near the wall, slowing down the flow. Despite the presence of this vortex, the flow on the outlet is linear. When the efficiency starts to drop (figure 5.47 b), at σ_S, the flow in the right channel begins to slow down. The vortex in the left channel becomes more intense and wider, expanding towards the outlet. Localized backflow phenomena are observed on the outlet. At $\sigma_{-1\%}$ in figure 5.47 c, in the right channel, the flow slows down more and more and the first vortexes start to form.

On the contrary, the vortex in the left channel is almost completely disappeared. No backflow phenomena are observed on the draft tube outlet.

Also the normalized helicity (figure 5.48) and the meridional velocity (figure 5.49) have been analyzed in the last part of the draft tube on three different cuts, perpendicular to the flow direction : before the pier (section **1**), after the pier (section **2**) and just before the draft tube outlet (section **3**).

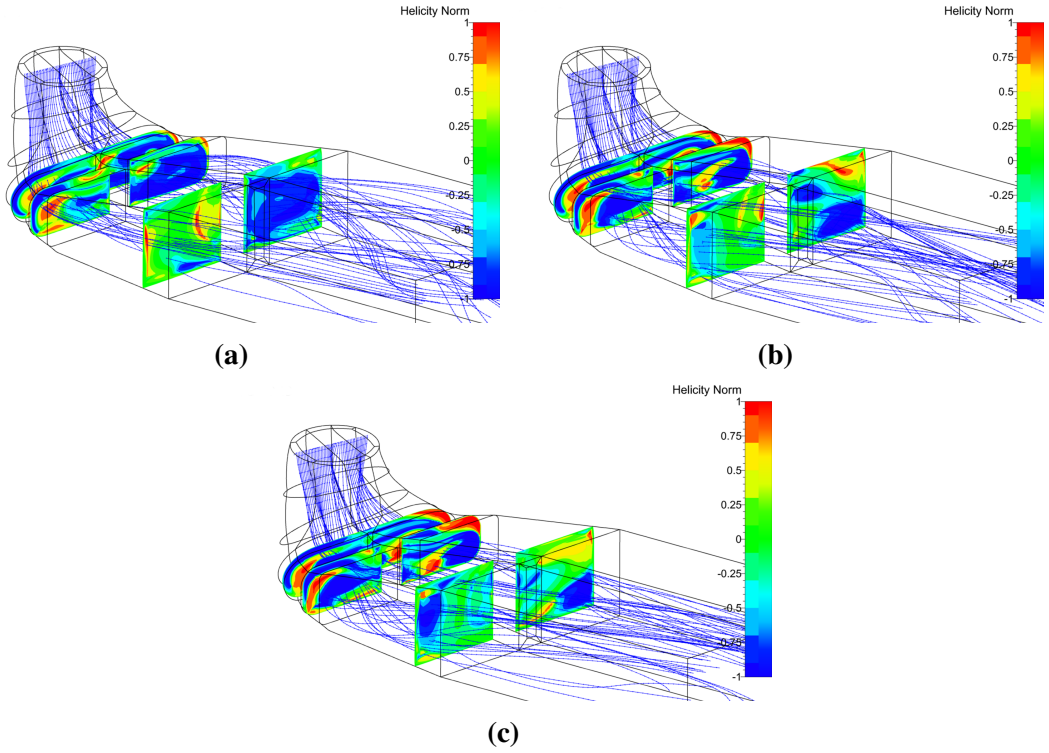

Figure 5.48 Normalized helicity plotted before **1** and after **2** the pier and **3** just before the draft tube outlet **(a)** in non-cavitating conditions, **(b)** at σ_S and **(c)** at $\sigma_{-1\%}$.

In non-cavitating regime (figure 5.48 a), the flow coming from the runner in section **1** is very chaotic. Great vortical structures characterized by negative and positive helicity values, are observed both near the wall and in the middle of the channel. In section **2**, the secondary structures on the left are almost unchanged while the positive helicity zone in the middle of the right channel disappeared. Close to the outlet (section **3**), the largest vortical structures are located in the right channel. The flow coming out from the left channel is almost uniform. Decreasing the σ value (figures 5.48 b and c), the main variation of the helicity field are observed mostly on **2** and **3**. In **2**, reducing the σ value, the vortex at positive helicity on the right channel grows. On the section **3**, as a consequence of the cavitation development, the vortex reduce on the right channel but increase on the left one.

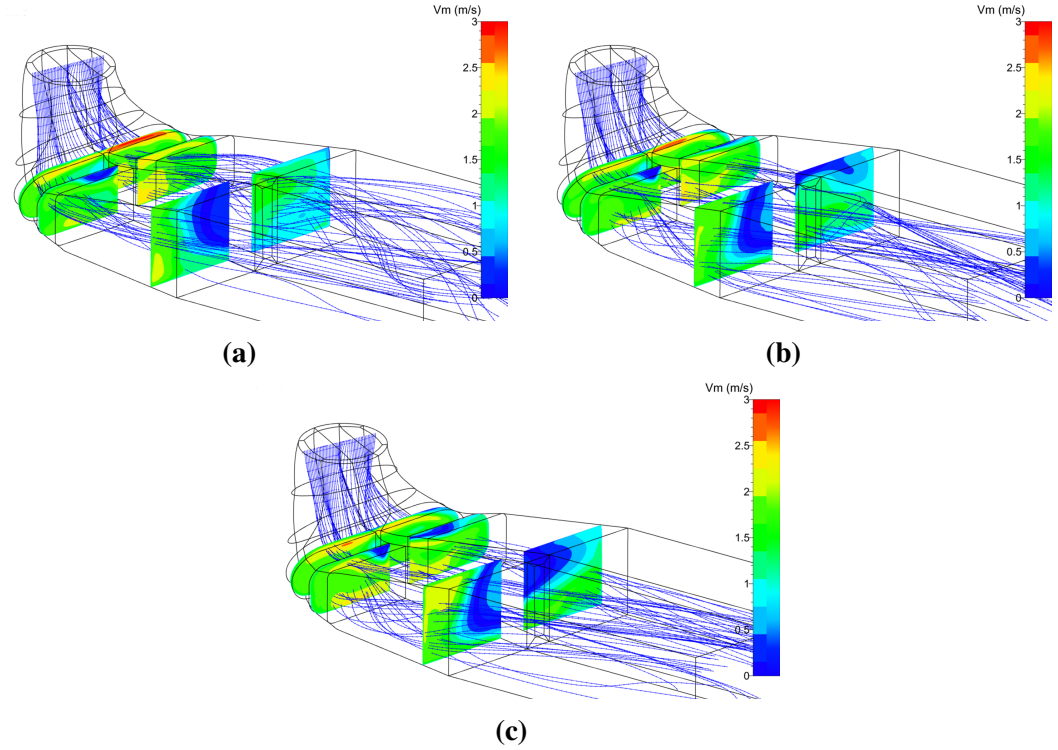

Figure 5.49 V_m plotted before **1** and after **2** the pier and **3** just before the draft tube outlet **(a)** in non-cavitating conditions, **(b)** at σ_S and **(c)** at $\sigma_{-1\%}$.

The analysis of the meridional velocity in the draft tube is very useful to visualize the partition of the flow in the two channels. In the first point of the σ-break curve (figure 5.49 a), the flow rate coming from the runner, before it separates in the two channels, is more on the right than in the left part of the section **1**. Deceleration zones are observed on the left channel, near the pier, on both sections **2** and **3**. With the reduction of the cavitation number (figures 5.49 b and c), the flow discharge in the inlet decreases on the right side, increasing on the left. The zones at V_m almost equal to zero, observed in the left channel in non-cavitating regime, become smaller and less intense. In the channel on the right deceleration regions appear in the efficiency drop starting point (figure 5.49 b) and they increase with the cavitation development (figure 5.49 c). Indeed, at $\sigma_{-1\%}$, the channel with the highest mass flow rate is the left. The observed deceleration regions are coherent with the vortical structures recognized in the streamlines analysis (figure 5.47). The evolution of the flow partition in the two channels accords well with the helicity field prediction (figure 5.48): more the secondary flows increase, more the discharge rate decreases.

Thus, the cavitation in the runner has an influence on the flow in the draft tube. In particular, more the cavitation structures in the runner increase, more the vortex structures in the draft tube getting stronger and after decrease, passing from a channel to the other one. As a consequence,

the flow partition between the two channels is modified during the cavitation development changing the performances values. However, it is important to keep in mind that steady analysis represent only a single position of the runner blades. In order to improve the cavitating flow numerical reproduction in the draft tube, unsteady simulations are required.

5.3 Chapter conclusions

In order to develop a numerical methodology able to predict the cavitation evolution inside a Kaplan turbine and the consequence on the machine performances, the optimal load operating point OP_1 has been analyzed in steady conditions.

Preliminary simulations performed on the reduce domain D_1 have been shown that the best agreement between numerical results and measurements is achieved refining the mesh and using the $k-\omega$ SST turbulence closure. However, the computed performance values still differ from the experimental data.

Thus, to approach the numerical operating point to the real one, an iterative procedure has been applied: the mass flow rate value on the inlet has been changed targeting the experimental torque. This parameter has been chose in order to obtain a fluid dynamic agreement with experiments since it is strictly linked to the flow incidence on the runner blade. A reduced difference between experimental and numerical torques ensures the correct reproduction of the turbine work. As a consequence of the inlet boundary condition modification, the mismatch between the numerical prediction and the measurement of the global quantities and of the velocity fields on the runner outlet has been reduced but the reproduction of the cavitating flow behavior has been deteriorated. The inadequate prediction of the flow in cavitating conditions results from a discrepancy between the numerical and experimental operating point at lowest sigma values.

To approach the computational domain to the real geometry the draft tube has been considered in the analysis and its influence on the flow has been investigated. Results in non-cavitating conditions have been shown that the presence of the draft tube affects the velocity profiles on the runner outlet and the losses distribution in the machine changing the performance values. The draft tube influence also the cavitating flow altering the evolution with the σ reduction of the global quantities and of the cavitation structures. So it is fundamental to include the draft tube in the analysis to achieve a correct simulation of the flow in the machine.

On the other hand, the mass flow rate imposed on the inlet of the domain does not allow to adequately reproduce the experimental conditions. Indeed, during cavitation break down laboratory tests, the machine head is imposed while the mass flow could vary. Thus, a new inlet boundary condition has been proposed instead of the classical one: the total pressure.

Imposing the total pressure on the inlet the prediction of the non-cavitating and cavitating flow is improved. The discrepancy between numerical and measured velocity distributions on the runner outlet has been reduced. During the cavitation development the head is fixed allowing to obtain performance curves with the same overall aspect of the experimental ones. The predicted σ value after the efficiency drop starting point are still higher than the measured ones. In order to try to reduce this difference and to improve the reproduction of the cavities structures unsteady simulations are required.

Chapter 6

Unsteady investigation

The steady investigation of the optimal load operating point OP_1 reported in chapter 5 has allowed to define a numerical methodology able to predict the cavitation development in the machine and to perform first analyses of the flow.

The scopes of the unsteady simulations that will be presented in this chapter was firstly to try to reduce the discrepancy between predicted and measured σ values in developed cavitation conditions and, secondly, to improve and complete the cavitating flow analyses. Furthermore, in order to test the generality of the calculation strategy, the full load operating point OP_2 is also investigated. Differently from the design operating conditions, this point is characterized by a very unstable flow making the steady simulations impossible.

6.1 Unsteady investigation of the optimal load point ($OP1$)

In the unsteady regime, only 6 points of the σ–break curve of OP_1 (reported in blue in figure 6.1) of the 8 considered in the steady analysis have been investigated. The calculation domain now also includes the guide vanes and the runner blades (domain D_3 presented in chapter 4). The used computational parameters are summarized in table 6.1.

Table 6.1 Numerical parameters used to perform the unsteady calculations on the optimal load operating point OP_1.

Domain	Mesh	Inlet BC	Outlet BC	Turbulence model	Cavitation model	Δt	$\Delta\tau$
D_3	M_4	P_{tot}	$P_{out} = P_{amb}$	$k-\omega$ SST	Barotropic law	1°	20

The same analyses of the cavitating flow presented in the steady case have been performed. The evolution of the machine performances, the vapor structures on the runner blade and the cavitating flow in the draft tube computed in the unsteady case have been compared with the steady results. In addition, the pressure fluctuations in the cone have been also analyzed.

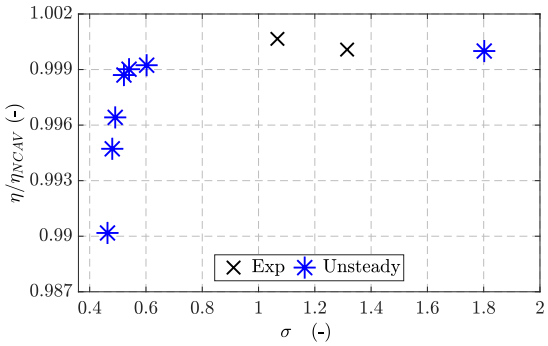

Figure 6.1 Experimental σ-break curve for OP_1. The points indicated by the blue stars are considered in the unsteady analysis.

6.1.1 Comparison of the performances and cavities structures predicted in steady and unsteady regimes

For unsteady case, the characteristic quantities of the machine, i.e., T, H and Q have been evaluated as the average of each time step over 3 turbine rotations. Considering that in this operating point the flow in non-cavitating conditions is very stable, the global quantities fluctuations are very small. So, the difference between the averaged quantities evaluated in unsteady regime and the corresponding values computed in steady conditions results to be less than 0.2%.

In figure 6.2, the σ-break curve plotted from unsteady results is compared with the steady curve and experimental data. The overall aspect of the two computed curves is very similar. Slight improvements in the σ values prediction are observed in developed cavitation conditions.

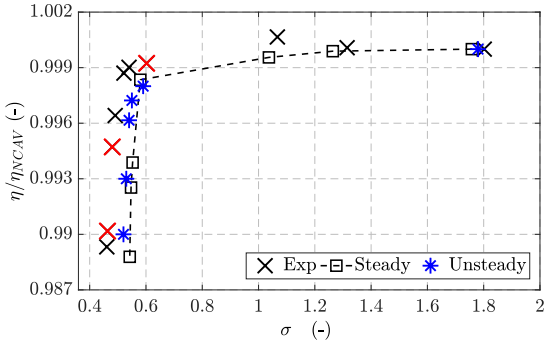

Figure 6.2 Comparison between measured (plotted by black crosses) and computed σ-break curve in steady (black dashed line with squares) and unsteady conditions (blue stars).The experimental points σ_s, $\sigma_{-0.5\%}$ and $\sigma_{-1\%}$ are plotted with red crosses.

Indeed, in the unsteady conditions, the discrepancy between the calculated and the measured Thoma number values at $\sigma_{-0.5\%}$ and at $\sigma_{-1\%}$ has been reduced of the 4% with respect to the

steady results. Also the torque values predicted in unsteady regime (figure 6.3 a) are close to the steady ones. Main differences are observable in the mass flow prediction (figure 6.3 b). For unsteady results at $\sigma_{-0.5\%}$ ($\sigma = 0.53$) the Q value decreases considerably, deviating from the experimental data, whereas at $\sigma_{-1\%}$ ($\sigma = 0.52$) the mass flow starts to increase following the experimental trend better than the steady case.

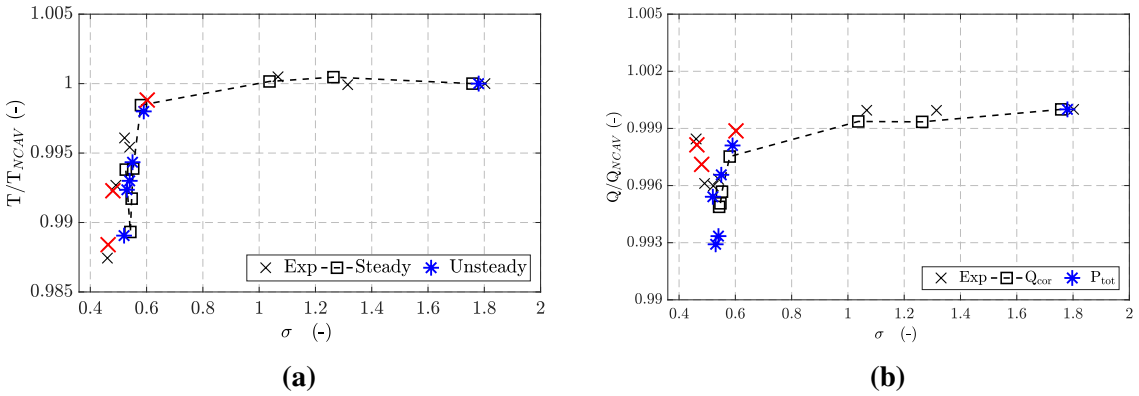

(a) **(b)**

Figure 6.3 (a) The torque and **(b)** the mass flow rate evolution with the σ reduction measured (black crosses) and computed in steady (black dashed line with squares) and unsteady (blue stars) conditions. The experimental points σ_s, $\sigma_{-0.5\%}$ and $\sigma_{-1\%}$ are plotted with red crosses.

The evolution of the vapor structures during a runner rotation at σ_s (figure 6.6) and at $\sigma_{-0.5\%}$ (figure 6.7) are compared with the iso-density surfaces computed in the steady simulations and with the experimental observations (reported in figure 6.4 and figure 6.5, respectively). The cavities predicted in unsteady conditions at σ_s and $\sigma_{-0.5\%}$ have the same shape, extension and position of the vapor structures computed in the steady case at the same points (figures 6.4 b and 6.5 b). In both of the analyzed points of the σ-break curve, the vapor structures at the tip and at the root of the blade do not change during the runner rotation.

From the experimental visualizations shown in figure 6.8 it is possible to observe that the cavity sheet on the blade root is not exposed to a clear volume change during the runner rotation, while the vapor structure on the tip is almost a vortex that leaves the blade surface, makes a turn and then approaches the blade surface again.

Moreover, the numerical method applied in this work does not allow to simulate the vapor shedding. On the other hand, the position and the overall shape of the cavities is correctly predicted.

It is then possible to conclude that due to the steady character of the flow in the optimal load operating point, the introduction of the time in the governing equations leads only to marginal improvements in the prediction of the performance evolution with the cavitation development.

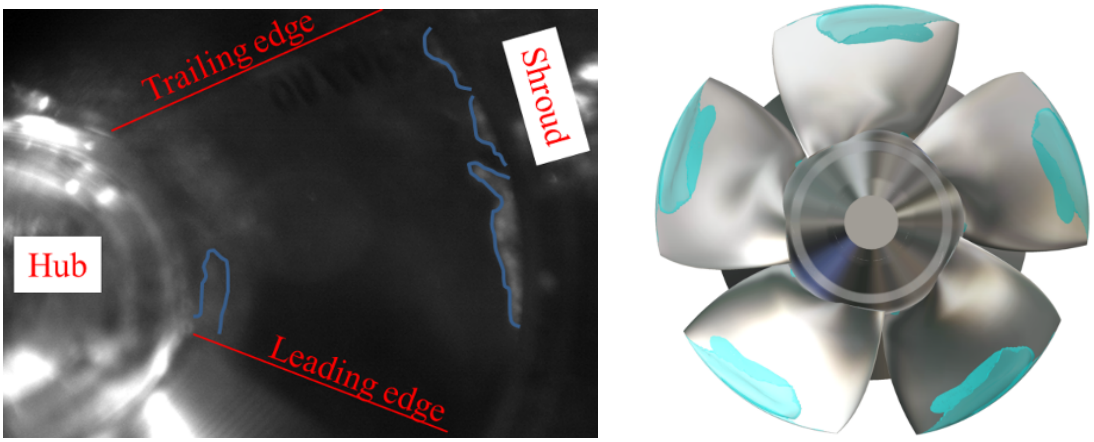

(a) **(b)**

Figure 6.4 **(a)** Experimental vapor structure ($\sigma_s = 0.602$) and **(b)** computed iso-density surfaces ($\rho = 980\ kg/m^3$) in steady conditions($\sigma_s = 0.580$).

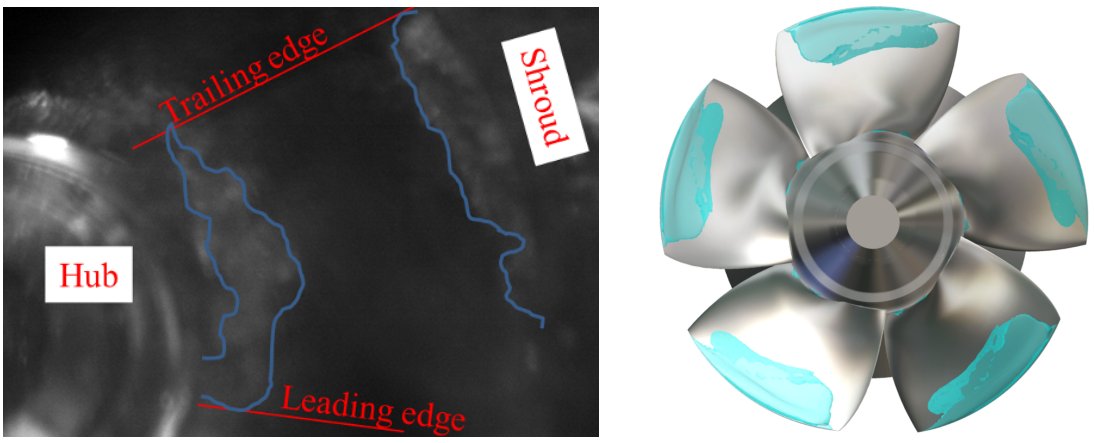

(a) **(b)**

Figure 6.5 **(a)** Experimental vapor structure ($\sigma_{-0.5\%} = 0.480$) and **(b)** computed iso-density surfaces ($\rho = 980\ kg/m^3$) in steady conditions($\sigma_{-0.5\%} = 0.560$).

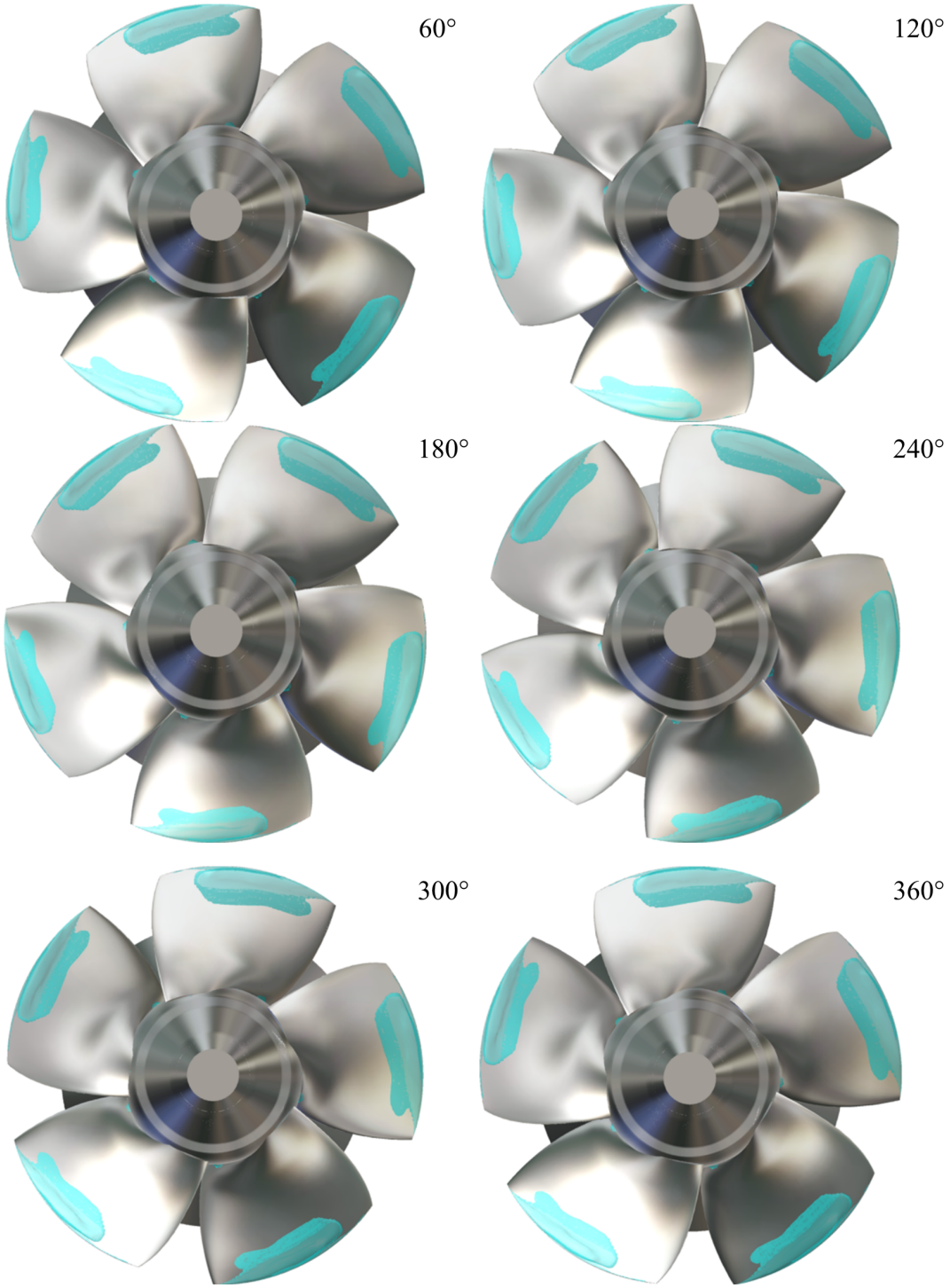

Figure 6.6 Iso-density surfaces ($\rho = 980\ kg/m^3$) computed in the unsteady conditions at σ_s ($\sigma = 0.590$) during a runner rotation each 60°.

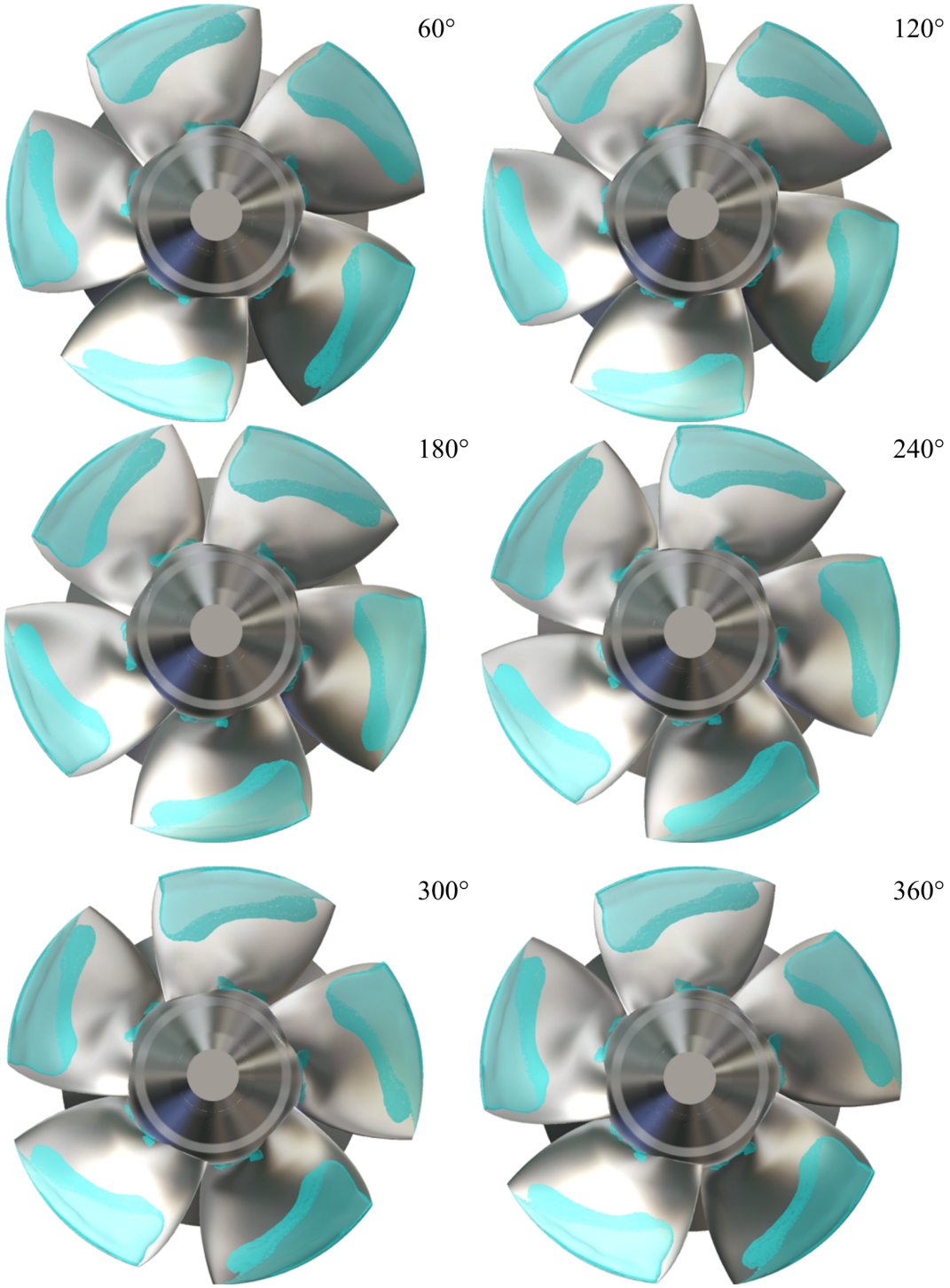

Figure 6.7 Iso-density surfaces ($\rho = 980\ kg/m^3$) computed in the unsteady conditions at $\sigma_{-0.5\%}$ ($\sigma = 0.530$) during a runner rotation each 60°.

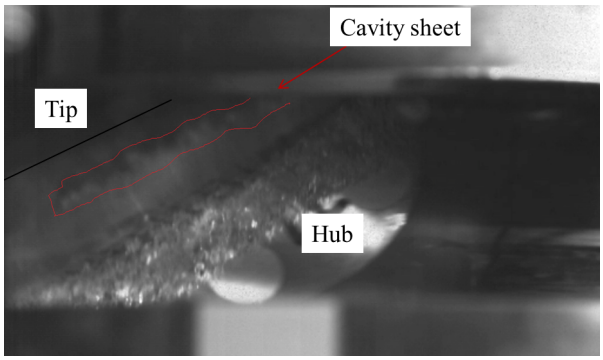

Figure 6.8 Experimental visualization of the tip vortex cavitation at $\sigma_{-0.5\%} = 0.480$.

6.1.2 Comparison of the cavitating flow in the draft tube in steady and unsteady regimes

The steady analyses presented in Chapter 5 have shown that the development of the cavitation influences also the flow in the draft tube. In particular, the presence of cavities on the runner blades modifies the vortices and the flow partition in the two channels of draft tube. Furthermore, a steady calculation is representative only of a single runner blades position. Therefore, to

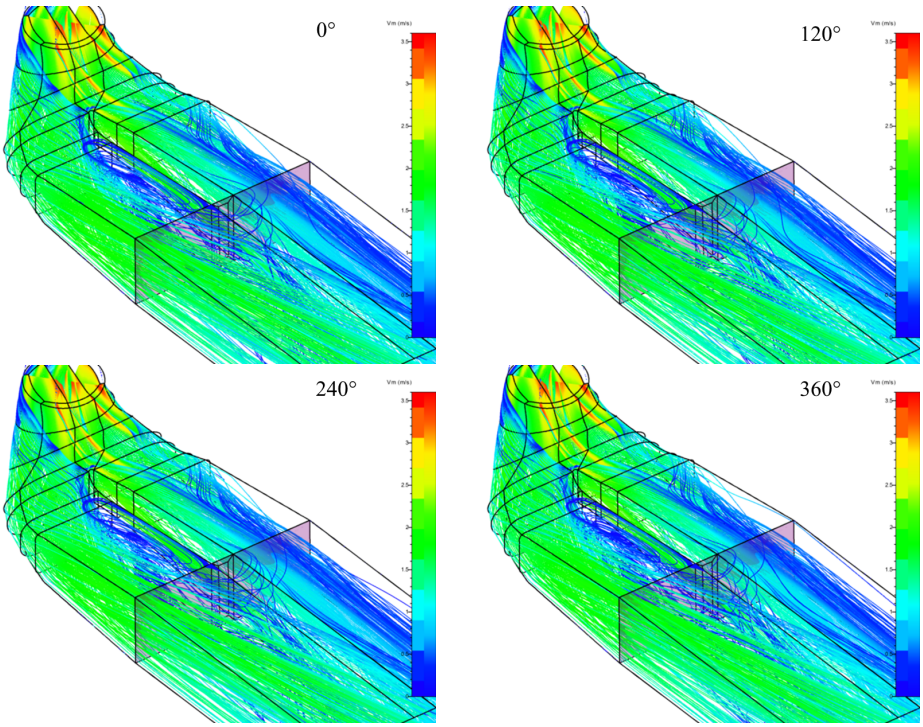

Figure 6.9 Streamlines evolution in the draft tube in non-cavitating conditions during a runner rotation each 120°.

further investigate this phenomena, the evolution of the stream lines in the draft tube during a rotation of the runner, in non-cavitating and in cavitating conditions has been analyzed. The

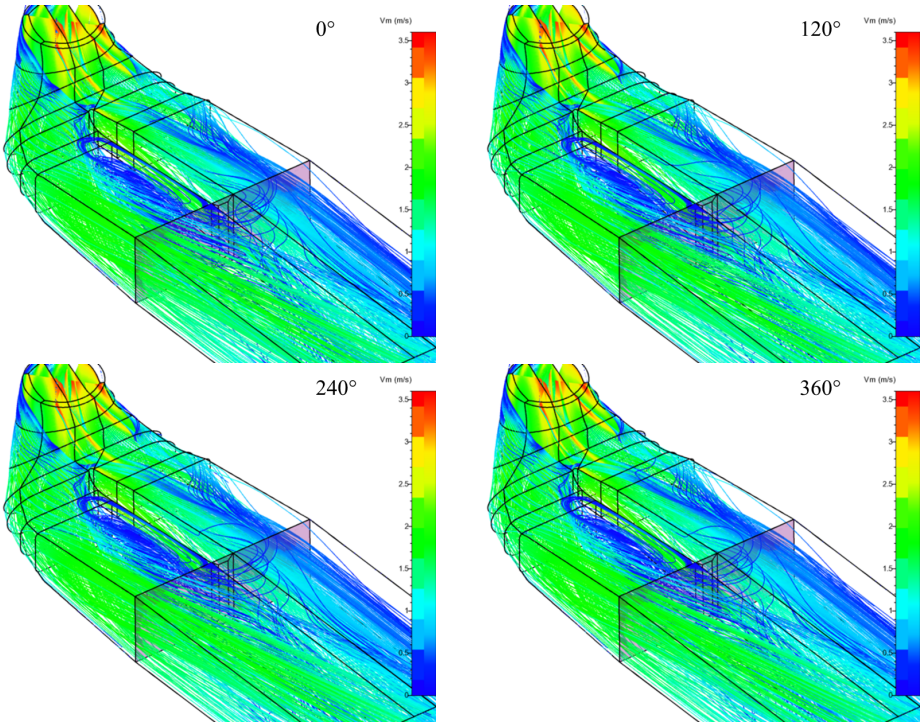

Figure 6.10 Streamlines evolution in the draft tube at $\sigma_s = 0.590$ during a runner rotation each 120°.

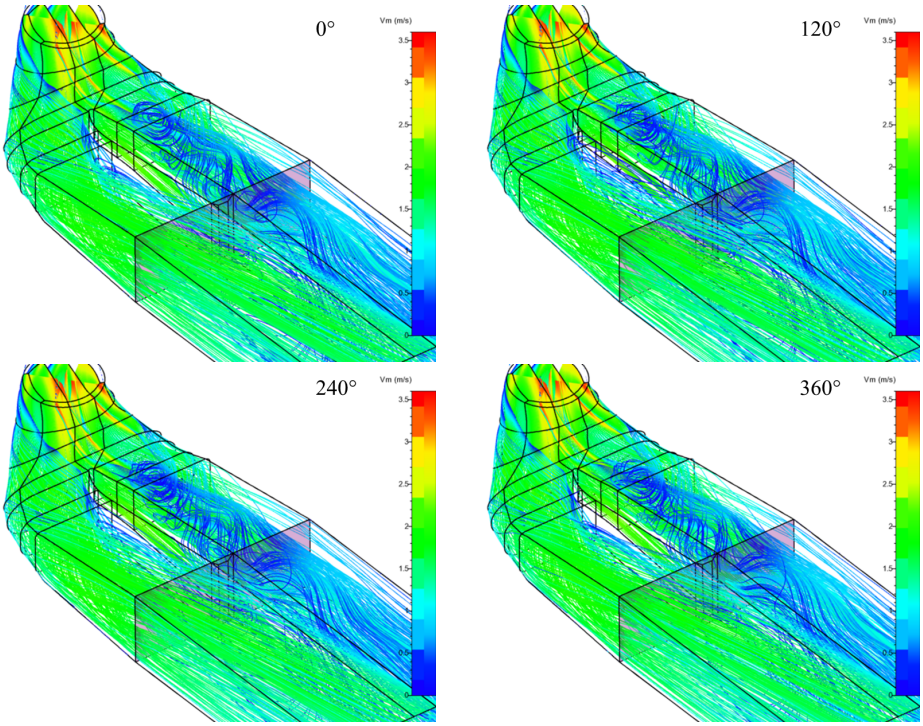

Figure 6.11 Streamlines evolution in the draft tube at $\sigma_{-1\%} = 0.520$ during a runner rotation each 120°.

points of the σ-break curve considered in the unsteady regime are the same investigated for the steady conditions: the first point (non-cavitating conditions), the efficiency drop starting point (σ_s) and at $\sigma_{-1\%}$. For each one of these points, four instant of time have been considered.

For all conditions, the flow in the draft tube is very stable: the vortical structures computed in the steady regime (see chapter 5) are observed also in the unsteady conditions. In non-cavitating conditions (figure 6.9), the vortex on the left channel is more extended than the one predicted with steady simulations, reaching the outlet of the draft tube. As a consequence, backflow phenomena are observed in the outlet section which have not been identified by steady calculations.

At σ_s (figure 6.10) when the first cavities structures begin to appear on the tip and on the root of the blade, according to the steady prediction, the vortex in the left channel expands and the back flow phenomena observed on the outlet, in non-cavitating conditions, become more intense. On the contrary, the deceleration of the flow observed in the steady analysis is not observed in the unsteady case.

At $\sigma_{-1\%}$, the unsteady results (figure 6.11) are in good agreement with the steady prediction: the vortex on the left channel is almost completely disappeared and the flow accelerates while a vortical structure begins to form in the right channel. The flow on the outlet is no more affected by the backflow phenomena.

So according to these results, the influences on the draft tube flow of the cavitation phenomena occurring in the runner which have been observed in the steady analysis has been confirmed also by the unsteady analyses.

6.1.3 Analysis of the pressure fluctuations

The main advantage of the unsteady analysis is the possibility to investigate the temporal fluctuations of the flow characteristic quantities, i.e. the pressure, the torque, etc.

The pressure fluctuations have been measured below the runner for 3 points of the σ-break curve: in non-cavitating conditions, at the efficiency starts drop point (σ_s) and when the efficiency is reduced of 1% ($\sigma_{-1\%}$). Four pressure taps have been located on the discharge ring, downstream of the runner blade, at 120 *mm* from blades axis (figure 6.12 a). The position of the pressure sensors on the circumferential section are reported in figure 6.12 b.

Indicating with f_0 the runner rotation frequency, the sample frequency used is equal to $f = 156\ f_0$ corresponding to a blade rotation of 4.5°. The pressure signals have been recorded along 360 rotation of the runner. More informations about the experimental setup are reported in chapter 3.

To identify the most energetic frequencies of the pressure signal a fast Fourier transform (FFT) has been applied. The amplitudes have been normalized by the the experimental head

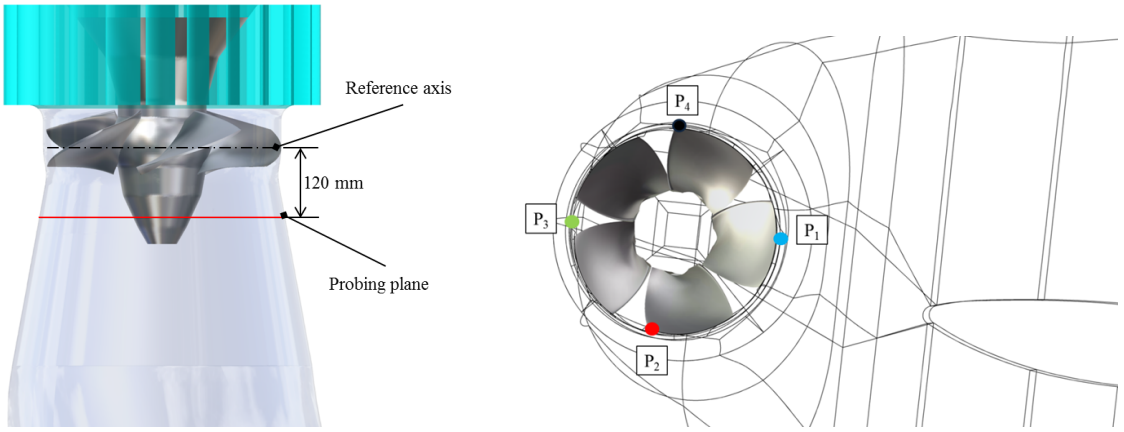

(a) **(b)**

Figure 6.12 The Position of the experimental four pressure taps**(a)** with respect to the reference axis and **(b)** on the runner circumferential section.

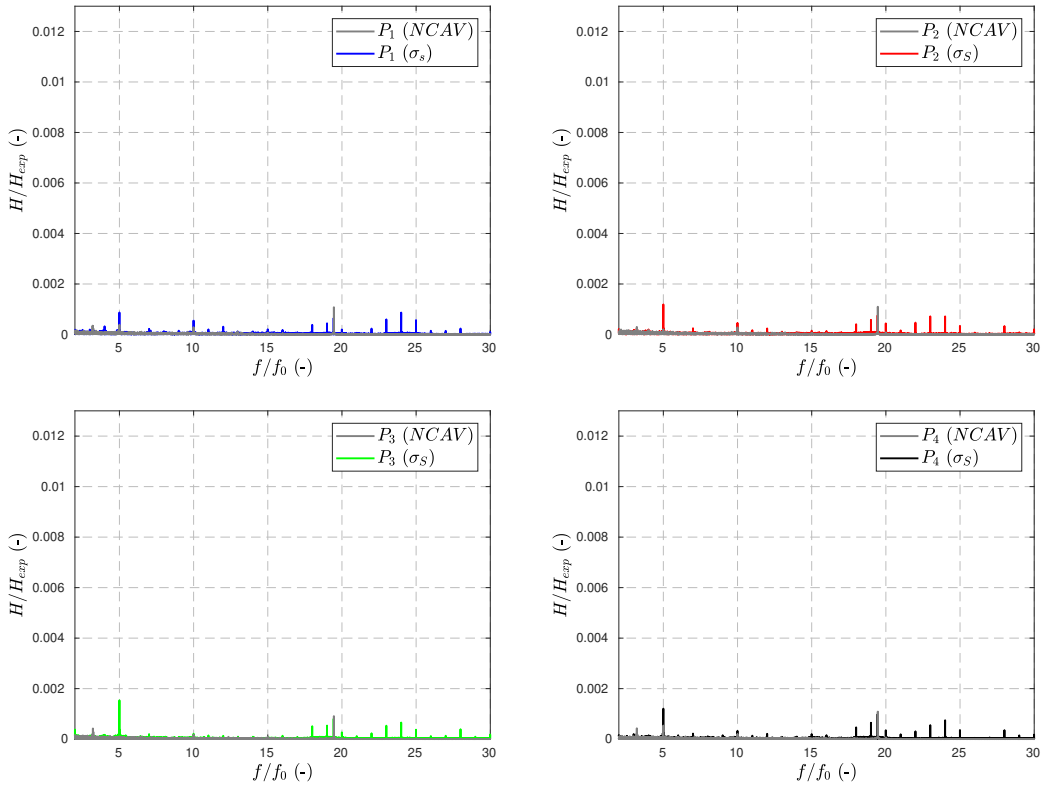

Figure 6.13 Measured pressure spectra in non-cavitating conditions at $\sigma_s = 0.602$. The frequencies are normalized by the runner rotation frequency f_0. The amplitude is divided by the experimental head H_{exp}.

value (H_{exp}). The study of vibrations, acoustic emissions and dynamic-pressure levels in the high frequency range is a well-known technique to detect cavitation activity (see [15]). The amplitude of a given frequency band can be compared for various points of the σ-break curve. Considering that the main objective is to recognize the signature of the cavitation, the signal spectrum in non-cavitating conditions is used as reference for the others two points. In all cases the signals have been cut to a frequency $f = 30\ f_0$ since in the experiments no interesting phenomena have been found in the high frequency region.

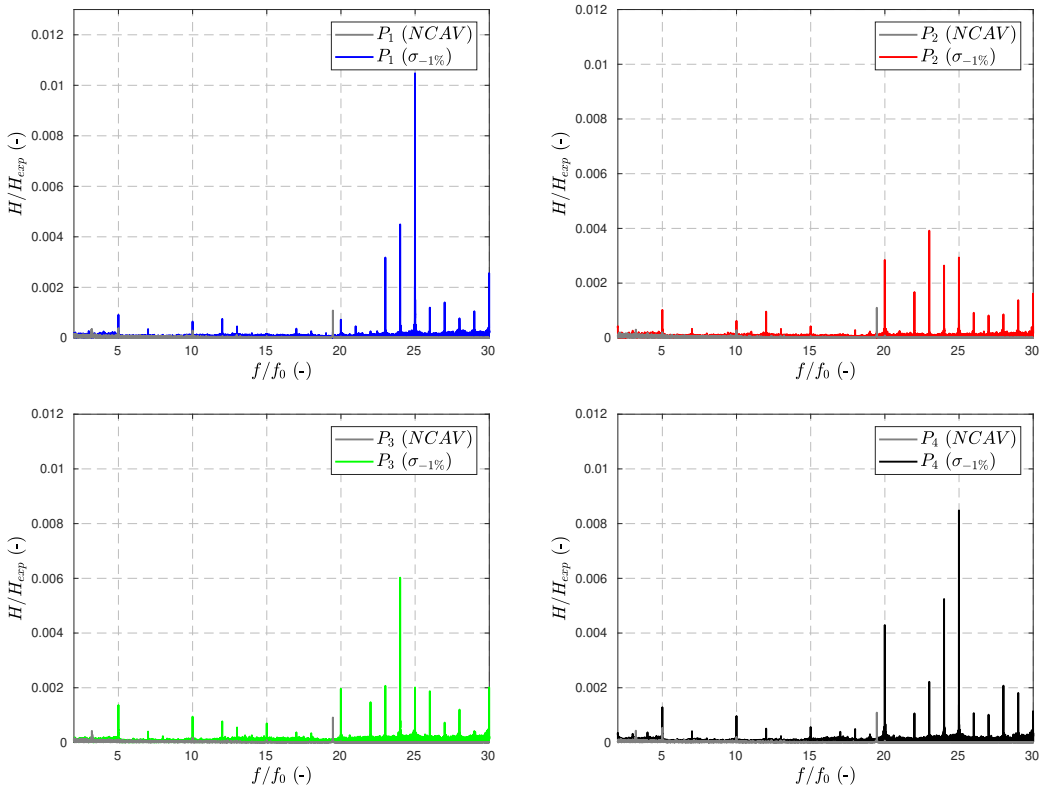

Figure 6.14 Measured pressure spectra in non-cavitating conditions and at $\sigma_{-1\%} = 0.460$. The frequencies are normalized by the runner rotation frequency f_0. The amplitude is divided by the experimental head H_{exp}.

At σ_s, first cavitation structures appear on the tip and on the root of the blade (figure 6.6). In the frequency domain, at the same point (figure 6.13) a very low intensity peaks are observed in all the four spectra between $f = 20\ f_0$ and $f = 26\ f_0$, close to the guide vane passing frequency ($f = 24\ f_0$). The most energetic peak is identified at $f = 5\ f_0$ corresponding to the runner passing frequency. In developed cavitation conditions at $\sigma_{-1\%}$ (figure 6.14), the intensity of the peaks in the range between $20\ f_0$ and $26\ f_0$ increases and the most energetic peak is located at $f = 24\ f_0$. This is evident mostly on the pressure taps P_1 and P_4. The intensity of the peak at $f = 5\ f_0$ does not change with the increase of the vapor amount in the runner.

To compare the experiments with the numerical simulations, four control points have been located in the numerical domain in the same position of the pressure taps. The sample frequency chosen in the simulations is $f/f_0 = 360$ corresponding to a blade rotation of 1°. To limit the computational costs, the pressure signal have been computed only for a single runner rotation. The experimental and the numerical spectra have been normalized by the highest computed and

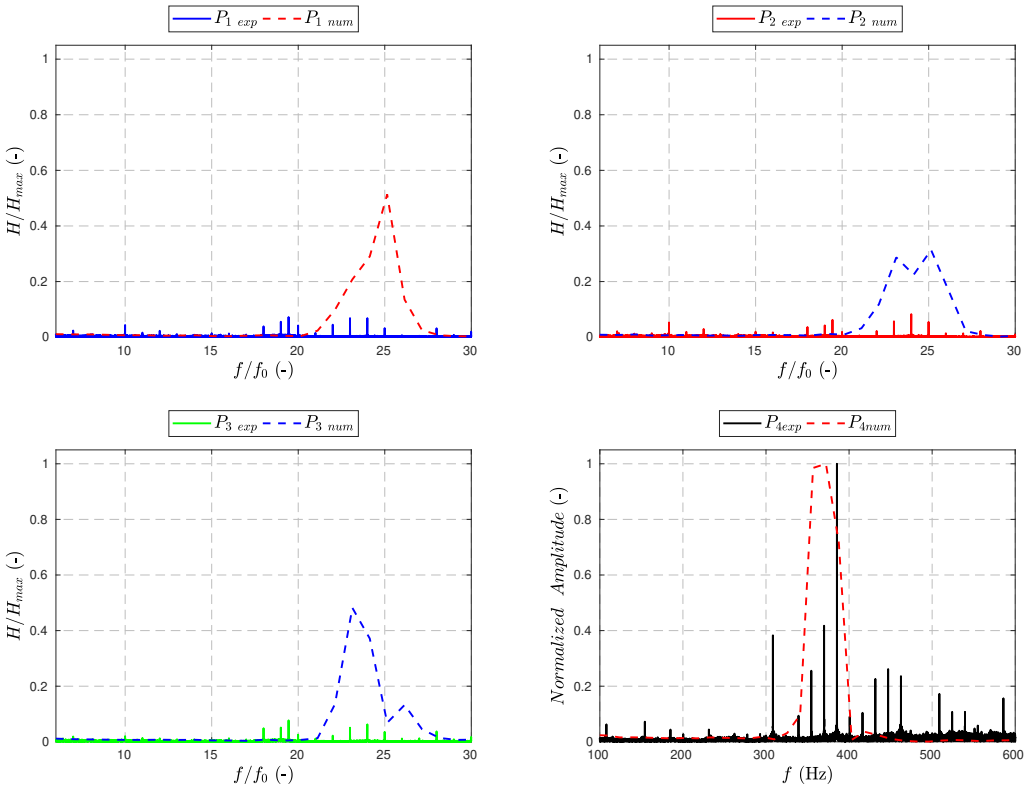

Figure 6.15 Comparison between computed and measured pressure spectra in the OP_1 at σ_s. The frequencies are normalized by the runner rotation frequency f_0. The amplitudes are normalized by highest computed and measured peak value, respectively.

measured peak value, respectively. The simulations show that the pressure starts to fluctuate when the cavitation phenomena begin to occur. At σ_s (figure 6.15), in all the four spectra, a single peak appears at 24 f_0, which corresponds to the guide vane passing frequency. At $\sigma_{-1\%}$ (figure 6.16) the amplitude of this peak increases. In agreement with the experimental measurements, the most energetic peaks are observed in the control points P_1 and P_4. However, the peak measured experimentally at 5 f_0 is not identified in the computed spectra. This could be due to the reduced length of the numerical signal and to the use of the URANS model that does not allow to simulate turbulence phenomena.

In both cavitating conditions, the computed peaks are overestimated but the overall shape of the numerical spectra is in good-agreement with the experimental data. The pressure

fluctuations increase with the development of the vapor structures nearby the guide vane passing frequency. Considering that the pressure transducers are located on the runner shroud, one could imagine that the rotor/stator interaction and the tip cavitation are linked. In the previous study proposed by Nennemann and Vu [73] has been demonstrated that in a Kaplan turbine the pressure amplitudes at the guide vane passing frequency are amplified in the tip cavities proximity. The flow on the guide vane trailing edge is not circumferential uniform. This uniformity is more pronounced near the guide vane discharge ring, where the change of direction of the flow entering in the runner is stronger. Due to the characteristic geometry of the Kaplan turbine, the streamlines originated near the bottom ring at the guide vane remain in the machine periphery.

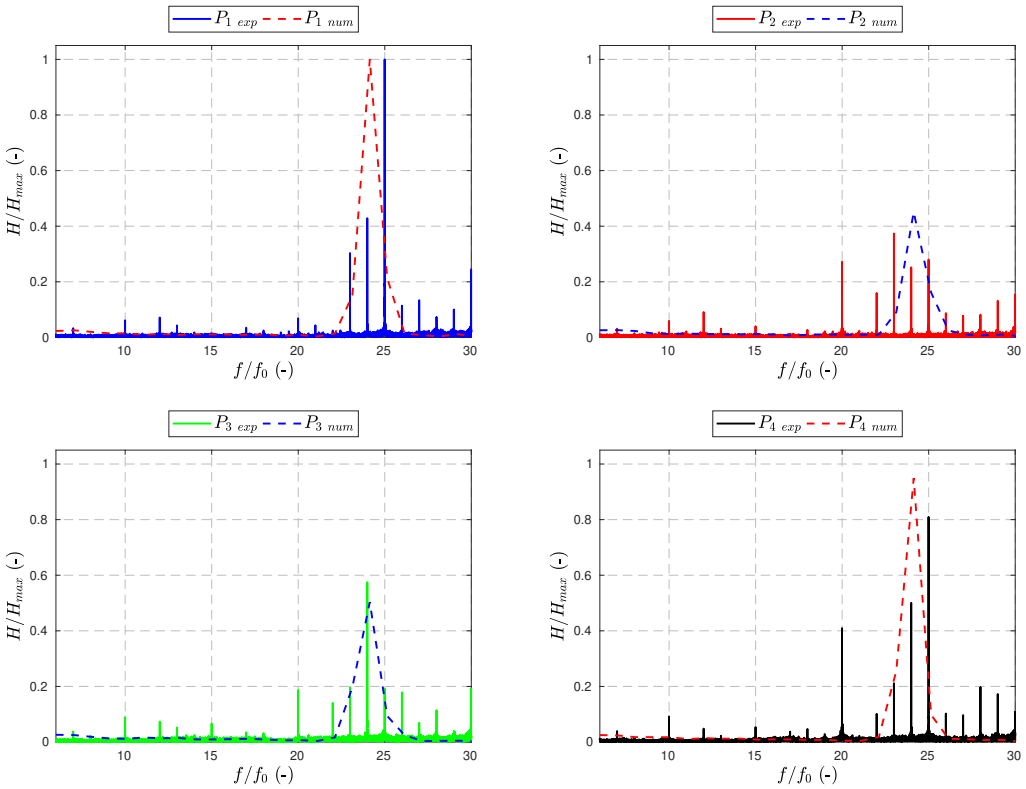

Figure 6.16 Comparison between computed and measured pressure spectra in the OP_1 at $\sigma_{-1\%}$. The frequencies are normalized by the runner rotation frequency f_0. The amplitudes are normalized by highest computed and measured peak value, respectively.

So the non-uniformity observed in the guide vane trailing edge gets transported into the lowest pressure area of the runner, i.e. the blade tip and the shroud gap, originating vortices and cavitation phenomena. The vapor structures further emphasize the non-uniformity of the flow in these regions, increasing the pressure fluctuations at guide vane passing frequency downstream. In the present work, both experiments and simulations have shown that reducing

the Thoma number the vapor structure on the tip expands along the blade length in the trailing edge direction (see figures 6.4 and 6.5). The development of the cavitation in the tip region could explain the increase of the peaks at $f = 24\ f_0$. As stated by Motycak et *et al.* [14], the tip cavitation does not have a great influence on the turbine efficiency but causes the cavitation pitting. The torque reduction is mainly due to the tip clearance flows and to the surfaces cavitation phenomena, i.e. the hub and the leading edge cavitation, as has been explained in the steady analysis 5. In order to find a signature of the cavitation structures responsible of the performance variation, analyses of the pressure fluctuations in other points of the turbine (i.e. the runner blade and the guide vane outlet [85], [76]) and of the torque spectra are required.

In conclusion the unsteady simulations have led only to marginally improve at the cavitation prediction methodology. On the other hand, the unsteady approach has allowed to confirm the results of the steady analyses in terms of evolution with the σ reduction of the cavities on the runner blades and of the vortical structures in the draft tube. The investigation of the pressure fluctuations has highlighted the existence of a correlation between the rotor/stator interaction and the cavitation development, finding a probable signature of the tip vortex cavitation. Further investigation of the cavitating flow are required in order to finally validate the results of the pressure spectra analysis.

6.2 Unsteady investigation of the full load point ($OP2$)

The validated unsteady numerical methodology is now applied to the full load operating point, OP_2. Contrarily to the OP_1, in the OP_2 the machine works out of these design conditions. Hence, the flow in the turbine is characterized by stronger pressure gradients, recirculation phenomena and unsteady vapor structures. Steady calculations are not longer suitable to correctly reproduce the flow in the machine in both non-cavitating and caviting regimes so only URANS calculations have been performed. Six points of the OP_2 σ-break curve (indicated by the blue stars in figure 6.17) have been analyzed. The guide vane opening (γ) and the blade angle (α) have been changed obtaining the numerical domain D_4 (see chapter 4). The simulations setup is recalled in the table 6.2.

Table 6.2 Numerical parameters used to perform the unsteady calculations on the full load operating point OP_2.

Domain	Mesh	Inlet BC	Outlet BC	Turbulence model	Cavitation model	Δt
D_4	M_5	P_{tot}	$P_{out} = P_{amb}$	$k-\omega$ SST	Barotropic law	1°

At first, the results of the unsteady calculations have been validated in non-cavitating regime comparing numerical and experimental performances values and velocity profiles on the runner outlet. Then, investigations in cavitating conditions have been performed trying to reproduce

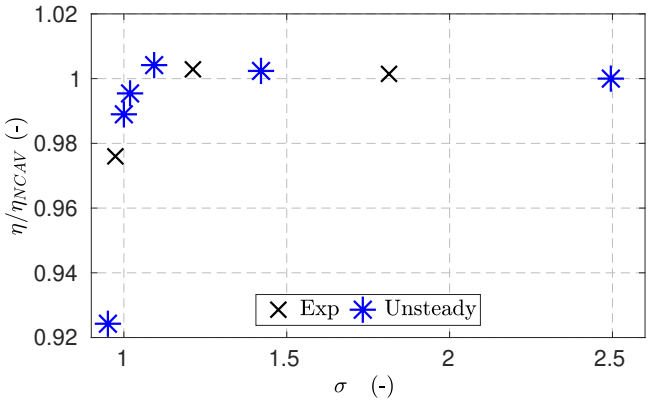

Figure 6.17 Points of the experimental σ-break curve computed in the unsteady conditions (reported by the blue stars).

the cavitation curves, the vapor structures and the pressure fluctuations observed during the experiments.

6.2.1 Analyses in free-cavitation regime

At first, unsteady simulations have been performed in free-cavitating regime imposing the experimental discharge value as inlet boundary condition ($Q = Q_{exp}$). In order to compare experimental and numerical performances, the computed values have been evaluated by the average of each time step over 5 turbine rotations. The results obtained are reported in table 6.3, in terms of difference from the experimental data.

Table 6.3 Performance parameters computed on D_4 imposing $Q = Q_{exp}$ on the inlet.

Inlet BC	$\Delta T = \frac{(T_{exp} - T_{num})}{T_{exp}}$	$\Delta H = \frac{(H_{exp} - H_{num})}{H_{exp}}$	$\Delta\eta = \frac{(\eta_{exp} - \eta_{num})}{\eta_{exp}}$
$Q = Q_{exp}$	14%	11%	17%

As observed for the calculations in the OP_1, imposing Q_{exp} at the inlet of the domain leads to a discrepancy between the calculated and the measured performances (T, H and η). This means that the numerical operating conditions differ from the experimental ones. Moreover, the mass flow on the domain outlet is 2% higher than the inlet value, so obtaining the numerical convergence with this inlet boundary condition value is more difficult that the OP_1.

Following the developed numerical methodology, the first step has been to approach, as much as possible, the numerical and the experimental operating points. For this purpose, the inlet discharge value has been iteratively changed targeting the experimental torque value. Once the difference between the numerical and the experimental torque values has been reduced to 0.5%, the computed inlet total pressure P_{tot} has been imposed as new inlet boundary conditions.

Table 6.4 Performance parameters computed on D_4 imposing P_{tot} on the inlet.

Inlet BC	$\Delta T = \frac{(T_{exp}-T_{num})}{T_{exp}}$	$\Delta H = \frac{(H_{exp}-H_{num})}{H_{exp}}$	$\Delta Q = \frac{(Q_{exp}-Q_{num})}{Q_{exp}}$	$\Delta \eta = \frac{(\eta_{exp}-\eta_{num})}{\eta_{exp}}$
P_{tot}	0.5%	8%	1.8%	7%

As shown in table 6.4, this has allowed to reduce the differences between the computed and the measured T, Q and η values, with a discrepancy on the Q equal to 1.8%. Considering that in this operating point, during the cavitation break down tests the mass flow can vary of $\pm 2.5\%$ this difference on the discharge value was considered acceptable. Furthermore, the new inlet boundary conditions has improved the calculation convergence, reducing the inlet/outlet mass flow difference to less than 0.05%.

Also for this operating point, measurements of the velocity profiles on the runner outlet (plane at 170 *mm* from the reference axis, see figure 3.6in chapter 3) in non-cavitating conditions are available. Contrary to the OP_1, now the flow velocity distribution changes greatly with the runner rotation. The azimuthal average of the meridional V_m and the tangential V_t velocity components has been computed every 10° over 3 turbine rotations (see figure 6.18). The

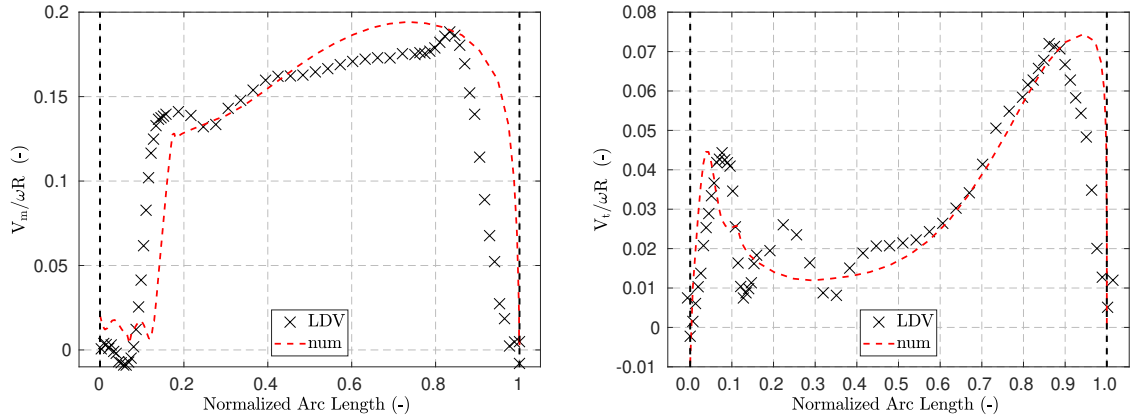

Figure 6.18 Evolution of the normalized **(a)** meridional, V_m, **(b)** and tangential, V_t, velocities along the normalized radius, measured by LDV (black crosses) and computed (red dashed line) in full load conditions (OP_2). 0 is the hub and 1 is the shroud.

mesh refinement level used in this case is not enough to correctly solve the viscous sublayer ($y^+ \geqslant 5$, see chapter 2). This is evident in both velocity profiles near the walls. The peak of V_t observed in the experiments in the shroud region is numerically predicted farther to the wall (figure 6.18 b). Near the tip, the computed V_t profile match with the measured curve but the exaltation is predicted slightly farther from the wall. Discrepancy between the experimental and the calculated profiles near the shroud can be observed also for V_m (figure 6.18 a). Indeed, the computed region where the V_m increases is wider that the measured one, extending from

the shroud to the middle of the channel. On the contrary, close to tip, the computed meridional velocity agrees well with the measurements. Yet, it is satisfying to observe a similar overall shape for both numerical and experimental distributions. The results obtained in non-cavitating conditions have shown that the calculation methodology based on the new inlet boundary condition, developed for OP_1, can be effectively applied to simulate another operating points. The predicted performances values and the velocity profiles on the runner outlet are in good agreement with the measured data. As in optimal load conditions, the numerical results can be further improved refining the mesh near the wall, to solve better the viscous sublayer.

6.2.2 Analyses in cavitating regime

6.2.2.1 Performances evolution

In figure 6.19 the experimental and the numerical σ-break curves are compared. The σ value of the first point of the computed cavitation curve is the 4.5% lower than the measured one.

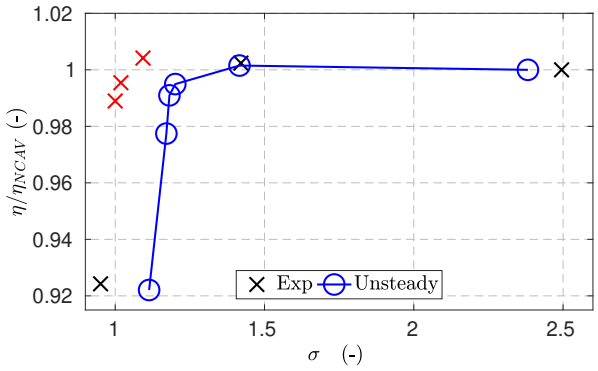

Figure 6.19 σ-break curves measured (black crosses) and computed (blue line with the circles) in full load operating conditions OP_2. The experimental points σ_s, $\sigma_{-0.5\%}$ and $\sigma_{-1\%}$ are plotted with red crosses.

On the contrary, the starting point of the efficiency drop, σ_s, and the points corresponding to an efficiency reduction of 0.5% ($\sigma_{-0.5\%}$) and 1% ($\sigma_{-1\%}$) are predicted for higher σ values. The error on the σ number evaluation at σ_s is higher than 10% and continues to increase with the cavitation development becoming the 18% at $\sigma_{-1\%}$. This mismatch in the Thoma number prediction has been already observed in optimal load conditions (see chapter 5). Considering that the H is constant all along the σ-break curve, the η depends mostly on the torque and on the discharge rate. The numerical and the experimental torque evolutions with the cavitation development are reported in figure 6.20 a. The computed T and η curves are very similar: as in the efficiency case, the numerical torque starts to decrease at higher σ and the last part of the curve is steeper than the measured one. Concerning the mass flow rate, experimentally (figure 6.20 b) it begins to decrease before σ_s reaching the minimum at $\sigma_{-1\%}$. Then in

developed cavitation conditions a sudden increase is observed. The numerical discharge curve fits well the experimental trend until σ_s. Indeed, after this point, contrarily to the experimental measurements, the Q starts to increase.

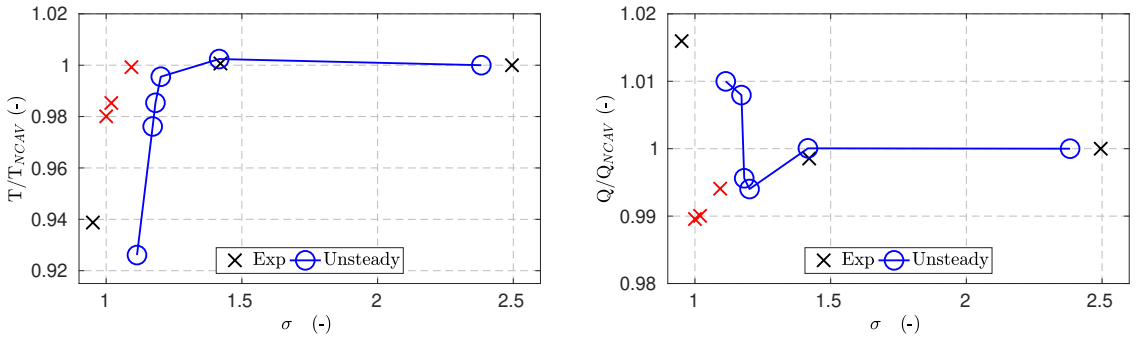

Figure 6.20 **(a)** T and **(b)** Q evolutions as function of σ measured (black crosses) and computed (blue line with the circles) in OP_2. The experimental points σ_s, $\sigma_{-0.5\%}$ and $\sigma_{-1\%}$ are plotted with red crosses.

As a conclusion of this analysis, it is possible to state that simulations on a coarse mesh allows to obtain numerical performances curves with a trend similar to the experimental ones. However, in order to reduce the mismatch on the Thoma number values, a finer mesh is required.

6.2.2.2 Vapor structures evolution

The computed vapor structures in different points of the σ-break curve will be now discussed. Two points have been considered for this analysis: the efficiency drop staring point ($\sigma_s = 1.10$) and the point that corresponds to an efficiency reduction of the 0.5% ($\sigma_{-0.5\%} = 1.02$). The experimental setup are reported in details in chapter 3. As for the OP_1 (see chapter 5), iso-density surfaces at $\rho = 980\ kg/m^3$ have been used to visualize the numerical vapor structures.

At σ_s (figure 6.21 a), the cavitation structures observed during the experiments are concentrated on the tip and on the root of the runner blade. In particular:

- In the tip region, a single cavity has been observed starting from the leading edge and extending along the $2/3$ of the blade length in the trailing edge direction.
- On the blade root, a vapor structure appears close to the leading edge developing in the direction opposite to the runner rotation and another one has been identified near the trailing edge.

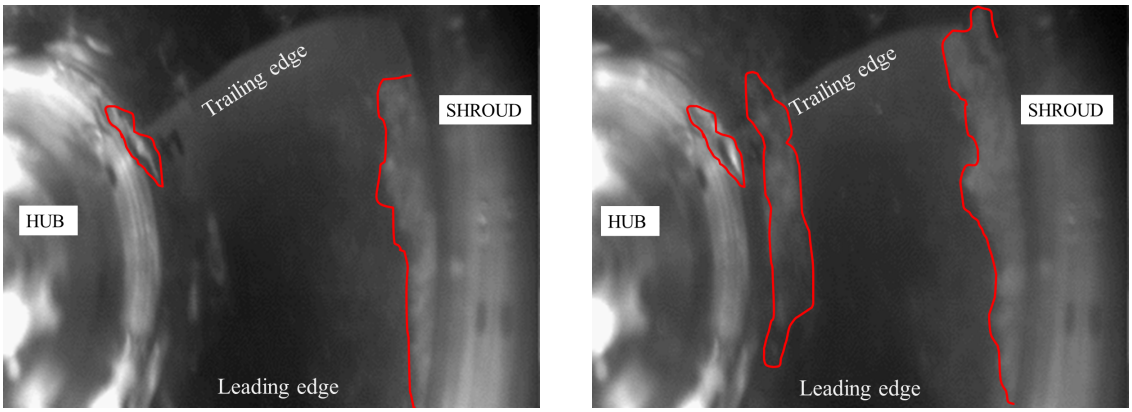

(a) **(b)**

Figure 6.21 Vapor structures at **(a)** $\sigma_s = 1.10$ and at **(b)** $\sigma_{-1\%} = 1.02$ observed in the OP_2.

In the efficiency drop starting point, the quantity of vapor numerically predicted is over estimated (figure 6.22). The cavity calculated on the tip is more widen than the experimental one, covering the entire blade length. The two vapor regions computed near the hub wrap almost all the blade profile and extend also on the runner hub, passing the limits observed experimentally. Moreover, a tip clearance cavitation structure appears in the simulations results that has not been observed during the experiments. At $\sigma_{-0.5\%}$ (figure 6.21 b), the vapor structures observed at σ_s increase their dimensions:

- the blade tip is completely covered by the cavity sheet, from the leading edge to the trailing edge.
- In the hub region, the cavitation structure near the leading edge covers a bigger part of the blade profile while the cavity near the trailing edge is unchanged.

In this point of the σ-break curve, the computed iso-density surfaces on the tip and on the root of the blade (figure 6.23) merge in the middle of the blade generating a single sheet cavity. Also in this case, calculations predict cavitation structures larger than the experimental ones. The over estimation of the vapor in the simulations is mostly due to a non adequate mesh level. Indeed, as already demonstrate in the case of the OP_1 (see chapter 5), a mesh refinement near the wall is required to correctly reproduce the cavitation structures.

Compared to the OP_1, this operating point is characterized by more unsteady cavitation phenomena that change shape and position during the runner rotation. Four different instants of time have been investigated for both points of the σ-break curve. At σ_s (figure 6.22), following a single blade (i.e. the blade **1**), it is possible to observe that the extension of the vapor structure on the blade root varies greatly, joining the cavity on the tip and after separating from it during the rotation. On the contrary, at $\sigma_{-0.5\%}$, the computed vapor structures become bigger and

more attached on the blade so only local variations of the cavity sheet near the hub are observed (see figure 6.23). In particular, during the rotation, the amount of vapor evolve, covering and uncovering the trailing edge on the blade root.

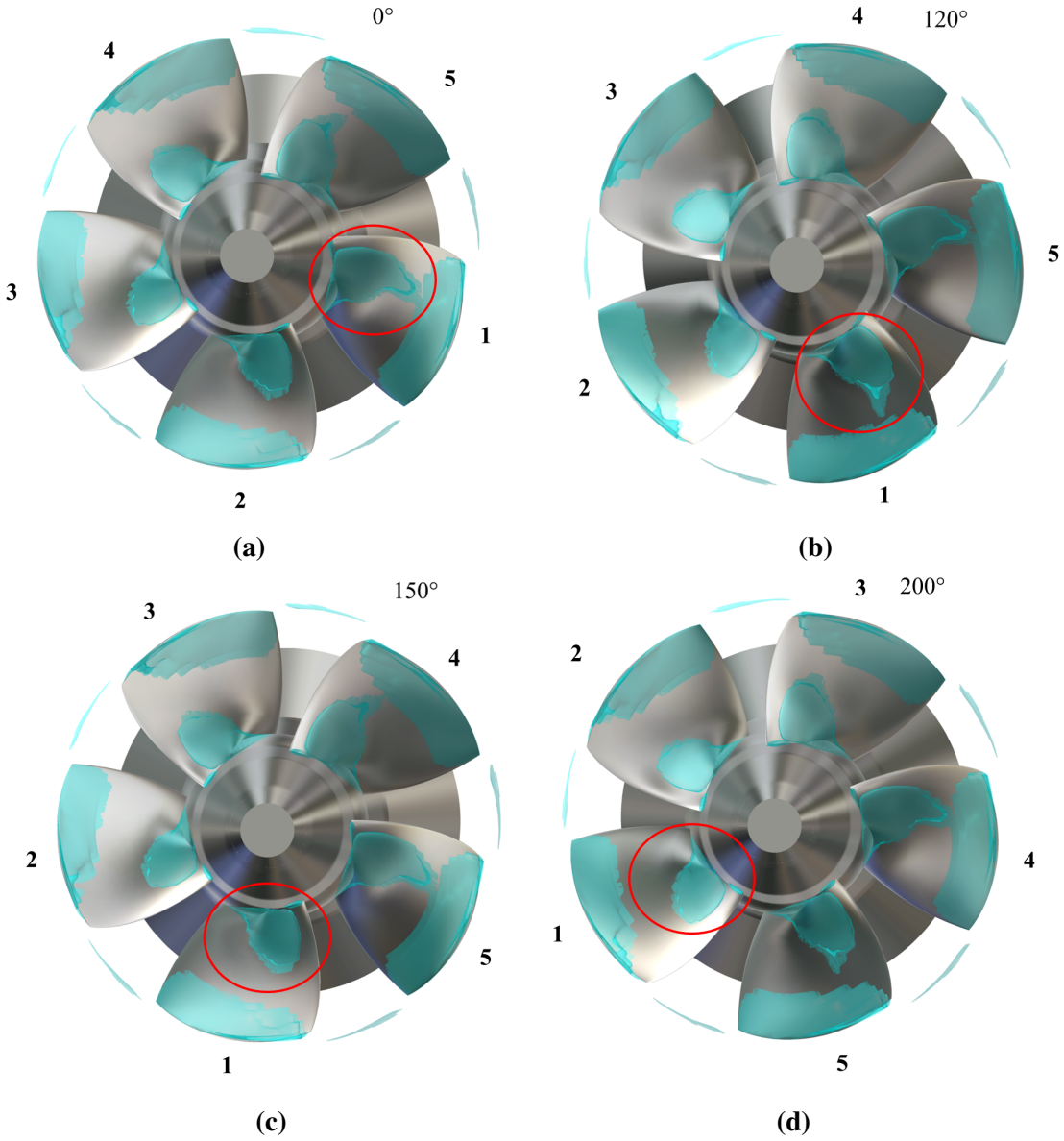

Figure 6.22 Computed vapor structures at σ_s in the OP_2 for four runner positions: **(a)** 0°, **(b)** 120°, **(c)** 150° and **(d)** 200°.

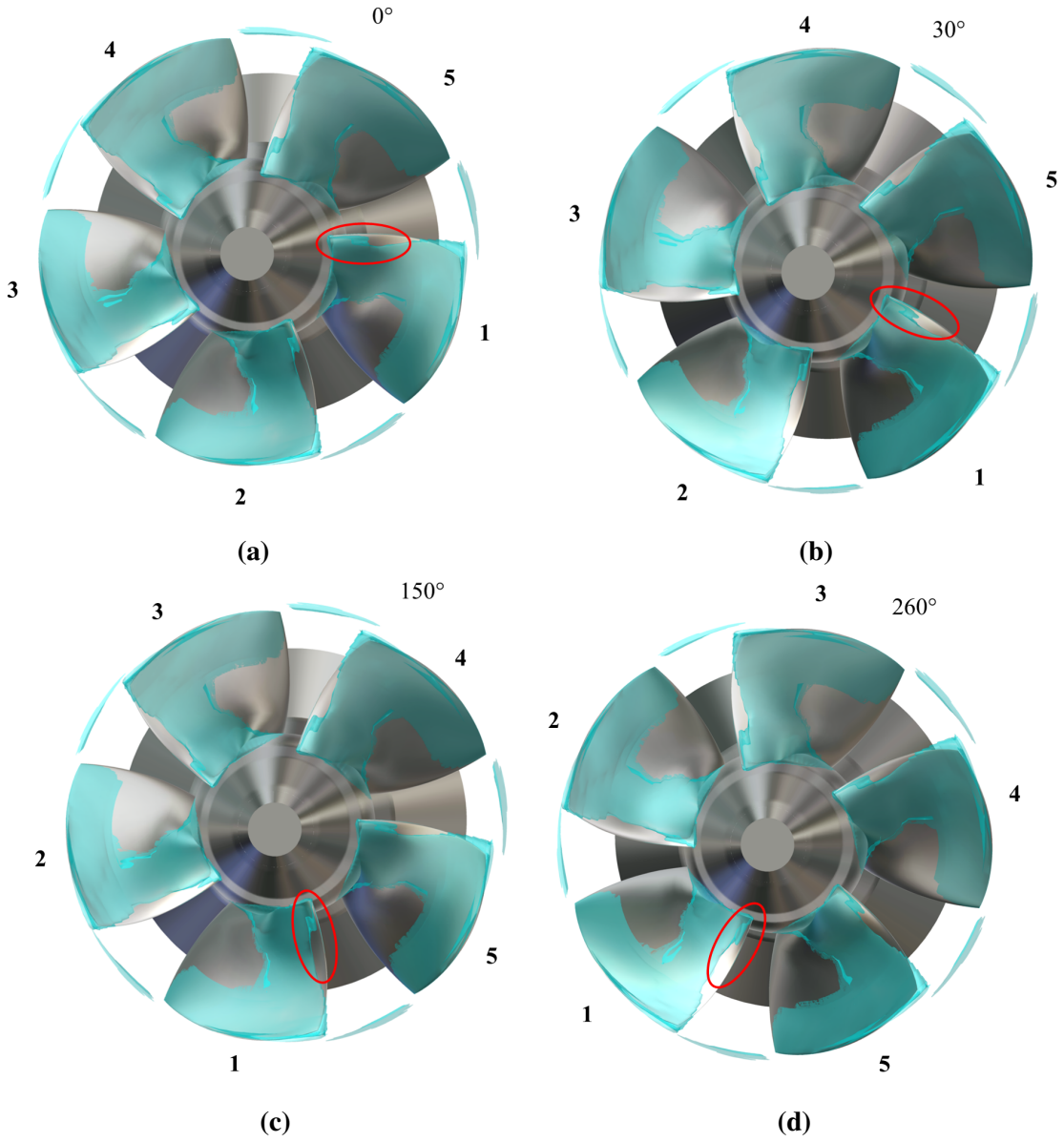

Figure 6.23 Computed vapor structures at $\sigma_{-1\%}$ in the OP_2 for four runner positions: **(a)** 0°, **(b)** 30°, **(c)** 150° and **(d)** 260°.

6.2.2.3 Pressure fluctuations

Contrary to the OP_1, the operating point OP_2 is characterized by a more unsteady flow that introduce noises in the signal. This means that in full load operating conditions is more complicated to isolate and to recognize the frequencies linked to the cavitation in the experimental pressure spectra. The experimental and the numerical setups are the same used for the analysis of the pressure fluctuations in the OP_1 (see paragraph 6.1.3). As for the OP_1, three points of the σ-break curve have been considered in the investigation: the point in free cavitation conditions,

the efficiency drop starts point σ_s and the $\sigma_{-1\%}$ corresponding to a loss of the efficiency of the 1%. The spectra of the first point of the cavitation curve is used as references for the other two investigated points. The analyzed frequencies domain are limited to $f/f_0 = 30$ since no interesting phenomena have been observed for higher frequency values.

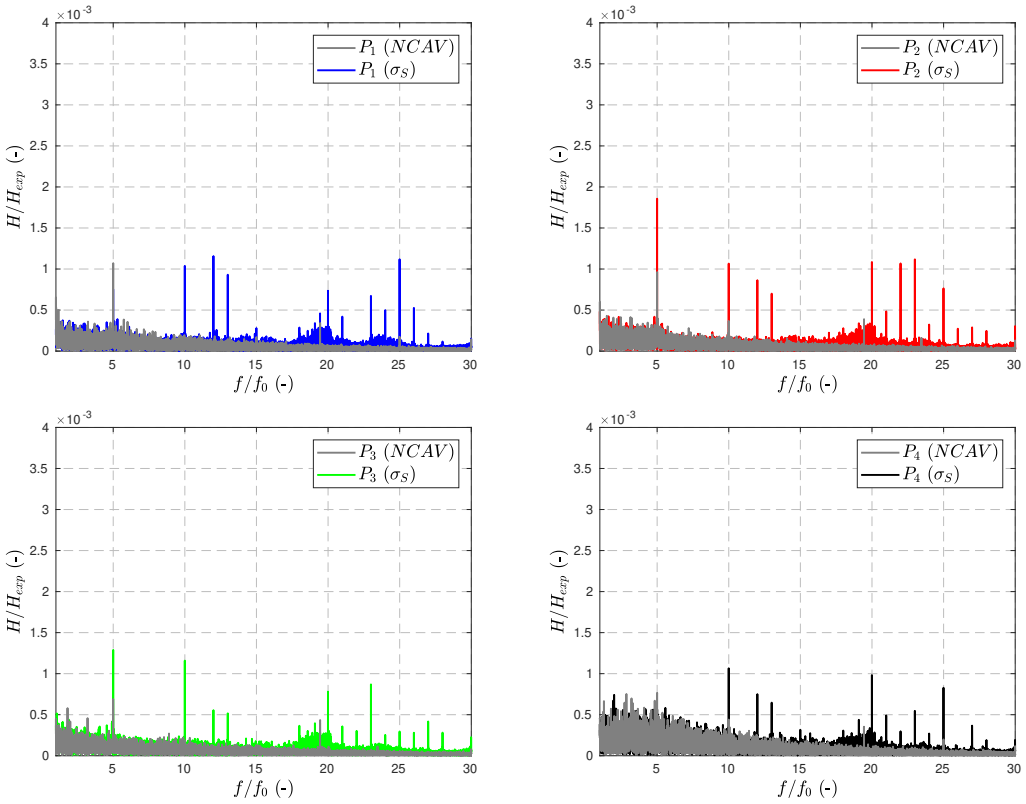

Figure 6.24 Measured pressure spectra in the OP_2 in non-cavitating conditions at $\sigma_s = 1.10$. The frequencies are normalized by the runner rotation frequency f_0. The amplitude is divided by the experimental head H_{exp}.

At σ_s (figure 6.24), a slight increase of the pressure amplitude is observed nearby the runner passing frequency ($f = 5\ f_0$) and the guide vane passing frequency ($f = 24\ f_0$). The other peaks identified for multiple values of these two frequencies (i.e. $f = 10\ f_0$) can be considered as high-order harmonics.

With the development of the cavitation structures in the runner at $\sigma_{-1\%}$, both peaks observed at $f = 5\ f_0$ and $f = 24\ f_0$ increase. The dominant frequencies are not the same for all the four transducers: for P_2 and in P_3 is the $f = 5\ f_0$, whereas for P_1 and P_4 is the $f = 24\ f_0$. Comparing the experimental observations of the cavitation structures at σ_s and at $\sigma_{-0.5\%}$ (reported in figures 6.21 a and b, respectively), it is evident that reducing the Thoma number the extension of the cavity on the tip increases reaching the trailing edge of the blade.

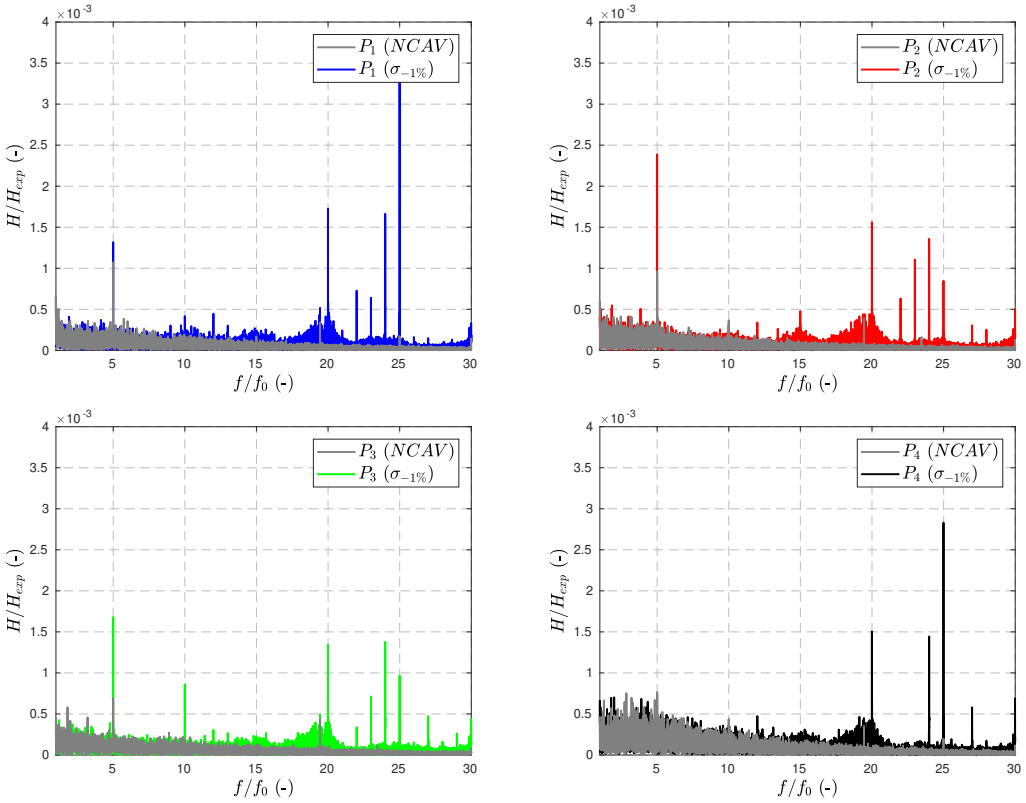

Figure 6.25 Measured pressure spectra in the OP_2 in non-cavitating conditions and at $\sigma_{-1\%} = 1.02$. The frequencies are normalized by the runner rotation frequency f_0. The amplitude is divided by the experimental head H_{exp}.

From the previous investigation of the pressure spectra in the optimal load operating point (see paragraph 6.1.3), it is reasonable to assume that also in this case the pressure fluctuations are linked to the appearance and the development of the cavitation on the blade tip.

Overlapping the numerical spectra on the experimental ones for the two points of the σ-break curve (see figure 6.26 and 6.27) it is possible to see that the simulations predict the presence of a single peak in the range comprised between $f = 20\ f_0$ and $f = 26\ f_0$ that increases with the cavitation development. Also for this operating point, the overall position of the most energetic peak is correctly predicted. More harmonics could be captured extending the numerical signal and refining the mesh but they will still be limited by the application of the URANS formulation.

In conclusion, the analysis of the full operating point has allow to test the generality of the developed numerical methodology of cavitation prediction. The use of a coarse mesh due to the necessity to limit the computational costs, has led to discrepancies between numerical results and experimental data in both non-cavitating and cavitating conditions, mostly concerning the velocity profiles and the cavitation structures development. The trend of the computed

performance curves approaches the measured ones, allowing to obtain a preliminary evaluation of the effect of the cavitation on the machine.

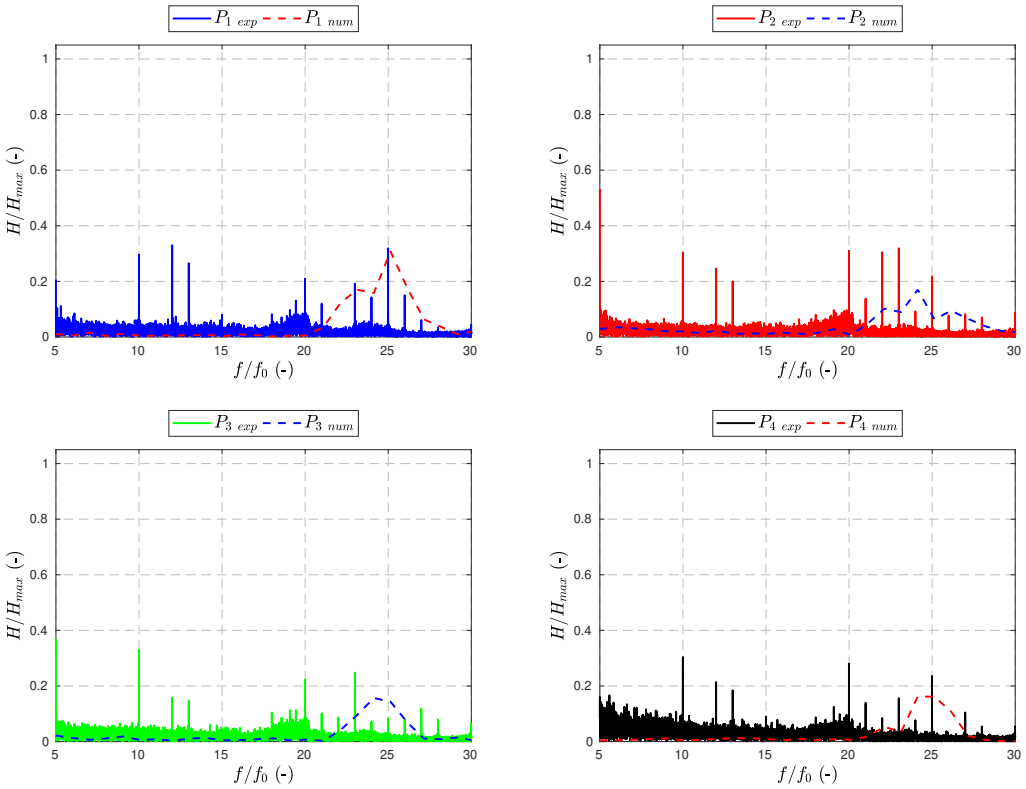

Figure 6.26 Comparison between computed and measured pressure spectra at σ_s. The frequencies are normalized by the runner rotation frequency f_0. The amplitudes are normalized by highest computed and measured peak value, respectively.

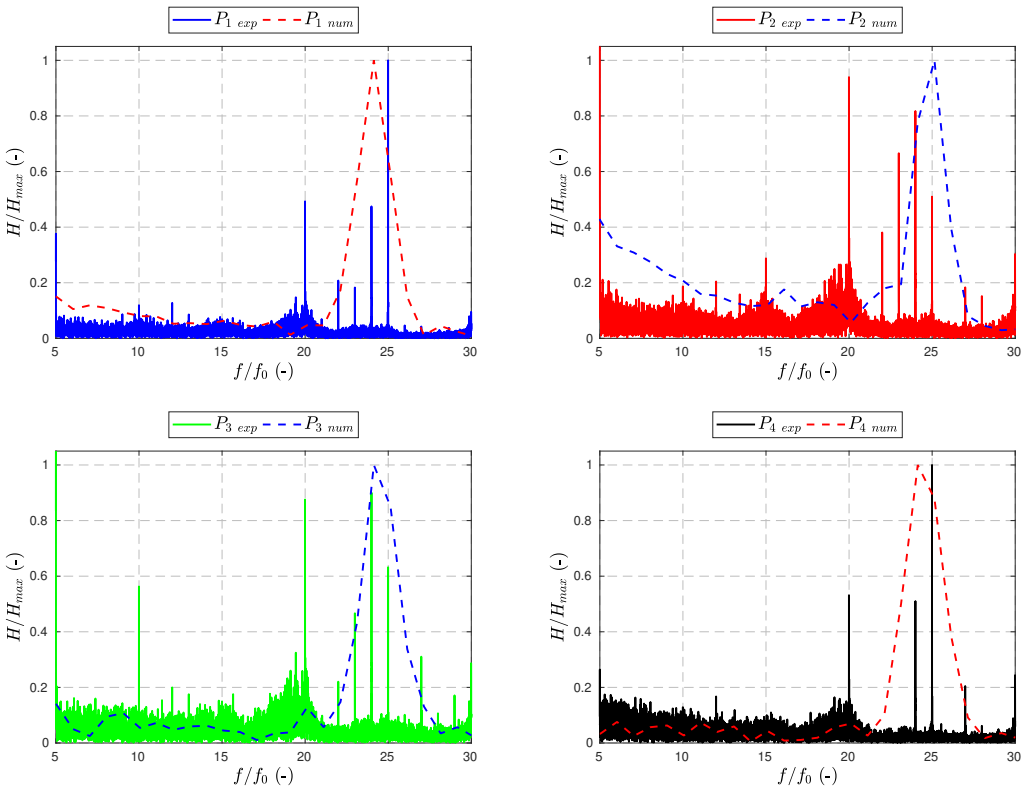

Figure 6.27 Comparison between computed and measured pressure spectra at $\sigma_{-1\%}$. The frequencies are normalized by the runner rotation frequency f_0. The amplitudes are normalized by highest computed and measured peak value, respectively.

6.3 Chapter conclusions

Unsteady simulations have been performed on the optimal load operating point (OP_1) in order to improve the numerical methodology developed in steady regime and to further investigate the cavitating flow behavior during the turbine rotation. The same analyses proposed in the steady regime have been performed introducing the time variables in the governing equations. In particular, the evolution of the machine performances curves, the cavitation structures and the flow in the draft tube have been recalculated in unsteady conditions and have been compared with the previous steady predictions. Slight improvements have been obtained in the cavitation curves trends, in terms of Thoma number values predictions, mostly in developed cavitation conditions. No important variations of the vapor structures shapes and positions during the runner rotation have been observed confirming the steady characteristic of the cavitating flow in operating conditions near the best efficiency point, according to the experimental investigations. The analysis of the time evolution of the stream lines in the draft tube has allowed to state that

the cavitation phenomena occurring in the runner influence also the downstream flow, changing its distribution and introducing vortex structures in the draft tube channels.

Furthermore, the pressure fluctuations downstream the runner blades have been investigated. Comparing the measured pressure spectra in four points on the discharge rings with the computed spectra in the same points, a correlation between the tip cavitation and the increase of the pressure peak has been found.

Therefore, by means of the unsteady investigations the numerical methodology has been finally validate. The agreement between steady and unsteady results have highlighted that in stable operating conditions, such as the OP_1, just steady simulations are required to correctly reproduce the behavior of the cavitating flows and their impact on the machine performances, containing the computational costs. The unsteady calculations were also useful to analyze time-variable phenomena, impossible to capture by simple steady simulations. The investigation of the pressure fluctuations on the runner downstream has allowed to identify the signature of the tip cavitation. To improve and complete the prediction numerical methodology, further analysis in different parts of the machine of the pressure variations are required to characterize the frequency signatures representative of the other cavitation types, which alter the machine efficiency.

Once the methodology has been completely developed, even in unsteady conditions, its generality has been validate considering another operating point. The full load operating point (OP_2) has been chosen since it is characterized by very unstable flow so only unsteady simulations have been possible. The methodology was applied identically to the OP_1: at first, the experimental flow rate value was imposed as inlet boundary condition, then it was iteratively changed targeting the experimental torque value and, finally, the total pressure value was imposed on the domain inlet, improving the simulations results and the calculations stability. However, for computational cost reasons, the OP_2 simulations have been performed on a mesh less refined than the OP_1. This has led to discrepancies between measured and numerical performances and velocity fields, already outside the cavitating regime. Prediction errors were also observed on the cavitation curves and on the vapor structures evolution. Despite this, these calculations have been allowed to obtain a preliminary estimation of the cavitating structures behavior during the runner rotation and their consequences on the machine performances. However, a more refined mesh is necessary to obtain more accurate results.

The analysis of pressure fluctuations was performed also for this operating point, in the same position as for the OP_1. Due to the unsteady characteristic of the flow in this operating conditions, the pressure signal is more noisy and the identification of the dominant frequencies is more complex. The analysis of the experimental pressure spectra have revealed the presence of other dominant frequencies additionally to the one identified in the OP_1. On the other hand,

in the simulations only the guide vane passing frequency linked to the tip cavitation has been recognized. This limit of the numerical methodology could be corrected refining the mesh and increasing the length of the numerical signal but it could be mainly related to the limit of the URANS formulation that averages the turbulent structures.

Chapter 7

Conclusions and perspectives

7.1 Conclusions

A new numerical methodology has been proposed to predict the cavitation phenomena in Kaplan turbine and their effects on the machine performances. It has been developed starting from the investigation of the optimal load operating point. Preliminary simulations have been performed on a reduced numerical domain comprising a single full-periodic interblade channel of the guide vane, the runner and the cone. In this first step, the adequate turbulence model, mesh refinement and boundary conditions setup have been defined. Indeed, this three aspects have a great impact on the stability and the results of the simulations.

The boundary condition imposed on the domain inlet has a key role in order to improve the numerical cavitation predictions. Hence, an iterative correction procedure has been proposed, consisting in modifying the inlet discharge to target the experimental torque value. Indeed, the correct reproduction of this parameter ensures the fluid dynamic agreement between experimental model and the simulated geometry since it strictly depends on the flow incidence on the blades and on the hub of the runner.

Once the numerical setup has been determined, the draft tube has been included in the computational domain. The modification of the numerical domain aimed to firstly evaluate the influence of the draft tube on the cavitating flow and the machine performances and secondly to further reduce the discrepancy between numerical and experimental conditions. Considering the draft tube in simulations, the total pressure can be used as the inlet boundary condition instead of the flow rate. As a consequence, the net head is constant during the Thoma number reduction, likely in experimental break down tests.

The results have shown that the draft tube has a great influence on the flow in the turbine in both non-cavitating and cavitating regimes. In order to accurately predict the effects of the cavitation phenomena in the turbine, it have to be considered in the analysis. Moreover,

changing the inlet boundary condition, the overall aspect of the T, H and Q numerical curves fit better with the experimental ones. However, the computed σ values after the efficiency drop starting point are still higher than the experimental ones.

The numerical results of the performance curves and the cavitation structures obtained applying the developed computational strategy are in good agreement with the experimental data. This ensure the prediction ability of the numerical methodology.

As soon as the steady calculation methodology has been completely defined, in-deep analyses of the cavitating flow have been performed. The alteration of the pressure distribution on the runner blades and the consequential modification of the torque with the cavitation number reduction have been related to the development of the vapor structures in the hub and in the shroud regions. On the contrary, the presence of the cavities have only slightly modified the flow in the interblade channel. Effects of the runner cavitation have been observed on the flow in draft tube. The intensity of the vortices and the flow distribution in the two channels are modified by the development of the cavitation, affecting the machine performances.

Furthermore, the influence of cavitation on global and local losses has been investigated. Despite the net head is constant during the σ-break curve, the losses distribution through the different parts of the machine changes, increasing in the runner and in the draft tube. In particular, when cavities occur, the losses in the runner increase mostly in the tip blade region, due to the presence of strong velocity gradients in the shroud gap.

Unsteady simulations have been performed for the same operating point in order to improve the performances prediction in developed cavitation conditions and to validate and complete the steady cavitating flow analysis. The introduction of the temporal variables in the governing equations has only marginally improved the cavitation prediction methodology. On the other hand, the unsteady approach has allowed to validate the steady analyses results in terms of cavities evolution and the vortical structures development in the draft tube. The pressure fluctuations downstream the runner have been investigated, correlating the peak of the pressure spectra to the presence of the vapor structures. This has allowed to find a link between the rotor/stator interaction and the cavitation development, finding a probable signature of the tip vortex cavitation.

Finally, the developed numerical methodology has been tested in full load operating conditions, in order to validate its generality. Due to the high unstable characteristic of the flow in this operating point, only unsteady simulations have been possible. to limit the computational cost, simulations have been performed on a mesh more coarse than the optimal load point. Applying the new strategy, numerical results are in better agreement with experimental ones. However, the coarse mesh is responsible for discrepancies between measured and numerical performances and velocity fields, already in free-cavitation regime. Prediction errors were also

observed for the cavitation curves and for the vapor structures evolution. In spite of this, these calculations have been allowed to obtain a preliminary estimation of the cavitating structures behavior during the runner rotation and their consequences on the machine performances. The analysis of the pressure spectra have confirmed the increase of the pressure fluctuations due to cavitation on the blade tip, stated in the optimal load point. The other experimental dominant frequencies have not observed in the numerical simulations.

7.2 Perspectives

The cavitation prediction ability of the computational strategy presented in this work has been widely validated. Nevertheless, further improvements could be considered:

- The mesh refinement level has a fundamental role to accurately reproduce shape and location of the cavitation structures and, as a consequence, to correctly predict the performances curves. Thus, simulations on a fine grid have to performed, also in full load operating conditions to obtain high quality results as for the optimal load point.

- The machine performances depend also on the draft tube energy recovering efficiency. Thus, more experimental investigation of the cavitation effects on the flow in the draft tube, in both operating conditions, are required. The analyses of streamlines and velocity and helicity fields have to be validated by means of further experimental investigations in the same cross-sections. Also the pressure fields and their fluctuations, with the cavitation development, have to be analyzed numerically and experimentally in different parts of the draft tube. Finally, a local losses analysis, as in the runner, can be useful in order to identify the loss sources linked to the cavitation.

- The presence of vapor structures in the runner involves pressure and torque fluctuations and pulsations. Different types of cavitation correspond to different frequency values. Experimental and numerical investigations of the pressure spectra in other parts of the runner (i.e. on the blade, on the hub, on the guide vane outlet,...) can be helpful to find other cavitation signatures. Moreover, the analysis of the evolution of the torque spectrum in various cavitating conditions can better clarify the alteration performance mechanism due to the cavitation. Also a low frequencies analysis can be of the great interest in order to discover more low frequencies phenomena linked to the cavitation.

- A preliminary validation of the generality of the developed cavitation prediction numerical methodology has been obtained by simulating the full load operating point. Further

validations must to be done applying the strategy in other operating conditions and for other machine geometries.

Bibliography

[1] International Energy Agency IEA, 2019. *Global Energy & CO2 Status Report.The latest trends in energy and emissions in 2018.*

[2] International Energy Agency IEA, 2018. *Renewables Information: Overview*.

[3] Wilhelm, S., 2017. "Analysis of head losses in a bulb turbine draft tube by means of unsteady numerical simulations". Phd thesis, Université Grenoble Alpes, Jan.

[4] Manitoba Hydro. https://www.hydro.mb.ca/corporate/teachers/producing_electricity/.

[5] Chapallaz, J.-M., 1995. *Turbines hydrauliques*. Office fédéral des questions conjoncturelles.

[6] Rey, R., Bois, G., Bakir, F., and Khelladi, S., 2009. *Turbomachines : calcul des écoulements incompressibles - Support théorique et simulation numérique*. Techniques de l'ingénieur.

[7] Meauzé, 1995. *Turbomachines : calcul des écoulements compressibles.* Techniques de l'ingénieur.

[8] Ješe, U., 2015. "Numerical study of pump-turbine instabilities : pumping mode off-design conditions". Phd thesis, Université Grenoble Alpes, Nov.

[9] Franc, J.-P., 1995. *La cavitation: mécanismes physiques et aspects industriels*. EDP Sciences, Jan.

[10] Franc, J.-P., and Michel, J.-M., 2006. *Foundamentals of cavitation*, Vol. 76. Springer.

[11] Escaler, X., Egusquiza, E., Farhat, M., and Avellan, F., 2006. "Detection of cavitation in hydraulic turbines". *Mechanical Systems and Signal Processing,* ***20***(4), pp. 983–1007.

[12] Avellan, F., 2004. "Introduction to cavitation in hydraulic machinery". *The 6th International Conference on Hydraulic Machinery and Hydrodynamics*, 01, pp. 11–22.

[13] International Electrotechnical Commision, 1999. *International standard IEC 60193, Hydraulic Turbines, storage pumps and pump-turbines*, model acceptance tests, 2nd ed.

[14] Motycak, L., Skotak, A., and Kupcik, R., 2012. "Kaplan turbine tip vortex cavitation-analysis and prevention". *IOP Conference Series: Earth and Environmental Science,* ***15***(3), p. 032060.

[15] Escaler, X., Egusquiza, E., Mebarki, T., Avellan, F., and Farhat, M., 2002. "Cavitation detection and erosion prediction in hydroturbines". In Proceedings of the Ninth of International Symposium on Transport Phenomena and Dynamics of Rotating Machinery.

[16] Mulu, B., 2012. "An experimental and numerical investigation of a Kaplan turbine model". Phd thesis, Lulea University of Technology, Department of Engineering Sciences and Mathematics, Fluid and Experimental Mechanics.

[17] Sagaut, P., Deck, S., and Terracol, M., 2013. *Multiscale and multiresolution approaches in turbulence - les, des and hybrid rans/les methods: applications and guidelines; 2nd ed.* World Scientific, Singapore.

[18] Baldwin, B., and Lomax, H., 1978. "Thin-layer approximation and algebraic model for separated turbulent flows". *AIAA, Aerospace Sciences Meeting*.

[19] Spalart, P., and Allmaras, S., 1992. "A one-equation turbulence model for aerodynamic flows". *AIAA, Journal*.

[20] Brammer, J., 2014. *CFD Guideline - Generalities.*, nt-ctex-cfd-3000 ed. Alstom Hydro France.

[21] Bradshaw, P., 1996. "Turbulence modeling with application to turbomachinery". *Progress in Aerospace Sciences, ISSN: 0376-0421,* ***32***(6), pp. 575–624.

[22] Jones, W., and Launder, B., 1987. "The prediction of laminarization with a two-equation model of turbulence". *International Journal of fluid mechanics,* ***177***, pp. 133–166.

[23] Casey, M., and Wintergerste, T., 2000. *Quality and trust in industrial CFD: Best Practice Guidelines.* ERCOFTAC. "Version 1: January 2000"–T.p.

[24] Wilcox, D., 1988. "Reassessment of the scale-determining equation for advanced turbulence models". *AIAA Journal,* ***26***(11), pp. 1299–1310.

[25] Menter, F., 1993. "Zonal two equation $k-\omega$ turbulence models for aerodynamic flows". *23rd Fluid Dynamics, Plasmadynamics, and Lasers Conference*.

[26] Menter, F., Kuntz, M., and Langtry, R., 2003. "Ten years of industrial experience with the sst turbulence model". *Proceedings of the 4th International Symposium on Turbulence, Heat and Mass Transfer*, pp. 625–632.

[27] Nezu, I., and Tominaga, A., 2002. *Suirigaku*. Asakura Shoten.

[28] Patel, V., Rodi, W., and Scheuerer, G., 1985. "Turbulence models for near-wall and low reynolds number flows - a review". *AIAA Journal,* ***23***, pp. 1308–1319.

[29] Shih, T., 1994. *A new $k-\omega$ eddy viscosity model for high Reynolds number turbulent flows: model development and validation*.

[30] Yang, Z., and Shih, T., 1993. "New time scale based $k-\varepsilon$ model for near-wall turbulence". *AIAA Journal,* ***31***(7), pp. 1191–1198.

[31] Hakimi, N., Hirsch, C., and Pierret, S., 2000. "Presentation and application of the new extended $k-\varepsilon$ model with wall functions". *ECCOMAS*.

[32] Kim, J., Moin, P., and Moser, R., 1987. "Turbulence statistics in fully developed channel flow at low reynolds numbers". *Journal of fluid mechanics,* ***177***, pp. 133–166.

[33] *Theoretical manual. FINE™/Turbo v13.1*.

[34] Decaix, J., 2012. "Modélisation et simulation de la turbulence compressible en milieu diphasique: application aux écoulements cavitants instationnaires". Phd thesis, Laboratoire des Ecoulements Géophysiques et Industriels (LEGI).

[35] Shams, E., Finn, J., and Apte, S., 2011. "A numerical scheme for euler–lagrange simulation of bubbly flows in complex systems". *International Journal for Numerical Methods in Fluids,* ***67***, 12, pp. 1865 – 1898.

[36] Maeda, K., and Colonius, T., 2018. "Eulerian-lagrangian method for simulation of cloud cavitation". *Journal of computational physics,* ***371***, pp. 994–1017.

[37] Giannadakis, E., Gavaises, M., and Arcoumanis, C., 2008. "Modelling of cavitation in diesel injector nozzles". *Journal of Fluid Mechanics,* ***616***, p. 153–193.

[38] Ma, J., Hsiao, C.-T., and Chahine, G., 2015. "Modelling cavitating flows using an eulerian-lagrangian approach and a nucleation model". *Journal of Physics: Conference Series,* ***656***, 12, p. 012160.

[39] Mimouni, S., Boucker, M., Laviéville, J., Guelfi, A., and Bestion, D., 2008. "Modelling and computation of cavitation and boiling bubbly flows with the NEPTUNE CFD code". *Nuclear Engineering and Design,* ***238***, 03, pp. 680–692.

[40] Goncalvès, E., and Charrière, B., 2014. "Modelling for isothermal cavitation with a four-equation model". *International Journal of Multiphase Flow,* ***59***, pp. 54–72.

[41] Coutier-Delgosha, O., Fortes-Patella, R., Reboud, J., Stoffel, B., and Hofmann, M., 2003. "Experimental and numerical studies in a centrifugal pump with two-dimensional curved blades in cavitating conditions". *Journal of Fluid Engineering,* ***125***(6), p. 970–978.

[42] Ješe, U., Fortes-Patella, R., and Antheaume, S., 2014. "High head pump-turbine : Pumping mode numerical simulations with a cavitation model for off-design conditions". *IOP Conference Series : Earth and Environmental Science,* ***22***(3), p. 032048.

[43] Jošt, D., Škerlavaj, A., Pirnat, V., Morgut, M., and Nobile, E., 2019. "Numerical prediction of efficiency and cavitation for a pelton turbine". *IOP Conference Series: Earth and Environmental Science,* ***240***, 03, p. 062033.

[44] Liu, S., Zhang, L., Nishi, M., and Wu, Y., 2009. "Cavitating Turbulent Flow Simulation in a Francis Turbine Based on Mixture Model". *ASME.Journal of Fluids Engineering,* ***131(5)***, pp. 051302–051302–8.

[45] Morgut, M., Jošt, D., Škerlavaj, A., Nobile, E., and Contento, G., 2018. "Numerical predictions of cavitating flow around a marine propeller and kaplan turbine runner with calibrated cavitation models". *Strojniski Vestnik/Journal of Mechanical Engineering,* ***64***, 01, pp. 543–554.

[46] Leguizamón, S., Ségoufin, C., Phan, H.-T., and Avellan, F., 2017. "On the efficiency alteration mechanisms due to cavitation in kaplan turbines". *ASME.Journal of Fluids Engineering,* ***139***, 02.

[47] Necker, J., and Aschenbrenner, T., 2010. "Model test and CFD calculation of a cavitating bulb turbine". *IOP Conference Series: Earth and Environmental Science,* ***12***, 08, p. 012064.

[48] Bankoff, S., 1960. "A variable density single-fluid model for two-phase flow with particular reference to steam-water flow". *Journal of Heat Transfer,* ***82***(4), pp. 256–272.

[49] Kunz, R., Boger, D., Chyczewski, T., Stinebring, D., Gibeling, H., and Govindan, T., 1999. "Multi-phase cfd analysis of natural and ventilated cavitation about submerged bodies". *Proceedings of FEDSM,* ***99***.

[50] Medvitz, R., Kunz, R., Boger, D., Lindau, J., Yocum, A., and Pauley, L., 2012. "Performance Analysis of Cavitating Flow in Centrifugal Pumps Using Multiphase CFD". *ASME.Journal of Fluids Engineering,* ***124***, 05, pp. 377– 383.

[51] Hanimann, L., Mangani, L., Casartelli, E., and Widmer, M., 2016. "Steady-state cavitation modeling in an open source framework: Theory and applied cases". In ISROMAC 2016, Symposium on Rotating Machinery.

[52] Singhal, A., Athavale, M., Li, H., and Jiang, Y., 2002. "Mathematical basis and validation of the full cavitation model". *Journal of Fluids Engineering, trans. ASME,* ***124***(3), p. 617–624.

[53] Athavale, M., Li, H. Y., Jiang, Y., and Ashok, K. Singhal, A., 2002. "Application of the Full Cavitation Model to Pumps and Inducers". *International Journal of Rotating Machinery,* ***8***, 01.

[54] Liu, S., Wu, Y., and Luo, X., 2005. "Numerical Simulation of 3D Cavitating Turbulent Flow in Francis Turbine". In ASME Fluids Engineering Division Summer Meeting.

[55] Balint, D., Resiga, R., Muntean, S., and Anton, I., 2006. "Numerical simulation and analysis of the two-phase cavitating flow in Kaplan turbines". In 23rd IAHR Symposium. Yokohama, Japan.

[56] Zwart, P. J., Gerber, A. G., and Belamri, T., 2004. "A two-phase flow model for predicting cavitation dynamics". *Fifth International Conference on Multiphase Flow, Yokohama,Japan,* ***152***.

[57] Liu, H.-L., Wang, J., Wang, Y., Zhang, H., and Huang, H., 2014. "Influence of the empirical coefficients of cavitation model on predicting cavitating flow in the centrifugal pump". *International Journal of Naval Architecture and Ocean Engineering,* ***6***(1), pp. 119 – 131.

[58] Escaler, X., Roig, R., and Hidalgo Diaz, V., 2018. "Sensitivity Analysis of Zwart-Gerber-Belamri Model Parameters on the Numerical Simulation of Francis Runner Cavitation".

[59] Li, D., and Merkle, C., 2006. "A unified framework for incompressible and compressible fluid flows". *Journal of Hydrodynamics, Ser. B,* ***18***(3), p. 113–119.

[60] Schnerr, G., and Sauer, J., 2001. "Physical and numerical modeling of unsteady cavitation dynamics". *Fourth International Conference on Multiphase Flow,* ***1***.

[61] Schmidt, D., 1997. "Cavitation in diesel fuel injector nozzles". Phd thesis, University of Wisconsin-Madison.

[62] Delannoy, Y., and Kueny, J., 1990. "Two phase flow approach in unsteady cavitation modeling". *ASME Cavitation and Multiphase flow forum*, p. 153–158.

[63] Sinibaldi, E., Beux, F., and Salvetti, M. V., 2006. "A numerical method for 3D barotropic flows in turbomachinery". *Flow, turbulence and combustion,* ***76***(4), 06, pp. 371–381.

[64] Pouffary, B., Fortes-Patella, R., Reboud, J., and Lambert, P., 2008. "Numerical simulation of 3d cavitating flows : analysis of cavitation head drop in turbomachinery.". *Journal of Fluids Engineering, Trans. ASME,* ***130***(6), p. 061301.

[65] Goncalves, E., and Fortes-Patella, R., 2009. "Numerical simulation of cavitating flows with homogeneous models". *Computers & Fluids,* ***38***(9), p. 1682–1696.

[66] Pouffary, B., 2004. "Simulation numerique d'écoulements 2d/3d cavitants, stationnaires et instationnaires: analyse specifique pour les turbomachines". Phd thesis, Laboratoire des Ecoulements Géophysiques et Industriels (LEGI).

[67] Fortes-Patella, R., Barre, S., and Reboud, J., 2006. "Experiments and modelling of cavitating flows in venturi. part ii: unsteady cavitation". *CAV 2006 Symposium*.

[68] Rolland, J., 2008. "Modélisation des écoulements cavitants dans les inducteurs de turbopompes: prise en compte des effets thermodynamiques". Phd thesis, Laboratoire des Ecoulements Géophysiques et Industriels (LEGI).

[69] Jameson, A., Schmidt, W., and Turkel, E., 1981. "Numerical simulation of the euler equations by finite-volume methods using runge-kutta time stepping schemes". *AIAA,* ***81-1259***.

[70] Hakimi, N., 1997. "Preconditioning methods for time dependent navier-stokes equations". Phd thesis, Vrije Universiteit Brussel.

[71] Balint, D., Resiga, R., Muntean, S., and Anton, I., 2006. "Numerical simulation and analysis of the two-phase cavitating flow in a Kaplan turbine". In 23th IAHR Symposium. Yokohama, Japan.

[72] Jošt, D., Morgut, M., Škerlavaj, A., and Nobile, E., 2015. "Cavitation prediction in a Kaplan turbine using standard and optimized model parameters". In 6th IAHR International Meeting of the Workgroup on Cavitation and Dynamic Problems in Hydraulic Machinery and Systems. Ljubljana, Slovenia.

[73] Nennemann, B., and Vu, T., 2007. "Kaplan turbine blade and discharge ring cavitation prediction using unsteady cfd". *Scientific Bulletin of the "Politehnica" University of Timisoara. Transactions on Mechanics,* ***52***, p. 66.

[74] Grekula, M., and Bark, G., 2001. "Experimental Study of Cavitation in a Kaplan Model Turbine". In CAV 2001: Fourth International Symposium on Cavitation.

[75] Rus, T., Dular, M., Širok, B., Hočevar, M., and Kern, I., 2007. "An Investigation of the Relationship Between Acoustic Emission, Vibration, Noise, and Cavitation Structures on a Kaplan Turbine". *ASME.Journal of Fluids Engineering,* ***129***(9), pp. 1112–1122.

[76] Escaler, X., Egusquiza, E., Farhat, M., and Avellan, F., 2006. "Detection of cavitation in hydraulic turbines". *Mechanical Systems and Signal Processing,* ***20***(4), pp. 983–1007.

[77] Jonssonn, P., Mulu, B., and Cervantes, M., 2012. "Experimental investigation of a Kaplan draft tube - Part II: Off-design conditions". *Applied Energy,* ***94***, 06.

[78] Alstom Hydro France, 2015. *Overview of Grenoble Global Technology Center Hydraulic Laboratory*. ix, 31.

[79] Dantec dynamics - measurement principles of lda. https://www.dantecdynamics.com/measurement-principles-of-lda.

[80] Figliola, R., and Beasley, D., 2015. *Theory and Design for Mechanical Measurements, 6th Edition*. Wiley.

[81] Alstom Hydro France, 2015. *Analyse fréquentielle des mesures au laboratoire : Rappels et définitions. Document interne de formation.* 42.

[82] Coutier-Delagosha, O., 2001. "Modélisation des écoulements cavitants : étude des comportements instationnaires et application tridimensionnelle aux turbomachines". Phd thesis, Laboratoire des Ecoulements Géophysiques et Industriels (LEGI).

[83] Jošt, D., Škerlavaj, A., and Lipej, A., 2014. "Improvement of efficiency prediction for a kaplan turbine with advanced turbulence models". *Journal of Mechanical Engineering,* ***60***, p. 124–134.

[84] Reboud, J.-L., Stutz, B., and Coutier-Delgosha, O., 2019. "Two-phase flow structure of cavitation: Experiment and modeling of unsteady effects".

[85] Bouajila, S., 2018. "Analyse expérimentale et numérique des écoulements à charge partielle dans les turbines Francis - Etude des vortex inter-aubes.". Phd thesis, Laboratoire des Ecoulements Géophysiques et Industriels (LEGI).

Appendix A

Distributor influence

In preliminary simulations on the simplified domain D_1, the experimental discharge Q_{exp} has been imposed as inlet boundary conditions (see chapter 4). Already in free-cavitation regime, discrepancies between the computed and the measured performances values (H and T) and velocity profiles at the runner outlet were observed (see chapter 5). In order to reduce this mismatch, the distributor has been included in the analysis. A decoupled simulation was performed. The numerical domain has been cut into two sub-domains:

- The D_d (reported in figure A.1 a) consisted in the spiral case, in the stay vane and in the guide vane;
- The D_s (shown in figure A.1 b) comprising the entire guide vane, runner and the first part of the draft tube, the cone.

Due to the complex geometry of the spiral case, the D_d has been discretized by means of an unstructured mesh approach. The meshing was performed by using the *Numeca* software *HEXPRESS*. The obtained mesh consists in 20 M elements. The mesh quality parameters (y^+, skewness and expansion ratio) have been respected. A steady simulation has been performed on the *Numeca* software *Fine/OPEN* imposing the Q_{exp} on the spiral case inlet and a constant static pressure on the guide vane outlet computed from the previous calculations on the domain D_1 (see chapters 4 and 5). To be consistent with simulations performed on the second sub-domain D_s, the $k-\omega$ SST turbulence model has been used. The numerical setup is summarized in table A.1.

Considering that no rotating frame have been included in D_d, the required computational resources was very low (10 cores and 5 CPU h). As it is shown in figure A.2, cylindric cutting plane has been created on the guide vane inlet. The velocity (V_m, V_t and V_r) and the turbulence (k and ε) profiles interpolated on this plane have been imposed on the inlet of the sub-domain D_s.

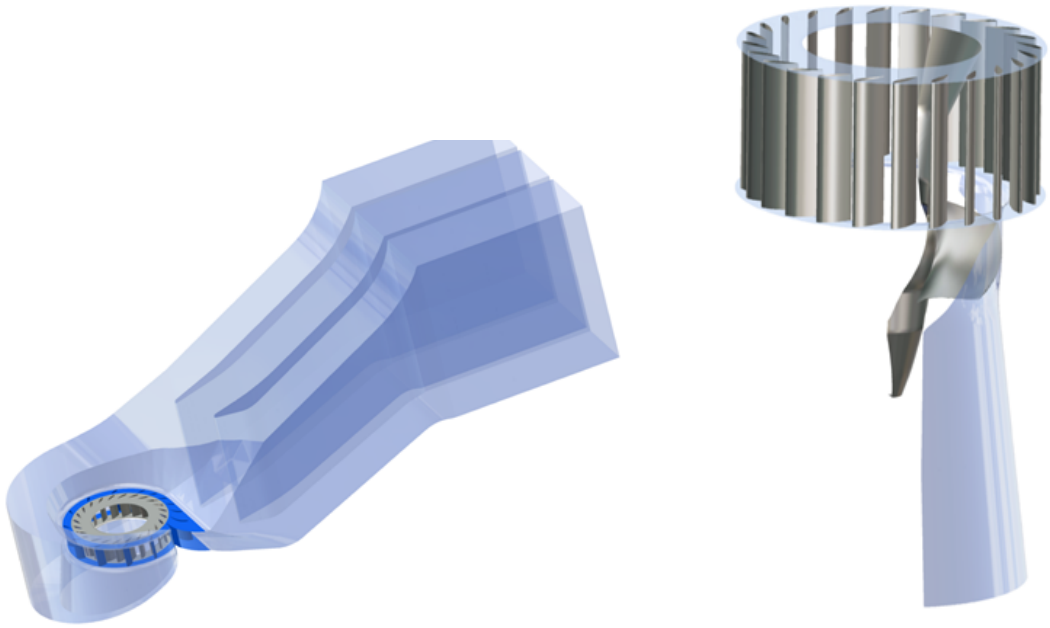

(a) **(b)**

Figure A.1 Sub-domains decoupled simulations: **(a)** the D_d composed by the spiral case, the stay vane and the guide vane; **(b)** the D_s comprising the 24 guide vanes and one full-periodic interblade runner channel.

Table A.1 Numerical setup for the decoupled simulation.

Domain	Inlet BC	Outlet BC	Turbulence model
D_d	$Q = Q_{exp}$	$P_{out} = P_{D1}$	$k-\omega$ SST
D_s	$Q = Q_{exp} + profiles$	$P_{out} = P_{amb}$	

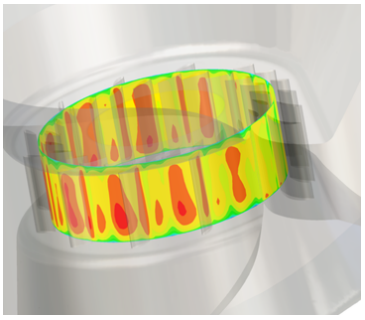

Figure A.2 Example of velocity profile used in the decoupled simulation.

The mesh sub-domain D_s was obtained replicating the discretization of the simplified domain D_1 for the 24 guide vanes. Hence, it has the same characteristics of the mesh M_2 (see chapter 4) but consists in 32 M elements. This has considerably affected the demanded computational resources, increasing the required cores from 32 to 48 and the CPU time from 224 h to 432 h.

A steady simulations has been performed by using the commercial code *FINE™/Turbo*. The velocity and turbulence profiles computed from the previous calculations on the sub-domain D_d and the Q_{exp} have been imposed on the guide vane inlet and a static pressure equal to the ambient one on the cone outlet. The $k-\omega$ SST model has been used as turbulence model. The numerical setup is reported in table A.1. The performances values (T, H and η) computed by the decoupled simulation have been compared with the ones calculated on the simplified geometry D_1 (as is shown in table A.2). The introduction of the distributor in the analysis has

Table A.2 Performances computed without (D_1) and with (D_s) distributor.

Domain	$\Delta T = \frac{(T_{exp}-T_{num})}{T_{exp}}$	$\Delta H = \frac{(H_{exp}-H_{num})}{H_{exp}}$	$\Delta\eta = \frac{(\eta_{exp}-\eta_{num})}{\eta_{exp}}$
D_1	10.8%	13.7%	3.4%
D_s	10.6%	13%	3.2%

not lead to significant improvements in the torque, head and efficiency values. The computed meridional (figure A.3 a) and tangential (figure A.3 b) velocity profiles on the runner outlet have a similar behavior using the two configurations. The computational resources demanded

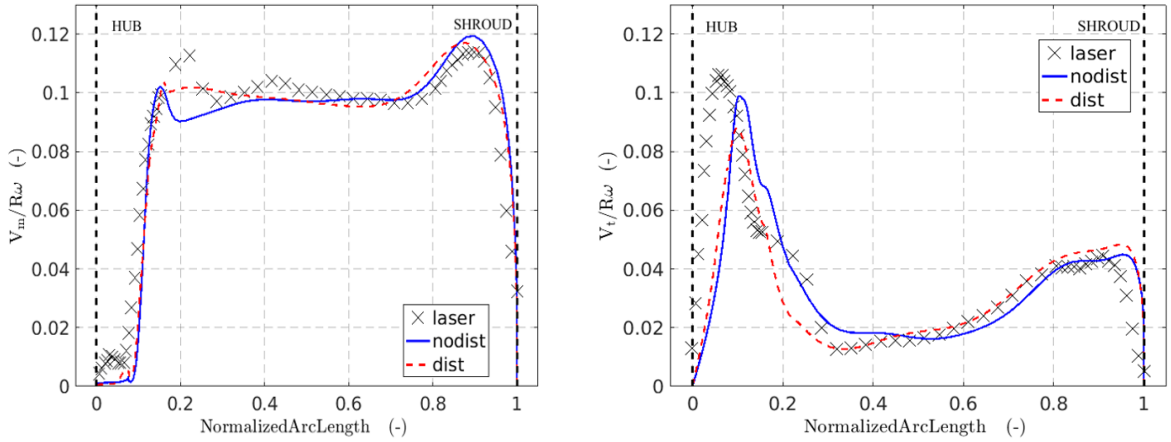

(a) **(b)**

Figure A.3 Evolution of the normalized **(a)** meridional, V_m, **(b)** and tangential, V_t, velocities along the normalized radius, measured by LDV (black crosses) and computed without (D_1 - blue line) and with (D_s - red dashed line) distributor.

to perform the decoupled simulation are too high against the marginal improvements of the predictions. Thus, this technique has not been consider applicable. On the other hand, the static an the total pressure difference value computed on the sub-domain D_d have been used in order to estimate the losses in the distributor.